INNOVATIVE SINTER PROCESSING OF NON-OXIDE CMC MATERIALS

by

Mary Casey, B.Sc.

A Thesis submitted in part fulfilment of the requirement for the degree
of

Doctor of Philosophy

Supervisors: **Dr. L. Looney**, School of Mechanical and Manufacturing Engineering Dublin City University, Ireland.
Mr. E. Bullock, , Joint Research Centre, Institute of Advanced Materials, Petten, The Netherlands.

DECLARATION

I hereby declare that

a) this has not been submitted as an exercise for a degree at any other university,

b) all un-referenced work in this thesis is entirely my own.

Furthermore, I agree that the library at Dublin City University may lend or copy this thesis upon request.

……………

Mary Casey
ID No. 95970916

May 2000

ACKNOWLEDGEMENTS

It is a delight for me to acknowledge the people who have supported me in bringing this thesis to completion.

Sincere thanks to Dr. Lisa Looney at DCU, for providing me with the opportunity to do this thesis and for consistent supervision and guidance. I am deeply indebted to Mr. Ted Bullock, at the JRC, NL, for taking over supervision of this project, his enthusiastic support and personal encouragement deserve particular mention. I would like to thank my colleagues of the former Composites Group and I would like to acknowledge the initial supervision of Dr. J. –B. Veyret., and particular thanks to Louise Plunkett and Endre Nagy for their valued technical assistance with experimental set up. I am appreciative to Boro Djuricic for our many scientific discussions and thank him for much beneficial advice.

I am grateful to numerous groups for use of their facilities plus aid and assistance. To Jürgen Ungeheuer, Richard Fordham, Burkhard Fischer, at the JRC, to Jan Dijkstra and Zbigniew Rak at ECN, Petten, NL and to the Ceramics Groups at Corus, Ijmuiden, NL. I am also thankful to the Jan Manten and Ruud Zitter for their kind assistance with compiling the final manuscript. A special word of acknowledgement goes to the Structural Analysis Group for their indispensable and always friendly service; Kurt Schuster, Peter Frampton, Rudi Van Nieuwhuizen, Pietro Moretto, Jap Van Eijk, Miguel Prieto and Paul Tambuyser.

It is my pleasure to thank all the staff at the JRC for creating a pleasant working environment, it is a bonus for me that my work there has brought in its wake many valued friendships. Love and thanks to 'the girls' for their long-distance support and good humour, and to Stephan for invaluable encouragement and understanding during the final months.

This project was funded by a training and mobility grant from the European Commission. The research work was carried out at the Joint Research Centre, Institute for Advanced Materials, The Netherlands, while the author was a registered student at Dublin City University, Dublin, Ireland.

This thesis is dedicated to my family whose love and support makes everything possible.

TABLE OF CONTENTS

ABSTRACT

Recent progress in the engineering of long fibre reinforced ceramic matrix composites (CMC) fabricated by hot pressing has led to the production of materials with high density and good mechanical properties. However, hot pressing limits the components to simple plate shapes, which often require very expensive machining. Pressureless sintering of CMC preforms to near net shape is a preferred alternative, greatly reducing costs and allowing the formation of complex component geometry.

However, there are major technical difficulties. Densification by infiltration of vapour or liquid precursors followed by pyrolysis, leads to unacceptable porosity (poor mechanical properties / no gas tightness) and very high cost. Densification from compacted powders is only possible at high temperatures, risking deleterious chemical interactions between the different constituents of the composite. Also, the achievement of a fully dense matrix in a composite manufactured by pressureless sintering is very difficult. The sintering/densification step requires the movement of partially liquefied ceramic particles to allow matrix shrinkage, while the fibre preforms are rigid, constraining shrinkage. Selection of more glassy, more mobile matrix phases assists densification but detracts from the high temperature mechanical properties of the product composite. Effective densification of a high temperature CMC has been achieved to date, only by the application of an external, mechanical pressure (hot-pressing).

The present work looks to improve the densification processing of a silicon nitride matrix composite reinforced with continuous carbon. Conventional low pressure processing requires extended heat treatment at temperatures up to 1850°C. This study has focussed on matrix phase sintering, principally to explore the ability of novel sinter additives to promote the synthesis of lower melting intergranular phases in-situ, thereby promoting matrix phase sintering at lower temperatures. This is targeted to reduce interphase reactions and to enhance matrix phase mobility at the densification temperature, while retaining the high temperature properties of the final ceramic. The primary goal was to identify sinter aid compositions which allow densification of the candidate matrix phases at lower temperatures by liquid phase sintering to greater than 95% Theoretical Density (TD). Si_3N_4 based ceramics were prepared containing sintering additive combinations of the form; $Y_2O_3 + Al_2O_3$, $Y_2O_3 + Al_2O_3 + AlN$, $Y_2O_3 + Al_2O_3 + CaZrO_3$.

The sintering behaviour, chemical stability, microstructural and phase development, and final properties, including hardness and oxidation of the sintered samples were examined.

Selected compositions were then used in the fabrication of a carbon fibre reinforced ceramic matrix composite by pressureless sintering, gas-pressure sintering and hot-pressing. The sinterability and compatibility of the densified composites were analysed and simple mechanical testing / microstructural analysis carried out in order to evaluate the degree of "composite" behaviour of the material subjected to mechanical deformation and fracture.

PUBLICATIONS ARISING

Arising from the present work the following papers have been published subsequent to presentations at the respective conferences.

- Influence of $CaZrO_3$ on the Sintering Behaviour and Microstructural Development of Si_3N_4 Based Ceramics, M. Casey, B. Djuricic, L. Looney, J.-B. Veyret and E.Bullock. *Presented at:* The International Symposium on Nitrides: ISN'T II,Limerick, Ireland, June 9-11, 1998. *Published in:* Nitrides and Oxides, Materials Science Forum, Vol. 325-326, pp. 161-167, 1999.

- Tailoring of Grain Boundary Phases for Pressureless Sintering of Long Fibre Reinforced Si_3N_4 Composites, M. Casey, B. Djuricic, L. Looney and J.-B. Veyret. Presented at: CCC IV, Mons, Belgium, Nov 18-20, 1997. *Published in:* Silicates Industriels, Vol. 64, No. 5-6, pp. 71-74, 1999.

1. INTRODUCTION

Silicon Nitride based ceramics are candidates for high and low temperature structural applications, owing to their good mechanical and thermal properties. In particular, Si_3N_4 based ceramics have excellent wear properties and high strength at high temperatures. They possess good thermal stress resistance due to a low coefficient of thermal expansion coupled with a moderate elastic modulus, which contributes to minimising stresses developed during severe temperature transients. Si_3N_4 ceramics have good resistance to oxidation and, because of their low densities, are attractive for the manufacture of low weight components. The major concern in using these ceramics and ceramics in general, is their inherent brittleness, which greatly restricts their reliability and applicability in service.

Minimising the quantity and size of structural defects, through careful control of raw materials and processing can enhance the toughness of ceramics. However, problems exist even if a "defect-free" ceramic could be manufactured since flaws are present as intrinsic microstructural features, such as grains or grain boundaries, which can cause cracking during loading. However, the toughness of a material can be considerably enhanced by incorporation of a second, reinforcing phase (whisker, particle or fibre) resulting in much a tougher ceramic material. These "ceramic matrix composite" (CMC) materials offer a novel opportunity for extending the temperature/stress capability of the most advanced structured components in current use, which is a major economic driver in today's industrial technologies.

1.1. Industrial Significance

The inexorable demand for heat engines to operate at ever-higher temperatures is driven by simple Carnot-cycle thermodynamics; for contained gases at constant pressure, increases in temperature means increases in volume, which in terms of engine output means increased in work and economic efficiency. High temperature reactions of this kind are inevitably gas phase. In principle, this means that for the reagents themselves there is theoretically, no absolute limit to raising process temperatures. The problem is containment, where, either the hot gases must be retained by a reaction vessel or where they must impinge upon solid mechanical components in order to do work. The limit to process temperatures and pressures is then only dependent upon the ability of structural materials to contain the process gas. At the present time, those components exposed to the most severe conditions of tensile stress, corrosion and high temperature are constructed from very advanced metallic alloys. However, the current demands for even higher temperature capability now surpass the capability of even the most sophisticated alloys, so that increasingly industry is turning to ceramics to provide solutions for the next generation of structural materials. Key industrial sectors are the gas turbine industry and heat exchangers for fossil fuel conversion.

1.2. Applications

1.2.1. Gas Turbine Engines

In a typical modern aircraft gas turbine power unit, air is ingested, compressed to 1.5MPa and then mixed with a pre-determined ratio of aviation fuel and combusted. The gas volume is thereby expanded some 20 times and is forced through a complex turbine stage comprising a series of static and rotating turbine rings, before exhausting to the air. The rotation of the turbine provides the power to drive the input air compressor and to force external air through peripheral annular (bypass) ducts giving thrust.

The efficiency of the engine increases with the temperature of the burnt gases exhausting from the combustion chamber the so-called turbine inlet temperature (TIT). The most critical components are the first row stator blades (nozzle guide vanes) and the first stage rotor blades which are exposed to a gas stream of about 1300°C and stresses, rotational (centrifugal) and bending of some 100 MPa. The property requirements of high temperature creep and fatigue strength, corrosion resistance, low density, toughness, micro-structural (thermal) stability, etc. mean that rotor blades are made of extremely sophisticated high temperature performance materials. This exceptional high capability is achieved by exhaustive alloying (often up to 12 elements), the development of single crystal components, coating with complex thermal barrier systems and extensive engineering of intricate cooling ducts leading cold air onto the blade surface. All of this engineering allows the blades, with a maximum intrinsic temperature capability of 1000°C, to operate in a gas stream temperature 300°C higher. However, ultimately the melting or softening temperatures of the alloys themselves limits the operating temperature of metallic components. In the case of the turbine superalloys the limit has been reasonably reached and the cost of squeezing out a further few degrees of operating temperature is not justified by the rewards. Further enhancement of operating efficiency will only be achieved by the introduction of an entirely new material system with higher intrinsic temperature capability.

Ceramics, by virtue of their chemical state, have a thermal stability, which far exceeds that of metals. The common "engineering" ceramics, metal oxides, carbides and nitrides, retain high temperature strength to several hundred degrees higher than the superalloys, and offer a major step-forward in high temperature structural component materials. However, the application requires a combination of properties, and enhancement of one particular property can often be achieved only at the cost of compromising another. For silicon nitride ceramics, the general balance of high temperature specific strength (strength per unit density), hardness, corrosion resistance, thermal stability, corrosion resistance, etc. are sufficient to accommodate a "skin" temperature capability uncooled, of at least 1350°C, that is well above the most advanced superalloys.

Curiously, the first benefit of this increased capability will almost certainly be to allow engines to operate at lower gas temperatures, since this gives significant environmental benefits. The drive to higher TIT values has been achieved for alloy components only by massive injection of cooling air through the component wall (both for blades and combustor chambers), which then flows over the metal surface to proved a cold insulation layer. While this confers a 300°C-temperature drop from the gas stream to the metal surface, this is gained at the expense of the overall gas temperatures. To compensate for this combustor temperatures are raised, often to 1350°C, with creates inevitably an increase in the formation of environmentally unfriendly gases of the NOx type. Ceramic structural components will eliminate the need for cold gas injection thereby allowing reduced combustor temperatures and a concomitant reduction in toxic gas emissions.

The main drawback of the ceramic systems is lack of toughness (resistance to impact) and extreme sensitivity to intrinsic flaws. Current attempts to improve toughness focus on the entrainment of long ceramic fibres within the ceramic matrix. The fibre-matrix interface can be engineered, usually by fibre coating, to provide a preferred fracture route with the absorption of otherwise catastrophic fracture energy. The incorporation of the fibres, however, introduces major processing difficulties and results inevitably in loss of strength, reduced thermal stability and most importantly an increase in cost. The benefits are, however, enticing as shown in a recent survey of European gas turbine industries by the consultants Quo-Tec Limited: Technological Forecast Study on Long Ceramic Fibres for High Temperature Applications [1]. Table 1.1 shows optimistic expectations for the uptake of these new materials in the next decades, from a technology sector that is notoriously cautious and safety conscious in evaluating new concepts.

Best estimates obtained from the above study indicate that CMC materials could represent 2.5% of an aero-engine by the year 2010. This represents a value of around $ 500 million.

YEAR	**2010**	**2020**
Engine Sales (US$ billions)	24	30
Ceramic Components %	2.5	20
CMC Component Value (US$ millions)	600	3,000
Forecasted Consumption of Advanced Ceramic Fibres		
World Total (kg)	150,000	600,000
European Total (kg)	50,000	200,000

Table 1.1 World growth forecasts for aeroengine production and CMC components [1]

1.2.2. Heat Exchangers

Another field of major impact for ceramic matrix composite materials in gas-burning heat engines is that of high temperature heat exchangers. Recuperative gas burners and associated high temperature heat exchanger components represent the best diversification opportunity for high performance CMCs (low mechanical stress, no impact problems). These components are targeted to continuous operation for several thousand hours at temperatures of up to 1400°C in corrosive (carbon, oxygen, and sulphur) gases at pressures up to 100 bar. The benefit of these materials has to be seen in higher operating temperatures and therefore thermal efficiency for power plant and other industrial applications. The US Department of Energy in a recent report [2] predicts that the thermal efficiency of power plant could be increased from 42 to 52 %, bringing an absolute energy saving for thermal power plant of 23.8 % and cost savings of millions of ECU over the whole of Europe. The market volume in the USA is higher, in response to which the Department of Energy (DOE) has recently initiated a major research programme on ultra high temperature heat exchanger materials.

The DOE report specifies the benefits expected from the progressive introduction of CMC materials in key components across a range of industrial applications, quantifying the expected gain in terms of energy savings, reduction in toxic gas emissions and in economic benefit for the year 2010 (Table 1.2)[2]. In addition to these benefits the US DOE has estimated the potential to create or save at least 100,000 industrial sector jobs for US citizens and including multiplier effects the number of affected jobs could be around 200,000.

TECHNOLOGY	**ENERGY BENEFIT (quadrillion btus)**	**ENVIRONMENTAL BENEFIT (reduction million tons)**		**ECONOMIC BENEFIT ($billions /year)**	**MARKET POTENTIAL ($billions /year)**
		NO$_x$/year	**CO$_2$/year**		
Gas turbines (large industrial)	0.4	0.3	22.6	1.3	1.5
Gas turbines (small industrial)	0.12	0.137	44.5	0.6	10
High Pressure Heat Exchangers	0.5	0.1	28.3	1.8	1.5-3
Waste incineration	0.5			2.5	0.3-0.6
Radiant Burners (steam burners)	0.066	0.24	3.7	0.33	0.75-1
Hot gas filters	0.1	0.023	5.7	0.5	0.4
Radiant burners (drying)	0.15	0.117	8.5	0.75	
Reformers	0.25		1.4		0.1-0.2
Radiant burners (high temp.)	0.075		4.2	0.38	0.4-0.8
Low Heat Rejection Diesel					
Diesel particulate traps					
Other Industrial					
Commercial/ residential	0.06	0.113	3.4	0.3	
Other non industrial					8
Total	**2.22**	**1.03**	**122.3**	**8.46**	**16**

Table 1.2 World growth forecast for CMC materials [2].

1.2.3. Brake Linings

A mass application currently under development is CMC materials for brake lining systems. These brake lining systems will be more expensive than current steel and carbon based systems and so will be initially targeted to the higher technology markets of aircraft, high-speed trains and large trucks. The potential market is estimated to be about 20 MECU per year for trucks alone. The total market in Europe will be about 200 MECU and is comparable to the market in the USA. For this particular application the tailoring of the fibre/matrix interface will enhance the applicability of carbon fibre-ceramic matrix materials since carbon/carbon composites are only applicable for short and extreme braking conditions: aircraft, racing cars. In particular, CMCs with tailored interfaces will help these problems with a cost effective fibre treatment remembering that any new solution of interphase tailoring will be easily adapted to different composite systems.

1.2.4. Future Developments

The successful development of these materials is controlled by the availability of reinforcing materials and efficient processing techniques. It is believed that innovative engineering in these areas will widen the range of potential applications and the practicability of Si_3N_4 based composites.

1.3. Materials Selection

The selection of the individual constituents that make up a CMC (ceramic matrix, reinforcement phase and reinforcement phase-matrix interlayer) is of the utmost importance since the performance of the final product depends both on their individual and combined properties. This new generation of structural materials is designed for components that will be subjected to tensile stress. The composite must therefore retain strength and structural integrity at high temperatures, initially for short to intermediate service lives (hundreds of hours) and in the future for longer lifetimes (years). These requirements will demand stability, both intrinsic (resistance to chemical decomposition, interphase reaction, phase changes, defect and crack growth) and to external constraints (resistance to plastic deformation under mechanical loading, to crack growth and fracture under impact loading, thermal shock resistance, resistance to oxidation/corrosion by external environment and so on).

Economic drivers will require that the composite is comparatively inexpensive to produce and that component manufacture is feasible without the need for costly shaping processes. These fabrication constraints will also influence materials selection, as, for example, the preferential selection of sinter phases that will allow low cost production while retaining composition and structure compatible with high temperature properties.

As indicated earlier, low toughness and low defect tolerance are primary problems, indeed, the necessity to find mechanisms to control fracture behaviour in the ceramic is the sole reason for the incorporation of the reinforcing phase. Here the combination of the matrix and fibre is important. The matrix should be bonded to the fibre to allow stress transfer from the matrix to fibre under loading, especially when the matrix begins to crack. Nevertheless the fibre-matrix bond must be weak, so that debonding along the interface is the preferred fracture mode, with the concomitant absorption of fracture energy and dispersion of crack tip stresses. Generally the reinforcement phase should have superior strength and/or refractoriness than the ceramic matrix but above all the selection should be based on minimising interactive effects between the reinforcing phase and the ceramic. These are primarily of two kinds, the mechanical and chemical.

The mechanical compatibility between the fibre and matrix arises from the essential requirement for the composite to transit between room temperature and high temperature (up to 1750°C) both during fabrication and service applications. The facility for relief of internal stresses by plastic deformation in the composite is extremely limited, especially at lower temperatures, so that any strain differences occurring as a result of thermal expansion mismatch between the phases must be accommodated by elastic strain within the composite phases. When fibre and matrix coefficients of thermal expansion (CTE) are significantly different, fracture of one of the phases by the other is inevitable. In normal practice, this is first evidenced after cooling from sintering temperatures. When the fibre CTE is lower than the matrix CTE, anisotropy shrinkage during cooling generates tensile stresses in the matrix, which become “frozen” into the structure. Above a threshold value these will crack the matrix to produce an array of parallel lateral cracks transverse to the fibre direction. Between two such cracks the matrix shrinkage is accommodated by matrix-fibre debonding and/or sliding to relieve the local residual stresses. Thus the intercrack spacing can provide a measure of the CTE mismatch between the phases, modified by the strength of the fibre-matrix bond and resistance to sliding.

Both of these modifiers can be manipulated and are engineered, usually by fibre coating. Nevertheless, when designing new composite compositions, the first consideration is to minimise CTE anisotropy between the phases. Fibres are not structurally isotropic and therefore exhibit different longitudinal and radial CTE values. Phase selection can, therefore, be used to enhance properties. Prerequisite is that the selection of phases should as far as possible ensure that the fibre-matrix bond strength is weaker than the fibre fracture strength, and that the fibre is not put into tensile stress by the cooling matrix to the extent that fibre fracture occurs. These properties can also be tailored. Thus for example, for optimum mechanical properties of the composite, the elastic modulus of the candidate fibre should be higher than the matrix, so that the fibres will bear a greater load than the matrix during loading and the fibre tensile strength should exceed that of the matrix to an extent that the fibres carry the load increasingly with progressive matrix-cracking.

In practical systems, composite fracture behaviour is controlled by the nature of the fibre-matrix interlayer, especially at high loading rates. Interlayer composition is determined by selection of sinter additives, which distribute to intergranular and interface sites during sintering, and if really necessary, the deposition of fibre coatings, although this option increases costs significantly. Here again material selection will control toughness, thermal shock resistance, gracile versus brittle behaviour, and fibre sliding after local matrix cracking. Compositions must be tailored to meet these requirements.

Chemical interaction gives rises most importantly to degradation of the reinforcing phase (and its beneficial properties) during the fabrication processes and subsequent service function at high temperature. The phases should be generally inert, not subject to spontaneous decomposition or to interphase reaction at high temperature. External environments at high temperature are especially reactive so that reinforcing phases should have good oxidation resistance and thermal stability. However, this is not limited to reinforcing phases. Non-oxide ceramic matrices and complex oxide-nitride interface layers are also susceptible to environmental attack at high temperatures so that here also a measure of oxidation resistance is essential.

Materials selection should also consider other properties as appropriate. Thus composites targeted to wear and tribological applications should be designed for hardness and wear resistance, while wear debris and possibly the reinforcing phases themselves can be engineered to enhance low friction properties of the sliding surface.

Finally the cost and availability of both the ceramic matrix and the reinforcing phase must be taken into consideration when making a selection. The effort to optimise combinations of phases almost invariably leads to more complex fabrication routes and increased costs. Possible processing routes for fabrication of the composite should therefore be chosen based on their cost effectiveness.

1.3.1. Practical Systems

1.3.1.1. Glass-Matrix Systems

Glass matrices in use are typically oxide materials, oxynitrides and glass-ceramics. Much work has been carried out on glass and glass-ceramics reinforced with SiC whiskers and fibres. Other reinforcements used are ZrO_2, mullite and alumina. However, most attention has focussed on a SiC fibre reinforced glass ceramic, Li_2O-Al_2O_3-SiO_2 (LAS) [3]. This composite however, has been shown to have a maximum use temperature up to about 1100^o. This is due to the fact that the glass-ceramic reaches its melting point leading to a loss in properties, which makes this composite (along with all glass-matrix composites) unsuitable for high temperature applications [4].

1.3.1.2. Oxide Matrix Materials

Alumina and zirconia are the principal oxide matrix materials most widely reported, of interest for commercial components. Alumina reinforced with SiC whiskers shows improved mechanical properties over the monolith, with the potential use as a cutting tool material [5]. Diamond additions to alumina were found to increase the hardness significantly [6]. Both Al_2O_3 and ZrO_2 have been used to form a series of particulate reinforced composites ($Al_2O_3 \rightarrow ZrO_2$ rich), where the most promising was the ZrO_2-toughened alumina [7] [8] [9]. Although the toughness of both of these monoliths can be greatly enhanced they are limited by their poor oxidation behaviour and creep properties [10].

1.3.1.3. Non-oxide Matrix Materials

Of greatest importance in this category of matrices are silicon nitride and silicon carbide. Strong covalent bonding, resulting in high-strengths and high melting points, and the intrinsic property of the compounds to form a protective SiO_2 layer at high temperatures in highly oxidising environments, make these non-oxide materials highly attractive for use in CMCs.

Significant experimentation has been carried out on the infiltration of SiC ceramic with fibres/fibrous structures of SiC, graphite and alumino-silicate materials [11] [12]. These SiC based composites show potential as both coating and bulk material in high-temperature engine applications.

The infiltration of Si_3N_4 into fibrous structures of carbon, titanium nitride and boron nitride and subsequent densification is easier than for SiC, primarily owing to the availability of a wide range of complex multi-component silicon oxynitride sinter phases with other metallic elements [13] [14] [15]. While the ultimate mechanical properties are intrinsically inferior, the easier fabrication of Si_3N_4 composites makes these more attractive as practical systems.

Particle reinforcement has been reported to improve the properties of Si_3N_4, for example, thermal shock resistance and electrical behaviour of Si_3N_4-based ceramics has been improved by the addition of BN particles [16]. ZrO_2-particulate reinforced Si_3N_4-based composites demonstrated almost double the strength of the monolith at temperatures higher than 1300°C [17]. SiC whisker composites show even higher toughness [18].

The greatest gain is shown, however, by long fibre reinforcements, as illustrated by work carried at the JRC Institute for Advanced Materials on carbon and silicon carbide fibre (both coated and uncoated) reinforced silicon nitride [19] [20].

1.4. Processing Developments

The processing of a ceramic matrix composite is an essential part of the design of a CMC component as it greatly influences the properties of the final product. Many processing routes are based on the corresponding monolithic fabrication route, but the requirement to combine two distinct phases together often means a more complex fabrication procedure together with increased costs. The ideal processing route should be cheap, result in a dense material, allow the fabrication of complex component shapes and prevent any damage to the reinforcing phase.

Chemical Vapour Infiltration (CVI) is to date the most widely developed process for the fabrication of fibre reinforced CMCs. Large, complex component shapes can be manufactured and a wide variety of matrices (oxides and non-oxides) can be used. One and two-dimensional carbon and silicon carbide fibre reinforced SiC with good mechanical properties have been manufactured successfully using this method [21] [22]. However, the process is extremely slow and expensive, with the ceramic matrix reaching at most 85% Theoretical Density.

Sol-gel and polymer infiltration pyrolysis (PIP) techniques are extensively used in the manufacture of monolithic ceramics and to a limited extent of CMCs. The sol-gel technique has been primarily applied to oxide systems, such as, Al_2O_3 and ZrO_2

using polycrystalline oxide fibres [23]. The PIP technique, on the other hand, has focussed principally on the production of SiC and Si_3N_4 matrix composites [24]. Although the processing temperatures for both routes are significantly lower than for conventional processing methods (thus saving costs and minimising fibre damage) [25], the fundamental disadvantage of both methods is that a very large shrinkage is incurred resulting in a low volume yield of ceramic.

1.5. Objectives of the Thesis

The present work researches the potential to improve densification, by low pressure sintering, of a long carbon fibre reinforced silicon nitride matrix composite. The first step of the project is to investigate the sinterability at lower temperatures of candidate Si_3N_4 matrix phase systems as monolith ceramics. This looks to the formation of sinter phases which melt at lower temperatures and so promote sintering of Si_3N_4 matrix and the composite to high density. The primary goal is to identify sinter aid compositions which would allow densification of the Si_3N_4 matrix to greater than 95%TD at lower temperatures while maintaining thermal stability at processing temperatures. The potential of selected compositions as suitable matrix phases for the fabrication of a C-Si_3N_4 composite is examined.

1.6. Structure of Thesis

The thesis is organised as follows:

- After this introductory chapter, Chapter 2 is a comprehensive literature review of the development of CMCs, their properties and fabrication methods. The factors involved in the slurry processing technique for fabrication of a carbon fibre reinforced Si_3N_4, is researched. Background theory of monolithic Si_3N_4 and composite densification behaviour, along with their basic properties is outlined.

- A description of all the processing steps involved in the fabrication of the monolith and composite samples is given in Chapter 3. Also outlined are the underlying principles, applications and limitations of the structural analysis techniques used throughout the project. Followed by a description of the property testing carried out.

- Chapter 4 contains the results and discussion of the project. The work pertaining to the identification of sintering additive composition for candidate matrix phases is outlined first (Section 4.1 – 4.7). This consists of the results of an extensive sintering study of a range of Si_3N_4 followed by detailed discussion on the densification behaviour, observations on microstructural analysis and phase development, and results and discussion of the basic property testing carried out.

- Following the monolith research, a selection of matrix phase compositions was chosen for use in the fabrication of composite materials. The densifcation behaviour and final microstructure of these composites, after densification by sintering and hot-pressing are outlined in Section 4.8. The results and discussion of some basic mechanical testing of the hot-pressed composite are given in Section 4.9.

- The conclusions of the work and suggestions for further work are presented in Chapter 5.

2. LITERATURE REVIEW

2.1. CMCs

2.1.1. Reinforcements

Reinforcements can be in the form of continuous fibre, short fibre, whisker, or particle as illustrated in Figure 2.1 [26].

2.1.2. CMC Principle

Table 2.1 lists fracture toughness (K_{1c}) values of monolithic compared with composite ceramic materials [27]. Increased fracture toughness of CMCs is greatest when long fibre reinforcements are used [28]. The reinforcing fibres act by permitting energy dissipating phenomena at the fibre/matrix interface during deformation. These phenomena include crack deflection and fibre bridging as illustrated in Figure 2.2 [29].

Deflection of the crack around the second phase reduces the stress-intensity at the crack tip, dissipating fracture energy, which increases the toughness of the material. The fibre bridging mechanism arises when the crack can pass through the matrix without damaging the fibres so that failure of the composite is dependent on fibre failure, which occurs by individual fracture and pull-out of the fibres. These mechanisms are essentially dependent on interface properties. The higher stiffness and strength of the fibres means that the failure of the composite occurs at a higher stress and strain than for the unreinforced matrix Figure 2.3 [30].

Material	**Fracture Toughness ($MPa*m^{1/2}$)**	**Critical Flaw Size µm**
Conventional Microstructure:		
Al_2O_3	3.5-4.0	25-33
Sintered SiC	3.0-3.5	18-25
Fibrous or Interlocked Microstructure:		
Hot-pressed Si_3N_4	4.0-6.0	33-74
SinteredSi_3N_4	4.0-6.0	33-74
SiALON	4.0-6.0	33-73
Particulate Dispersions:		
Al_2O_3-TiC	4.2-4.5	36-41
Si_3N_4-TiC	4.5	41
Transformation Toughening:		
ZrO_2-MgO	9-12	165-294
ZrO_2-Y_2O_3	6-9	74-165
Al_2O_3-ZrO_2	6.5-15	86-459
Whisker Dispersions:		
Al_2O_3-SiC	8-10	131-204
Fiber Reinforcement:		
SiC in borosilicate glass	15-25	
SiC in LAS	15-25	
SiC in CVD SiC	8-15	
Aluminium	33-44	
Steel	44-66	

Table 2.1 Fracture toughness and critical flaw size of monolithic and composite ceramic materials compared with metals [27].

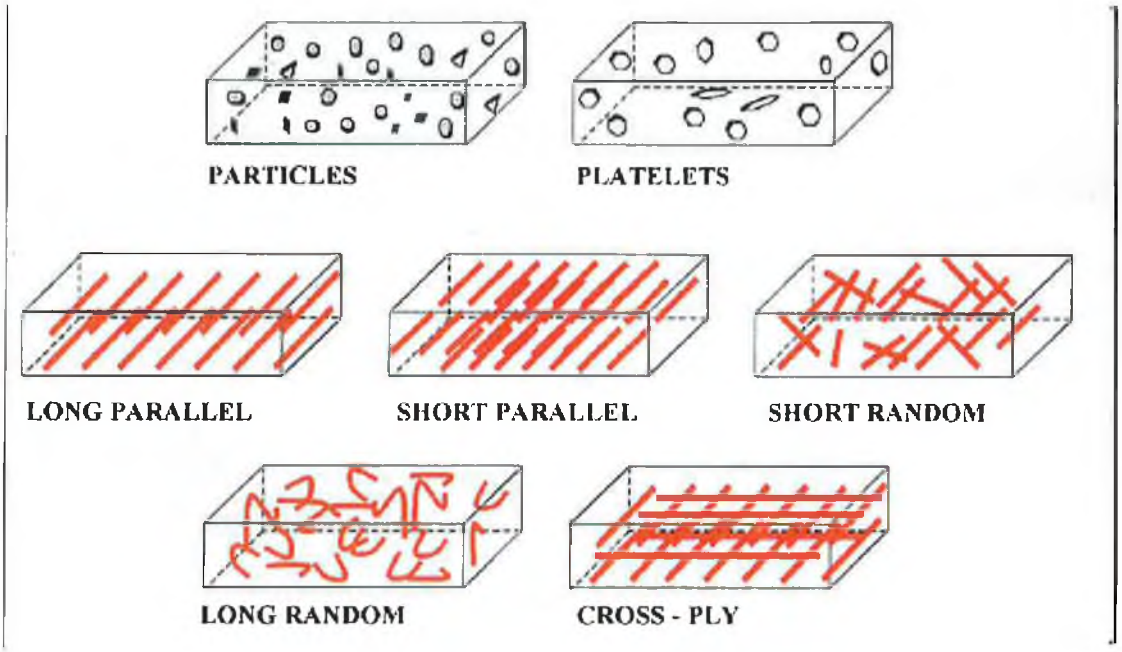

Figure 2.1 Schematic illustration of principal composite microstructures [26].

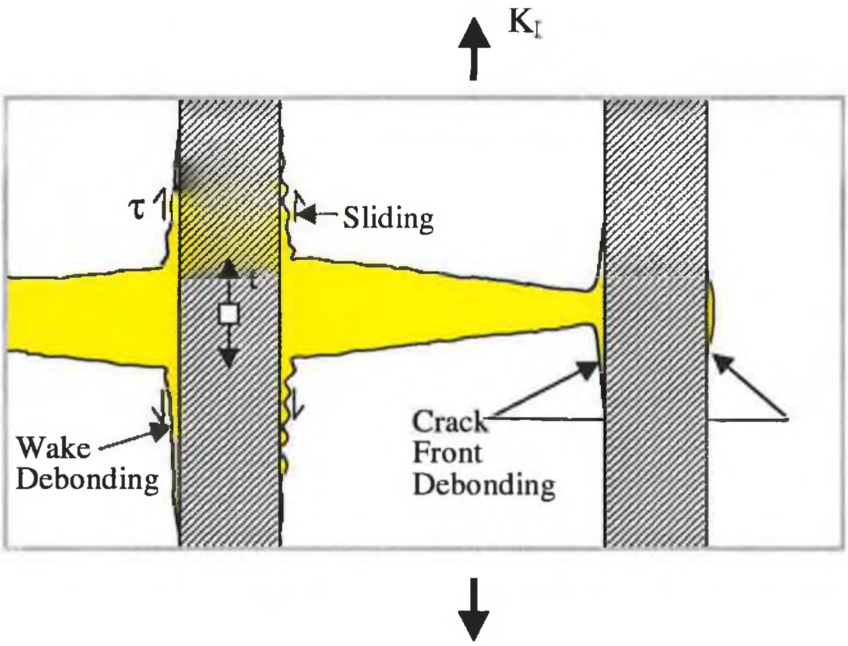

Figure 2.2 Crack deflection and fibre bridging mechanisms [29].

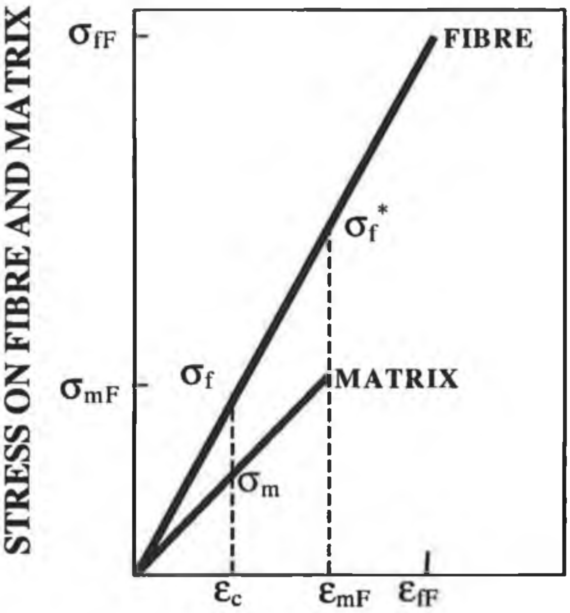

Figure 2.3 Stress-strain relationship curves of the fibre and matrix in a unidirectional, long-fibre reinforced composite. At composite strain, ε_c, the fibre and matrix stress are σ_f and σ_m, respectively. [30].

It is clear that the mechanical properties of CMCs are closely related to the fibre-matrix bonding. The composite will be brittle when this bonding is too strong and tough when it is weak enough to allow the crack deflection mechanism. Composites that demonstrate good damage tolerance behaviour have a fibre/matrix interface bond which is weak due to the presence of an interphase layer between the fibre and the matrix. To date, the only reported successful interfacial compositions are pyrolitic carbon (Pyr-C) and boron nitride (BN) because of their unique layered crystal structure oriented parallel to the fibre surface. Under such conditions a matrix microcrack propagating in the matrix can be easily deflected at the interface due to the low cohesive energy between the crystallographic planes. Unfortunately, Pyr-C and BN have poor oxidation resistance (>600°C). One key technological challenge is to identify an interphase that is thermally stable at high temperatures while having the required properties for crack deflection.

2.2. Manufacturing of CMCs

The processing of a ceramic matrix composite is an essential part of the design of a CMC component as it greatly influences the properties of the final product. CMC processing has evolved from the development of glass-matrix fibre composites in the 1960's [31]. However, for ceramic matrix composites, the requirement for crystalline ceramic matrices and relatively low processing temperatures does not allow the simple infiltration of a fibre preform by the matrix in the molten state.

Chemical Vapour Infiltration (CVI) is to date the most widely developed process for the fabrication of continuous fibre reinforced ceramic matrix composites because large complex shapes can be manufactured and a wide variety of matrices (oxides and non-oxides) can be used. Also, in specific systems, the process involves low risk of thermal, chemical and mechanical damage to the reinforcing fibres [32] [33] [34] [35]. This process basically involves the preforming of the fibres into the shape and dimensions desired in the final composite, they are then placed into reactant gases constituted of monolith precursors and heated to the required temperature, so that the monolith is formed and deposited in the interstices between the fibres. One- and two-dimensional carbon and SiC fibre structures have been successfully impregnated with SiC (CH_3SiCl_3 as the gaseous precursor) by the CVI process [35] [36] [11]. However, composites processed by CVI are porous, reaching at most a matrix of 85% Theoretical Density (TD). In addition the process is extremely slow and expensive. A more recent "gradient" CVI process has been developed at the Oak Ridge National Laboratory [38] [39] [40], which greatly reduces the infiltration time by manipulating pressure and thermal gradients in the manufacturing system, but still remains extremely costly, and the problem of scaling-up to large structures has yet to be overcome.

Sol-Gel and polymer infiltration and pyrolysis (PIP) techniques are extensively used in the manufacture of monolith ceramics and for the infiltration of fibre preforms to fabricate CMCs. Both techniques are based on the formation of a "green" structure using a ceramic precursor matrix, both inorganic and organic, followed by a calcination, or pyrolysis treatment to convert to ceramic and achieve a degree of densification. Some of their advantages for making composites are the same as those for making monolith ceramics:

- processing temperatures are lower by hundreds of degrees Centigrade than for conventional processing methods
- excellent compositional homogeneity can be achieved in single phase matrices
- these processes have the potential for forming unique multiphase matrices.

The sol-gel technique has been primarily applied to oxide systems, using polycrystalline oxide fibre preforms infiltrated with oxide matrices, such as Al_2O_3, ZrO_2, SiO_2 and $2SiO_23Al_2O_3$ [41] [42]. The polymer pyrolysis technique has focused principally on the production of SiC [36] and Si_3N_4 [43]. A composite containing Si_3N_4 reinforced with C fibre has been successfully manufactured using this method [44] [45]. However, the cost of the chemical precursors is high, and numerous infiltration/densification cycles are required, making the processing routes quite expensive. A further refinement of PIP technology, used extensively in the fabrication of C/SiC composites, is based upon metal vapour reactions with an infiltrated carbon matrix. In the most widely developed system a high char resin is infiltrated as liquid into a fibre preform, converted to carbon by heat-treatment and then to SiC by infusing with Si liquid at approximately 1500°C. However, the fundamental disadvantage of both processes, is the very large shrinkage incurred resulting in relatively low volume yield of ceramic.

The fabrication of glass and glass-ceramic matrix composites has been successfully developed using a slurry impregnation/liquid sintering method [31] [46] [47]. In this method, fibres in the form of multi-filament continuous tows are passed through a slurry (containing the matrix material, solvent and binder) and then wound on a mandrel and removed as a prepreg. The prepregs are then stacked into piles and densified by sintering or hot-pressing. The advantage of a glass matrix using this method is that because of its low viscosity it can flow around the reinforcing fibres to achieve full density without damaging the fibres.

Sintering of SiC and Si_3N_4 matrices utilises secondary additives which form liquid intergranular phases allowing sintering by liquid phase transport [48] (discussed in detail in Section 2.3). However the densification temperatures are still very high (>1550°C) compared to glass ceramics. Green-forming of composites by infiltration of ceramic powders is one of the critical parameters, which requires high uniformity and powder packing in the fibre preform. It includes slurry infiltration assisted by gas pressure or electrophoretic infiltration [49]. Densification by hot-pressing can result in composites with high strength and toughness.

However, hot pressing limits the component geometry to simple plate shapes that often require very expensive machining. Pressureless sintering of CMCs at lower temperatures is a preferred alternative, greatly reducing costs and allowing the formation of more complex component shapes.

However, there are major technical difficulties. Achievement of a fully dense non-oxide matrix in a fibre-reinforced composite manufactured by pressureless sintering is very difficult. Generally during the sintering/densification step, the ceramic matrix shrinks, while the fibres are rigid, constraining shrinkage and densification of the matrix phase (discussed in detail in Section 2.4.2). Typically, the sintered structure of the composite contains areas of well-densified matrix but with a high intrinsic volume of macro porosity [50]. Complete densification of the whole composite has been achieved, to date, only by the application of an external mechanical pressure (hot-pressing).

Traditionally long fibre/Si_3N_4 matrix composites are sintered using approximately 10wt% Y_2O_3/Al_2O_3 additives in the YAG ratio (1:1 molar ratio). Dense composites can be achieved by hot-pressing at 1750°C. Guo [51] successfully manufactured a C fibre reinforced Si_3N_4 composite at 1450°C, by using lower melting sinter phases (LiF-MgO-SiO_2), but with detrimental effects to the high temperature mechanical properties. The simple replacement of the tradition Y_2O_3/ Al_2O_3 oxides by, for example a low melting glass is not sufficient, as the final composite should have good mechanical properties at temperatures greater than 1350°C. Ideally what is required is a sinter-aid combination which has a low-melting point but which crystallises by post-sintering heat-treatments to crystalline phases which are thermally stable at higher temperatures.

2.2.1. Slurry Processing

The more direct processing method of CMCs involves the infiltration of a fibre preform with a dispersion of ceramic powder as a slurry. Slurry processing involves simply the infiltration of a fibre preform with a dispersion of the matrix phase material, consisting of the ceramic and sinter aids, prepared as a simple powder-mix. Uniform and optimum infiltration of the fibre preform to high density is of the utmost importance in this processing method [52]. The parameters of particular importance are:

- stable and well-dispersed suspensions (high repulsive forces between particles) with maximum solid content compatible with low viscosity,
- excellent wetting of the fibres by the slurry,
- small powder particle size to interfibre spacing ratio to allow easy access through the fibre pre-form channels,
- a controlled consolidation technique to optimise uniform microstructure and high packing density in green compacts.

2.2.1.1. Powders in Liquids

The optimisation of the dispersion characteristics of a ceramic suspension can be achieved once the behaviour of the ceramic powders in the medium used is known. Finely divided ceramic powders have a high surface area to volume ratio so the chemical and physical properties of their surfaces tend to control their behaviour in liquid suspension. The interaction between two particles in dispersion has been examined independently by Derjaguin and Landau [53] and Verwey and Overbeek [54], leading to the well-known DVLO theory. According to this theory, ever-present attractive and repulsive forces between particles in solution govern the stability of a suspension. When Van der Waals attractive forces dominate a suspension the particles coagulate or flocculate, resulting in particle agglomerates and aggregates which sediment out of solution. The Van der Waals attractive force is a function of the dielectric constant of the medium and the mass and separation distance of the particles.

For two small spherical particles of diameter a, the potential energy of attraction U_A is

$$U_A = -\frac{A_a}{24h} \qquad \textbf{2.1}$$

Where h is the separation between the surfaces of the two particles and A is the Hamaker attraction constant ($A = \pi^2 q^2 \beta$, where q is the number of atoms per cm^3 and β is the attraction between 2 atoms 1cm apart).

Repulsion may be provided by the electrostatic interaction between two particles. Once added to a liquid, the surface of a particle may become charged by desorption or adsorption of ions at the surface of the material, or by a chemical reaction (for example, hydrolysis, dissociation and complexation) between the surface and the liquid medium [55]. Coulombic forces will repel like-charged ions but attract polar liquid molecules and oppositely charged ions into a region near the surface, thereby forming what is termed an electrical double layer around the particle. The charge distribution can be divided into two regions; (1) a compact layer close to the particle surface where the adsorption of ions and chemical reactions occur; and (2) a diffuse layer extending out to the bulk solution in which only electrostatic effects play a part. The Gouy-Chapman-Stern model of the double-layer is illustrated in Figure 2.4 [56]. The shear plane depicted in the diagram defines the boundary between the fluid, which moves with the particle under an applied electrical field, and the bulk solution. This boundary is characterised by its potential, termed the zeta potential, ζ, which is regularly used as a measurement of the stability of the suspension.

Influence of pH

The pH at which ϕ_ζ is zero is termed the isoelectric point, IEP. This pH should not be confused with the Point of Zero Charge, PZC, the pH where the charge on the particle surface is zero. The interaction between electrical double-layers leads to repulsive forces in the solution.

The magnitude of the repulsion depends on the size and shape of the particles, the distance between their surfaces, the permitivity of the liquid media, ε_r, and the double-layer thickness. The thickness of the a double-layer, K^{-1},is determined using [57]:

$$K^{-1} = \left(\frac{F^2 \Sigma Ni Zi^2}{\varepsilon_r \varepsilon_0 K_B T} \right)^{-\frac{1}{2}} \qquad \mathbf{2.2}$$

where,

Ni = concentration of each type of ion in the dispersion
Zi = valance of each type of ion in the dispersion
F = Faraday's constant
ε_0 = permitivity of free space.

For each system there is a critical zeta potential and range of double-layer thicknesses for which the repulsive potential energy exceeds the attractive potential energy, thus producing an energy barrier to coagulation and flocculation. As the distance between the double-layers increases to the order of the particle size, a secondary minimum in the potential energy curve appears Figure 2.5 [57].

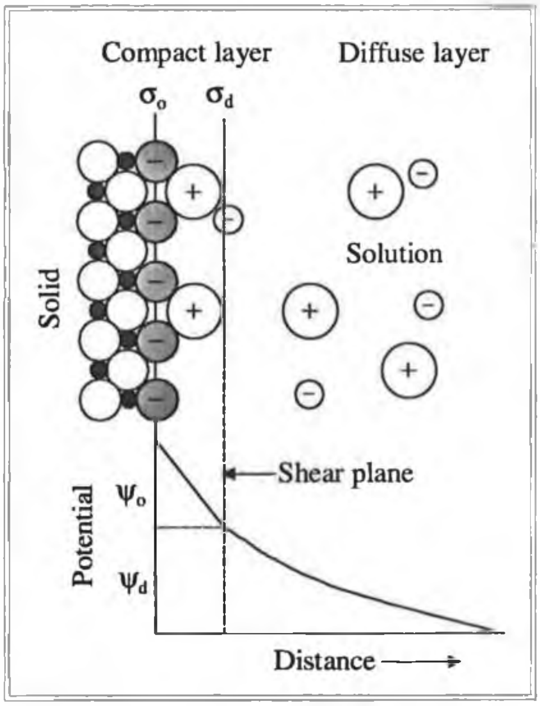

Figure 2.4 Gouy-Chapman-Stern model of the electrical double-layer and potential decay at an oxide-water interface: o, lattice oxygen; θ, surface oxygen; •, metal ion; ⊕ θ, solution ions [56].

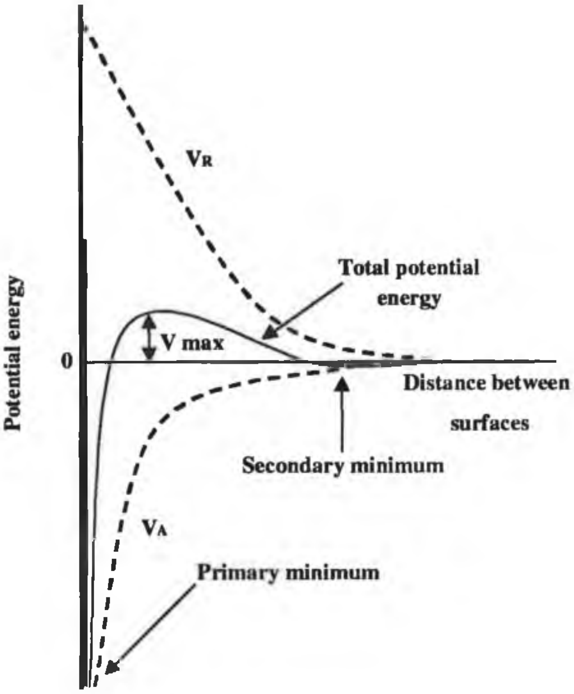

Figure 2.5 The potential energy between two particles in a liquid resulting from the effects of the Van der Waal's attraction and double layer repulsion [57].

Use of Organic Additives

As can be seen from Equation 2.2, the thickness of an electrical double-layer, and thus the repulsion between two double-layers can be controlled by varying the ionic strength of the bulk solution. Also, by changing the degree or even the sign of the particle surface charge, by addition of an electrostatic surface-active agent, a surfactant [58]. In nonpolar liquids steric hindrance (which prevents or retards inter- or intramolecular interactions as a result of the spatial structure of the powder particles) produces repulsion. Agents that promote repulsion/deflocculation are either simple or polymer electrolytes.

For Si_3N_4 aqueous suspensions, polyelectrolyte dispersants provide stability through electrosteric repulsive forces and interact strongly with surface sites on the powder [59]. The surface structure of silicon nitride, is composed of acidic silanol (Si-OH) and basic silazane (Si_2=NH) groups [60]. The relative abundance of these sites varies with the surface oxide content [61]. When added to water, Si-OH and Si_2=NH sites generate surface charge by the adsorption of OH^- and H^+ ions, as shown in Figure 2.6 [60]. These sites may also complex with dissolved ionic species. The electrical properties of the dispersed Si_3N_4 particles, as a result of these interactions, will govern their interactions with each other and with other charged species in the suspension. The isoelectronic point of Si_3N_4, reported in literature, lies in the range of pH 3→9 [62].

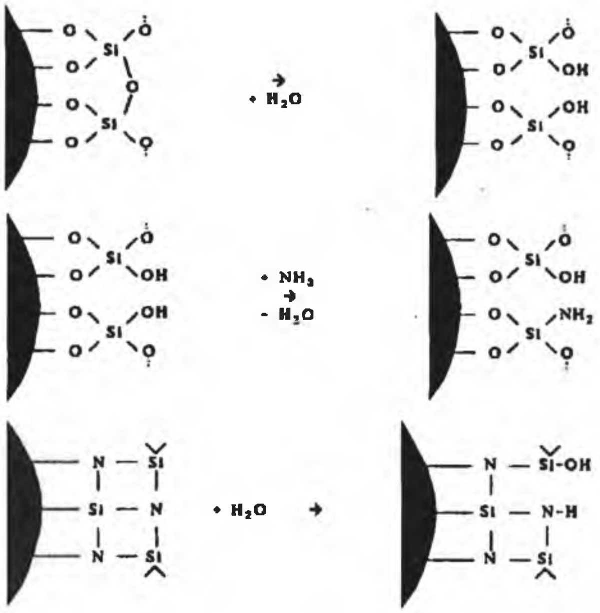

Figure 2.6 The potential reactions of silicon nitride in water [60].

Rheology of Dispersions

The flow of a liquid can be described by its viscosity η, defined by

$$\eta = \frac{\tau}{\gamma} \qquad 2.3$$

where τ is the shear stress and γ is the shear rate. A liquid is termed Newtonian if its viscosity is independent of γ. If η is not independent of the shear rate, then the liquid is non-Newtonian and then its viscosity is defined by

$$\eta(\gamma) = \frac{\partial \tau}{\partial \gamma} \qquad 2.4$$

Therefore, by plotting the shear stress versus shear rate, the slope of the resulting curve is η.

The stability of a ceramic dispersion, as discussed before, is of the utmost importance in the slurry processing of ceramic based composites. Rheological measurements can be used to obtain information on the state of dispersion to optimise the flow behaviour of the suspension.

In the 1900's, Einstein derived a detailed theoretical expression defining the effect of the addition of particles on liquid viscosity. His derivation is explained in detail in The Principles of Colloid and Surface Chemistry [63]. The derivation results in the equation:

$$\frac{\eta}{\eta_0} = 1 + 2.5f \qquad \textbf{2.5}$$

where,

η = the viscosity of the suspension.

η_0 = the viscosity of the liquid medium.

f = the volume fraction of particles.

However, the use of this theory is extremely limited, as it assumes that the particles are hard spheres, large compared to solvent molecules (to permit the solution being referred to as a continuum) and it neglects the presence of electric double-layers. It is now recognised that the rheology of a suspension depends on the concentration of particles and on the interparticle forces between them (as described previously).

Dilute, dispersed ceramic slurries exhibit Newtonian rheology. At high volume fractions of powder, the viscosity of the slurry increases with increasing shear rate (shear thickening). This behaviour occurs due to the kinetics of rearrangement and because the system must increase its volume to allow closely spaced particles to slip past one another.

It can be described using the expression

$$\tau = \mathrm{K}\gamma^{\eta} \qquad \textbf{2.6}$$

where,

K = consistency index

η = the exponent that indicates the deviation from Newtonian behaviour.

If, $\eta = 1$, the suspension exhibits Newtonian behaviour.

$\eta < 1$, the suspension exhibits shear thinning or pseudoplastic behaviour.

$\eta > 1$, the suspension flow is described as shear thickening or dilatant.

Flocculated dispersions show pseudo plastic or thixotropic rheology (when the viscosity depends on the shear rate and also on time), because the separation of particles attracted to each other (flocs), depends on the shear rate. When the suspension is sheared, the flocs are separated and distributed in the suspension. Regeneration of the flocs, and thus destabilisation of the suspension, is therefore time dependent. A material is named a Bingham plastic, if it requires a finite stress, yield stress, τ_y, to initiate flow. This type of suspension obeys the equation:

$$\tau - \tau_y = \eta_p \gamma \qquad \textbf{2.7}$$

where η_p is independent of the shear rate.

Figure 2.7, demonstrates the different types of rheological behaviour [64]. As is apparent the rheology of a suspension depends on the concentration of particles and on the interparticle forces between them.

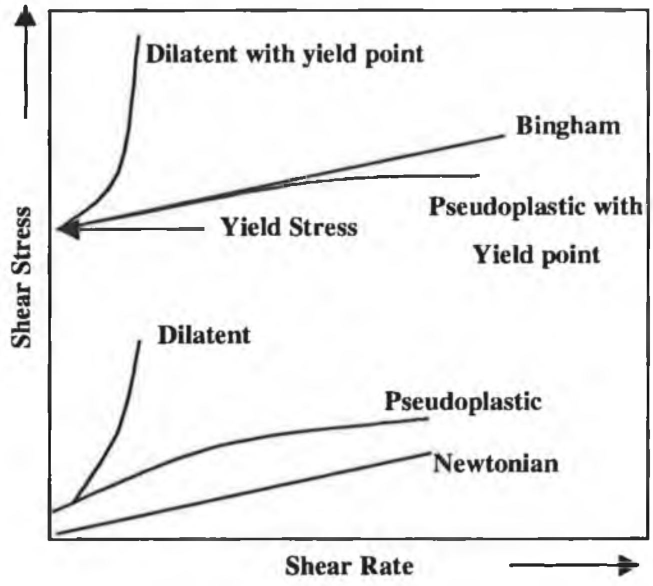

Figure 2.7 Dependence of shear stress on shear rate for Newtonian, Bingham, and pseudoplastic on dilatant systems with and without a yield point [64].

2.2.2. Consolidation of the Green Body

2.2.2.1. Casting

A ceramic slurry can be consolidated by a casting processes. Conventionally, an aqueous clay slurry is called a slip and the casting method, slip casting. This method simply involves the pouring of the slip into a permeable mould and, as a result of capillary suction and filtration forces, the suspending liquid is removed and the solid particles are concentrated on the wall of the mould, forming a cast [65]. When an acceptable thickness of the cast has formed, the excess slurry is poured off and the mould and cast are allowed to dry. During the drying process the cast will shrink away from the mould and can be easily dislodged. Slip casting is frequently used for the consolidation of a variety of ceramic slurries. For each slurry, the powder characteristics; particle size, and shape, must be optimised, also the degree of flocculation and pore size of the mould, in order to obtain casts with high particle packing densities.

The rate of casting is defined by Darcy's Law [66] which describes the flow of liquid through a porous medium

$$J = \frac{KP}{\eta_L} \qquad \textbf{2.8}$$

where,

J = the flux of liquid

P = the pressure gradient in the liquid

η_L = the viscosity of the liquid

K = the permeability of the porous medium.

After integration of this equation, and the application of appropriate boundary conditions, Tiller and Tsai [65] related the thickness of the consolidation layer, L^2, to the casting time:

$$L^2 = \frac{2Hpt}{\eta_L} \qquad \textbf{2.9}$$

where, the function H is dependent on the properties of both the consolidated layer and the mould,

p = the total filtration pressure

t = time

η_L = the viscosity of the liquid

It is clear from Equation 2.9 that applying an external source pressure to the slurry in the mould can reduce the casting time. This procedure is termed pressure casting or pressure infiltration and is widely used in industry to consolidate solids in slurries. Highest packing densities are achieved with well-dispersed slurries. The packing density is independent of the applied pressure in this case, ≈ 0.5MPa. Whereas for flocculated slurries, the packing densities are dependent on the pressure (Figure 2.8) [67]. Pressure infiltration has been successfully employed in the consolidation of long carbon fibre preforms with a submicron silicon nitride aqueous slurry [68]. Figure 2.9 represents the system used.

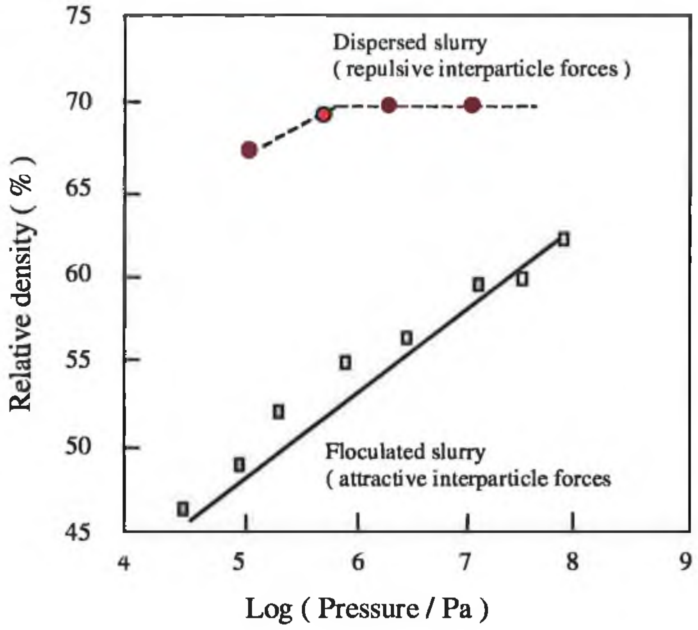

Figure 2.8 Dependence of packing densities of flocculated slurries on pressure [67].

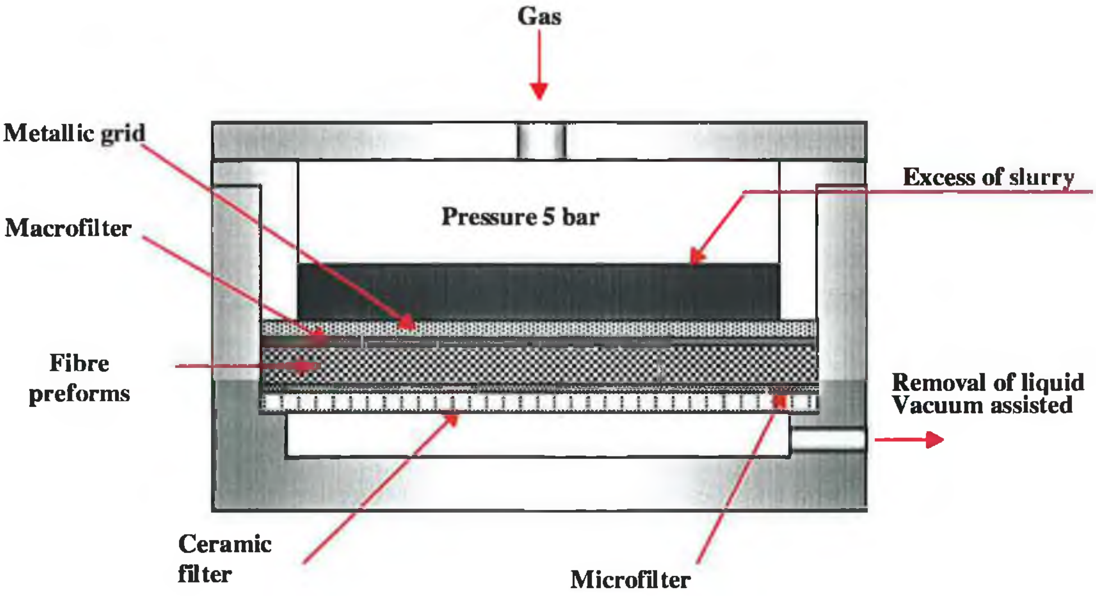

Figure 2.9 Pressure Infiltration system [68].

2.2.3. Pre-Sintering Processes

2.2.3.1. Drying

Drying of a ceramic green body formed by casting or plastic forming, is an important step prior to organic burnout and firing. While the problems arising during drying of these ceramics are not as great as those processed using the sol-gel method [69], careful control of drying conditions is essential because cracking and warping can occur, due to differential stresses caused by pressure gradients and non-uniformities in the green body.

The three stages of drying are shown in Figure 2.10. The first stage is termed the constant rate period (CRP), because the rate of evaporation of liquid is independent of time and moisture content [70] [71], and can be described by

$$V_E = H(p_w - p_a) \qquad \textbf{2.10}$$

where,

p_w = vapour pressure of the liquid at the surface

p_a = ambient vapour pressure

H = evaporation constant, dependent on the temperature, velocity of the drying atmosphere and geometry of the system.

Before drying the meniscus is flat, stage (A) in Figure 2.10. During evaporation dry patches form on the surface and are re-wetted by stretching of the liquid surrounding the particles. As a result of stretching, tension develops in the liquid, stage (B) in Figure 2.10, and to balance this, the solid phase goes into compression, and the liquid meniscus remains at the surface. As drying continues the contraction of the solid phase reduces the porosity and the particles bond together forming a stiff body. The liquid meniscus then deepens and the tension in the liquid increases to a maximum possible value. Beyond this point the liquid tension cannot overcome the stiffness in the solid phase and the evaporation rate decreases. This is the critical point and it marks the end of the CRP stage. Drying now enters the falling rate period (FRP), stage (C) in Figure 2.10 which can be divided into two parts, in the first, evaporation of liquid still occurs from the surface and in the second evaporation takes place from inside the body by diffusion of vapour.

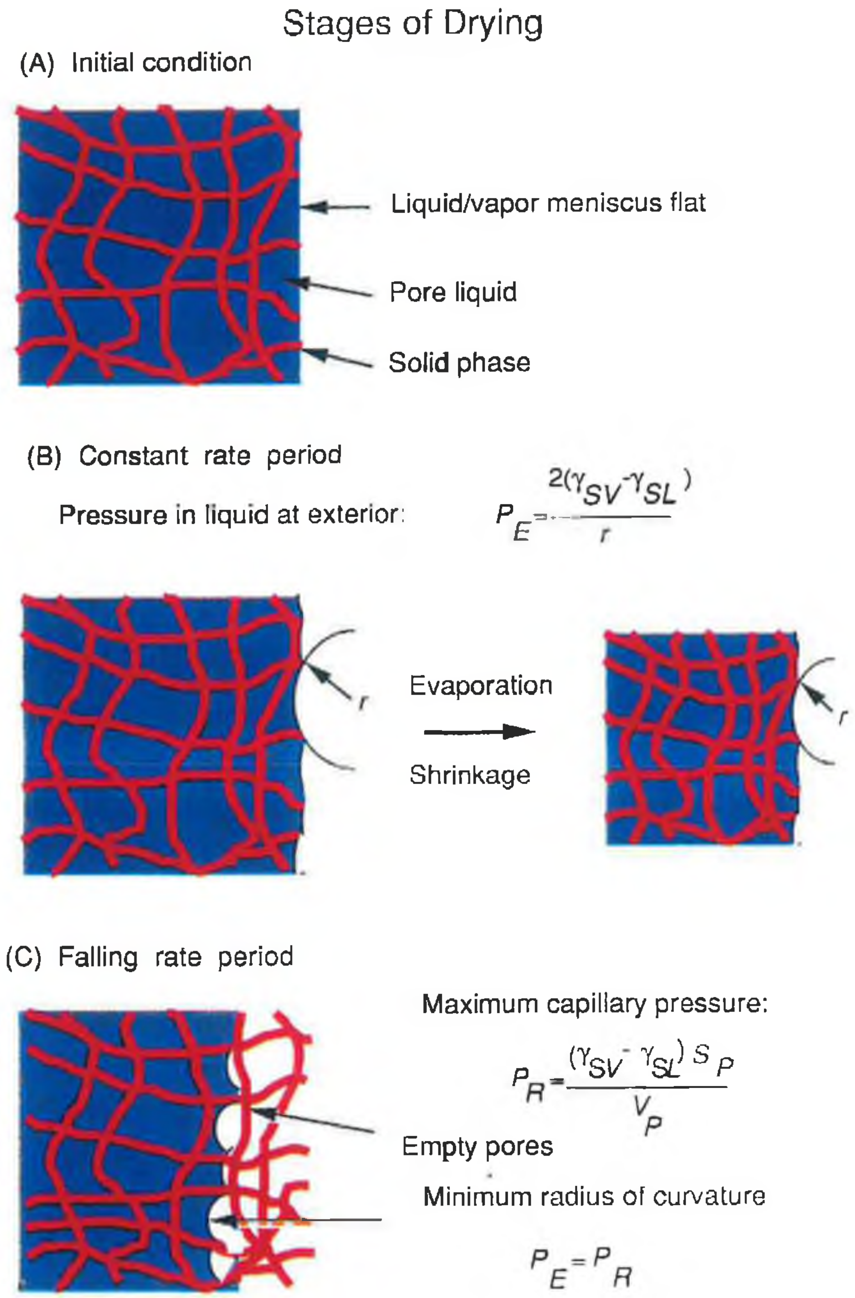

Figure 2.10 Schematic illustration of drying process [69]. Where, red network represents solid phase and blue area is liquid filling pores. γ_{SV} and γ_{SL} are the solid/vapor and solid/liquid interfacial energies, respectively. S_P/V_P is the surface-to-volume ratio of the pore space.

As was mentioned earlier, cracking and warping result from differential stresses. Pressure gradients may be responsible for introducing stresses according to the following equation:

$$\sigma_x = \sigma_y \cong < p > - p \qquad \textbf{2.11}$$

where,

p - negative pressure in the liquid (tension)

<p> - average pressure in the liquid

If the tension which develops in the liquid is uniform then the stress in the solid phase is zero. However, p may vary through the thickness causing a differential strain as the solid phase contracts more when p is high. The differential strain/stress will then cause warping and cracking.

A high evaporation rate can also introduce pressure gradients and thus problems according to

$$V_E = \frac{k}{\eta_L \nabla_p} \qquad \textbf{2.12}$$

where,

V_E - evaporation rate

k - permeability of the solid phase

η_L - viscosity of the liquid

∇_p - pressure gradient

If V_E is high then a large pressure gradient exists in the liquid and this as explained above leads to warping and cracking. The influence of pressure and stress has been outlined in detail by Scherer [69].

However even if the body is dried uniformly and at a slow rate, cracking and warping may still occur. Differential liquid concentration in the body due to forming methods leads to differential shrinkage and thus warping. Differential shrinkage may also occur due to gradients in particle size within the solid. Figure 2.11 illustrates the development of warping [71]. Drying of a composite fabricated by a wet-forming method, for example slurry infiltration will require extra attention to prevent damage to the green body, since the reinforcing phase will introduce mechanical constraints to shrinkage and thus hinder uniform drying.

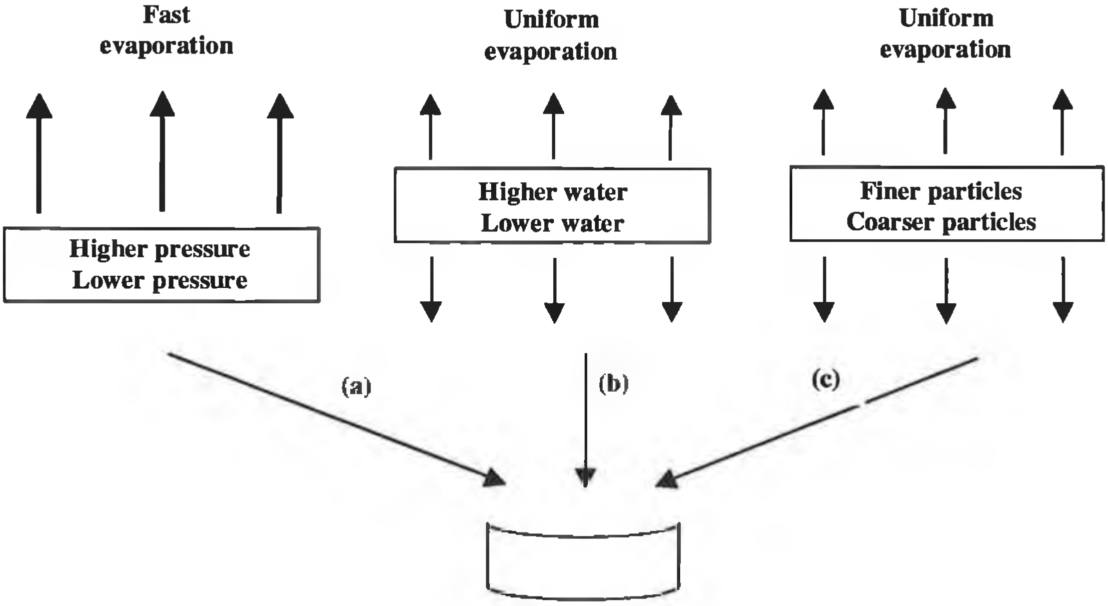

Figure 2.11 Development of warping during drying [71].

2.3. Densification of Si_3N_4 Matrix by Liquid phase sintering (LPS)

As was outlined in the Introduction, Silicon Nitride based ceramics are attractive materials for high temperature applications due to their high-strength and melting point, resulting from the strong covalent nature of the Si-N bond. However, these high-energy covalent bonds are problematic in the formation of dense monolithic Si_3N_4 in massive form from a powder compact. The low self-diffusivity of these covalently bonded materials mean that the species become mobile enough for sintering only at high temperature (>1850°C) which is approximately the temperature at which Si_3N_4 starts to decompose. Consequently, early attempts to sinter pure Si_3N_4 were unsuccessful [72]. Shimada et al. [73] did fabricate fully dense pure Si_3N_4 but only with the use of extremely high pressures (gigapascals). Today, successful fabrication of massive dense silicon nitride from powder precursors is usually achieved by a solution-precipitation process using a low volume fraction additive mix which melts at lower temperatures – liquid phase sintering (LPS).

The fundamental basis of the LPS procedure is that at a particular temperature, the sintering additives react with each other and with the surface layers of the ceramic powder particles to form a partially liquid continuous intergranular phase. This liquid phase promotes densification by a series of successive, overlapping steps, (i) rearrangement, (ii) solution and precipitation and (iii) microstructural coarsening.

The densification mechanisms occurring during these three steps are outlined in Section 2.3.3. But at the outset, the driving force for LPS and the key kinetic and thermodynamic factors affecting each step are outlined.

2.3.1. Driving Force for Densification

The liquid phase present at sintering temperature during LPS enhances densification by accommodating particle rearrangement (since the friction between particles is considerably reduced) and by promoting matter transport (since diffusion through a liquid is significantly faster than in a solid. The driving force for densification by LPS stems from the capillary pressure in the liquid surrounding the solid particles. In cases where the liquid phase wets and spreads well over the solid particles, it removes all solid-vapour interfaces in the system. Although this results in an energy decrease in the system it also results in the formation of pores in the liquid phase. It is the removal (or reduction) of the resultant liquid/vapour interfacial areas that provides the driving force for shrinkage and densification of the system. The equation of Young and Laplace (Equation 2.1) describes the pressure difference across a curved surface:

$$\Delta p = -\frac{2\gamma_{lv}}{R} \qquad \textbf{2.12}$$

where, Δp is pressure difference

γ_{lv} – the liquid-vapour surface energy

R – radius of the pore in the liquid

The pressure in the liquid is lower that in the pore, thus placing the solid particles under a compressive stress, which can be of a magnitude sufficient to provide the driving force for sintering.

2.3.2. Kinetic and Thermodynamic Factors

2.3.2.1. Wetting of Particles/Grains

The contact between a liquid and a solid at equilibrium is illustrated in Figure 2.12 [74]. Equation 2.13 derived by Young (1805) and Dupre (1869) describes the relationship,

$$\gamma_{sv} = \gamma_{sl} + \gamma_{lv}\cos\theta \qquad \textbf{2.13}$$

where, γ_{sv}, γ_{sl}, and γ_{lv} are the specific energies of the solid-vapour, solid-liquid and liquid-vapour interfaces respectively, theta is natural contact angle between the solid surface and the liquid meniscus.

A small contact angle, less than 90°, is opened with good wetting of the solid particles. It is generally found that liquids with low surface tension form a low contact angle with most solids resulting in good wetting.

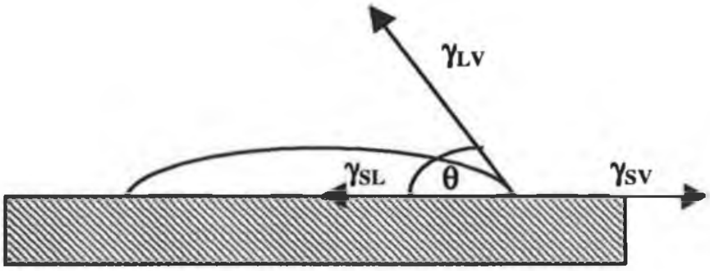

Figure 2.12 Wetting behaviour between a liquid and a solid, showing the balance between the interfacial tensions for a liquid with a contact angle of θ [74].

2.3.2.2. Liquid Spreading

Perfect spreading of the liquid phase across the solid surface occurs to reduce the total interfacial energy of the system, that is when:

$$\gamma_{lv} + \gamma_{sl} - \gamma_{sv} = 0 \qquad \textbf{2.14}$$

Referring to equation 2.13, the contact angle must be zero to satisfy equation 2.14, and thus ensure perfect spreading of the liquid.

2.3.2.3. The Dihedral Angle

The dihedral angle, ψ, is defined as the angle between solid-liquid interfacial tensions, illustrated in Figure 2.13 [75]. Rahaman [76] defined the equation for this situation as,

$$\cos\left(\frac{\Psi}{2}\right) = \frac{\gamma_{ss}}{2\gamma_{sl}} \qquad \textbf{2.15}$$

γ_{ss} and γ_{sl} are the solid-solid and solid-liquid interfacial energies (or tensions) respectively.

When $\gamma_{ss}/\gamma_{sl} < 2$, the dihedral angle is between 0° and 180°, and the liquid does not completely penetrate the solid-solid interface (grain boundary). In the case where $\gamma_{ss}/\gamma_{sl} > 2$, no value of ψ will satisfy equation 2.15, and the liquid will completely penetrate the grain boundary. Complete liquid penetration of the grain boundary leads to a reduction in the total energy of the system, as when $\gamma_{ss}/2\gamma_{sl} > 2$, the sum of the 2 solid-liquid interfacial energies ($2\gamma_{sl}$) is less than that of the solid-solid interface $\gamma_{(ss)}$.

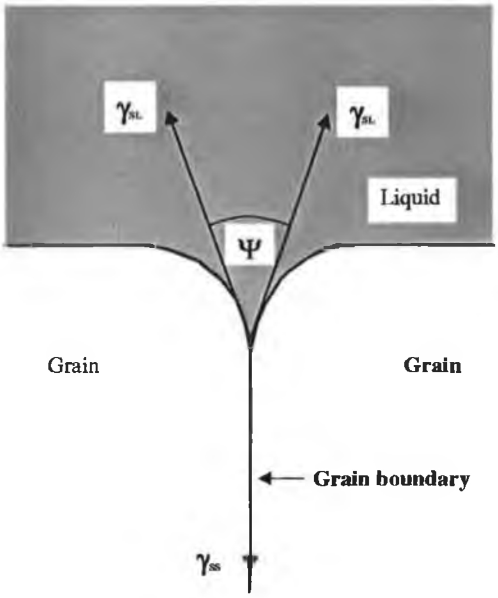

Figure 2.13 The definition of the dihedral angle ψ for a liquid in contact with the corners of the grains [75].

2.3.2.4. *Solubility*

The solubility of the liquid in the solid and also the solid in the liquid influences densification by LPS. Ideally the degree of liquid solubility in the solid phase should be such that sufficient liquid is present during sintering to ensure good densification, after which it is incorporated into the structure. This type of sintering is termed transient liquid phase sintering. Successful fabrication of Si_3N_4 solid solutions (SiALONs) is achieved in this manner, in which the amount of residual liquid phase, which is glassy, is substantially reduced, and improvements in material properties are seen. These type of materials are discussed in Section 2.3.7.

Good densification by LPS also requires that the solid has a high degree of solubility in the liquid since as outlined earlier, rearrangement during stage 1 is enhanced by the dissolution of sharp edges and contact points of the solid particles. Also during stage 2, good solubility is essential for the solution-precipitation mechanism. According to equation 2.16 (derived by Rahaman [77]), a solid phase with a small particle size is most favourable for good solubility.

$$\ln\left(\frac{S}{S_0}\right) = \frac{2\gamma_{sl}\Omega}{KTR} \qquad \textbf{2.16}$$

where, S – solubility of dissolved solid in liquid

S_0 - solubility of dissolved solid in liquid at equilibrium

Ω - atomic value

2.3.2.5. *Capillary Forces*

As was outlined earlier in the present section, the driving force for densification by LPS is the presence of a compressive force on the solid particle as a result of the reduced pressure in the liquid phase. The magnitude and nature of the compressive forces is determined by several factors including the contact angle, the volume of liquid, the separation and the particle size. Equation 2.17 describes semi-quantitatively, the effects of these factors on the compressive force for an idealised model illustrated in Figure 2.14 [78].

$$F = -\pi X^2 \Delta p + 2\pi X \gamma_{lv} \cos\beta \qquad \textbf{2.17}$$

where, F is positive when the force is compressive, Δp is the pressure difference across the liquid-vapour interface (described in Equation 2.12) and γ_{lv} is the liquid-vapour interfacial energy (surface tension).

Following the detailed discussion by Rahaman [79] a small contact angle (θ) is required for F to be positive. This reiterates that a small contact angle between the liquid and solid phases, that is a good wetting liquid is a prerequisite for the achievement of dense materials by liquid phase sintering.

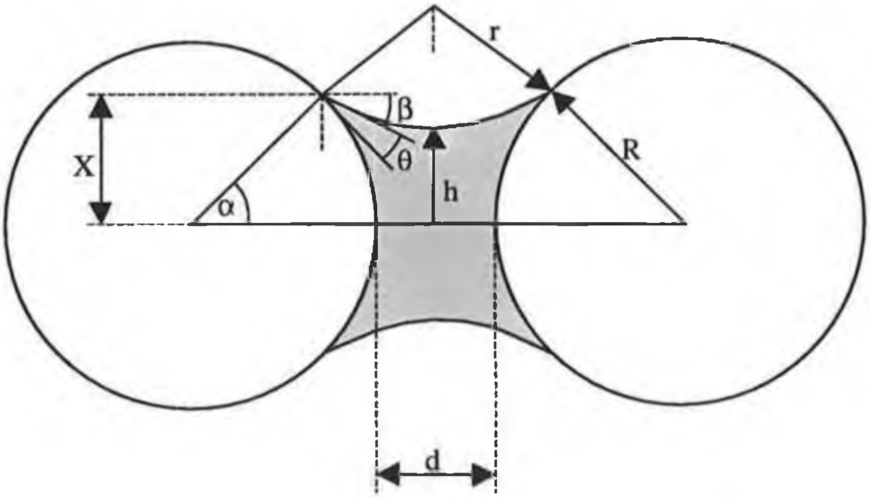

Figure 2.14 Geometrical parameters for an idealised model of two spheres separated by a liquid bridge [78].

2.3.3. Densification Mechanisms

Figure 2.15 illustrate the three overlapping stages are observed during LPS [80]. A dominant densification mechanism has been dentified for each stage. [48][81].

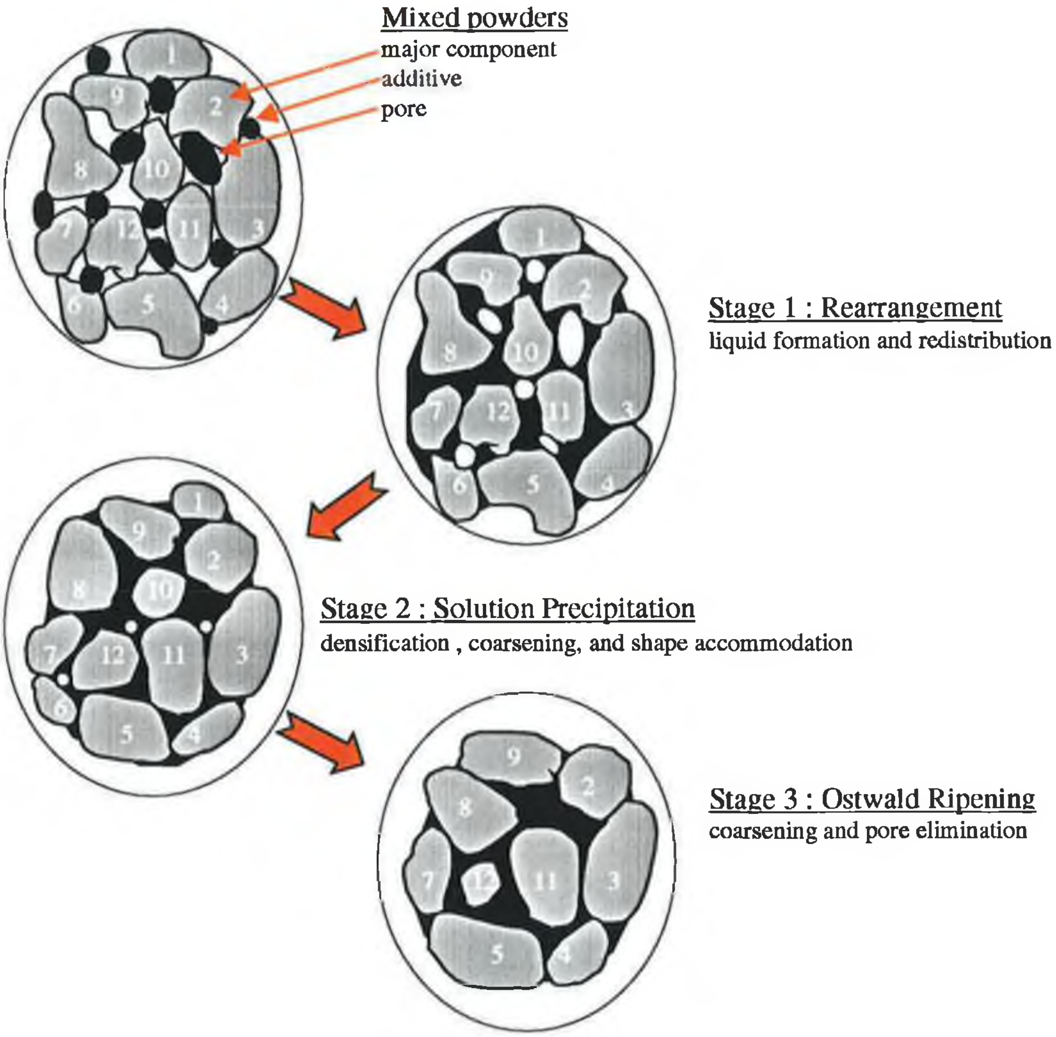

Figure 2.15 Liquid phase sintering [48].

2.3.3.1. Stage 1: Rearrangement

During stage 1, rearrangement is the dominant mechanism. If the liquid formed has good wetting properties, the surface tension forces (solid-vapour interfacial energy) on the solid particles lead to their rearrangement to produce a more stable packing. Good solid solubility in the liquid phase means the dissolution of sharp edges and contact points between grains can take place, enhancing particle rearrangement thus packing of the system. Additionally, capillary forces in the liquid phase act to bring about liquid distribution across the solid grains and into pores, leading to further rearrangement of the solid particles.

Liquid Distribution

Kwon and Yoon [82] studied the liquid distribution during the LPS of fine tungsten powder containing coarse nickel particles. They found that substantial redistribution of the liquid phase took place, with sequential filling of the pore occurring in such a way that small pore are filled first and larger pores later.

Shaw [83] analysed the redistribution of the liquid during LPS of a two-dimensional model of circular particles and showed that initial homogeneous liquid distribution across the solid particles is essential for further redistribution of the liquid. Analysis of a more complex model based an array of circles containing pores with a range of sizes was also carried out by [83]. This analysis showed that after the formation of an initial amount of liquid phase, the pores with the smallest size will the first to be filled, as they have a high surface to volume ratio, so that a given volume of liquid eliminates more solid-vapour interface (greater reduction in overall energy of the system). As the volume of liquid is increases the sequential filling of pores will occur. Shaw's analysis highlights the importance of (i) homogeneous packing of particles to produce a narrow range of pore size, (ii) homogeneous mixing of the main powder and the sintering additive to promote the homogeneous distribution of the liquid phase. It is also important that the sintering additive powders have small particle sizes, otherwise huge voids will remain when the liquid phase forms and fills the smaller pores.

Particle Rearrangement

Kingery [48] analysed the particle rearrangement during LPS by using an empirical approach, in which the surface tension forces driving densification are in competition with the frictional forces resisting rearrangement. Equation 2.18 describes the simple kinetic relationship he derived for the variation of shrinkage with time:

$$\frac{\Delta L}{L_0} \approx t^n \qquad \textbf{2.18}$$

where ΔL is the observed change in length of the material, L_0 is the original material length and the exponent n, is slightly greater than unity. Although this approach allows a quantitative estimation of the shrinkage rate during particle rearrangement, it is an idealised approach as the sintering process is treated as an isotropic and uniform.

Another approach to the mechanism of particle rearrangement involves the analysis of the capillary forces between particles separated by a liquid bridge [84] and although this model considers the effect of many parameters, its axial symmetry introduces significant limitations on its applicability to real systems.

Liquid Volume and Densification (during rearrangement)

The volume of liquid phase present during the rearrangement stage has a significant effect on the densification achieved during this stage. If the volume fraction of liquid is greater than 36%, full densification is achieved by rearrangement alone [85]. However, in advanced ceramics, the volume fraction of liquid phase is generally much lower, so that although a certain degree of densification is achieved by rearrangement, full densification requires the contribution from other processes.

2.3.3.2. Stage 2: Solution-Precipitation

During the second stage of sintering by LPS, rearrangement decreases considerably, and solution-precipitation becomes the dominant mechanism. Two models have been proposed to describe this stage; (i) Kingery's model (densification by contact flattening) [48], (ii) Densification accompanied by Ostwald ripening [86] .

Kingery's Model

According to this model, the compressive capillary force of the wetting liquid means that the solubility (or chemical potential) at the contact points between the particles is higher than that at other solid surfaces. A reduction in the energy of the system is thus achieved by matter transport away from the contact points (high chemical potential) to other surfaces (low chemical potential). Providing the solid has good solubility in the liquid phase, solid particles at the contact points go into solution and are precipitated at points with lower chemical potential. This allows center-to-centre approach of the particles under the action of the surface tension forces. Using this model for the solution-precipitation mechanism quantitative estimates of the shrinkage rate can be made. According to Equation 2.19, which describes the situation when the rate of matter transport is controlled by the diffusion of the solid particles through the liquid phase, the shrinkage is proportional to the one-third power of the time and inversely proportional to the four-thirds power of the initial particle size. Equation 2.20 describes the situation when the interface reaction leading to solution (or precipitation) is the rate controlling mechanism, in which case, the shrinkage is predicted to be proportional to the square root of the time and inversely proportional to the initial particle size.

$$\frac{\Delta L}{L_0} = K\left(\frac{t^{1/3}}{r^{4/3}}\right) \qquad \textbf{2.19}$$

$$\frac{\Delta L}{L_0} = K\left(\frac{t^{1/2}}{r}\right) \qquad \textbf{2.20}$$

Regardless of which mechanism is rate controlling, it is clear that a powder with a small particle size aids in increasing the shrinkage rate during this stage.

Densification Accompanied by Ostwald Ripening:

Ostwald Ripening applies to the coarsening of precipitates (particles) in solid or liquid medium [87] [88] [89]. Smaller particles have a higher concentration of solute (liquid phase) surrounding them and so a net flux of matter from the smaller particles to the larger ones occurs. Studying the LPS of W(Ni) powder mixtures, Yoon and Huppmann [86] observed Ostwald Ripening as the fine tungsten powder particles dissolved in the nickel liquid phase and precipitated on the coarse tungsten spheres. It is generally thought, however, that although these observations show that Ostwald Ripening does occur, it accompanies densification rather than causes it.

Grain Shape Accommodation

In systems where the volume of liquid is insufficient to completely fill the voids between the rounded or spherical shaped grains, grain shape accommodation is often observed to occur during stage 2. This produces polyhedral grains with flat contact surfaces, leading to more efficient packing of the grains, and the liquid is released from the well-packed regions and flows into the pores. In systems where the liquid volume is fairly large the decrease in energy associated with filling in the remaining pores will be not be great, and the grains maintain their original (spherical) shape.

As densification during stage 2 slows down, coarsening begins and becomes the dominant process in stage 3.

2.3.3.3. *Stage 3: Microstructural Coarsening*

Densification

As mentioned above, densification slows down considerably during this stage of LPS. In cases where the volume of liquid is relatively small, the elimination of any remaining isolated pores takes place slowly by continued solution-precipitation and grain shape accommodation. Kang et al. [90] observed that for a larger volume of liquid, the filling of remaining pores occurred by grain growth in a discontinuous manner, resulting in a more rounded grain shape and also improved homogeneity of the microstructure. Also the analysis by Park et al. [91] determined that densification achieved by the filling of remaining isolated pores during stage 3 is controlled by grain growth.

Coarsening and Grain Growth

Coarsening by Ostwald ripening is the dominant mechanism in the final stage of LPS. Greenwood [87], Lifshitz, Slyozov [88], and Wagner [89] independently developed the basic theory, which is termed the LSW theory. This theory is applicable to systems with a relatively high volume fraction of liquid, and gives the following reaction for the rate of grain growth during stage 3:

$$R^m - R_0^m = Kt \qquad \textbf{2.21}$$

where, R_0 is the initial radius of the grain, R is the radius of the grain after time, t, K is a temperature dependent parameter and the exponent m is dependent on the rate-controlling mechanism during grain growth. When m = 3, diffusion through the matrix is rate-controlling and when m = 2, interface reaction is rate-controlling.

In most ceramic systems diffusion through the matrix is found to be the rate-controlling step for grain growth. Thus the temperature will affect the rate of grain growth, since as the temperature increases, so does the solubility of the solid in the liquid and also the diffusion of the solute particles through the liquid. The grain growth rate is also affected by the dihedral angle. As the dihedral angle increases, the solid-liquid contact area is reduced and thus the rate of matter transport is also reduced.

2.3.4. Hot-pressing in the Presence of a Liquid Phase.

A significant increase in the densification rate of a material is observed when a high uni-axial mechanical pressure is applied during sintering at high temperatures. This is due to an increase in the chemical potential of the atoms at the contact points. In order to decrease the energy of the system transport of matter away from these points is enhanced, resulting in an increase in the densification rate [92].

2.3.5. The Role of Additives in the Densification of Silicon Nitride

The guidelines outlined earlier for successful densification of a material by liquid phase sintering must be taken into account when selecting a suitable sintering additive combination for Si_3N_4. These criteria include, (i) the liquid phase formed has good wetting properties (forming low contact angle with the solid phase), (ii) the particle sizes of the additive powder and the Si_3N_4 powder are similar and small, (iii) the liquid phase is formed well below the decomposition temperature of Si_3N_4, (iv) Si_3N_4 is partially soluble in the liquid phase, (v) if transient liquid phase sintering is required, the liquid phase forms a solid-solution with Si_3N_4.

The choice of sintering additive combination is balanced by the requirement of full densification and the desired properties of the final product [93]. A material's properties are influenced by many factors, including, (i) the degree of density achieved, (ii) the microstructure of the final body, (iii) the amount, composition and properties of the intergranular phase.

The role of the sintering additive during LPS of silicon nitride can be summarised by Equation 2.22 [94]. The oxide additive, M_xO_y, reacts with silica (SiO_2) layer around each Si_3N_4 particle, forming a liquid phase, above the lowest eutectic temperature of the system [94].

$$Si_3N_4 + SiO_2 + M_xO_y \rightarrow Si_3N_4 + \text{M-Si-O-N phase} \qquad \textbf{2.22}$$

Initially magnesium oxide, MgO, was employed as a sintering additive for LPS of Si_3N_4. It is an effective sintering aid, forming a low viscosity liquid at temperatures well below the decomposition temperature of Si_3N_4 ($MgO\text{-}SiO_2$ eutectic $\cong$ 1550°C) [95] [96]. However, any secondary or intergranular phases remaining in the sintered body are glassy. The presence of such glassy phases are detrimental to the high material's high temperature properties as a primary property of glasses is that they begin to soften at temperatures well below their melting point [97]. Another drawback with glasses is that any impurities present in the material tend to be located in the glassy intergranular phase, further lowering the melting point [98].

Studies by Gazza [99][100] suggested that the high temperature properties of liquid phase sintered Si_3N_4 could be improved by using yttria, Y_2O_3 as a sintering additive, as it forms a refractory glass on cooling. Thus strengths of silicon nitride densified with yttria are reported to be significantly higher than materials in the Mg-Si-O-N system [101] at temperatures greater than 1200°C. However, the sinterability of the Y-Si-O-N system is low, as the lowest eutectic is approximately 1600°C. The addition of Al_2O_3 along with Y_2O_3 was found to improve the sinterability by lowering the eutectic temperature of the $Y_2O_3\text{-}SiO_2$ melt. However, due to the glass-forming ability of Al^{3+}, Al_2O_3 promotes the formation of residual glassy phases, and thus leading to poor high-temperature properties [102]. Many studies into the composition of the glassy phase in Si_3N_4 containing Y_2O_3 and Al_2O_3 have been carried out it was generally found that if Y_2O_3 and Al_2O_3 are added to Si_3N_4 in the ratio $3Y_2O_3 : 5Al_2O_3$, on cooling the liquid phase crystallises to an yttrium-aluminium garnet (YAG) phase, and due to its high melting point and good oxidation resistance YAG was realised as a desirable intergranular phase in sintered Si_3N_4 [103][104][105].

2.3.6. α- to β-Si_3N_4 Transformation

Si_3N_4 has two structural polymorphs α and β, first discovered by Turkdogan et al. [106]. On comparing the structure of Si_3N_4 to that of phenacite (Be_2SiO_4), in which the oxygen and beryllium are replaced by nitrogen and silicon, respectively. Hardie and Jack [107] determined that the β form is made up of tetrahedra linked along the [001] plane in an ABAB packing sequence. In this structure there are continuous channels parallel to the c direction. While the α form has an ABCDABCD packing sequence, where the CD layers are the mirror image of the AB layers but displaced by 4Å. This c-glide means that the channels observed the β structure are closed in the α structure and as result there exists two large interstitial sites per unit cell.

Early investigations suggested that the α- and β-forms were low and high temperature structural modifications of Si_3N_4, but this hypothesis is not consistent with the evidence that both forms can be synthesised over a range of temperatures. Although the exact phase stability has been debated for many years, it is now generally accepted that the synthesis of Si_3N_4 by a vapour-phase reaction favours the formation of the α-structure [108][109] while the reaction with nitrogen dissolved in a silicon melt results in the β-Si_3N_4 form [110].

Transformation from the α- to the β-form is observed during liquid-phase sintering of Si_3N_4. A solution-precipitation mechanism is suggested to occur at temperatures >1400°C: dissolution of α-Si_3N_4 into the liquid phase, reconstruction of the Si-N bonds, and precipitation of β-Si_3N_4. The extent of transformation depends on (i) the initial concentration of the α- and β-forms in the starting Si_3N_4 powder, (ii) the amount of liquid phase present (iii) the viscosity of the liquid phase, (iv) the solubility of Si_3N_4 in the liquid phase and (v) the sintering temperature and time at temperature.

2.3.7. SiAlON ceramics

As outlined earlier, Si_3N_4 can be sintered effectively by LPS using a transient liquid phase process where the liquid phase is one which is soluble in Si_3N_4, the resulting materials are called SiAlONs. SiAlON is the acronym for phases in the Si-Al-O-N system. SiAlONs can be divided into two categories: β-sialons with the general formula: $Si_{6-z}Al_zO_zN_{8-z}$, where $=<z<4.2$ [111][112] and α-sialons with the general formula: $Me_{m/x}Si_{12-(m+n)}Al_{m+n}O_nN_{16-n}$, where Me is a metal ion, x is the valency of the metal [113].

β-sialons are based on the β-Si_3N_4 crystal structure. During liquid phase sintering of Si-Al-O-N materials, Si_3N_4 forms a solid solution with Al_2O_3, by the replacement of Si^{4+} and N^{3-} by Al^{3+} and O^{2}. However, metal oxides are still required for near theoretical density by pressureless sintering. In α-sialons partial replacement of Si^{4+} by Al^{3+} occurs with charge compensation taking place by the accommodation of other cations into the two interstitial sites present in its structure [114]. There exists a size limit to the cations that can be incorporation into the α-sialon lattice, successful cations, from their metal oxides, include, Y_2O_3, CaO, SmO [113].

Compositional ranges of α- and β-sialons are represented conventionally by a Jänecke prism.. Figure 2.16 illustrates a Janecke prism for the Y-Si-Al-O-N system [115]. As can be seen the α- and β-sialons phases are compatible with each other and in recent years α + β sialon composite materials have been fabricated successfully. By careful control of the starting compositions and processing conditions, the final composite can be tailored to produce a material with the beneficial properties of both α-sialons and β-sialon.

The reader is referred to a number of reviews, in particular the work by Jack [112], Hampshire [115] and Ekstrom et al. [116].

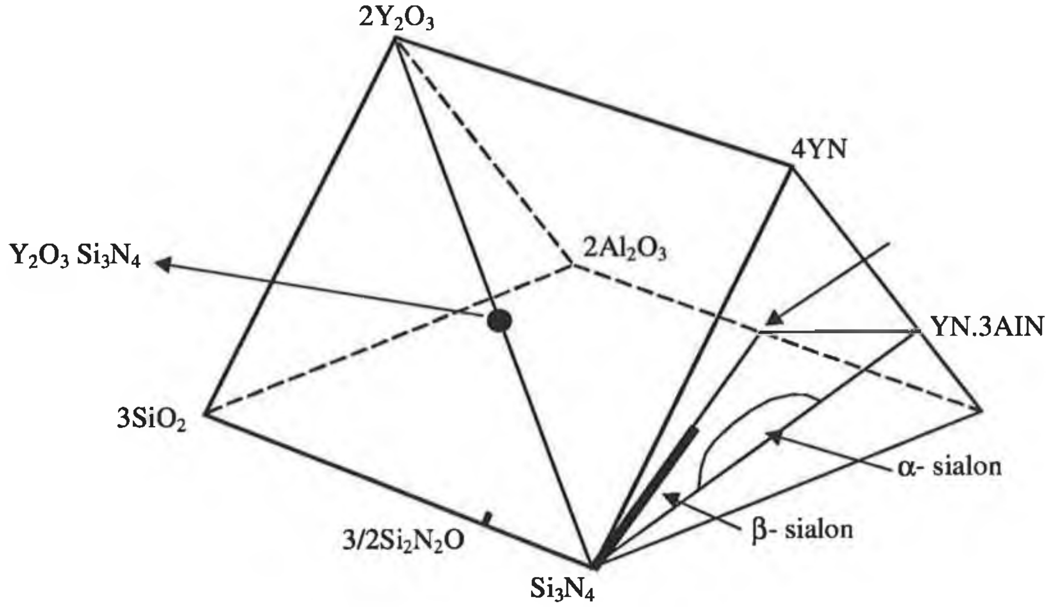

Figure 2.16 Janecke prism representation of the Y-Si-Al-O-N system. [ref]

2.4. Incorporation of Reinforcements

2.4.1. Fibre - Matrix Interactions

Another difficulty arises in processing CMCs with chemical interaction between the different constituents in the composite. A direct fibre/matrix reaction for the composite of interest, carbon fibre reinforced silicon nitride composite, can be expressed as,

$$Si_3N_4(s)+3C(s) \Leftrightarrow SiC(s)+2N_2(g) \qquad \textbf{2.23}$$

This reversible reaction was found to proceed to the right under 1 bar nitrogen pressure and at sintering temperatures >1440°C [117]. Simple free energy of formation thermodynamics in this system, suggest that a stable C fibre reinforced silicon nitride composite can be attained if the nitrogen partial pressure and sintering temperatures are maintained above the upper equilibrium curve in Figure 2.17 [117].

The compatibility of additional oxide additives with the reinforcing C phase must also be considered. Equilibrium calculations have been carried out for many high-melting oxides and the results are illustrated in Figure 2.18 [118].

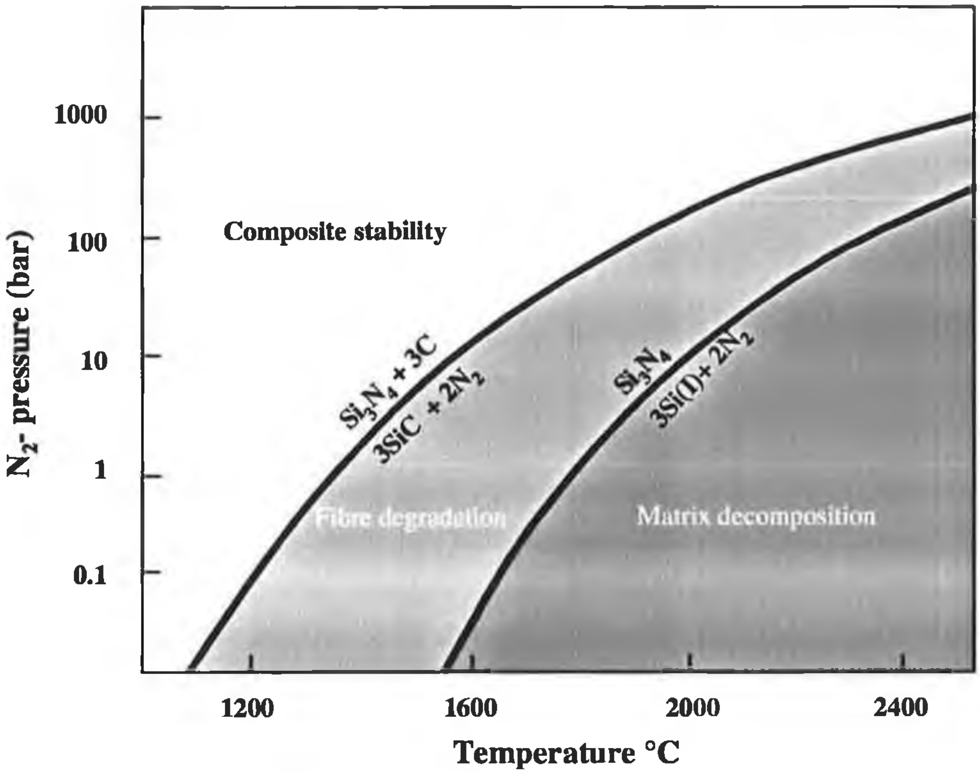

Figure 2.17 Nitrogen partial pressures as a function of temperature for Si_3N_4 decomposition and carbonisation. (Adapted from Nickel et. al. [117]).

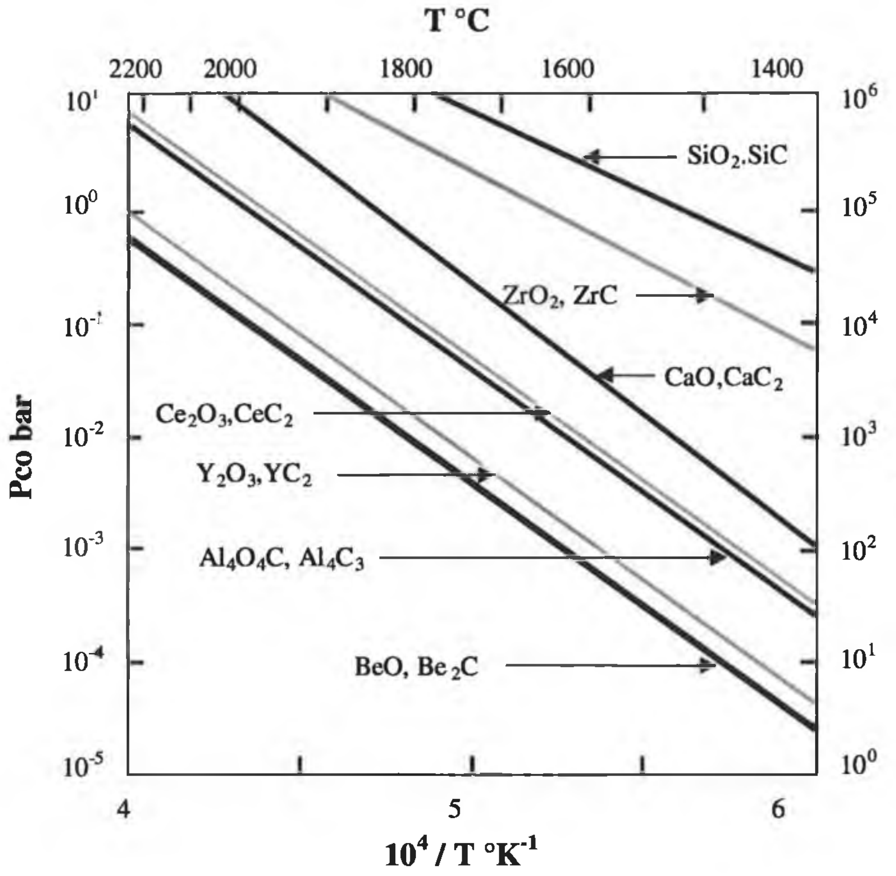

Figure 2.18 Equilibrium partial pressure of CO oxides in contact with carbon [118].

Reversible reactions between C(s) and the individual oxides result in the formation of the corresponding metal carbide and carbon monoxide gas (reactions 2.24-2.28) [118].

$$3C(s)+SiO_2(s)\Leftrightarrow SiC(s)+2CO(g) \qquad \textbf{2.24}$$

$$3C(s)+ZrO_2(s)\Leftrightarrow ZrC(s)+2CO(g) \qquad \textbf{2.25}$$

$$3C(s)+CaO(s)\Leftrightarrow CaC_2(s)+CO(g) \qquad \textbf{2.26}$$

$$6C(s)+Al_4O_4C(s)\Leftrightarrow Al_4C_3(s)+4CO(g) \qquad \textbf{2.27}$$

$$7C(s)+Y_2O_3(s)\Leftrightarrow 2YC_2(s)+3CO(g) \qquad \textbf{2.28}$$

Reactions of this type involving solid to gas changes in state can be considered using The Second Law of Thermodynamics in the form:

$$\Delta G = G_0 + nRT(\ln p) \qquad \textbf{2.29}$$

where;

ΔG = change in free energy of the system

G_0 = standard free energy term

p = pressure of products/pressure of reactants

This suggests that the reaction direction is dependent upon the local gas pressure at the point of reaction. If the CO gas can easily escape from the reaction interface, via pores or cracks in the matrix, then the reaction, which is the carbothermic reduction of the oxides, will continue. In a dense, pore-free matrix the carbon monoxide cannot move away freely from the interface, and the only method of transport of CO being by solid-state diffusion, which through this system is expected to be extremely difficult.

During sintering the additional oxides can react with the Si_3N_4 matrix and the reactivity between the compounds formed and carbon must also be taken into account. SiO_2 (present on the surface of silicon nitride powders) may have an effect on the C/Si_3N_4 composite stability. From thermodynamic calculations SiO_2 is unstable in the presence of Si_3N_4 and under all feasible sintering conditions outlined for a C/ Si_3N_4 system, reaction 2.30 proceeds to the right.

$$SiO_2(s,l) + Si_3N_4 \Leftrightarrow 2Si_2N_2O(s) \qquad \textbf{2.30}$$

The reaction product, silicon oxynitride (Si_2N_2O) is thermodynamically very stable. There is no data on its reaction with C but it may react with the Si_3N_4 matrix. It is necessary also to include the product of reaction (2.12) SiC, in the thermodynamic considerations. It was found that both Si_3N_4 and SiC are stable in the presence of Si_2N_2O up to 1838°C (1 bar N_2) and that the same equilibria in the ternary system Si-N-C (examined earlier) are found in the quaternary system Si-C-O-N but with the additional presence of Si_2N_2O. Thus, it is reasonable to apply directly the conclusions drawn from thermodynamic calculations of the ternary system Si-C-N, to the system also containing SiO_2, Si-N-O-C.

Experimental investigations [119] (as outlined in section 2.3.7) on the systems containing Al_2O_3 as a sintering aid have shown that a Si_3N_4 solid solution (sialon) is formed. At higher temperatures a β- Si_3N_4 solid solution is formed and is in equilibrium with C and Si_2N_2O over the temperature range of interest. Y_2O_3 present as a sintering aid is found to form an additional phase (Y-α-sialon) in equilibrium with β-Si_3N_4. Almost all available oxygen atoms from both Y_2O_3 and Al_2O_3 will react to form more stable Si_2N_2O phases.

The composition of these silicon oxynitride phases may well influence the sintering behaviour, mechanical properties, and oxidation resistance [120] of the resulting composite but, as explained earlier, Si_2N_2O phases will not affect the stability/compatibility limits of the matrix (Si_3N_4) and reinforcing phase (C) as outlined in Figure 2.18 [118].

2.4.2. Sintering Constraints

The non-sintering fibres in a continuous fibre reinforced ceramic matrix composite constrained densification of the matrix occurs. Hseuh et al. [121] and Raj [122] modelled this effect on the densification of glass matrices with rigid inclusions. These models were based on the supposition that as the matrix densifies it shrinks onto a rigid inclusion placing it under a compressive stress. Accordingly a uniform tensile stress within the matrix results. The magnitude of this tensile stress was predicted to be high and constrains matrix densification either by crack/void forming or differential densification. However Scherer [123] later showed that the large tensile stresses predicted by the above models result from incompatible parameters that generate negative value's for Poisson's ratio. Thermodynamically, a negative Poisson's ratio value is feasible but it is never observed during the sintering of a porous solid [124].

Based on the viscoelastic deformation of a porous material during sintering, Scherer [123] developed a model for the densification rate of a composite material, allowing only positive values of Poisson's ratio. This model predicted that the transient stresses generated during sintering of composites are relatively small compared to the stress values predicted by Raj and Hseuh. On comparing densification rates predicted by Scherer's model and those observed experimentally for glass matrix composites, Rahaman and De Jonghe [125] surmised that the model fitted well to densification rates observed for composites with a low volume fraction of inclusions (≤ 15vol%), but deviated significantly from the densification rates observed for composites with increased volume fraction inclusions.

On increasing the volume fraction of inclusions, a stage is reached where inclusion-inclusion contacts form and result in a continuous network of inclusions, termed a percolating network throughout the sample. The volume fraction of inclusions when a percolating network is first formed is called the percolating threshold. Rigid inclusion-inclusion contacts within the percolating network will retard sintering and sintering will stop if the structure is completely rigid. According to Rahaman and De Jonghe [125] composites with an inclusion volume fraction of ≥16% (percolation threshold) will be impossible to densify by pressureless sintering. Nonetheless many composites, particularly glass matrices and ceramics with good liquid forming properties, with much higher volume fraction inclusions can be successfully densified. The reason for this is that at sintering temperature the glass of liquid phase formed sufficiently wets and lubricates the inclusions, preventing the rigid nature of the network and thus significantly minimising the constraint on densification of the matrix.

Combining the observations of Rahaman and De Jonghe [125] and his earlier experimental results [126], Lange et al. [127] put forward a model based on the theory that it is interaction between the inclusions that constrain densification of the ceramic matrix in CMCs. This model analysed a 2-D array of reinforcements on a simple cubic lattice, Figure 2.19 [127]. A basic geometrical analysis showed that the shrinkage strain and thus densification of the matrix between two inclusions depend on the amount of matrix phase between the inclusion pair. Assuming that the shrinkage strain of each network pair is equal to the linear shrinkage of the composite, the distance between the inclusions thus effects densification. In the 2-D array, the relative amounts of powder (that is the ratio of amount of powder between reinforcements to the distance between them) is greater between inclusions on diagonal sites than between inclusions on edge sites. Thus during sintering, the powder between the edge sites will densify better relative to the powder between diagonals, leading to differential densification of the powder compact within the composite. This model was supported by the experimental observations of Dagleish et al. [128] who observed differential densification which led to the formation of large cracks and a lower than full theoretical density in Al_2O_3 powder matrices containing large ZrO_2 inclusions.

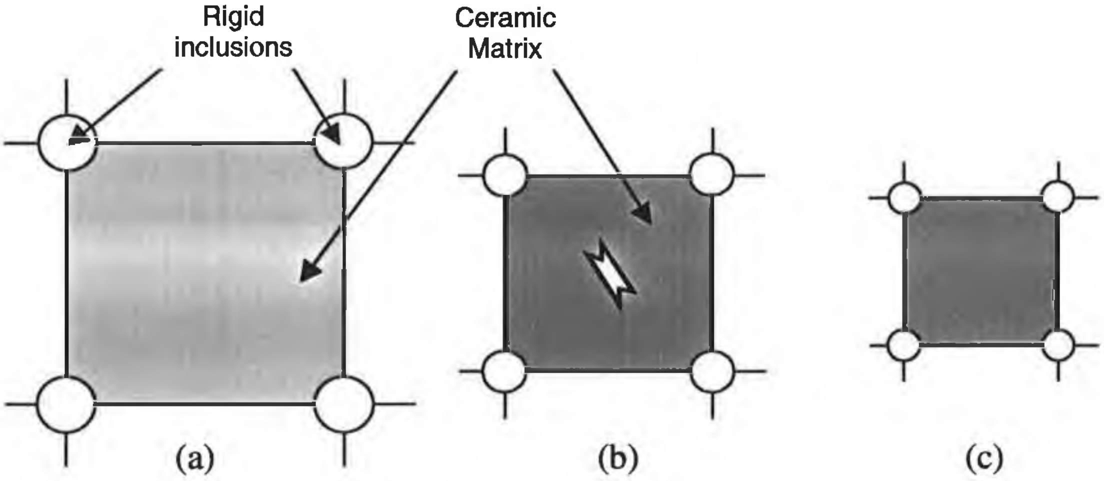

Figure 2.19 Constrained shrinkage in the sintering of a composite [127].

The presence of incipient cracks in the matrix influence densification as they open during constrained sintering to relieve the constraint [126]. The production of well-dispersed slurries and consequently crack-free composite green bodies is thus of the utmost importance. However, density distributions have also been observed in un-cracked composite green bodies. This was attributed to formation of regions of dense matrix (between inclusions on edge sites, as outlined above), which resist the

Microhardness measurements have been commonly used in the past to characterise silicon nitride [131][132][133][134]. Pratt [132] was the first to report that the α and β-phases of Si_3N_4 could be distinguished by their microhardness behaviour and found that polycrystalline α-Si_3N_4 was harder than the β-phase. Further investigations [135] into the microhardness of both single crystal and polycrystalline α and β-Si_3N_4 supported initial observations. It has been seen that the indent in the single crystal β-Si_3N_4 phase has a much larger diameter than that in the harder α-phase [135]. Discrepancies in measurements due to differences in crystallographic orientation as outlined by Chakraborty et al.[136], were avoided in this case, as measurements were taken with both phases in similar orientation. Calculated hardness values for this system are shown in Table 2.2 [135]. The Vickers microhardness (VMH) of single crystal α-Si_3N_4 was determined to be approximately 28% higher than β-Si_3N_4. Similarly single-phase polycrystalline α-Si_3N_4 had higher VMH than polycrystalline α + β-Si_3N_4, suggesting that polycrystalline α-Si_3N_4 is harder than polycrystalline β-Si_3N_4 [135].

Nature of Si_3N_4	**100g load VHM_{100} (kgf.mm^{-2})**	**200g load VHM_{200} (kgf.mm^{-2})**	**300g load VHM_{200} (kgf.mm^{-2})**	**500g load VHM_{200} (kgf.mm^{-2})**
α-Single Crystal	4527	3784	n.d.	n.d.
β-Single Crystal	3577	2957	2408	1987
α-Polycrystalline	3784	2664	2286	1755
α + β-Polycrystalline	2239	1648	1390	1037

n.d. : not determined

Table 2.2 The variation of Vickers microhardness (VHM) with sample and load. *(Selected data from Chakraborty et al. [135]).*

The reason why the α-phase of Si_3N_4 is harder than the β remains unclear. The two structural forms have similar densities, both are hexagonal and constructed from covalently bonded SiN_4 tetrahedra joined in a 3-dimensional network [137]. However, as explained in detail earlier (Section 2.3.7), in the β-form the tetrahedra are packed in an ABAB packing sequence, the α-form on the other hand has an ABCDABCD packing sequence. The different packing sequences result in long, continuous channels parallel to the c-axis in β-Si_3N_4, but only large, closed holes in α-Si_3N_4. Also the α-form unit cell's c-axis is approximately twice that of the β-structure. Greskovich et al. [138] suggested that the decreased microhardness of β-Si_3N_4 is due simply to the ease of movement of material through the continuous channels during indentation. However, the hardness of a material has been related to its Peierls stress for dislocation motion, which itself is related to the c-axis Burgers vector of a material [139]. This led Erkstrom [140] to suggest that the long c-axis in the α-form of Si_3N_4 gives a higher resistance to dislocation motion compared to the β-structure, resulting in higher hardness.

2.5.1.2. Fracture Toughness

The strength of a given material is determined by two factors, the 'fracture toughness or resistance to crack extension' and the 'largest or most severe flaw [141][142][143]. The presence of a crack decreases the strength of a structure and this strength decreases progressively with increasing crack size [144]. As outlined in Section 2.1.2, the resistance to cracks, that is the fracture toughness, K_{1c} of ceramics is inherently poor ($K_{1c} = 0.5 – 5MNm^{-3/2}$) [145].

Unlike the attractive thermomechanical properties of Si_3N_4-based materials outlined in Sections 1.3.1.3 and 2.3, its low fracture toughness hinders its potential use for some applications. Accordingly, much research has focused on controlling the microstructure of Si_3N_4 ceramics (via controlled processing) in an attempt to improve fracture toughness. Most improvements have been reported for materials where the Si_3N_4 grains are grown *in situ* during processing (*in situ* toughening). The resultant microstructure consists of elongated Si_3N_4 grains which can increase fracture toughness by dissipating energy (if the interface is weak [146]) upon crack propagation [147][148]. In these *in situ* toughened materials the fracture toughness is dominated by the morphology of the Si_3N_4 grains, that is the grain size and aspect ratio. [149]. The influence of grain boundary phase composition on the fracture toughness of Si_3N_4-based materials has also been realised. Studying the Si-Y-Mg-Al-O-N, Peterson and Tien [150] found that the presence of residual stresses in the grain boundaries, caused by thermal expansion mismatch, resulted in improved fracture toughness. While Becher et al. [151], researching β-Si_3N_4 whiskers in oxynitride glasses, found that the interfacial bonding was influenced by the glass chemical composition. Debonding, and thus improved fracture toughness, was observed when the glass had a low nitrogen and oxygen content. Following these observations and supported by his own results for Si_3N_4 with a range of second-phase chemistry, Kleebe et al. [152] concluded that the fracture toughness of the Si_3N_4 materials was influenced not only by the Si_3N_4-grain morphology, but by the glass composition at the interface (influencing the interfacial bonding) and the residual stresses at grain boundaries, all of which are controlled by the chemical composition of the grain boundary phase.

2.5.1.3. Oxidation Behaviour

Oxidation of Pure Silicon Nitride

Four oxidation reactions have been identified for Si_3N_4:

$$Si_3N_4(s) + 3O_2(g) = 3SiO_2(g) + 2N_2(g) \qquad \mathbf{2.31}$$

$$4Si_3N_4(s) + 3O_2(g) = 6Si_2N_2O(s) + 2N_2(g) \qquad \mathbf{2.32}$$

$$2Si_2N_2O(s) + 3O_2(g) = 4SiO_2(s) + 2N_2(g) \qquad \mathbf{2.33}$$

$$2Si_2N_2O(s) = 4Si(s,l) + 2N_2(g) + O_2(g) \qquad \mathbf{2.34}$$

Based on a collection of thermodynamic data [153] [154], Singh et al. [154] derived the Si-O-N phase stability diagram, following which the theoretical overall reaction for the oxidation of Si_3N_4 is,

$$Si_3N_4(s) + 3O_2(g) \rightarrow 3SiO_2(s) + 2N_2(g) \qquad \Delta G_{(1600K)} = -1661 kJmol^{-1} \qquad \mathbf{2.35}$$

It has been shown that Si_3N_4 possesses intrinsically good oxidation resistance due to the initial formation of a surface SiO_2 layer, which is resistant to oxidants, and so the oxidation becomes self-passivating. The oxidation kinetics of Si_3N_4 are generally found to follow a parabolic rate law.

$$\left(\frac{\Delta m}{S}\right)^2 = Kt + b \approx Kt \qquad \textbf{2.36}$$

where Δm is the mass gain per unit area, K is the parabolic rate constant, t is time and b is a constant related to the additive content. Deviations from this model do occur and are well documented. Derived from Fick's first law, the parabolic rate law suggests a diffusion controlled process [155]. The oxidation of pure silicon nitride has been observed to be controlled by the diffusion of oxygen through the oxide SiO_2 layer to the Si_3N_4 surface.

Oxidation of Si_3N_4 + Sintering Addtives

The required use of sintering additives, most commonly metal oxides, for the fabrication of Si_3N_4 results in an intergranular phase in the sintered body (Section 2.3). Many investigations into the oxidation behaviour of Si_3N_4 ceramics sintered with Y_2O_3 and Al_2O_3 have been carried out [156] [157] [158]. It is generally accepted that the oxidation behaviour of these ceramic materials changes with temperature, where the temperature boundaries of behaviour depend on the additive content and the composition of the intergranular phases. At lower temperatures (~<1050°C) oxidation of Si-Y oxynitrides and silicate glasses occurs and the rate of oxidation is relatively rapid and dependent on the inward diffusion through grain boundaries [159]. This is accompanied by volume expansion and the growth of an oxide film on the Si_3N_4 surface. A gradual change in oxidation behaviour takes place as the temperature increases. Controlled by oxygen diffusion through the oxide film, growth of the film takes place at the Si_3N_4/film interface. Parabolic kinetics are observed as the resultant silica dissolves in the silicate glass, until the liquidus composition of silica is reached. Crystalline silica is then formed at the reactive surface, which results in a significant reduction in the oxidation rate observed as the diffusivity of oxygen is reported to be slower through crystalline silica than through amorphous silicates [160]. At higher temperatures (~>1450°C) an acute increase in oxidation rate is observed due to the dissolution of crystalline SiO_2 into the glassy phase and further heating leads to the disintegration of the protective oxide scale.

The addition of zirconia to $Si_3N_4 + Y_2O_3 + Al_2O_3$ ceramics notably effects the oxidation kinetics. Small additions of ZrO_2 have been reported to improve the oxidation resistance of these materials [161] [162] whereas when the ZrO_2 content in the starting powder exceeds approximately 20wt% severe degradation occurs resulting in catastrophic failure [163]. This degrading oxidation is attributed to the presence of Zr-oxynitride phases in the Si_3N_4 ceramic, formed by the incorporation of nitrogen into the tetragonal zirconia structure, according to the following reaction [164],

$$xSi_3N_4 + ZrO_2\,(t) \rightarrow ZrO_{2-3/2}N_x + (3x/2)Si_2N_2O \qquad \textbf{2.37}$$

At low temperatures, 600-1000°C, the Zr-oxynitride phase reacts with oxygen to produce monoclinic ZrO_2,

$$ZrO_{2-3x/2}N_x + 3xO_2 \rightarrow ZrO_2\,(m) + (x/2)N_2 \qquad \textbf{2.38}$$

Accompanying the formation of monoclinic zirconia is a molar volume increase and in systems with relatively high volumes of zirconia, this molar volume increase leads to significant build up of compressive stresses at the surface. Surface spalling and disintegration of the sample surface occurs to relieve the compressive stresses [163]. At higher temperatures (>1000°C), the compressive stresses are relieved by deformation [98] and so catastrophic failure is not observed.

It is thus essential to avoid the potential formation of Zr-oxynitride phases during the fabrication of $Si_3N_4 + Y_2O_3 + Al_2O_3 + ZrO_2$ ceramics. This may be achieved simply by limiting the amount of ZrO_2 in the starting composition to less than 20wt%. In cases where high quantities of ZrO_2 are required (to enhance fracture toughness [165] [166]), evidence exists that the stabilisation of the starting zirconia by a stabiliser

(Y^{3+}, for example) on reaction with Si_3N_4 prevents the formation of Zr-oxynitride phases [163]. In addition, it has been reported that the use of lower sintering temperatures avoids the formation of ZrN and Zr-oxynitride [167].

2.5.2. Si_3N_4/C Composite

2.5.2.1. Mechanical Properties of Ceramic Matrix Composites

The main aim in the development of composites is to produce a material that has improved properties over the individual components. In CMCs the addition of continuous fibres significantly increase the toughness of the inherently brittle ceramic matrix.

In general, long fibre reinforced composites are designed to function as unidirectional load beading materials with the stress placed along the fibre direction [168]. When a composite is placed under stress the load is shared initially between the matrix phase and the fibres, in amounts proportional to their volume fractions. This continues as the load increases until the cracking stress of the matrix is reached. After matrix cracking begins the load is transferred to the fibres and ultimately either single crack or multiple crack failure of the composite occurs. In cases where the volume fraction of fibres is less than a critical value or when the fibre-matrix bond is strong, the fibres cannot sustain the load and the crack extends through the matrix resulting catastrophic failure. In cases where substantial fibre failure does not occur, the composite does not fail catastrophically (in contrast to monolithic ceramics after initial matrix cracking). Instead energy-dissipating mechanisms such as fibre-matrix debonding, crack deflection and fibre pullout occur as illustrated earlier in Figure 2.2. This stage is characterised by the progressive cracking of the matrix orthogonally to the applied stress until a saturated level is reached when the composite consists of transverse parallel cracks perpendicular to the fibre direction, a distance x apart. According to the Aveston, Cooper, Kelly (ACK) model [169], which assumes a constant interfacial shear stress, τ, the distance x, is given by,

$$x = \left(\frac{V_m}{V_f}\right)\frac{\sigma_{mu} r}{2\tau} \qquad \mathbf{2.39}$$

where V_m and V_f are the volume fractions of the matrix and fibres respectively, σ_{mu} is the ultimate fracture strength of the matrix and r is the fibre radius.

In characterising the failure behaviour of composites, the following parameters are generally considered.

- The Elastic Modulus, E_m, of the composite as a whole (matrix plus fibres) which reflects on the stiffness of the material under mechanical loading.
- The onset of matrix micro-cracking (at stress σ_c), which is marked by the initial departure from linearity/elastic region in the stress/displacement curves.
- The development of a regular array of transverse matrix cracks. This is a widely reported feature of continuous fibre ceramic composites where the periodicity of the cracks (crack spacing) is dictated by a characterised stress transfer length associated with the bridging fibres. This length is determined by the ability of the interface to accommodate the local stress. Figure 2.20 shows a simplified model. For a composite with $E_{matrix} > E_{fibre}$ (designed), the matrix is progressively subject to tensile strain (elastic) until this exceeds the matrix fracture stress, when it cracks. The local interfacial stress at the crack then becomes zero. The matrix segments then shrink away from the crack (crack opening) and, in a well-designed composite, the crack is deflected along the fibre-matrix interface, debonding the phases. Also in a well-designed system, with a glissile interphase structure, the matrix cracks may slide along the fibre surface. The distance, x, between successive matrix cracks is dependent upon these interfacial properties. Finally, when the composite fractures, the debonded fibre lengths emerge from the fracture surfaces as `pulled-out`fibres. The length of the pull-out also reflects the debonding properties.
- As outlined above, matrix microcracking continues to saturation level, at which the fibres bear the entire load. After this the stress-displacement curve steepens as the fibres are strained elastically to their failure stress, σ_f, dictated by the

ultimate strength of the fibres [170], followed by catastrophic failure of the composite.

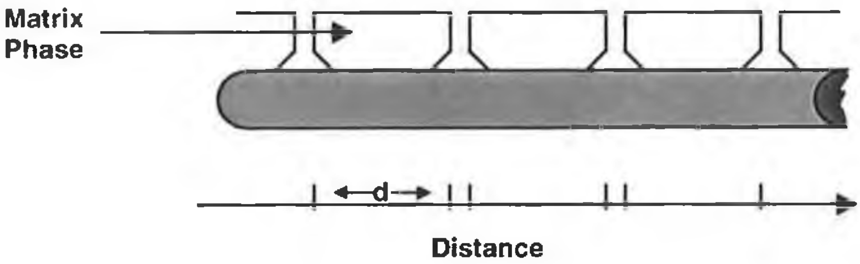

Figure 2.20 Simplified model of periodic matrix microcracking in a composite with characteristic crack spacing, d.

3. EXPERIMENTAL PROCEDURE

3.1. System Selection

An analysis was made of the literature survey into the most promising candidates for lower temperature liquid phase sintering of Si_3N_4. From this analysis two series were selected for further study, with compositions based upon an Al_2O_3-Y_2O_3 composition in which the Al_2O_3 content is replaced incrementally by 1wt%AlN and by 1wt%CaO initially and then incrementally by 0.5wt%CaO, respectively. These are compared with a reference mixture with the standard YAG composition ($3Al_2O_3$: $5Y_2O_3$ molar ratio) as sintering additive. The compositions studied are listed in Tables 3.1 - 3.3. As outlined in the Introduction, for the pressureless sintering of a Si_3N_4/C composite, a Si_3N_4 matrix with good sinterability at lower temperatures, with good mechanical properties is required. Thus the first step of the current study was to carry out a sintering study of the monolithic Si_3N_4 with different sintering additive combinations.

3.1.1. $Si_3N_4 + Y_2O_3 + Al_2O_3 + AlN$

The introduction of increments of AlN into the sinter additive mixture was made in order to determine the effect of the AlN: Al_2O_3 ratio on the sintering of the Y-Si–Al-O-N. This combination was selected following the encouraging results obtained by Komeya et al. [171] for the composition Si_3N_4 + 5wt%Y_2O_3 + 4.5Al_2O_3 + 2wt%AlN. In the present series the Y_2O_3 content was kept constant to prevent any influence on the sintering behaviour of changing the total wt% sintering additive (changes in the vol%liquid formed). It was also anticipated that AlN as a sintering aid will play a beneficial role in the liquid forming and liquid composition in this system, by introducing excess Al^{3+} into the liquid and that the excess nitrogen should result in a secondary phase with improved properties. AlN is often employed in the fabrication of α-sialons, which as reported by Hwang and Cheng [173] can be pressureless sintered to near full density at temperatures <1600°C.

3.1.2. $Si_3N_4 + Y_2O_3 + Al_2O_3 + CaZrO_3$

CaO was considered as a candidate sintering additive in the present study as it forms very low temperature eutectic with SiO_2 at approximately 1170°C [173], and thus should promote good densification of Si_3N_4 at low temperatures. It is recognised that the presence of Ca^{2+} in any secondary or intergranular phases in the final material may be deterimental for high temperature properties. However, the solubility of CaO in the α-Si_3N_4 structure is extremely good [113] and it was expected that by incorporation into the Si_3N_4 structure any residual phases will be cleaned of Ca^{2+}. Since the additive CaO cannot be dispersed in aqueous solution, a pre-cursor, $CaZrO_3$, was used. Under high temperature sintering, it is predicted that at CaO-SiO_2 melting temperature, $CaZrO_3$ will dissociate into CaO and ZrO_2 [174]. Zirconia has also been reported as a successful sintering agent for Si_3N_4 [165] and recently has gained considerable interest as an additional additive in the Si_3N_4 - Y_2O_3 - Al_2O_3 system, where it is thought to act as a growth modifier promoting crystallisation of residual glassy phases [175][176][177]. The amounts of $CaZrO_3$ chosen reflect the initial addition of 1wt%CaO and further increases to 1.5 and 2wt%. To maintain the total additive content at 10wt%, the wt% of Y_2O_3 and Al_2O_3 added were adjusted accordingly.

Sample Label	Si_3N_4	Y_2O_3	Al_2O_3	AlN
0AlN				
wt%	88.5	5	6.5	-
mol%	88	3	9	-
1AlN				
wt%	88.5	5	5.5	1
mol%	84	3	7	4
2AlN				
wt%	88.5	5	4.5	2
mol%	84	3	6	7
3AlN				
wt%	88.5	5	3.5	3
mol%	83	3	4.5	9.5
4AlN				
wt%	88.5	5	2.5	4
mol%	81	3	3	13

Table 3.1 Compositions of ceramic samples in the Si_3N_4 + Y_2O_3 + Al_2O_3 + AlN series investigated.

Composition Label	Si_3N_4	Y_2O_3	Al_2O_3	CaO	ZrO_2
3.2CaZ					
wt%	90	3.4	3.4	1	2.2
mol%	88	2	5	2.5	2.5
4.8CaZ					
wt%	90	2.6	2.6	1.5	3.3
mol%	88	1.5	3.5	3.5	3.5
6.4CaZ					
wt%	90	1.8	1.8	2	4.4
mol%	88	1	2	4.5	4.5

Table 3.2 Compositions of the ceramic samples in Si_3N_4 + Y_2O_3 + Al_2O_3 + $CaZrO_3$ system investigated.

Composition Label	Si_3N_4	Y_2O_3	Al_2O_3
REF			
wt%	90	6.9	3.1
mol%	91	4	4

Table 3.3 Composition of the reference ceramic samples investigated.

3.1.3. Powders

Starting powders were submicrometer dimension α-phase Si_3N_4 powder with sinter additives, Y_2O_3, Al_2O_3, AlN (coated - to improve dispersion) and $CaZrO_3$ (Table 3.4).

Powder	Producer	Specific Surface Area (m^2/g)	Mean Particle Size $d_{50}\mu m$
Si_3N_4 (SN-E10)	UBE	10-14	0.55
Y_2O_3 (Grade C)	H. C. Starck	10-16	<1
Al_2O_3 (RA207LS)	Alcan Chemicals	7	0.5
AlN	Alfa	3	1.4
$CaZrO_3$	Condea Chemie	29.9	<15

Table 3.4 Powder Characteristics.

3.2. Powder Dispersion Analysis

3.2.1. Dispersion Experiments

The quality of the final sintered ceramic is directly dependent upon the formation of a green form of maximum density, agglomerate-free and with the powder particles uniformly close packed. Irregular packing or the inclusion of agglomerates automatically introduces significant flaws which cannot be removed by subsequent treatment and which intrinsically contribute to loss of strength and toughness in the final product. The formation of an optimally packed green form is crucially dependent upon the quality of the powder dispersion, where ideally the powder particles should be suspended separately, be mutually repulsive and be supported in the suspension by simple Brownian movement with no tendency to sediment. Unfortunately, the economics of green forming require that the slurries are also castable in finite time and form green bodies of maximum density, therefore requiring a maximum powder content in the dispersion. Inevitably then, the optimal green forming process is a compromise between suspension quality and castability.

Despite these constraints, much can be done to optimise the quality of the dispersion by careful control of the electro-chemical interaction between solvent and the powder particles and in the physical processing of the slurry and the casting technique.

Evaluation of dispersion quality was made by measuring the Electrokinetic Sonic Amplitude (ESA) of suspended particles using a Matec™ Applied Sciences, Electrokinetic Sonic Analysis System™. This analysis system generates relative motion between particles and the liquid surrounding them as a sound wave passes through a suspension. The amplitude of the motion is controlled by the solvent/particle density difference, the size and shape of the particle and the frequency of the sound wave. A ceramic powder suspended in a polar solvent generates an electrical double layer, which distorts during relative motion. This distortion results in the displacement of the charge of the particles, producing an alternating electric dipole. The amalgamation of the electric dipoles from all the particles produces an electric field. The opposite phenomenon also takes place, that is, when an electric field is applied to a dispersion an acoustic wave is generated. The Matec™ system works on this principle by applying an electric field to a dispersion and measuring the many electroacoustic effects which are produced. These effects are then related to transport properties and hence the "microstructure" in the dispersion [178], that is, the electrochemical-relationship between the particles and the solvent (2.2.1.1, Figure 2.4). High Electro Sonic Amplitude (ESA) of the resultant acoustic wave indicates a highly charged particle surface producing repulsion and hence a stable dispersion. The expression,

$$ESA(\omega) = c\Delta\rho\phi\, G_f\mu_d(\omega) \qquad \mathbf{3.1}$$

relates the measured acoustic wave amplitude (ESA) to dispersion properties and suspension mobility parameters.

In Equation 3.1 [178], c = velocity of sound in suspension, $\Delta\rho$ = solvent/particle density difference, ϕ = powder volume fraction, G_f = electrode geometry factor, μ_d = dynamic mobility. At solid volume fractions > 10% this expression loses validity, as interparticle spacing and electrical double layer thickness become comparable, and the amplitude of the acoustic wave produced is no longer linear with dispersion concentration. The specificity of the technique also implies that ESA values can only used when comparing dispersions of the same material and solids content.

The technique provides a measure of particle zeta potential (ζ), using Equation 3.2 (Smoluchowski's equation)

$$\mu_d = \frac{\varepsilon\zeta}{4\pi\eta} \qquad \mathbf{3.2}$$

where, (ε) is the solvent di-electric constant and (η) is the solvent viscosity.

Matec^{TM} experiments were carried out on ultrasonically dispersed aqueous solutions of AlN(coated) and $CaZrO_3$ powders. The individual dispersions contained 200mls H_2O and 2vol% powder. Each one was mixed on a magnetic stirrer and then subjected to high shear rate agitation by means of a dip in ultrasonic probe (Branson B30 Sonifier Cell Disruptor). In addition to ESA, probes are included to monitor temperature, conductivity and pH of the suspension. The experiments were carried out in titration mode, using an automated burette that allows the timed delivery of additive solutions (acids, bases, surfactants). 0.1M solutions of NaOH and HNO_3 were used to vary the pH. Figure 3.1 illustrates the system used.

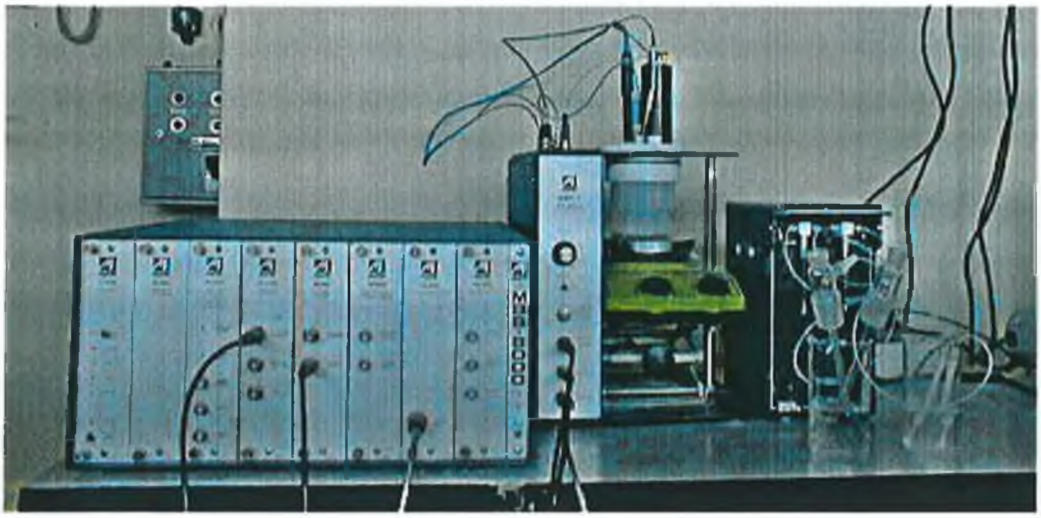

Figure 3.1 Matec^{TM} system.

3.3. Green body formation

Figure 3.2 describes the basic processing route for green body fabrication. The individual steps are described in detail in the following sections.

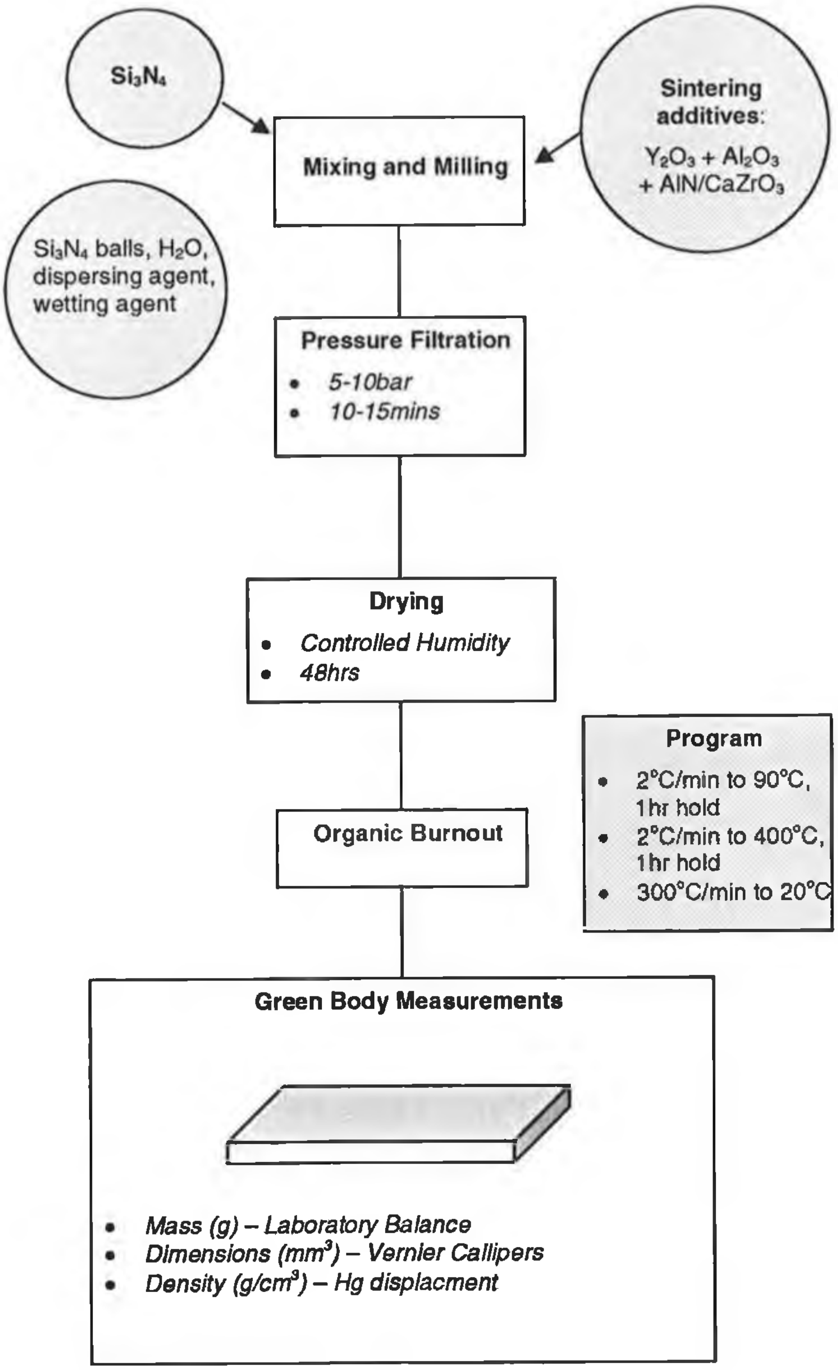

Figure 3.2 Basic Processing Route.

3.3.1. Mixing and Milling

Deionised water based slurries were prepared with a solid content of 65wt%. The slurries were attrition milled with 2mm diameter silicon nitride balls for 1.5hrs to break up agglomerates. When $CaZrO_3$ was used as an additive it was necessary to mill the calcium zirconate powder for up to 2 hours prior to the addition of the other powder, in order to reduce the agglomerate size as much as possible. The coated AlN powder was added towards the end of the attrition milling for just 15 minutes at slow speed to minimise damage to the protective coating. For this system, an organic phosphate ester, Emphos CS, was employed as a wetting agent to encourage dispersion of the coated AlN powder. The dispersions were stabilised with 1.1wt% ammonium polymethlyacrylate (Darvan C) and brought to pH 10.3-10.5 using tetra-methyl ammonium hydroxide (TMAH) to maintain a stable dispersion.

Earlier experience [68] had shown that the complete break up of all agglomerates in these slurries could be achieved only by attrition milling. Attrition milling is one of the most efficient dispersing or comminuting techniques, in which the power input from the attritor is used directly to agitate the media. This contrasts with more commercial processes which rotate or vibrate a large heavy vessel containing the media charge. Three types of attritors are currently available; (1) batch, (2) continuous, (3) circulation. A batch attritor was employed in this project, being most suitable to the scale of the experiments (Figure 3.3)[179]. The material to be ground or dispersed is placed in the stationary attritor tank with a charge of grinding balls. The central rotating shaft with several horizontal arms provides agitation of the material and the balls. The balls move randomly through the slurry, causing irregular movement and promoting individual impacts rather than a laminar flow movement (Figure 3.4)[179] . The balls are also spinning in different rotation directions while randomly moving through the media, thereby exerting shearing forces on the adjacent slurry. Both the impact action and shearing force promote efficient grinding and dispersing (Figure 3.5)[179] and encourage micro mixing by breaking up agglomerates of different material particles and dispersing them in a slurry.

Figure 3.6 illustrates the media agitation in the attritor [179]. Maximum agitation is seen to occur at about 2/3 the radius from the centre. Grinding does not occur against the vessel walls so that vessel wear is small and thinner walled vessels can be used with better heat transfer, thus enhancing temperature control of the media inside the vessel. The horizontal arms attached to the central rotational shaft are designed to move the slurry not only around the vessel but also laterally, in and out of its most effective zone.

The major contribution to contamination of the slurry comes from the wear of grinding balls so that the selection of balls of composition the same as the slurry powder is of the utmost importance. Other sources of contamination are the tips of the agitator arms, the vessel lining wall and the grid plates. In the current system the potential for contamination was almost completely removed by employing grinding balls made of high purity silicon nitride (2mm) and using a vessel liner, grid plates and arms made of silicon nitride.

Following attrition, the slurry was rocked in a low frequency vibrating table to encourage separation of the milling balls, and was filtered through a sub-millimetre metal mesh. To prevent contamination of consecutive slurry runs the balls were washed thoroughly between batches. The beaker of collected slurry was then agitated on a magnetic stirring plate until casting.

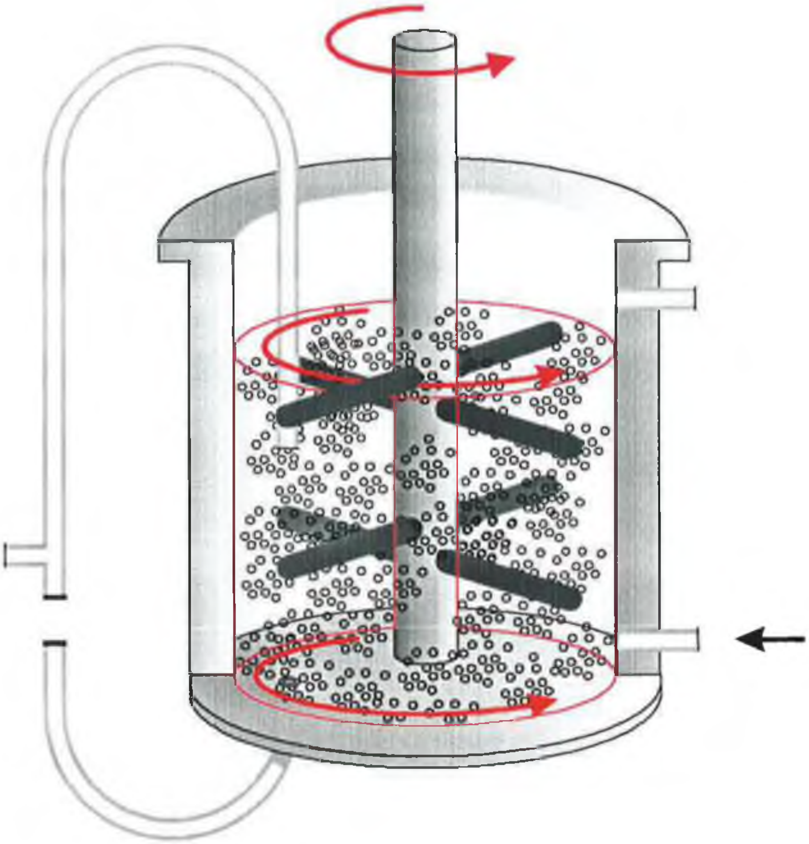

Figure 3.3 Batch Attritor [179].

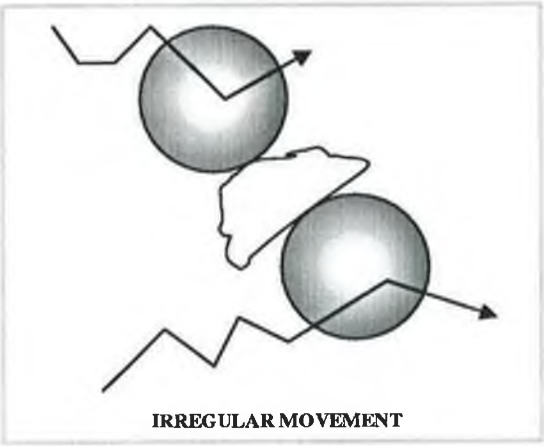

Figure 3.4 Irregular Movement [179].

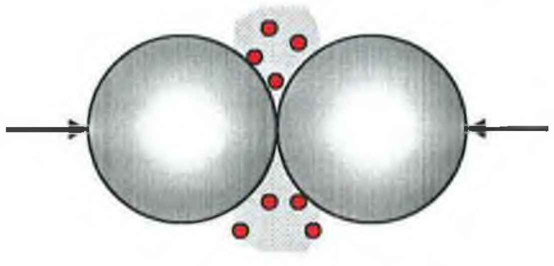

IMPACT

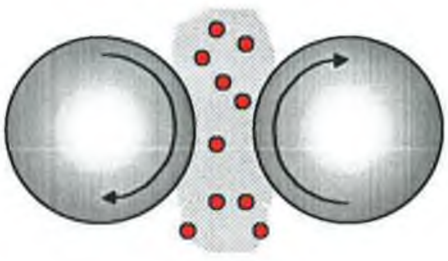

SHEAR

Figure 3.5 Impact and Shear [179].

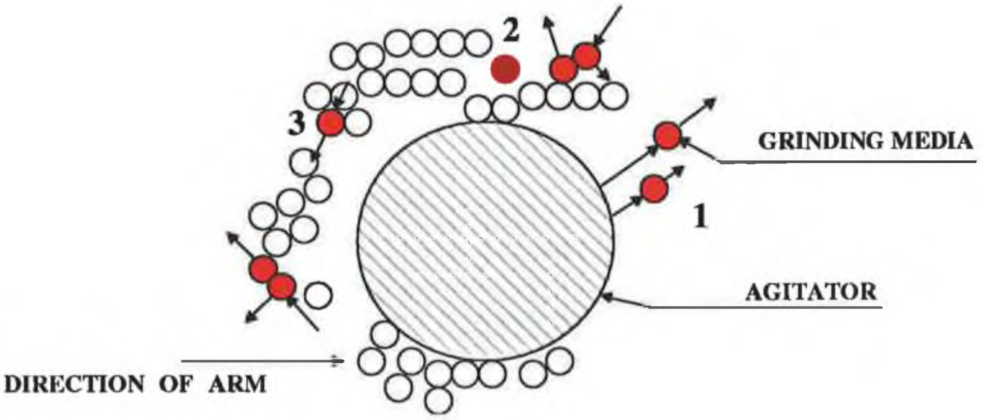

Figure 3.6 Attritor Action [179]

3.3.2. Viscosity Measurements

Prior to pressure casting viscosity measurements were made on each aqueous slurry prepared. A rotational technique was used, as outlined in Section 2.2.1.1, this method provides the simplest, general method for taking quick and intermittent measurements. A simple cone and plate viscometer is illustrated in Figure 3.7.

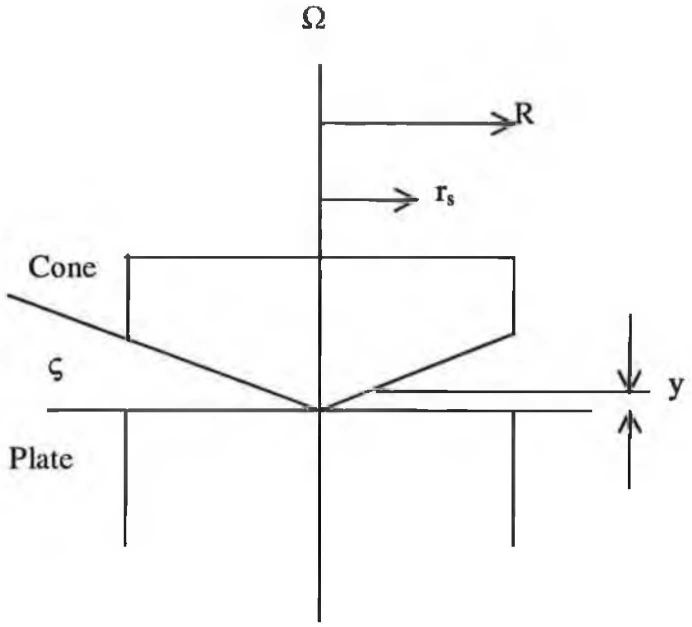

Figure 3.7 A simple cone and plate viscometer.

A concentric cylinder viscometer, which is an advanced model of the cone and plate viscometer, was used. Attached to a shaft, a rotating cylinder (the bob) is rotated in the slurry within a concentric cylinder (the cup). Although the calculation of viscosity is automated, a brief outline of the calculation is described. Since the viscosity of a fluid is $\eta = \tau/\gamma$, measurements of shear stress, τ and shear rate, γ are required.

The shear stress is determined from

$$\tau = \frac{M}{2\pi r^2 h} \qquad \mathbf{3.3}$$

where M is torque, r is the radius of measurement and h is the height of the bob. For a steady state flow of fluid, the torque throughout the gap is constant and so can be measured at the bob surface and the shear stress calculated for any point within the fluid. For a Newtonian fluid the viscosity is independent of shear rate, so that as the shear stress decreases across the gap in proportion to r^{-2}, the viscosity stays constant and correspondingly the shear rate decreases with respect to r^{-2}. An average shear rate is thus calculated for the centre of the gap

$$\gamma = \Omega\left(\frac{R_c^2 + R_b^2}{R_c^2 - R_b^2}\right) \qquad \mathbf{3.4}$$

where Ω is angular velocity and R_c and R_b are the radii of the cup and bob respectively.

In the present study a Contraves Rheomat 115 rate controlled viscometer was used for viscosity measurements. The instrument has a DIN 145 cup/bob assembly with a 3mm gap width (R_c = 48.5mm, R_b 0 45.5mm). An average shear rate of $130s^{-1}$ was in the centre of the gap (as determined by Equation 3.4), by ramping the shear rate from 0 to 100 revolutions per minute.

3.3.3. Pressure Filtration

Figure 3.8 illustrates the equipment used for pressure casting of green forms (this figure is also Figure 2.9, in Section 2.2.2.1 and is shown again here for clarity). Casting of monolith green bodies in the present work employed the same system, without the grid. Two larger filter papers (0.45µm, 90mm diameter) and one smaller (0.45µm, 50mm diameter) were placed on the porous surface of the ceramic filter, sprayed with water and held in place by vacuum. It was essential that these papers were smooth and flat as the base of the cast body forms on that surface. The inside walls of the mould were sprayed with a releasing agent (CIL Release Agent 1711E, Compounding Ingredients Limited) to prevent the slurry drying and sticking to the walls during casting. The mould was then mounted on the base of the vessel. The slurry was poured carefully into the mould and the vessel lid attached and sealed tightly. A gas-pressure of 5 to 10bar was applied for 10-15 minutes.

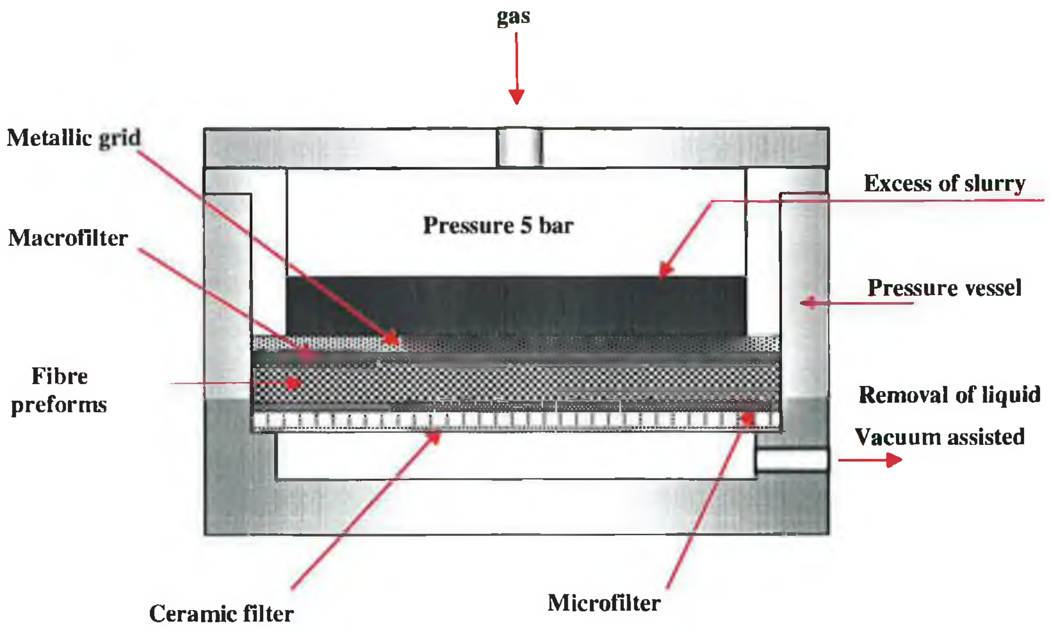

Figure 3.8 Pressure Infiltration System [68].

3.3.4. Drying

Drying slowly and uniformly is important to avoid anisotropic shrinkage and cracking. The wet green bodies were placed in a drying box, and the humidity slowly lowered by intermittent spraying of the interior glass walls with water, followed by drying in laboratory air. After 48 hours samples were selected for organic burnout and the remainder were stored in a dessicator for future use.

3.3.5. Organic Burnout

Selected samples were heated to 400°C for 1 hour (see Figure 3.2 for program details) to remove remaining intrinsic water and organics (dispersing and wetting agents).

3.4. Densification Experiments

3.4.1. Pressureless Sintering

Monolithic and composite samples were sintered in a graphite crucible (outer diameter: 100mm, inner diameter: 50mm, height: 150mm) as illustrated in Figure 3.9. The sinter furnace is equipped with a single in-situ dilatometer and for each sintering run of the monolithic samples, one sample for in-situ dilatometry was included. Samples were embedded in a powder bed in order to reduce volatisation [180]. The powder bed contained 25% of the sample composition and 75% inert boron nitride to inhibit sintering of the ceramic additives in the powder bed. Graphite pieces (45mm × 45mm × 3mm) were placed above a layer of powder bed to keep the specimen flat, since non-uniformities in the green body density and anisotropic cooling both lead to differential shrinkage, bending, and porosity during sintering. Sintering temperatures ranged from 1400°C-1650°C for the AlN series and the reference material, while materials containing calcium zirconate were sintered at 1450°C, 1650°C, and 1750°C. A heating rate of 5°C/min was used, for hold times of up to 4 hours, followed by fast cooling (8°C/min). A low over-pressure of 10bar N_2 pressure was introduced at low temperatures and to encourage further closure of porosity, it was maintained for 30 minutes after the hold time at sintering temperature. Both sample compositions were held after each sinter run, at 1300°C for 2 hours on cooling to help induce crystallisation of the secondary grain boundary phase. The crystallisation step was omitted during the cooling of the composite sample in order to minimise fibre-matrix interaction and the cooling rate was reduced to 3°C/min, to help prevent potential matrix-microcracking occurring as a result of the CTE mismatch between the ceramic matrix and the fibres. Temperatures lower than 720°C were measured by a Pt/Pt-Rh thermocouple positioned inside the wall of the furnace. At higher temperatures the thermocouple degrades and is unreliable for temperature control. A pyrometer was used at temperatures >720°C. To maintain accurate sintering temperatures both the thermocouple and pyrometer were calibrated at regular intervals throughout the study. The recently developed Philips Temperature Control Rings (PTCRs) were also used regularly during sintering runs. The shrinkage of the PTCR diameter reflects the actual temperature at the point where the ring is located in the furnace. In the present study, the rings were placed in the lid of the graphite crucible. The measured ring diameter is then converted to ring temperature using a conversion table supplied by the manufacturer. Two temperature ranges of PTCRs were used, 1340°C - 1520°C and 1450°C - 1750°C. These rings offer an accuracy of within ±3°C.

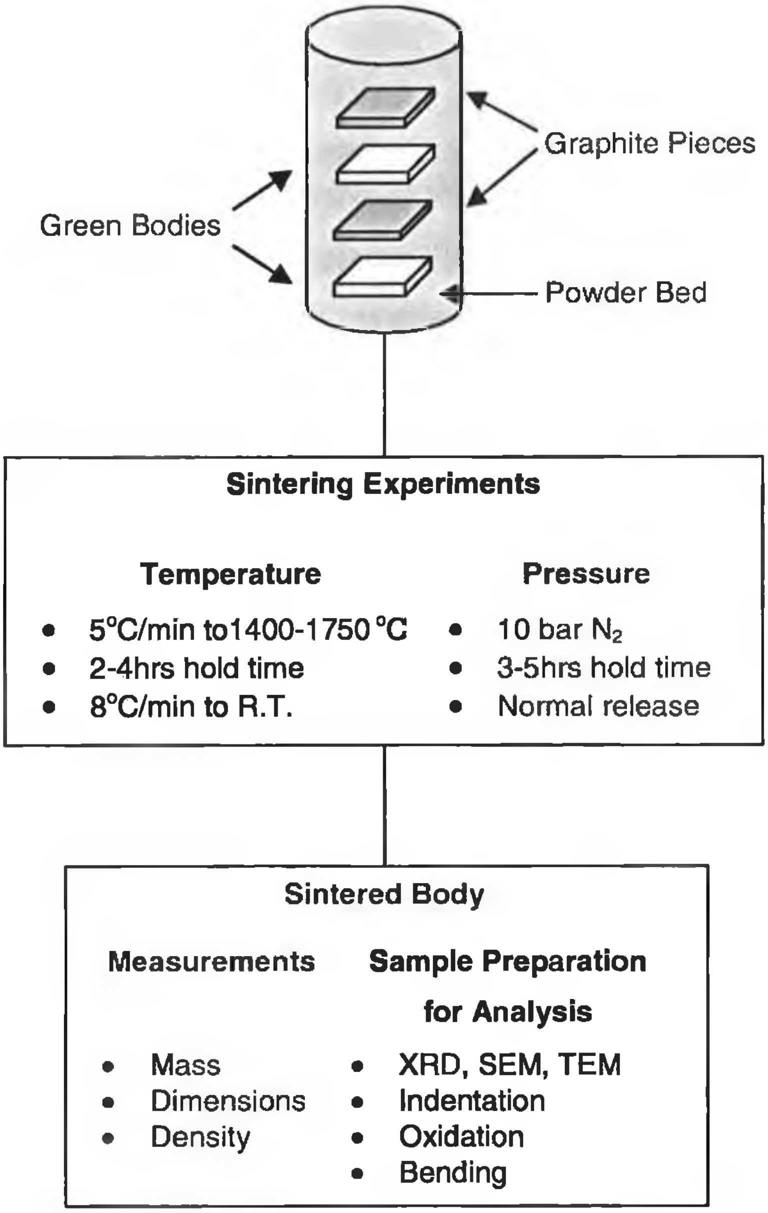

Figure 3.9 Sintering Experiments and Analysis.

3.4.2. Dilatometry Experiments

A series of dilatometry experiments were carried on monolithic sample compositions, which were selected based on early densification results. Cut green body samples (20mm × 10mm × 5mm) were set up in a Netzch table-top dilatometer, model 402E. The samples were heated at a constant heating rate of 5°C/min to 1600°C for 2 hours.

3.4.3. Gas Pressure Sintering

Composite samples were sintered at 1600°C for a 2 hour hold time, under 60bar N_2 pressure. The samples were set up in a graphite crucible in the same manner as described for the pressureless sintering experiments and heated to temperature at a rate of 5°C/min. A gas over-pressure of 10bar was introduced at low temperatures and increased at approximately 1200°C (the temperature of initial liquid phase formation determined from the dilation curves of the monolith matrix) to promote densification and then raised to reach the maximum 60bar at 1500°C. The pressure was held for 30 minutes after the 2 hour hold at 1600°C, which along with a very slow cooling rate, is expected to help reduce matrix micro-cracking.

3.4.4. Hot-pressing

Green body samples were cut to dimensions of 72mm × 45mm to fit the graphite mould used in the hot-press. The samples had, on average, green body thickness of 5mm. The samples were hot-pressed in a N_2 atmosphere and a mechanical load of 88kN, corresponding to a pressure of 127bar was applied to the mould. Heating ramps were set to 10°C/min and the mechanical pressure was introduced around the temperature of liquid phase formation (1200°C) and increased to reach maximum 100°C below the peak temperature.

3.4.5. Shrinkage, Mass Loss and Density Measurements

Basic shrinkage and mass loss values of samples were calculated on the simple basis of the sample thickness and sample mass differences respectively, after heat treatment. The percentage shrinkage, %S, was calculated from:

$$\%S = \frac{\Delta L}{L_0} = \frac{Thickness\,Difference}{Original\,Thickness} \qquad \textbf{3.5}$$

And the percentage mass loss, %ML, was calculated from:

$$\%ML = \frac{\Delta M}{M_0} = \frac{Mass\,Difference}{Original\,Mass} \qquad \textbf{3.6}$$

Sample dimensions were measured using Vernier callipers. Sample masses were measured on a balance with an accuracy to ±0.01g.

Monolithic green and sintered body density was determined by an Archimedes immersion technique using a mercury balance (Figure 3.10) [181]. Archimedes' principle states that a body immersed in a fluid is buoyed up by a force equal to the weight of the displaced fluid. Using a Hg balance, the upthrust force is defined as:

$$F = V\rho_{hg}g \qquad \textbf{3.7}$$

Where, V is the volume of displaced liquid, ρ_{hg} is the density of mercury and g is the acceleration due to gravity. In the Hg balance method, the sample is submerged in the mercury by a saddle and so must exert an equal, but opposite downward force to the upthrust force, F. This force is represented as a mass value on the balance. Inserting this value into Equation 3.7 (F=m.a, with a equal to g), the volume of the ceramic body can be determined and used to calculate its density (density = mass/volume).

The irregular, porous surfaces of the composite green bodies may lead to entrapment of mercury and serious contamination during sintering and hot-pressing, only the densities of heat-treated composite samples were measured using the Hg balance technique.

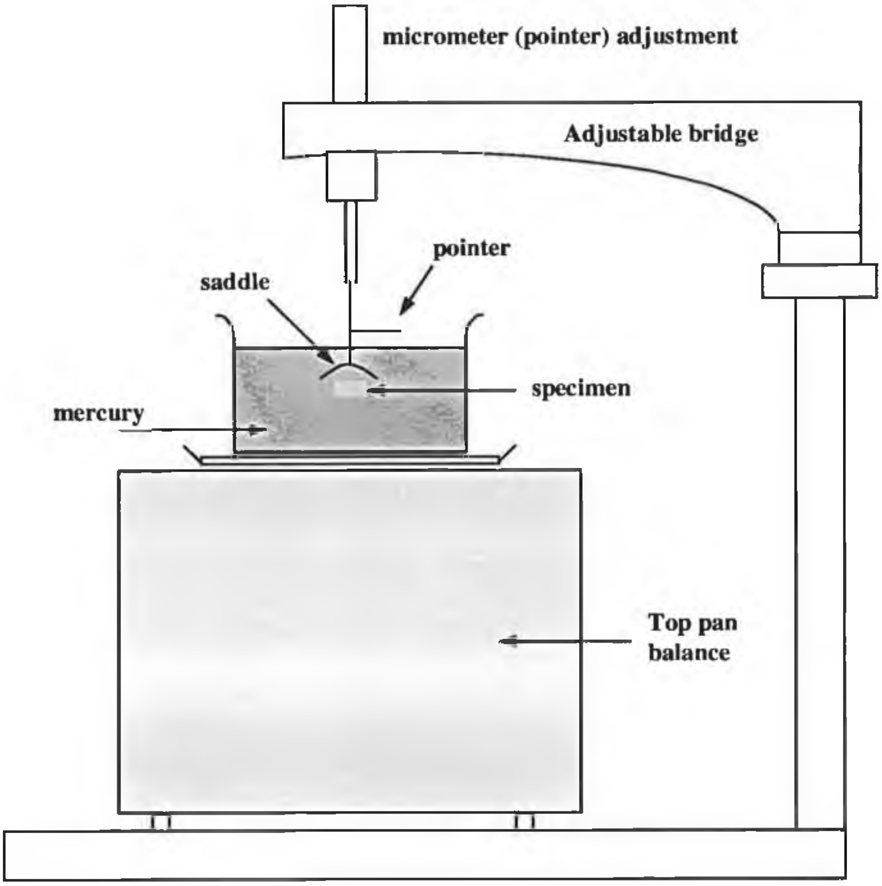

Figure 3.10 Schematic diagram of the mercury balance used for bulk density measurements.

The rule of mixtures was used to calculate theoretical densities.

$$\text{Monolithic Theoretical Density} = \frac{Total\ Mass\ of\ Powders}{\frac{M(Si_3N_4)}{\rho(Si_3N_4)} + \frac{M(Y_2O_3)}{\rho(Y_2O_3)} + \frac{M(Al_2O_3)}{\rho(Al_2O_3)} + \frac{M(X)}{\rho(X)}} \quad 3.8$$

where M and ρ are the mass and density of the given powders and X represents AlN or $CaZrO_3$.

$$\text{Composite Theoretical Density} = \left[V_f \rho_f + \left(100 - V_f\right)\right] \times \rho_m \qquad \textbf{3.9}$$

where V_f is the volume fraction of fibres and ρ_f and ρ_m are the densities of the fibre and matrix respectively.

3.5. Materials Characterisation

3.5.1. Introduction

Liquid-phase sintering of the Si_3N_4-based ceramics studied here, produces a dense material consisting mainly of the two Si_3N_4 phases α and β, and intergranular phases of varying composition. The performance of these ceramics depends primarily on the properties of the primary Si_3N_4 phases but is also greatly influenced by the chemical composition of the intergranular phases. Also the microstructure of the material is an important parameter, as the size and shape of the Si_3N_4 grains and the volume fraction of the intergranular phases may influence the material's performance. There exists therefore a complex relationship between low and high temperature behaviour and material composition and morphology.

X-ray Diffraction (XRD), Scanning Electron Microscopy (SEM), Energy Dispersive X-ray Analysis (EDX), Image Analysis and Transmission Electron Microscopy (TEM) techniques were used in this study to analyse the phase composition and microstructure in the dense materials.

3.5.2. X-ray Diffraction (XRD)

Identification of the phases present in the sintered ceramic bodies was carried out using X-ray diffraction (XRD). The acquisition of information is rapid, non-destructive and can be obtained from powder, single crystal, or flat polished crystalline materials. X-rays are diffracted by the lattice planes of crystals, the diffraction path and the resulting diffraction pattern being dependent on the arrangement of atoms in the crystal and is thus characteristic of the crystal. Monochromatic radiation of known wavelength is used in all XRD instruments where the diffraction angle is always 2θ and constructive interference between the diffracted beams occurs when the Bragg Law (Equation 3.10) is satisfied:

$$\lambda = 2d \sin \theta \qquad \textbf{3.10}$$

where θ is the incident angle, d is the distance between lattice points (lattice spacing) and λ is the wavelength.

Identification of complex atomic structures require detailed indexing of the diffraction pattern and intricate corrections to the collected intensity data [182][183]. In practise, experimentally accessed diffraction patterns are identified by reference to a compilation of "standard" patterns (JCPDS) which have been developed for most known compounds.

3.5.2.1. Equipment used

In this study, phase analysis was made using a standard Philips PW 3700 x-ray diffractometer configuration Be filtered Cu Kα radiation with a long fine focus beam (0.4mm × 12mm). The samples were scanned for a period of 2hours 10mins. Analysis of the final diffraction patterns was computer assisted using the Rietveld^{TM} analysis system that utilises a "best-fit" method between the unknown phases and a database of reference spectra of phases.

3.5.2.2. Sample Preparation

The sintered bodies were cut into approximately 1cm^2 pieces and polished to 1μm surface finish using a series of diamond pastes. A flat surface helped to improve the quality of the diffracted signal. It was observed after sintering that certain samples had a variation in colour from the surface to the centre. The gas composition through a bulky porous pre-ceramic form during high temperature sintering will vary from the outside to the centre, which may result in the formation of different reaction products. To study this tendency, analysis was made at different depths from the surface of the cross-sections of a number of samples submitted for XRD analysis.

3.5.3. Scanning Electron Microscopy (SEM) and Energy Dispersive Analysis (EDX)

The principles behind the techniques of SEM and EDX are based either directly or indirectly on the interaction between an applied electron beam and the sample. The incident (primary) beam is directed onto the material, where it is partly reflected from the surface and partly undergoes a number of different interaction events with either the electrons or nuclei of the sample atoms or both. These interactions occur in a region of the sample known as the interaction volume. Elastic events are those that result in little or no beam electron energy loss and occur when the incident beam interacts with the nucleus of the sample. Interactions between the beam and the atomic electrons result in a high loss of beam electron energy and are termed inelastic events. Each incident electron can trigger more than one event.

X-rays are generated when electrons of high velocity are bombarded onto a solid. The electrons decelerate as they fall into the sample generating a continuous spectrum called Bremsstrahlung. Superimposed on the continuous spectrum is a line spectrum with a few high-intensity, sharp peaks whose energy and wavelength are characteristic of the composition of the sample. These peaks arise as a result of the interaction of the incident beam with the electrons of the sample.

According to the Bohr model of the atom, sample electrons are arranged in increasing energy level or shells labelled, K, L, M,... corresponding to the principal quantum numbers, n = 1, 2, 3....The incoming electron beam excites atomic electrons their stable energy levels to higher energy shells. These electron then casade back to the lowest energy level possible, emitting "quantum" of energy proportional to the difference in shell energy level. This quantum is emitted as an X-ray photon with a characteristic wavelength (Figure 3.11) [184]. The relationship between the wavelength of the photon and the energy is given in equation 3.11. Each element in the periodic table has a unique number of electrons and thus a unique set of quantum numbers, such that the energy and wavelength of the X-ray spectrum produced is characteristic of the particular element.

$$E = h\upsilon \, and \, \upsilon = \frac{c}{\lambda} \qquad \textbf{3.11}$$

where, E = energy, h = Planck's constant (6.626 X 10^{-34} JHz^{-1}), υ = frequency, c = speed of light (2.998 X $10^{8}ms^{-1}$), and λ = wavelength.

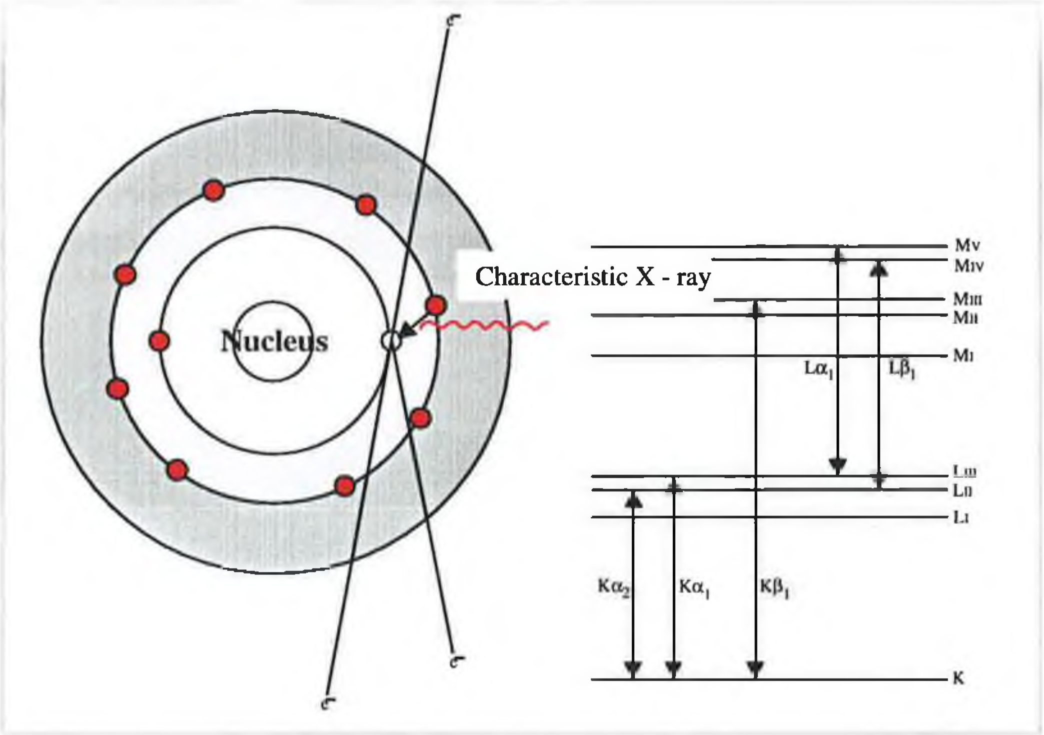

Figure 3.11 The Bohr model of the atom and characteristic X-rays emitted [184].

Secondary electrons are produced by inelastic interactions between primary electrons and loosely held sample electrons, which are displaced and enable them to escape from the surface. Also, primary electrons may be deflected several times within the atom losing significant amounts of energy and those close to the surface may escape as secondary electrons. Regardless of origin, secondary electrons have very low energy (<50eV) and only those in the outermost regions of the sample can escape. Thus they contain important information about the sample surface (topography). Detection of these low-energy secondary electrons is possible as they are produced in large quantities. The yield decreases exponentially with the depth of their generation, with over half the total yield of secondary electrons being emitted within a depth of approximately 0.5nm (5Å) [185]. The angle between the primary electron beam and the sample surface greatly influences the yield of secondary electrons since the area of emission increases as the beam hits the surface with a small angle. This provides a grey level difference determined by local topography.

Backscattered electrons (BSE) are produced as a result of elastic interactions between the primary electron beam and the nucleus of the sample. Little or no energy loss is expected although the BSE leave the surface over a wide spectrum of energies (50eV→50keV). The energy distribution of the BSE is more dependent on the angle of the incident beam with the sample rather than its energy. At a low angle the primary electrons have a higher probability of being backscattered by atoms close to the surface. Since BSE are produced as a result of elastic interactions with the nucleus of the sample, the yield of BSE and thus the intensity of the signal is directly dependent on the atomic number of the scattering element.

The basic interactions between an incoming electron beam and a sample are shown in Figure 3.12 [185].

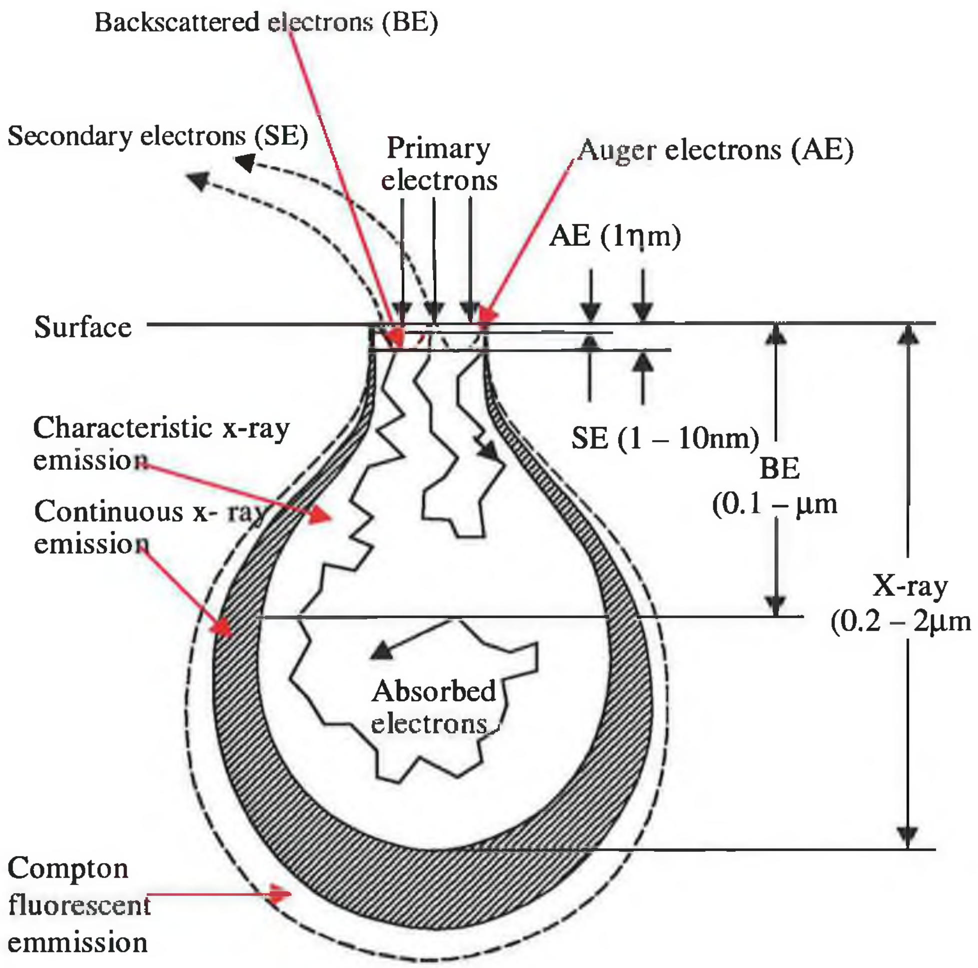

Figure 3.12 Types of electron-beam-excited electrons and radiation and the depth of the region below the specimen surface from which information is obtained [185].

One of the most versatile instruments for investigating the morphology of materials is the Scanning Electron Microscope (SEM). It covers a wide range of magnification extending from 10,000× up to 150,000×. Some advantages include; easy magnification adjustment, large depth of field (depth of focus), and stereographic image display. Also the images formed are easy to interpret and clear pictures of as-polished and etched specimens are possible. The sample under investigation is irradiated with a finely focused electron beam (5-10ηm) which is scanned across the sample surface. Secondary and Back Scattered electrons will be emitted from each point of scanning (as described before). The emitted electrons are induced to move to a collector (electron detector) under a positive potential of approx. 10keV (accelerating voltage). When they strike the scintillator they generate photons which are then amplified by a photomultiplier. The amplified beam controls the brightness of the spot on the cathode ray tube (CRT) that is shown in real time with the electron beam scanning the surface. The magnification achieved is a function of the ratio between the area scanned to the area of the image on the CRT, so the magnification is increased by scanning smaller areas on the sample.

One minor disadvantage is that, in non-conductive materials, the incident electrons induce electrostatic charging of the surface that interferes with the emergent electrons causing loss of resolution. This problem is overcome by pre-coating the specimen with a conductive layer; carbon if chemical analysis is required or gold to enhance topographical contrast.

Contrast between topographical features can be observed because the intensities of both SE and BSE are dependent on the angle of incidence of the primary electron beam and the surface. However, since SE are emitted from areas close to the surface (as outlined above) SE signals are most suitable for discriminating topography; variations in the roughness in the surface cause changes in the incident beam angle and thus the development of contrast in the final image. Secondary electrons are emitted from all directions from the sample resulting in shadowless images. These characteristics provide accurate and well-contrasted images of sample topography, giving especially good depth of focus from rough surfaces.

The backscattered electron image shows a contrast more dependent on the atomic numbers of the sample constituent elements rather than on the topography of the surface. The intensity of the BSE beam increases as the atomic number increases, resulting in a brighter image, thus it is possible to identify the elemental composition of the scanned area. If the surface is evenly polished the BSE signal can be used to distinguish between phases which have identical elements present but in different concentrations.

A LEO 430 Scanning Electron Microscope was used for this study. It has a magnification range of 15× to 300,000× and an accelerating voltage range from

300V to 30kV. As described earlier, this potential is applied to the collector and when positive SE are collected and when the collector is at a negative potential only BSE are detected.

3.5.3.1. Energy Dispersive X-ray Analysis (EDX)

Qualitative chemical analysis of the sample was carried out using an EDX system within the LEO 430 SEM. Characteristic X-rays emitted from the specimen have energies corresponding to individual elements. The X-rays are absorbed by an Si[Li] semiconductor detector placed at the tip of the electron detector. The X-ray photons generate current pulses, the height of which are proportional to the individual X-rays. The signal is amplified and passes through a multichannel analyser, where the pulses are grouped according to their voltages. The information is processed in a microcomputer and displayed on the screen as an "elemental map" of peaks. Elemental analysis of a very small area can be performed by locating the fine electron beam on the spot to be studied. The information is obtained from an area approximately 1 to 10μm in the X and Y planes. An average of the elemental composition of an area can be obtained by scanning the beam over the area. Elements with high atomic numbers are easily separated by their significant lines however, lighter elements are difficult to detect. Elements below atomic number 11 (sodium) cannot be analysed owing to the presence of a beryllium window in front of the crystal detector which absorbs low energy X-rays. Advanced systems use a diamond window which allows analysis down to N, but this is very expensive. A windowless detector could also be used but this is not recommended for reasons of detector cleanliness.

A Link ISIS computer analysis system (Oxford Instruments) was used in this study. It utilises a Windows 95 user interface allowing the user to easily and quickly master the application.

3.5.3.2. Sample Preparation

Cross-sections were embedded and back-filled in an epoxy resin block and then polished with a buffing machine to a 1μm finish. Since a SEM analyses the surface layer of a sample, it is essential that the sample surface is clean. The samples were carbon coated and silver paint was used to make contact between the sample and the holder.

3.5.4. Quantitative Image Analysis

In the simplest terms, the morphological features of a material may be displayed on a visual display unit as an electronic image. The two most widely used imaging techniques are by the scanning of optical micrographs, or directly from a digital camera and detector (for example in a scanning electron microscope). The "digital" image consists of a matrix of points called pixels, each with a grey or colour value. In material science applications the images are usually black and white, and one byte is dedicated to every pixel; every pixel can assume 256 different grey values. Quantitative Analysis is then achieved by setting a "grey-level" threshold, which separates or rejects the pixels on the basis of their grey value. The retained pixels may then be counted electronically. Increasingly sophisticated algorithms are now developed to allow determination of more and more complex geometry features, for example to discriminate between features of different aspect ratio, size, shape, orientation, straight or branched, and so on.

In practise, the methodology is fraught with sources of inaccuracy. Reproducibly accurate and reliable analysis demands rigid procedural standardisation and discipline. The operation of image analysis involves three main stages, Specimen Preparation, Image Acquisition and Image Analysis, all of which introduce assumptions and errors. Typical examples include; during Stage One, (Specimen Preparation), the accurate definition of the edge of a feature, especially where the hardness changes across the feature edge is a major source of error and is wholly dependent upon the quality of metallographic preparation. The risk of material damage during preparation, pullout and rounding off of edges all artificially increase the size of a feature. Similarly, lack of focus during Stage Two, (Image Acquisition) leads to deceptively high values. Here, also, the discrimination of the grey-level is a primary source of error. In very few practical cases is the edge of a feature sharp to the accuracy of one pixel. The selection of the boundary is totally dependent upon the algorithm selected for grey level separation, the so-called thresholding or segmentation operation. Finally during Stage Three, (Image Analysis) image sample size, (very many images are better than very few, but larger features are better than smaller), feature shape and dimension, all lead to lower precision of measurement.

Recent International Round Robin exercises [186] including several major European organisations have gone some way toward normalising the procedures for the quantitative analysis of defect structures in ceramic materials, and the methodology developed in these exercises has been used in the present study.

3.5.5. Transmission Electron Microscopy (TEM)

Transmission electron microscopy (TEM) allows very detailed microstructural analysis of materials to be carried out. Magnifications ranging from 1000 to 450,00 are possible, with resolution to the Angstrom Unit level. Crystal structure determination along with qualitative and semi-qualitative analysis of areas as small as 30ηm in diameter are possible.

TEM operates in two modes, imaging mode and diffraction mode. In both modes the source of illumination in a TEM is an electron beam of at least 10keV, which is directed onto the specimen surface. As the electrons strike the specimen they undergo different interactions depending on the internal microstructure of the specimen. The electrons may simply pass through amorphous regions (be transmitted), or be diffracted by crystalline regions in the specimen. When using the microscope in the imaging mode the resultant transmitted or diffracted beam is then captured, to form an image on a fluorescent screen. The angle of the incoming beam is adjusted to select only one electron beam to form the image; a bright field image is formed if the directly transmitted beams are selected, and a dark field image if diffracted beams are selected. The contrast observed is a function of the diffraction patterns of the crystalline regions in the specimen. These electron images can be used to distinguish between amorphous and crystalline regions.

3.6. Investigation of the Monolithic Ceramics' Properties

3.6.1. Hardness Tests

The Vickers hardness (HV) test is one of the most common techniques used for measuring hardness in ceramics. Figure 3.13 illustrates the shape of the Vickers indenter and resulting impression [187]. This technique is extremely economical and simple. The greatest advantage of the technique is that only a small amount of specimen is required; typically some 100 indentations can be made on a single surface of edge dimension 10mm. It does have its limitations however. Results from a Hardness Round-Robin test in ceramic materials [188] indicate that errors (as high as 15%) and biases lead to high levels of uncertainty, which increase with increasing hardness level.

The many factors that may influence the quality of microindentation tests (these also apply to bulk hardness tests) are outlined in Table 3.5 [187].

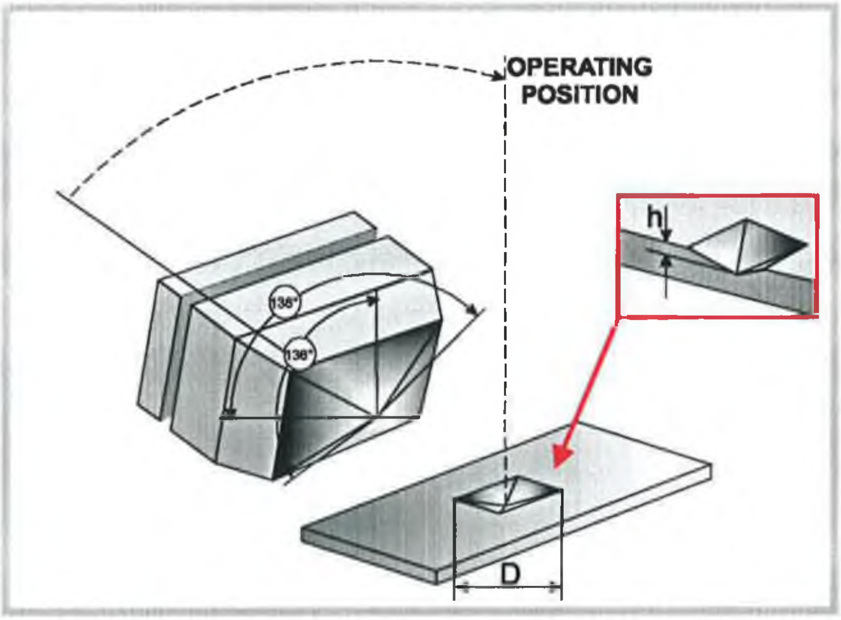

Figure 3.13 Schematic diagram of the shape of the Vickers indenter and impression [187].

Instrument factors	Measurement factors	Material factors
Accuracy of applied load	Calibration of the measurement system	Heterogeneity in composition or microstructure
Inertia effects, speed of loading	Resolving power of the objective	Crystallographic texture
Angle of indentation	Magnification	Quality of the specimen preparation
Lateral movement of the indenter or specimen	Operator bias in sizing	Low reflectivity or transparency
Indentation time	Inadequate image quality	
Indenter shape deviations	Nonuniform illumination	
Damage to the indenter		
Insufficient spacing between indents or from edges		

Table 3.5 Factors affecting precision and bias in microindentation hardness testing [187].

The following guidelines have been suggested for optimum measurements [187][188].

- The indenter should be examined periodically for correct geometry and surface damage.
- The indenter should be properly aligned ($\pm 1^{\circ}$) to the stage plate.
- The specimen surface should be perpendicular to the indenter.
- The indentation must be larger than the microstructural features.
- An adequate number of indentations should be used (5-10).
- Badly damaged indentation must be ignored. Spacing of indents is important as indenting produces plastic deformation and a strain around the indent. If the spacing is too small then the new indent will be affected. ASTM recommends spacing of 2.5 times the Vickers diagonal length.
- Specimen preparation is important. A clean, flat, mirror surface is essential. For low loads ASTM recommends a sample thickness of 2.5 times the Vickers diagonal length.
- Hardness can vary with indentation load, at low loads. Loads >9.8N(1kg) are suggested.

Samples within each series were chosen based on their densities ensuring that the influence of porosity on hardness is minimised, so that the effect of composition and residual α-Si_3N_4 could be observed. To correlate residual porosity with hardness and to determine the quantitative nature of porosity dependence on hardness, samples with the composition 3.2CaZ with a range of densities were selected.

The samples (approximately 10mm × 5mm × 5mm) were mounted in epoxy resin and polished to mirror finish with 1μm diamond paste. The polished samples were subjected to Vickers diamond pyramidal indentation under a load of 5kg, for 10 seconds. Care was taken to make indentations only on those areas which had no visible pores, as it was essential to minimise the influence of porosity on the hardness behaviour. The guidelines for obtaining optimum values (outlined earlier) were closely adhered to. The indented samples were then examined by optical microscopy with magnification of 200× (in reflected polarised light) and the dimensions of the indent measured to the highest accuracy possible. Vickers Hardness (HV5) was calculated using the standard equation,

$$HV = \frac{1.8544F}{d^2} \qquad \mathbf{3.12}$$

where,

F = the indentation load (grams-force)

d = the average indentation diagonal (μm)

Resulting hardness values are expressed in kgf/mm^2 rather than the equivalent gf/μm^2. 5-10 indentations were made for each specimen and the error of measurement was estimated in terms of standard deviation from the mean.

3.6.2. Fracture Toughness

For the evaluation of fracture toughness, the critical stress intensity factor, K_{Ic}, of a material, can be determined by measuring the size of cracks formed around the indent during Vickers hardness indentation [189] [190]. A schematic diagram of the twp type of crack geometries, Palmqvist and median cracks, that form around Vickers indentations is illustrated in Figure 3.14. Often termed Indentation Fracture this method is widely used as it is very quick and cost-effective, requires a small volume of material and can be carried out in tandem with Vickers indentation tests. The guidelines for optimum Vickers hardness results (as outlined earlier) also apply to K_{Ic} measurements. In addition, it was essential that the crack length be measured immediately after indentation, as postindentation crack growth is reported to occur in ceramics with glassy grain boundary phases [191].

The difficulties with this technique include (i) the accuracy to which the crack lengths can measured, (ii) the expressions given in literature assume that the crack formed is one of the two ideal fracture model type cracks, and (iii) the wide range of expressions reported in literature and (iv) and the inconsistency between reported indentation fracture toughness values and fracture toughness values measured by the conventional single edge notched beam (SENB) test. The reader is refereed to the many review papers that exist which assess the Vickers indentation fracture toughness test and the many indentation toughness equations [192][193][194].

Indentation fracture measurements were conducted on each of the samples subjected to Vickers hardness tests, Section 3.6.1. Equations were selected from literature and are outlined in the Results and Discussion, Section 4.6.1.

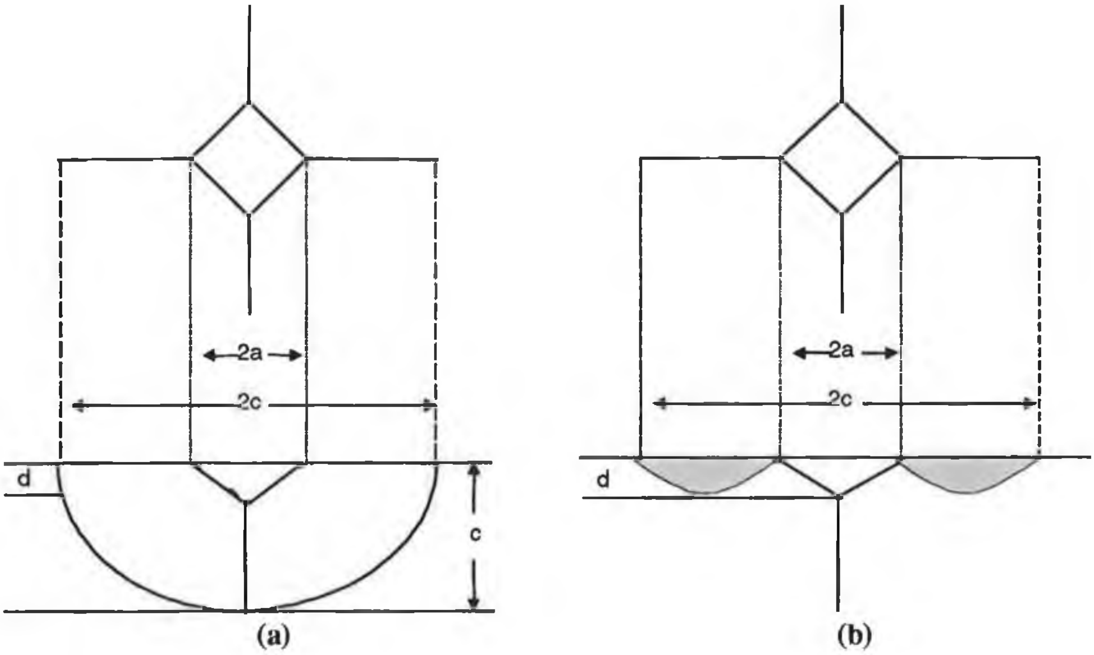

Figure 3.14 Comparison of (a) median cracks and (b) Palmqvist cracks around a Vickers indentation.

3.6.3. Oxidation Behaviour

A series of oxidation experiments were carried out on monolithic samples with the composition 3.2CaZ (Si_3N_4 + 3.4wt%Y_2O_3 + 3.4wt%Al_2O_3 + 3.2wt%$CaZrO_3$) sintered at 1600°C. Although no Zr-O-N type phases were detected in this particular material as was outlined in Section 2.5.1.3, even trace amounts of such phases in Si_3N_4 ceramics result in catastrophic degradation of the materials oxidation resistance, which, of course, would lessen its suitability as a matrix phase for the fabrication of a Si_3N_4/C composite in the present study.

3.6.3.1. *Sample Preparation*

The sintered samples were cut into test samples of dimension 5mm × 5mm × 4mm, (suitable for the thermobalance). The cut surfaces were polished with a range of diamond pastes to 0.1μm, subsequently ultrasonically cleaned in ethanol and finally dried in an oven at 100°C to a constant weight, ±10μg.

3.6.3.2. *Long Term Oxidation Tests*

The samples were subjected to long term oxidation tests (100 hours) at each 100°C interval within the temperature range $600^{\circ}C \leq T \leq 1000^{\circ}C$, over which (range) Zr-O-N phases are reported to cause catastrophic oxidation. Sample weights before and after long term tests were weighed to ±10μg.

3.6.3.3. *Thermogravimetric Analysis and Short Term Oxidation Tests*

Oxidation tests were carried out in a Cahn TG171 automatic recording thermobalance, Figure 3.15. The samples were placed in a high purity alumina crucible, which was suspended in the furnace from a sapphire fibre support attached to the balance. The furnace was then raised, sealed and the sample exposed to dry air (<5ppm H_2O) flowing at 55ml/min.

The onset of oxidation was determined by thermogravimetric analysis carried out by heating the samples at a heating rate of 2°C/min to 1500°C, with a 2 hour hold time at temperature. Following the results of the thermogravimetric analysis, an initial investigation into the oxidation kinetics of the material was carried out by a series of short term tests (20 hours) at 1200°C, 1300°C and 1400°C. A slow heating rate was set to 250°C and then increased to 40°C/min up to the hold temperature. After the isothermal holds, the furnace was cooled slowly at a slow rate set so that the natural cooling curve of the thermobalance was followed.

Weight measurements recorded on the thermobalance in the present study, have an accuracy of ±1μg, in a 1g change every 30 seconds. To ensure reproducibility, duplicate runs were carried out at each oxidation temperature and the initial and final weights of the samples were measured on a separate balance to check the calibration of the thermobalance. Also the weight data recorded for each run were corrected for any effects of heating and Pt evaporation by subtracting the data recorded for a blank run with a "dummy" alumina specimen.

Figure 3.15 Cahn TG171 automatic recording thermobalance.

3.7. Investigation of Composite Properties

3.7.1. 3-point Bend Tests

Composite samples of both matrix phase compositions (1AlN and 3.2CaZ) gas-pressure sintered at 1600°C and hot-pressed at 1600°C and 1700°C were tested in 3-point bending. The composite samples were cut with a diamond saw to dimensions of 45mm × 4mm × 3mm. 6 to 7 bars of each material were tested. The experiment set up is illustrated in Figure 3.16. A silicon carbide jig was used with an outer span dimension (l) of 30mm and inner span (l_i) of 10mm. The samples were loaded in a direction parallel to the fibre direction. The failure stress, σ_f, was calculated according to

$$\sigma_f = \frac{3F(l-l_i)}{2bh^2} \qquad \textbf{3.13}$$

where F is the peak force at fracture (N), b is the test piece width (mm) and h is the test piece height (mm).

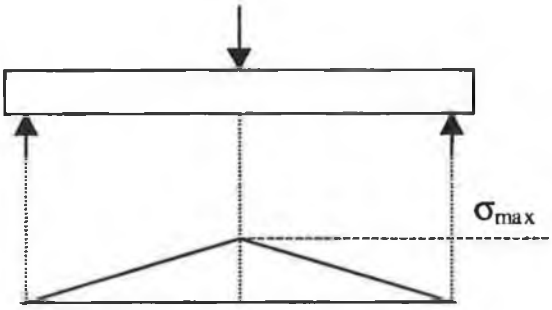

Figure 3.16 3-point bend test set up.

4. RESULTS AND DISCUSSION

4.1. System Selection

As outlined in Section 3.1, Tables 3.1 and 3.2, the ceramic compositions studied comprise of two types of materials based on sintering additives, and a reference material. For clarity the chemical compositions are listed again in Tables 4.1- 4.3. The chemical compositions are expressed here in both mol% and wt%, in the remainder of the text they are expressed only in wt%.

Sample Label	Si_3N_4	Y_2O_3	Al_2O_3	AlN
0AlN				
wt%	88.5	5	6.5	-
mol%	88	3	9	-
1AlN				
wt%	88.5	5	5.5	1
mol%	84	3	7	4
2AlN				
wt%	88.5	5	4.5	2
mol%	84	3	6	7
3AlN				
wt%	88.5	5	3.5	3
mol%	83	3	4.5	9.5
4AlN				
wt%	88.5	5	2.5	4
mol%	81	3	3	13

Table 4.1 Compositions of ceramic samples in the $Si_3N_4 + Y_2O_3 + Al_2O_3 + AlN$ series investigated.

Composition Label	Si_3N_4	Y_2O_3	Al_2O_3	CaO	ZrO_2
3.2CaZ					
wt%	90	3.4	3.4	1	2.2
mol%	88	2	5	2.5	2.5
4.8CaZ					
wt%	90	2.6	2.6	1.5	3.3
mol%	88	1.5	3.5	3.5	3.5
6.4CaZ					
wt%	90	1.8	1.8	2	4.4
mol%	88	1	2	4.5	4.5

Table 4.2 Compositions of the ceramic samples in Si_3N_4 + Y_2O_3 + Al_2O_3 + $CaZrO_3$ system investigated.

Composition Label	Si_3N_4	Y_2O_3	Al_2O_3
REF			
wt%	90	6.9	3.1
mol%	91	4	4

Table 4.3 Chemical composition of the reference ceramic samples investigated.

4.2. Powder Dispersion Analysis

4.2.1. Dispersion Experiments

The methodology used for fabrication of green bodies in this study (Section 3.3) requires that the starting ceramic powders remain stable in aqueous suspension for up to 6 hours. Earlier studies [19] found that Si_3N_4, Y_2O_3, Al_2O_3 aqueous suspensions can be stabilised for up to 8 hours. Since AlN and $CaZrO_3$ powders will also be added to these powders in significant quantities, their stability in water was examined over a period of 10 - 24 hours, using a commercial ESA equipment (Matec^{TM}). As reviewed in Section 2.3.3 the measurement of Electronic Sonic Amplitude (ESA) can be used to evaluate the dispersion characteristics of powder particles in liquid suspension. When the ESA value of a dispersion is a high value (positive or negative), then the liquid suspension is most stable (the balance between attractive and repulsive charges of the double layer is optimum for stability). Change in this value towards zero indicates progressive loss of stability and an increase in tendency to agglomerate.

The analysis of an aqueous solution of regular AlN powder confirmed earlier reports that aluminium nitride is unstable in water [195] [196]. Results for a 2vol% AlN aqueous suspension are illustrated in Figure 4.1. The suspension remains at a negative ESA value (within a maximum range of values) that is, it retains stability, over a period of approximately 2.5 hours, after which its ESA values deviates quickly from its maximum value range and the suspension becomes unstable. Agglomeration of the suspension, along with an increase in temperature and evolution of ammonia was observed. Coinciding with the decrease in stability was a rise in pH of the dispersion (Figure 4.2), which can be explained by the hydrolysis of the AlN according to the following reactions [195]:

$$AlN + 2H_2O \rightarrow AlOOH_{(amorph)} + NH_3 \uparrow \tag{4.1}$$

$$NH_3 + H_2O \leftrightarrow NH_4^+ + OH^- \tag{4.2}$$

$$AlOOH + 2H_2O \rightarrow Al(OH)_{3(cryst)} + H_2O \tag{4.3}$$

This problem was overcome by using a coated, water-resistant AlN powder, denoted here as AlNWR (supplied by Advanced Refractory Technologies Incorporation). The individual AlN powder particles are coated with an organic compound, which increases the stability of the powder in water. The organic coating is hydrophobic so that for good dispersion in a water medium, a wetting agent is required. ESA results for a 2vol% AlNWR aqueous suspension (plus 1wt% wetting agent, Emphos CS-1361, Witco Chemical) are illustrated in Figure 4.1. The presence of a wetting agent is not expected to affect greatly the stability of the suspension and so should not invalidate the comparison between the stability of the two AlN powder suspensions. The suspension maintains its maximum ESA value range, and hence stability for up to 7 hours before slowly deviating away from its maximum. However, no coagulation was observed and no rise in pH, similar to that for the uncoated AlN powder, occurred (Figure 4.2).

Figure 4.3 illustrates the variation of ESA with time for a 2vol% $CaZrO_3$ aqueous suspension. The suspension is stable (remains within its maximum negative ESA value range) for up to 7 hours, after which time the ESA value was seen to move towards zero, but no agglomeration of the suspension was observed. The pH of the suspension remained constant.

For both the uncoated and coated AlN, and the $CaZrO_3$ suspensions the initial time delay observed in reaching their maximum stability (Figure 4.1, Figure 4.3) is simply the time required for the powders to become well dispersed in the aqueous media. The coated AlN powder requires a slightly longer time than the uncoated powder to become well dispersed due to its poorer wettability (even with the use of a wetting agent). The relatively long time taken for both powders to achieve stable dispersions may be due to the fact that the suspensions were ultrasonically dispersed and mixed on magnetic stirrer while the ESA measurements were taken. Dispersion of individual particles requires breaking up the original agglomerates. This requires massive input of energy and while these dispersion techniques result in well dispersed suspensions, they are slow. The observed time delay is expected to be greatly reduced in the green body formation process used in preparing the samples, as the ceramic dispersions are mixed using a highly effective mixing and milling process for up to 1.5 hours, as outlined in Section 3.3.1.

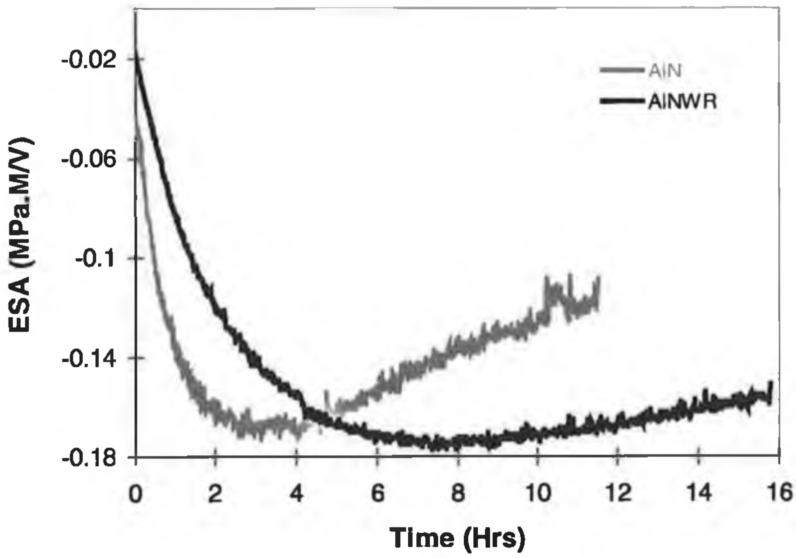

Figure 4.1 Variation of ESA with time for AlN and coated AlN, AlNWR.

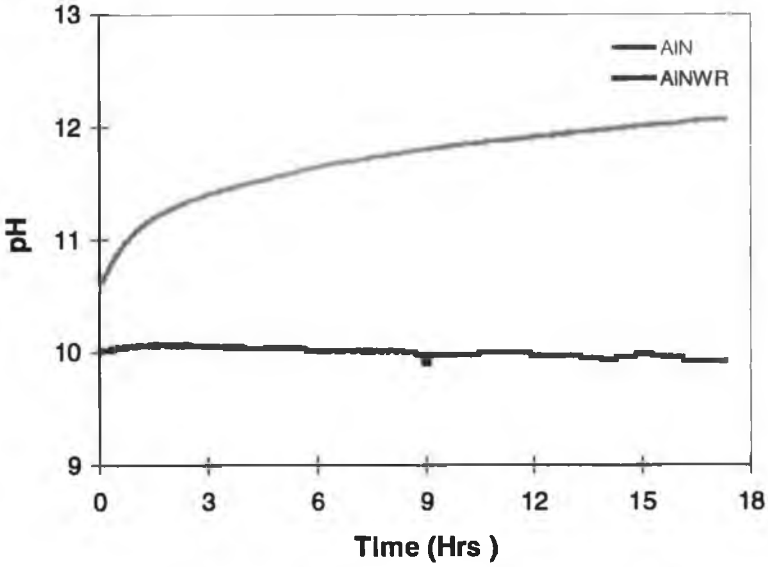

Figure 4.2 Variation of pH with time for AlN and coated AlN, AlNWR.

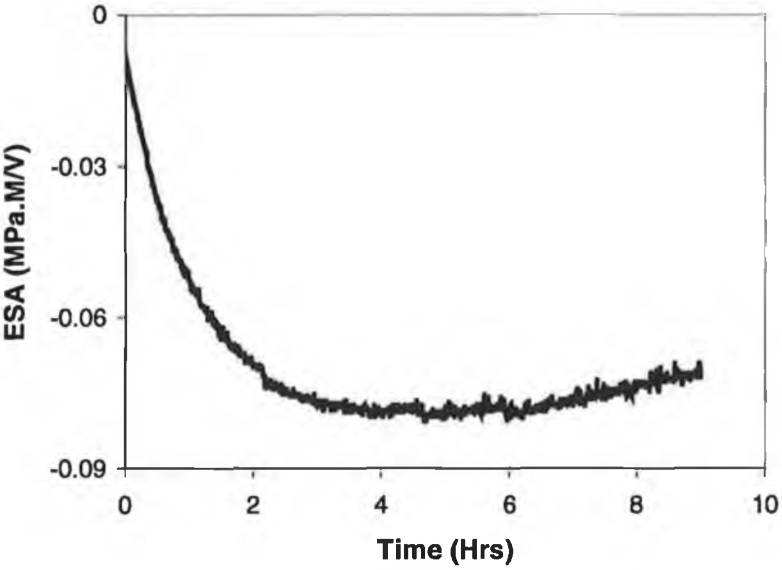

Figure 4.3 Variation of ESA with time for $CaZrO_3$.

Having established chemical stability for the reactant species, the next step was to optimise the suspension conditions, in order to guarantee a stable, uniform distribution of single particles of maximum concentration in the suspension. A better understanding of powder particle stability in suspension is obtained by establishing the zeta potential across a range of pH values. ESA provides a measure of the particle mobility in the suspension, which is related to zeta potential and so provides an equivalent guide to particle stability.

Dispersions containing coated AlN (AlNWR) and $CaZrO_3$ were prepared as explained in Section 3.2.1 and were titrated with 0.1M HNO_3, while measuring ESA. Figure 4.4 (a) and (b) show that the isoelectronic points of AlN and $CaZrO_3$ in water are equal to 5 and 5.5 respectively. Previous studies [197] found the IEPs of Si_3N_4, Y_2O_3, and Al_2O_3 in water to be 6.2, 8.7 and 8.2 respectively and a stable dispersion of a mixture of these powders has been achieved once the pH of the dispersion is maintained above 10. These results suggest that the AlN or $CaZrO_3$ powders, reach a maximum ESA value at pH 10, beyond which stability is not improved, and thus they will be stable under the same conditions as the Si_3N_4, Y_2O_3, and Al_2O_3 powders.

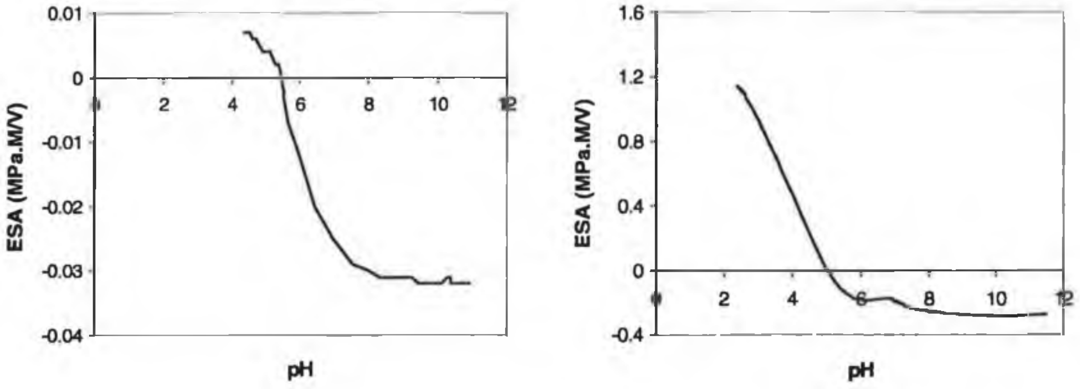

(a) **(b)**

Figure 4.4 Titration of 1M HNO_3 in 2vol% suspensions of (a) AlNWR and (b) $CaZrO_3$.

4.2.2. Suspension Rheology

Green form morphology is a decisive factor in determining the structural quality of the final sintered ceramic – flaws in the green body are inevitably retained in the microstructure of the sintered form. The quality of both monolithic and composite green form morphology depends crucially upon the rheology of the ceramic slurry (powder dispersion). An earlier in-depth study by Plunkett et al. [198] determined the conditions for optimum dispersion for the fabrication of green bodies of a carbon fibre reinforced Si_3N_4 composite containing a sinter additive mixture of 5wt% each of Al_2O_3 and Y_2O_3 (this was used as the reference composition in this study), by attrition milling an aqueous suspension containing:

- 65wt% powder content
- 0.1wt% dispersant (Darvan C)
- 0.1wt% wetting agent (Aerosol OT) for composite fabrication
- at a pH 10.4
- The resultant viscosity of the slurry should lie within 12- 20 cps.

Aqueous slurries of the compositions outlined in Tables 4.1-4.3, were prepared according to these parameters and their resultant rheological behaviour and viscosity measured to confirm their suitability for use in the filtration and infiltration processes for each series.

Shear stress versus shear rate plots of selected slurries from each composition series show near Newtonian behaviour, Figure 4.5,. When the shear stress was converted to differential viscosity (using the average shear rate method) and plotted against shear rate, near Newtonian behaviour was seen down to a shear rate of approximately $20s^{-1}$ (Figure 4.6). The observation of an initial high viscosity/high shear rate, was also observed by Plunkett et al. [198], and was attributed to the formation of networks between polar water molecules and amino groups of the dispersant. The viscosity of each slurry composition was seen to lie well within the range of 12-20cps outlined above, ensuring that these compositions are suitable for fabrication of monolithic and composite green forms by the filtration and infiltration methods respectively.

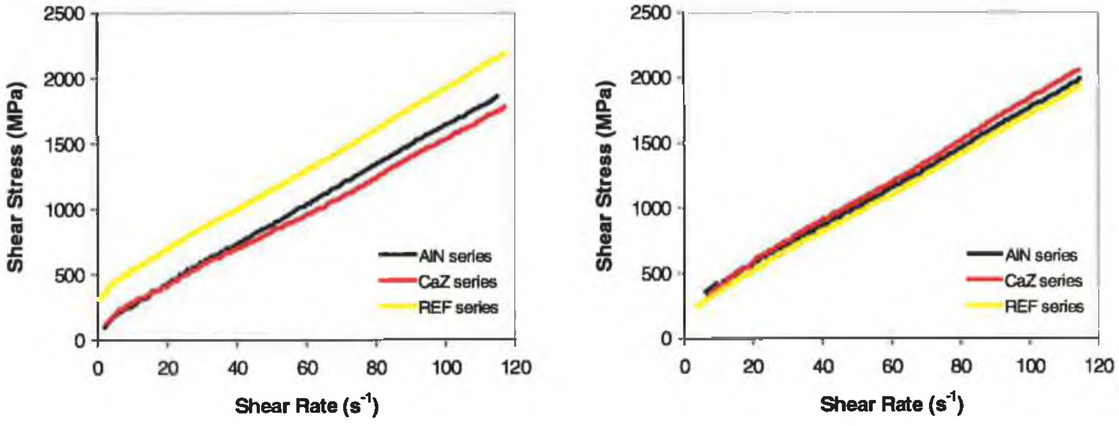

(a) **(b)**

Figure 4.5 Shear stress plotted against shear rate for slurries used for (a) monolithic fabrication and (b) composite fabrication.

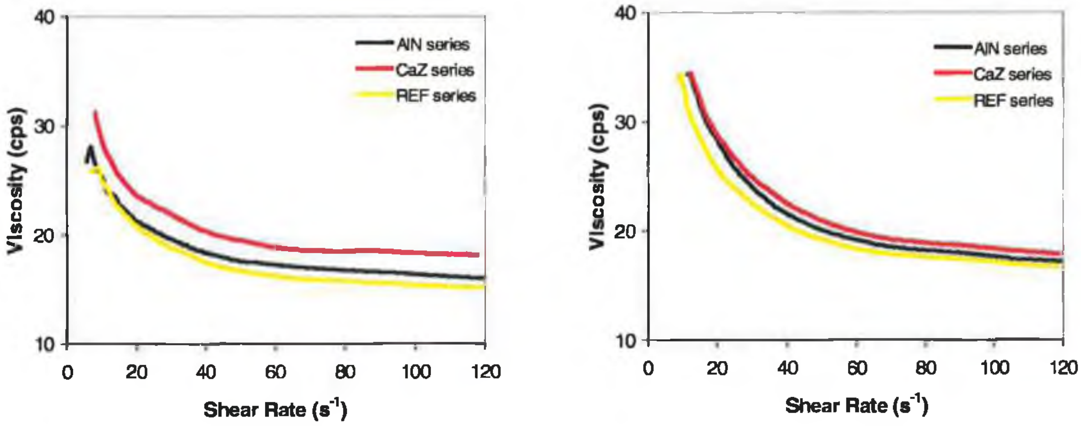

(a) (b)

Figure 4.6 Viscosity profiles of slurries used for (a) monolithic fabrication and (b) composite fabrication.

4.3. Green Body Formation

Monolithic and composite green bodies were cast using pressure filtration and pressure infiltration respectively. A slurry charge, introduced into the mould (Figure 3.8) was filtered under 20 bar gas pressure. Initial casting experiments established that the time required to express the water from the sediment mat, varied between 12 and 15 minutes. A shock of sudden gas pressure change can result in the development of dry channels and cracking of the ceramic cake. Also the green forms were difficult to remove from the mould. These problems were overcome by controlling gas pressures, limiting time at maximum pressure to 10 minutes followed by very slow pressure release, and the application of a mould release agent. Finally a casting time of 10 minutes and pressure of 7 bar were used as optimum parameters for fabrication of the green bodies. For some samples it was necessary to apply a vacuum for 10-15 minute to completely dry the surface before removing the sample from the casting mould. After drying in the controlled humidity box, and organic burnout of the samples, green densities of up to 60%TD were achieved.

4.4. Sintering Studies and Sample Analysis

4.4.1. Introduction

The conditions under which the monolithic silicon nitride based samples were sintered are outlined in Section 3.4.1. Initial sintering experiments were carried out with a 2 and 4 hour hold time at the sintering temperature. However, the longer hold time resulted only in very minor increases in final density (~ 0.5%). A shorter production time is more cost-effective and possible fibre/matrix reactions in the final composite should be minimised by shorter holding times, as explained in 2.4.1. A two hour hold time at sintering temperature was then selected for the main study. The different compositions were sintered over a range of temperatures between 1400°C and 1750°C. The general reproducibility of sintering for each series was evaluated by the inclusion of a number of replicates for a particular composition/temperature. The results were found to be very consistent, with an average standard deviation range of 0.08 – 0.2, calculated for the density values calculated at each sintering temperature.

To gain a greater understanding of the sintering mechanisms and the potential of the ceramics in the present study; the $Si_3N_4 + Y_2O_3 + Al_2O_3 + AlN$ series and the $Si_3N_4 + Y_2O_3 + Al_2O_3 + CaZrO_3$ series, a comprehensive study was made of both the microstructure and chemical composition after sintering at selected temperatures. The microstructure of dense Si_3N_4-based ceramics materials can consist mainly of the two Si_3N_4 phases α and β, and intergranular phases of varying composition (see details in Section 2.3.6). The quantitative determination of the α and β content in the selected samples was made using X-ray diffraction (XRD). The interpretation of the XRD data was made with care, taking into account the limitations of the technique:

- Poor crystallinity of the intergranular phase
- Distortion of peaks due to solid-solution or impurities means that the data is, at best semi-quantitative
- Grain orientation effects are not considered

- Minimum detectable phase concentration is roughly 5%, so that many crystalline grain boundary phases may not be detected

Figure 4.7 shows three typical X-ray diffraction patterns corresponding to the green body material, a partially transformed material and a fully transformed sintered body. The figure shows the peaks selected for *semi*-quantitative determination of the α/β content in each sample. The presence of a crystalline intergranular phase can be seen in Figure 4.7 (b). The semi-quantitative analysis of the data was carried out by normalising the intensity of the phase detected (I) to the intensity of the pure standard (I_0).

The degree of transformation from the α- to the β-Si_3N_4 structure in the materials is discussed in terms of the amount of β estimated, which is expressed as a percentage of the total amount of Si_3N_4 detected:

$$Degree\,of\,Transformation = \%\beta = \frac{\beta}{(\alpha+\beta)} \qquad \textbf{4.4}$$

The results and discussion of the sintering behaviour and analysis of the Si_3N_4 + Y_2O_3 + Al_2O_3 + AlN series and the Si_3N_4 + Y_2O_3 + Al_2O_3 + $CaZrO_3$ series are presented separately. They were investigated not to compare directly with each other, but as individual novel Si_3N_4-based materials. A range of sintering additive compositions within each individual series was studied. Some comparisons are made with the reference material.

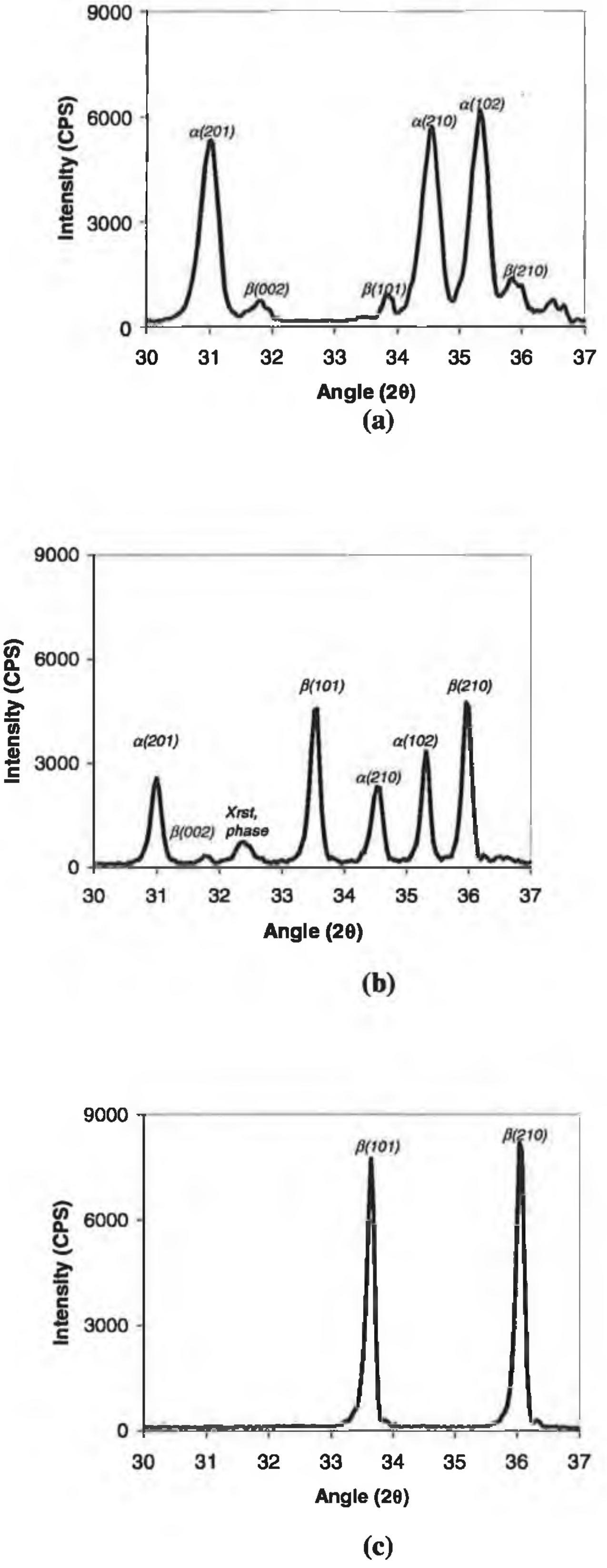

Figure 4.7 X-ray patterns corresponding to (a) green body material, (b) partially transformed material and (c) fully transformed material.

4.4.2. $Si_3N_4 + Y_2O_3 + Al_2O_3 + AlN$ Series

4.4.2.1. Densification Results

Figure 4.8 illustrates the variation of percent theoretical density (%TD) of the sintered samples with increasing sintering temperature. As would be expected for these systems, samples with constant grain boundary chemistry, that is a constant AlN and Al_2O_3 content, increased in density with increased sintering temperature. Thus the density of sample 4AlN (4wt% AlN, 2.5wt% Al_2O_3) increases from 69.3%TD after sintering at 1400°C to 98.5%TD at 1650°C, and similarly the density of 2 AlN (2wt% AlN, 4.5wt% Al_2O_3) increases from 86.35%TD at 1400°C to 98.4%TD at 1650°C. The results show that the addition of AlN lowers the temperature required for sintering to closed porosity (approximately 94- 95%TD). This temperature is reduced by at least 150°C for all AlN concentrations, 1- 4AlN as compared to the reference material and by 200°C for 1wt% AlN addition, from 1650°C.

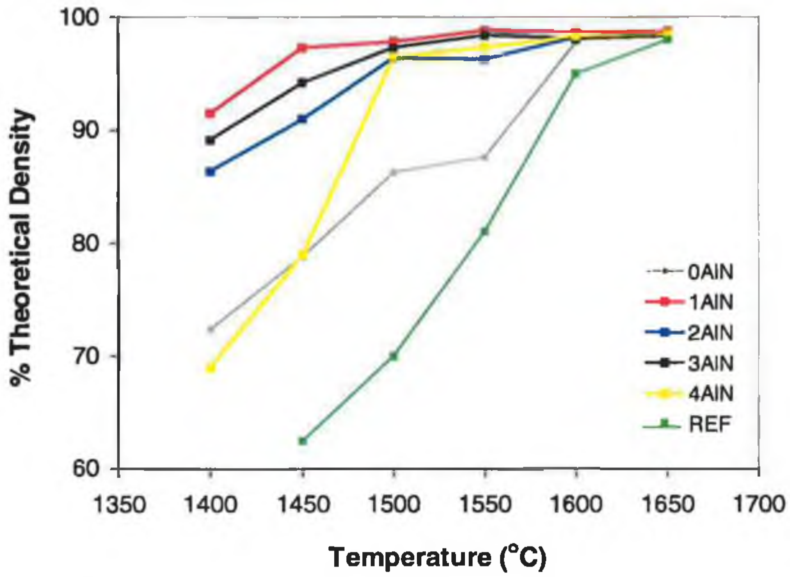

Figure 4.8 Variation of %TD with temperature for each composition in the AlN series and the reference material.

The densification results of the 1-4AlN compositions between 1500°C and 1650°C are shown in more detail in Figure 4.9. The 1AlN composition performs best, producing a >98%TD at all temperatures above 1500°C, as does the 3AlN sample above 1550°C.

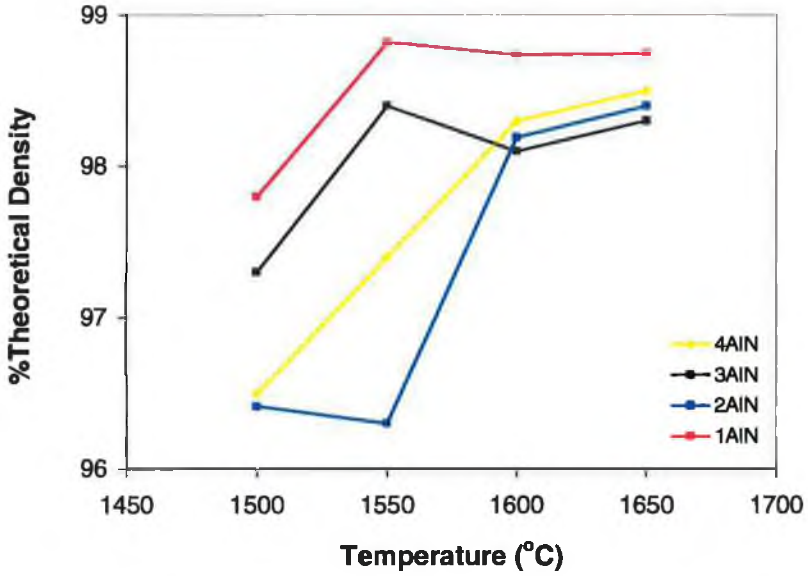

Figure 4.9 Variation of %TD with temperature (>1500°C) for selected compositions.

Densification of Si_3N_4 ceramics by liquid-phase sintering, as discussed in Section 2.3, involves three mechanisms or stages; rearrangement, solution-diffusion-reprecipitation and coalescence [48]. The contributions of the different stages to densification are dependent on the type of sintering additive used. Since the amount of yttrium added was kept constant in the series studied here, the differences in sintering mechanisms and the resultant percent TD at each temperature is considered to be dependent on the AlN and Al_2O_3 content in the different compositions. Figure 4.10 illustrates the variation of sintered TD with AlN and Al_2O_3 content over the range of sintering temperatures studied. In this representation of the densification results, the significant effect of the addition of AlN on the sintering behaviour within the Y-Si-Al-O-N system can easily be seen. However, explanation of the results of varying the AlN and Al_2O_3 content over a range of values on the sinterability of these Si_3N_4 based ceramics is certainly not simple. As seen previously in Figure 4.8, and more clearly in Figure 4.10, the addition of 1wt%AlN improves the ceramic density at lower sintering temperatures. For example, the density obtained at 1400°C for 0AlN (0wt% AlN and 6.5wt% Al_2O_3) was 72.34%TD, whereas sample 1AlN with 1wt% AlN and 5.5wt% Al_2O_3, reached 91.48%TD. The final density of the sintered samples does not however, increase further with increasing amounts of AlN (decreasing amount of Al_2O_3). Sample 2AlN (2wt% AlN, 4.5wt% Al_2O_3) exhibits poorer sinterability than 1AlN at each temperature up to 1600°C, reaching 90.94%TD at 1450°C compared to 97.31%TD reached by 1AlN. Increasing the AlN content to 3wt% in sample 3AlN resulted in improved sinterability from the 2AlN composition but yet is not as good as 1AlN. A further increase in AlN content to 4wt% resulted in a ceramic with significantly poorer sinterability, reaching just 79%TD after sintering at 1450°C, showing similar %TD values to the sample with no AlN.

The observed variation in sintering behaviour with AlN and Al_2O_3 content was not observed when the samples are sintered at temperatures 1600°C and 1650°C.

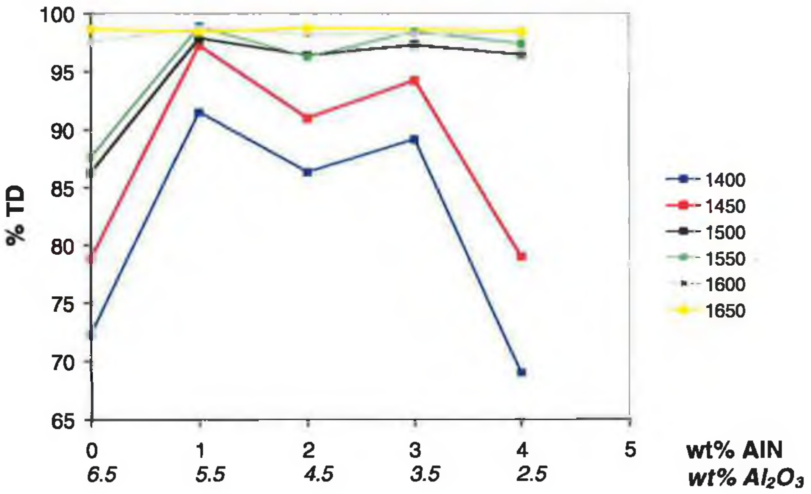

Figure 4.10 Influence of AlN and Al_2O_3 content on the final density after sintering for 2hrs at the given temperatures.

4.4.2.2. Mass Loss Measurements

Very low mass losses (from 0.1% to 0.86%, with a standard deviation ±0.03) were observed in the present work for all compositions at all temperatures (Table 4.4) compared to those observed by Itturiza et al [199] (typically 3-6%) and in other comparable compositions [200][201]. This is most probably due to the use of lower temperatures, the application of a low over-pressure (10 bar N_2), and the use of graphite pieces to compact the sinter powder bed around the sample, which, in combination, prevent decomposition of Si_3N_4 and inhibit volatilisation of gaseous products from the sample surface [180] [202]. Moreover, Lange et al [203] have reported that mass losses are minimised when the densification kinetics are rapid, which has been taken into account in selecting the sintering condition for the present study.

Sample Composition Label	**% Mass Loss**					
Sintering Temperature (°C)	**1400**	**1450**	**1500**	**1550**	**1600**	**1650**
0AlN	0.61	0.62	0.71	0.1	0.45	0.4
1AlN	0.56	0.51	0.44	0.66	0.4	0.5
2AlN	0.51	0.49	0.46	0.4	0.6	0.6
3AlN	0.56	0.49	0.4	0.5	0.4	0.5
4AlN	0.5	0.86	0.78	0.5	0.1	0.3
REF	0.4	0.32	0.43	0.5	0.55	0.5

Table 4.4 Measured % mass losses for compositions sintered at the given temperatures.

4.4.2.3. Shrinkage Results

It is clear at this stage that the sintering mechanisms occurring especially at lower temperatures are strongly dependent on the AlN/Al_2O_3 content ratio. To further analyse and help understand the effect of varying the AlN and Al_2O_3 content, a set of dilatometry experiments was carried out on compositions 1-3AlN. Rectangular green bars of samples of the compositions were heated to 1600°C at a rate of 5°C/min and held at temperature for up to 8 hours (See Section 3.4.3 for details). The resultant dilation curves are illustrated in Figure 4.11. As expected from the sintering results, sample 1AlN reached the highest shrinkage of 15.75% and again 2AlN has the minimum shrinkage of 14.36%. The shrinkage of all compositions is seen to start at around 1350°C, and increases with increasing temperature. The influence of hold time at temperature on resultant shrinkage values is outlined in Table 4.5. As can be seen, for each composition, the greatest increase in shrinkage (approximately 2%) occurs during the first 2 hours at constant temperature. Holding the samples for a longer time at temperature proved only slightly beneficial to shrinkage. After 8 hours, shrinkage of sample 1 and 2 AlN increased by approximately 0.2% and sample 3AlN by 0.5%. These results confirm densification results in preliminary experiments, outlined earlier, that a hold time of 2 hours is sufficient for good densification.

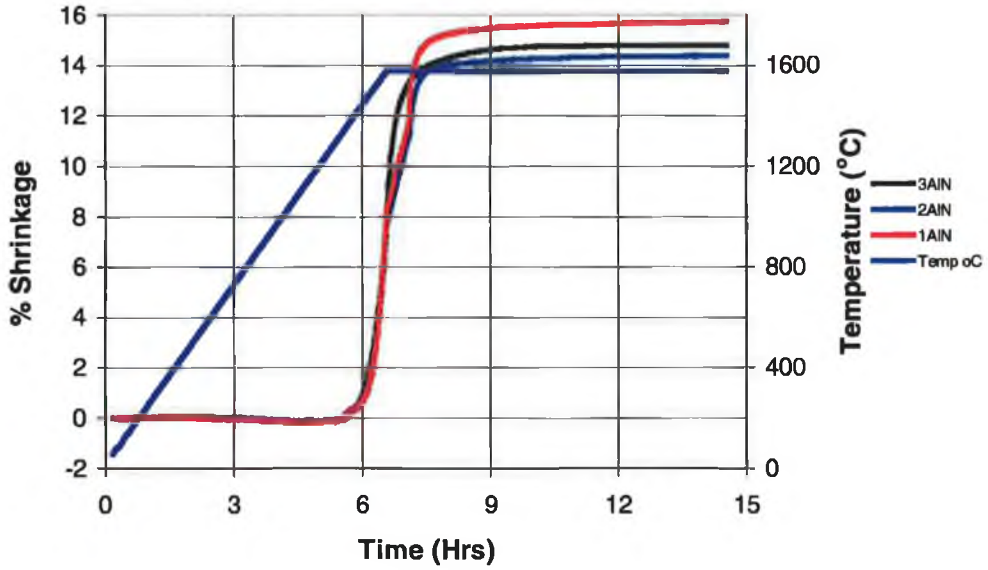

Figure 4.11 Dependence of dynamic shrinkage on temperature and time for compositions 1-3AlN.

Sample Composition Label	% Shrinkage				
Hold Time at Temperature (hrs)	**0**	**2**	**4**	**6**	**8**
1AlN	13.6	15.5	15.62	15.71	15.75
2AlN	11.9	14.18	14.32	14.36	14.36
3AlN	11.86	14.08	14.70	14.78	14.78

Table 4.5 Shrinkage values after holding at temperature.

4.4.2.4. α- to β-Si_3N_4 Transformation

Table 4.6 outlines the %β-Si_3N_4 content detected in each composition within the Si_3N_4 + Y_2O_3 + Al_2O_3 + AlN series after sintering at the given temperature. As expected the degree of transformation increases as the sintering temperature increases, for example, the sample with composition 0AlN consists of 46.57% β-Si_3N_4 after sintering at 1400°C and is completely transformed to β-Si_3N_4 after sintering at 1600°C, similarly in the sample with composition 2AlN, 21.74%β-Si_3N_4 was detected in the sample sintered at 1400°C and complete transformation was observed in the sample sintered in 1600°C. This behaviour is as expected, since the α-phase is thermodynamically unstable at temperatures ≥1400°C and transforms to the more stable β-phase [106].

The influence of the sintering additive composition, that is the AlN/Al_2O_3 ratio, on the transformation behaviour is illustrated in Figure 4.12. The addition of AlN to the Y-Si-Al-O-N system is seen to have a significant effect on the α to β phase transformation. The addition of 1wt% AlN favours the transformation at lower temperatures, for example the β-Si_3N_4 detected at 1400°C for 0AlN was 15%, whereas sample 1AlN had 21.74% β-Si_3N_4. The β-Si_3N_4 detected in the sintered samples does not however increase with further increasing amounts of the AlN/Al_2O_3 ratio, sample 2AlN (2wt% AlN, 4.5wt% Al_2O_3) has a lower % β-phase than 1AlN after sintering at each temperature from 1450°C to 1600°C, consisting of 68.3% β-Si_3N_4 at 1500°C compared to 96.15% β-Si_3N_4 detected in 1AlN. When the AlN content was increased to 3wt% in sample 3AlN the transformation from α to β-Si_3N_4 was improved slightly in the same temperature range but the degree of transformation is still less than sample 1AlN. Sample 4AlN (4wt% AlN, 2.5wt% Al_2O_3) exhibits much poorer transformation behaviour, with just 5% β-Si_3N_4 after sintered at 1400°C, showing a lower degree of transformation at all temperatures to the sample with no AlN.

Comparing Figure 4.10 and Figure 4.12, the α to β phase transformation seems to be concurrent with densification.

Sample Composition Label	**Temperature (°C)**				
	1400	**1450**	**1500**	**1550**	**1600**
0AlN	15	35	62	75	94
1AlN	21.49	58.82	96.15	95.2	100
2AlN	21.74	43.75	68.3	77.8	100
3AlN	19.96	48.69	78	82.83	95.23
4AlN	5	16.67	50	68	83.5

Table 4.6 %β-Si_3N_4 detected using XRD in materials densified at the specified temperatures.

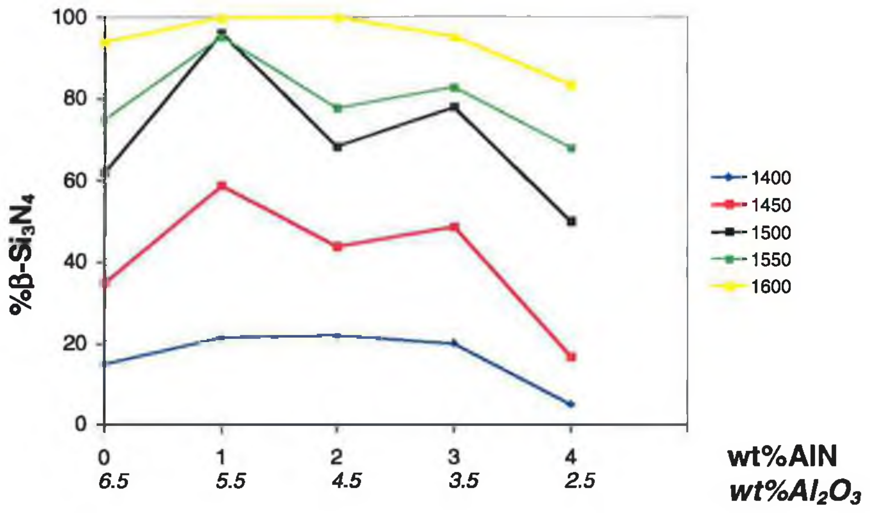

Figure 4.12 Influence of AlN and Al_2O_3 content on the %β-Si_3N_4 measured after sintering for 2hrs at the given temperatures.

4.4.2.5. Discussion on Reaction Sequences during Sintering

A closer picture of the influence of varying the AlN/Al_2O_3 ratio is seen from the differential shrinkage behaviour shown in Figure 4.13. Here the shrinkage values of Figure 4.11 have been differentiated with respect to time to show the shrinkage rate with increasing temperature. The start of measurable shrinkage occurs between 1150°C and 1200°C for each sample, and has been attributed to the formation of YAM ($Y_4Al_2O_9$) [204]. The total shrinkage at this temperature is very small and is most likely due to some degree of particle rearrangement. With increasing temperature the shrinkage rate shows two maxima. The first occurs at around 1335°C. It is most probable that this step also contributes little to overall shrinkage see Figure 4.11(b). The second maximum, occurs at around 1550°C for sample 1AlN and 2 AlN and 1575°C for 3AlN. Sample 3AlN exhibits a different behaviour at this step, in that it seems to require a higher temperature to reach its maximum shrinkage rate.

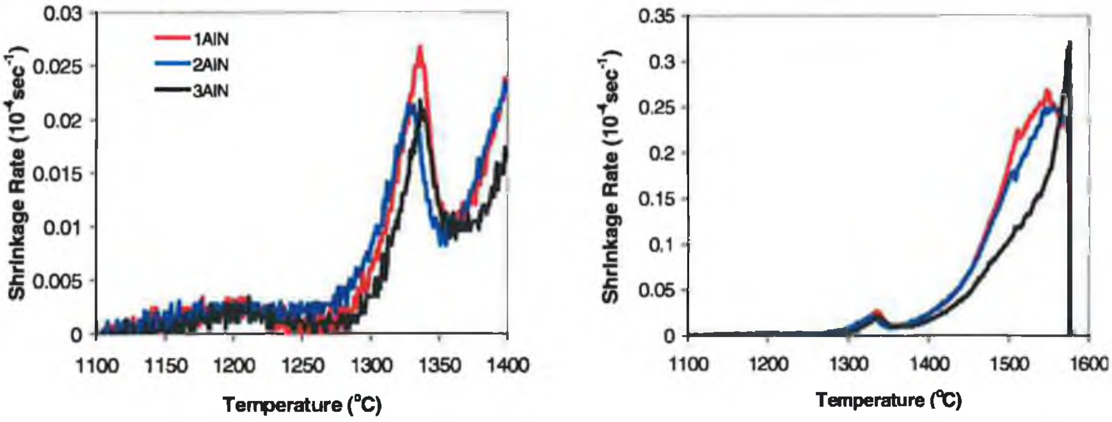

(a) (b)

Figure 4.13 Variation of shrinkage rate with temperature in the temperature range (a) 1100-1400°C, and (b) 1100-1600°C.

The first distinct shrinkage step at approximately 1335°C has been associated with the formation of the SiO_2-Y_2O_3-Al_2O_3 ternary oxide eutectic [205]. This step contributes very little to the overall shrinkage since the amount of SiO_2 in the starting compositions is very small (~1wt%) thus limiting the amount of eutectic melt formed and so is essentially independent of starting compositions (AlN/Al_2O_3 ratio).

At temperatures greater than approximately 1350°C, Y_2O_3 and Al_2O_3, crystallise out of solution as YAG ($Y_3Al_5O_{12}$), as detected by XRD in each composition after sintering at 1400°C and detailed in Table 4.7. The precipitation of YAG reduces the amount of liquid phase present, resulting in the retardation in shrinkage observed. Compared with Bandyopadhyay et al [204] who reported a total absence of shrinkage from 1400°C to 1500°C due to the YAG formation, the degree of retardation is small in the present case. This is considered a result of the small amounts of YAG formed in the grain boundary phases in the present case, compared to the bulk amounts formed in the α-SiAlON ceramics studied by reference [204], so that the effect is much less pronounced.

At higher temperatures, >1400°C, YAG redissolves into the liquid phase and the amount of liquid phase increases significantly. The amount of liquid phase formed during this step plays a major role in sample densification behaviour. XRD analysis of the sample with composition 1AlN showed that YAG is completely redissolved into solution at temperatures >1400°C while temperatures >1450°C are required for the redissolving of YAG in 2AlN and 3AlN (Table 4.7). An increased volume of liquid phase rich in Y, Al, and O is thus present in 1AlN at lower temperatures, contributing to the superior densification achieved by 1AlN (97%TD) after sintering at 1450°C.

Sample Composition Label	**Phases Detected (I/I_0)**				
Temperature	**1400**	**1450**	**1500**	**1550**	**1600**
1AlN	YAG(30)	-	-	-	-
2AlN	YAG(40)	YAG(40)	Y_2SiAlO_5N(15)	-	-
3AlN	YAG(40)	YAG(30)	Y_2SiAlO_5N(t)	-	-

Table 4.7 Crystalline phases detected in the selected materials after sintering at the given temperatures.

In addition, the amount of Al_2O_3 in the starting composition influences volume of liquid phase formed and thus densification [93][206]. In the present study density increased with increasing alumina content (with the exception of composition 2AlN) at all temperatures. After sintering at 1450°C composition 4AlN (2.5wt% Al_2O_3), 3AlN (3.5wt% Al_2O_3) and 1AlN (5.5wt% Al_2O_3) reached densities of 79%TD, 94%TD, 97%TD respectively. However, when the alumina content was once again increased in composition 0AlN (6.5wt% Al_2O_3) the densification achieved was just 79%TD (see Figure 4.8). Identical densification behaviour was observed by Bandyopadhyay et al. [204] who found that on moving the SiAlON compositions towards the Al_2O_3-rich side of the Si_3N_4-Y_2O_3.9AlN tie line, as the composition becomes richer in alumina, a larger volume of liquid phase is formed and better densification occurred and above a certain amount of Al_2O_3, the amount of liquid phase reduced, hence poorer densification occurred. Also the existence of an optimum Al_2O_3 concentration (approximately 6wt%) has been observed by Itturiza et al [199] in their study on the densification of sintered and HIP-sintered Si_3N_4 with Y_2O_3 and Al_2O_3 addition.

Bandyopadhyay et al [204] suggested this behaviour was due to formation of increased amounts of β-SiAlON acting as a 'sink' for aluminium and oxygen by changing either its level of substitution in Si_3N_4 or its volume fraction formed. Although no β-SiAlON was detected in the present samples at lower temperatures, this does not rule out the above explanation, since, as mentioned earlier, the amount of the grain boundary phases in these samples is very small and could not be detected by XRD.

The poorer sinterability at lower temperatures of composition 2AlN (2wt% AlN, 4.5wt% Al_2O_3) which is most likely a real effect, remains difficult to explain. As outlined in Table 4.7, the crystalline phase, Al-substituted N-α-wollastonite (Y_2SiAlO_5N) was detected in the 2AlN and 3AlN materials after sintering at 1500°C. Y_2SiAlO_5N forms by glass devitrification and is unstable at temperatures above 1100°C [207]. This suggests that it forms during cooling and thus does not affect the densification. However, it is reported that Y_2SiAlO_5N forms instead of YAG [208] when the Al content in the liquid phase sintering medium is reduced. This leads to the speculation that this specific composition encourages the removal of Al, and O, into the Si_3N_4 structure (forming a β-sialon) which then reduces the amount of liquid phase available for densification as outlined above.

The temperature at which maximum shrinkage rate occurs for each composition, corresponds to the highest dissolution rate of Si_3N_4 and AlN into the liquid phase. An extensive wetting study carried out by Hwang and Chen [172] revealed a significant difference between the physical and chemical affinity of AlN and Si_3N_4 to the oxide melt. AlN was found to exhibit faster reaction kinetics than Si_3N_4 at temperatures around 1420°C due a much lower contact angle with the oxide melt. Depending on the amount of liquid oxide phase and AlN present, liquid 'trapping' can occur in localised areas rich in AlN. Dissolution of Si_3N_4 and corresponding macroshrinkage is then delayed until the temperature is high enough to cause the redistribution of the liquid phase. This reasoning may be used to explain the slightly high secondary eutectic temperature of compositions 1AlN and 2AlN compared to that for the Si_3N_4-Al_2O_3-Y_2O_3 system [172] and the delay in macroshinkage of composition 3AlN, richer in AlN.

The liquid forming abilities and wetting behaviour of the nitrides (Si_3N_4 + AlN) in these samples will also influence the α- to β-Si_3N_4 phase transformation behaviour which occurs by solution/reprecipitation. The good liquid forming properties at temperatures >1400°C of the sample with composition 1AlN is reflected in the higher percent of β-Si_3N_4 detected. The lower degree of transformation exhibited by 2AlN supports the explanation given for its poorer densification behaviour, that is, this particular combination of sintering additives forms a low volume of liquid phase during sintering. The relatively high degree of transformation exhibited by 3AlN at lower temperatures corresponds to its liquid phase forming and densification behaviour. However, the %β-Si_3N_4 detected in samples sintered at temperatures ≥1500°C are slightly lower than expected from the densification results. Similar behaviour is seen for 4AlN, that is in relation to the other compositions, the degree of transformation at temperatures ≤1500°C is low, corresponding to the poorer liquid phase formation and densification (due to low Al_2O_3 content), but at higher temperatures the transformation is considerably lower although the density is relatively good. These observations correspond to the delay in macroshrinkage observed in 3AlN due to presence of increased amounts AlN in Y-Si-Al-O-N which leads to delayed dissolution of α-Si_3N_4 in the oxide liquid phase and thus precipitation of β-Si_3N_4 until a slightly higher temperature [172].

Figure 4.14(a)-(e) shows the densification and transformation after sintering at the given temperatures, suggesting that although transformation occurs concurrently with densification, they take place at different rates. That is, each sample composition within the Si_3N_4 + Y_2O_3 + Al_2O_3 + AlN series achieved maximum densification before the completion of the α to β transformation. This is attributed to the formation at temperatures ≥1500°C of a sufficient volume of liquid phase and transport of this liquid by viscous flow and/or diffusion into the pores leading to densification (corresponding to the maximum densification rates observed at approximately 1500°C for compositions 1-3AlN, see Figure 4.13). Since the transformation of α- to β-Si_3N_4 takes place via solution of α-Si_3N_4 and reprecipitation of β-Si_3N_4, this mechanism can continue after densification is achieved.

To summarise, the densification results of a range of compositions in the AlN series selected show a distinct improvement over the standard Si_3N_4 + YAG system. Within the AlN series, composition 1AlN (1wt%AlN, 5.5wt%Al_2O_3) shows superior sinterability at each temperature. The intergranular phase formed in this sample composition is most probably near to the Al_2O_3 rich side of the Si_3N_4-Y_2O_3.9AlN tie line as studied by Bandyopadhyay et al [204], and the addition of 5.5wt% Al_2O_3 being the optimum concentration for maximum densification. This composition thus appears to have the most potential as a matrix phase material for the pressureless sintering of a ceramic matrix composite.

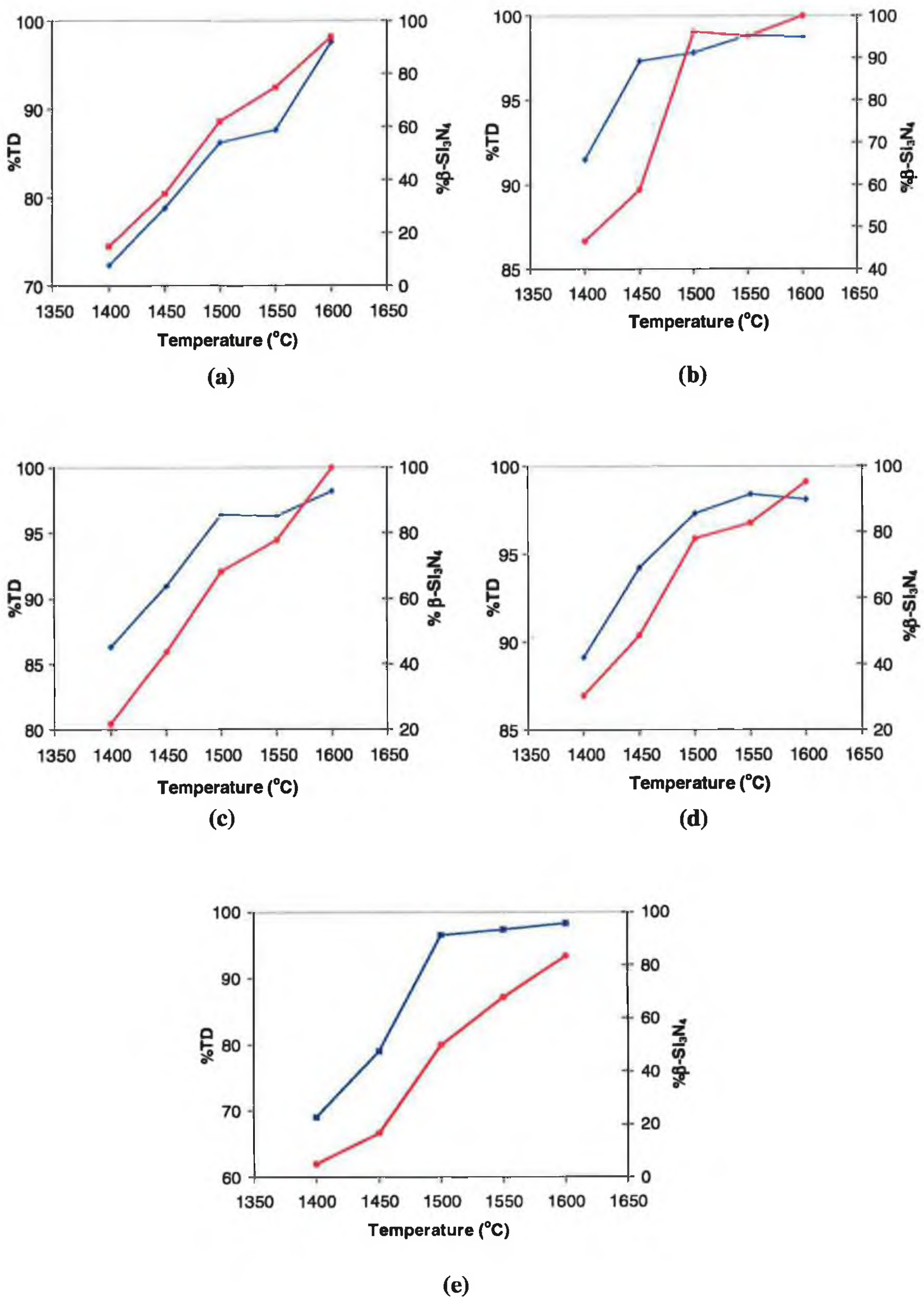

Figure 4.14(a-e) Densification (blue line, primary y-axis) and degree of transformation (red line, secondary y-axis) as a function of sintering temperature for composition 1-4AlN respectively.

4.4.2.6. Microstructural Analysis

SEM Analysis

The variation in the sintered microstructure of the sample with composition 1AlN (1wt% AlN, 5.5wt% Al_2O_3) with temperature is illustrated using the series of micrographs in Figure 4.15 (a)-(c). After sintering at 1400°C the sample microstructure consists of a small population of isolated macro pores but is predominantly made up of uniformly distributed micro pores smaller in size than in the starting compact (approximately 1μm). These micro pores are most likely remnants of the fine interparticle spacing in the green body, which have not been fully removed at this sintering temperature. On sintering at 1450°C, all the micro porosity has been filled by the increased volume of liquid phase formed at this temperature (as discussed in sub-section 4.4.2.5). A limited number of macro pores are still present which have in general developed a more spherical and slightly larger shape compared to the macro pores in the sample sintered at 1400°C. Further development of the microstructure is seen in the sample sintered at 1600°C. Small quantities of well-separated macro pores remain which again are slightly larger than those in the samples sintered at lower temperatures. The observed sequential filling of smaller pores first occurs because such pores have a high surface to volume ratio so that a given volume of liquid removes more solid/vapour interface. This follows the analysis by Shaw [83] and corresponds to the observations by Kwon and Yoon [82], referred to in Section 2.3.3.3. Removal of larger pores requires an increased volume of liquid phase, which corresponds to the almost complete elimination of porosity after sintering at 1600°C. It should be noted that although the macro/globular pores in the present samples grow slightly with increasing temperature they remain relatively small in size (≤1μm).

The removal of porosity with temperature observed in the microstructure corresponds well with the calculated percent theoretical densities. The density increased from 90%TD to 97%TD to 99%TD after sintering at 1400°C, 1450°C and 1600°C respectively.

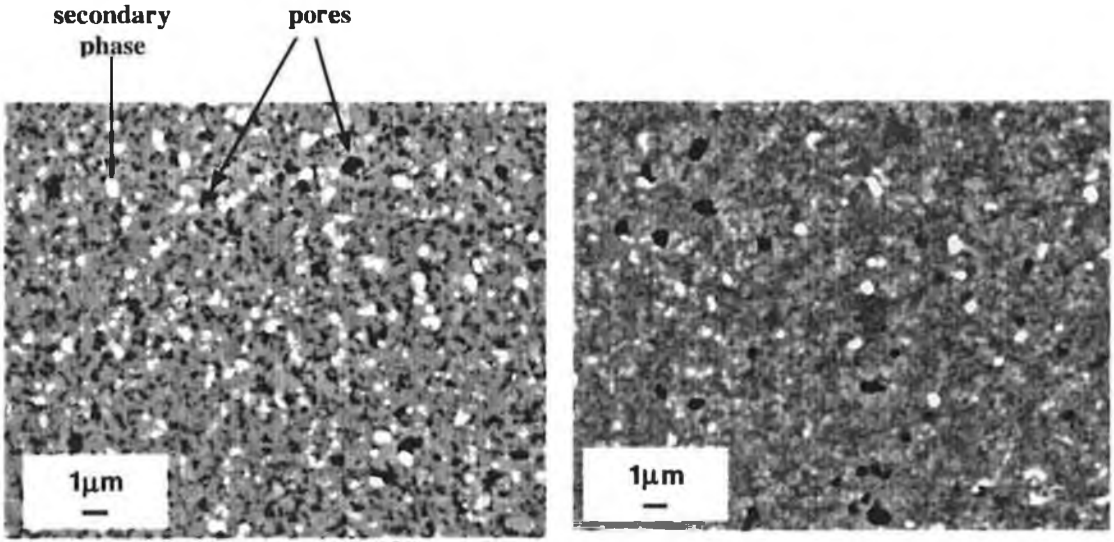

(a) – sintered at 1400°C

(b) – sintered at 1450°C

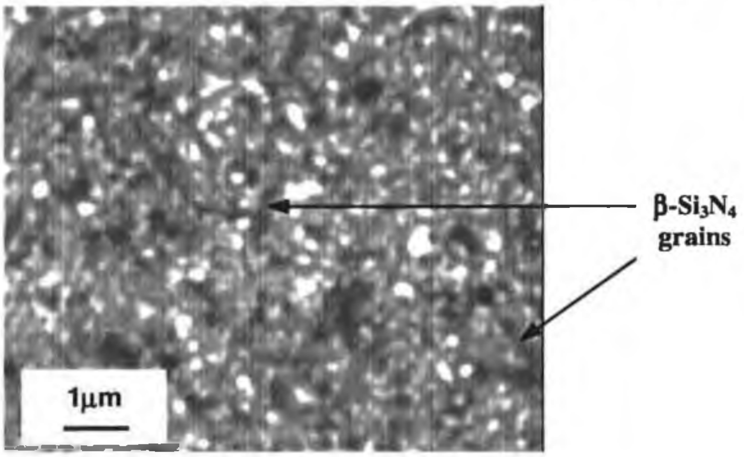

(c) – sintered at 1600°C

Figure 4.15 Variation of microstructure of sample 1AlN sintered for 2hrs at the specified temperatures.

Density distribution is seen to be relatively uniform throughout the samples, apart from a porous region approximately 5µm from the surface of the samples illustrated in Figure 4.16 (slightly out of focus), which is most likely a sintering edge-effect.

Changes in the morphology of the Si_3N_4 grains with sintering temperature are also observed. The observed deepening/darkening of grey colour of the bulk Si_3N_4 matrix with increasing density is a real effect and accompanies increased densification [209]. Etching of the samples, which would show the Si_3N_4 grains more clearly, proved difficult with the present material. However, the $\alpha \rightarrow \beta$-Si_3N_4 transformation (equiaxed → rod-like morphology) with temperature (as detected by XRD) can be seen to some extent in the samples sintered at 1400°C and 1450°C (Figure 4.15(a) and (b)). Although out of focus, due to the high magnification, the micrographs of the sample sintered at 1600°C (Figure 4.15(c)) and at a higher magnification in Figure 4.17) show the rod-like facetted prism shaped β-Si_3N_4 grains.

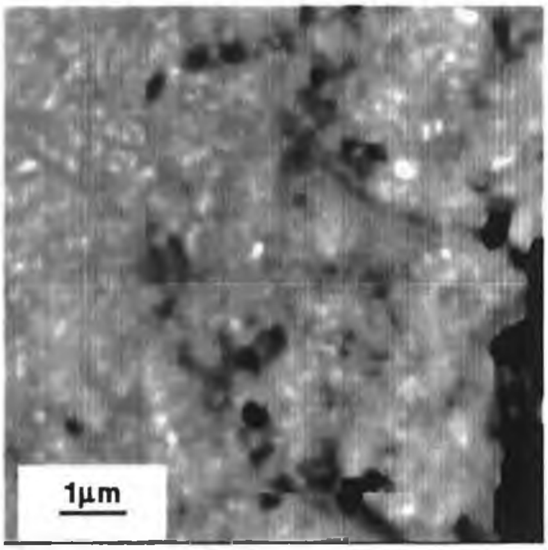

Figure 4.16 Density gradient observed near the surface of sample 1AlN sintered at 1600°C.

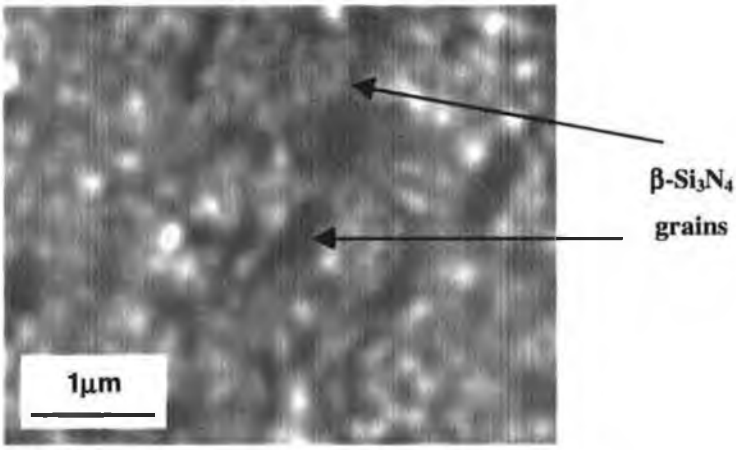

Figure 4.17 β-Si_3N_4 grains in sample 1AlN sintered at 1600°C

As outlined in Section 3.5.3, back-scattered electron imaging (BSE) distinguishes between phases by elemental contrast where heavier elements appear brighter. EDX analysis (Figure 4.18) confirmed that the white phases observed in the present materials are yttrium rich. These secondary phases are present in fine quantities and materials are yttrium rich. These secondary phases are present in fine quantities and no clear pattern of distribution is observed. In the sample sintered at 1400°C the "white" secondary phase is most probably precipitates of YAG since XRD analysis (discussed previously in sub-section 4.4.2.5 and outlined in Table 4.7) detected YAG in this sample. No crystalline phases were detected in the samples sintered at 1450°C and 1600°C suggesting that in these cases the "white" secondary phases observed in the SEM images are yttrium-rich glassy phases.

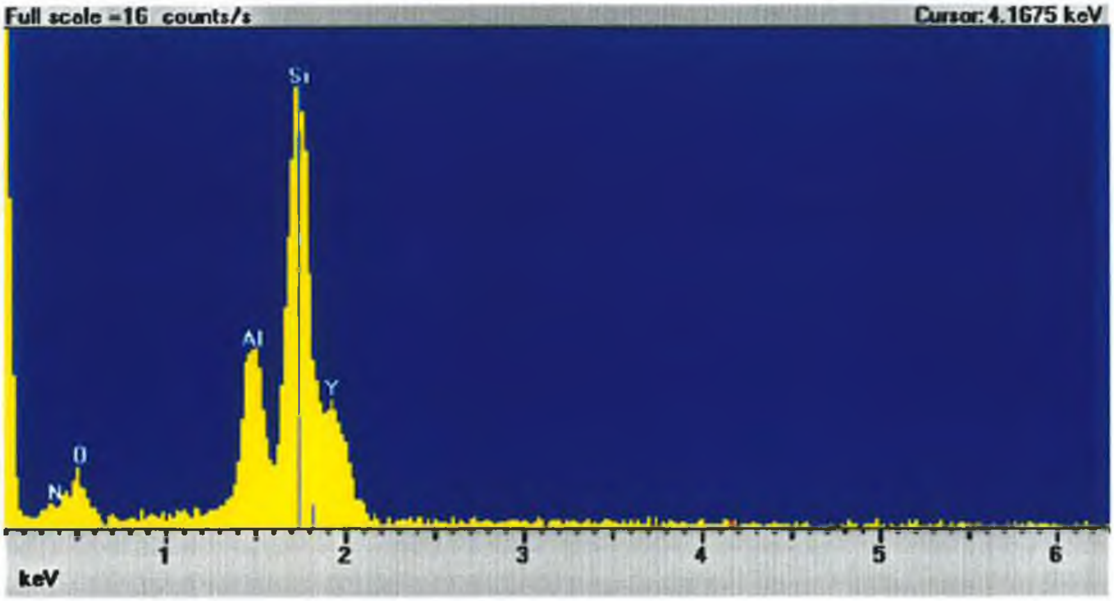

Figure 4.18 EDX trace for a spot analysis of the light area observed in micrograph Figure 4.15(c).

The effect of sintering additive composition on the microstructure after sintering at 1600°C is illustrated in Figure 4.19 (a) to (d). The variation in the AlN and Al_2O_3 content between samples 1AlN, 2AlN, 3AlN and 4AlN does not have a significant effect on the microstructural development. A limited quantity of closed porosity is observed in each sample, the development of β-Si_3N_4 grains can be seen and the content and distribution of an yttrium-rich phase is very similar in each sample. The improved densification behaviour of the compositions within the Si_3N_4 + Y_2O_3 + Al_2O_3 + AlN series compared with the reference material (Si_3N_4 +YAG) is confirmed by the large quantities of closed porosity still present in the reference material after sintering at 1600°C (Figure 4.19 (d)).

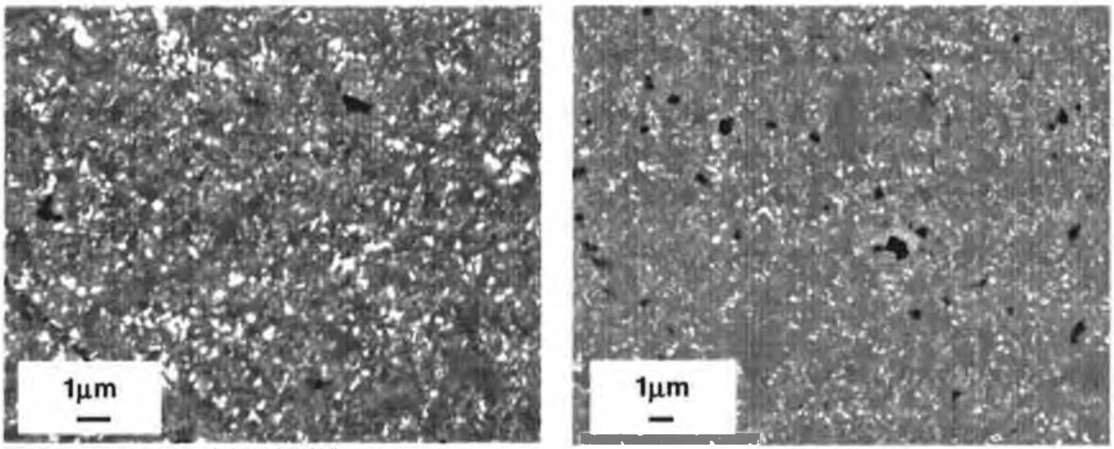

(a) – 1AlN (b) – 2AlN

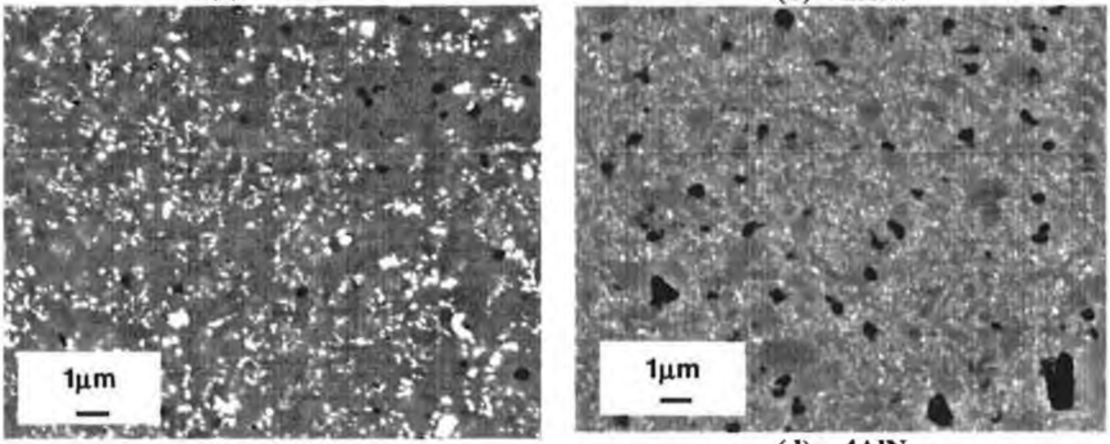

(c) – 3AlN (d) – 4AlN

Figure 4.19 Variation of microstructure with sample composition after sintering for 2 hours at 1600°C (grey-Si_3N_4; white:Y-rich phase, black-pores).

TEM analysis

The volume of intergranular "sinter" phase proved generally too low for detection by conventional bulk XRD measurement. An attempt was made using one sample, 1AlN sintered at 1500°C, to establish grain boundary phase composition and microstructure using Transmission Electron Microscopy (TEM). In situ EDX analysis was performed to determine the composition of the secondary phases.

Typical bright field images of the sample are shown in Figure 4.20. The microstructure formed in this sample is seen to contain globular/rounded α-Si_3N_4 grains and hexagonal/prismatic β-Si_3N_4 grains, some porosity and an intergranular phase. Selected area diffraction of the intergranular (secondary) phase around the Si_3N_4 grains showed no diffraction pattern suggesting that this is a non-crystalline (glassy) phase. Moreover, the contrast of the intergranular phase did not alter during sample tilting that is when a dark field image was created (Figure 4.21). These observations confirm the XRD analysis that the intergranular phase is completely glassy. Semi-quantitative EDX analysis revealed that the glassy phase contains N, O, Al, Si, and Y (29.8, 41.9, 6.5, 14.2 and 7.4 atomic % respectively). This composition was consistent (±2%) for three selected areas (Figure 4.22) suggesting that the composition of the intergranular phase is homogeneous.

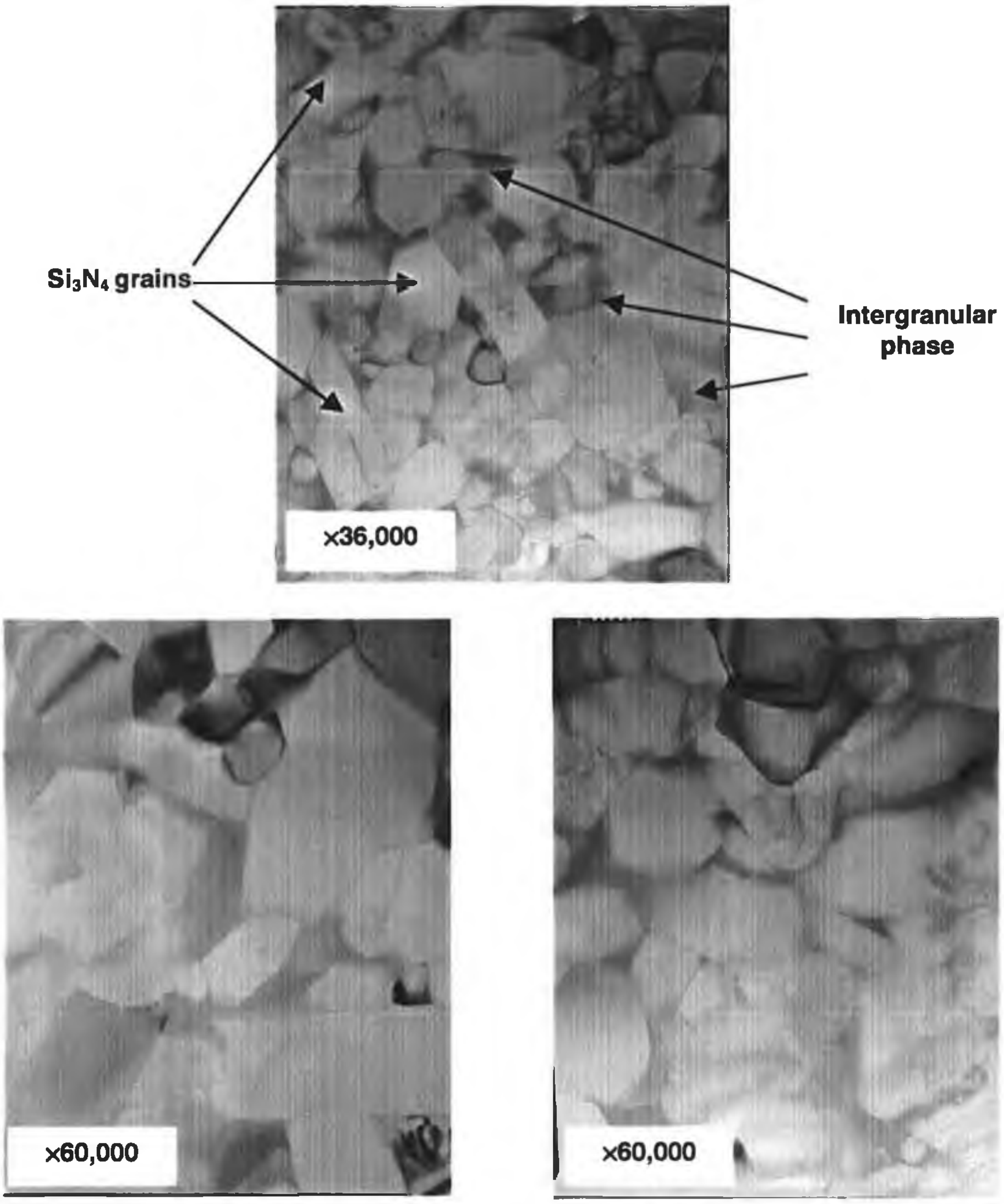

Figure 4.20 TEM bright field images of sample 1AlN after sintering at 1500°C.

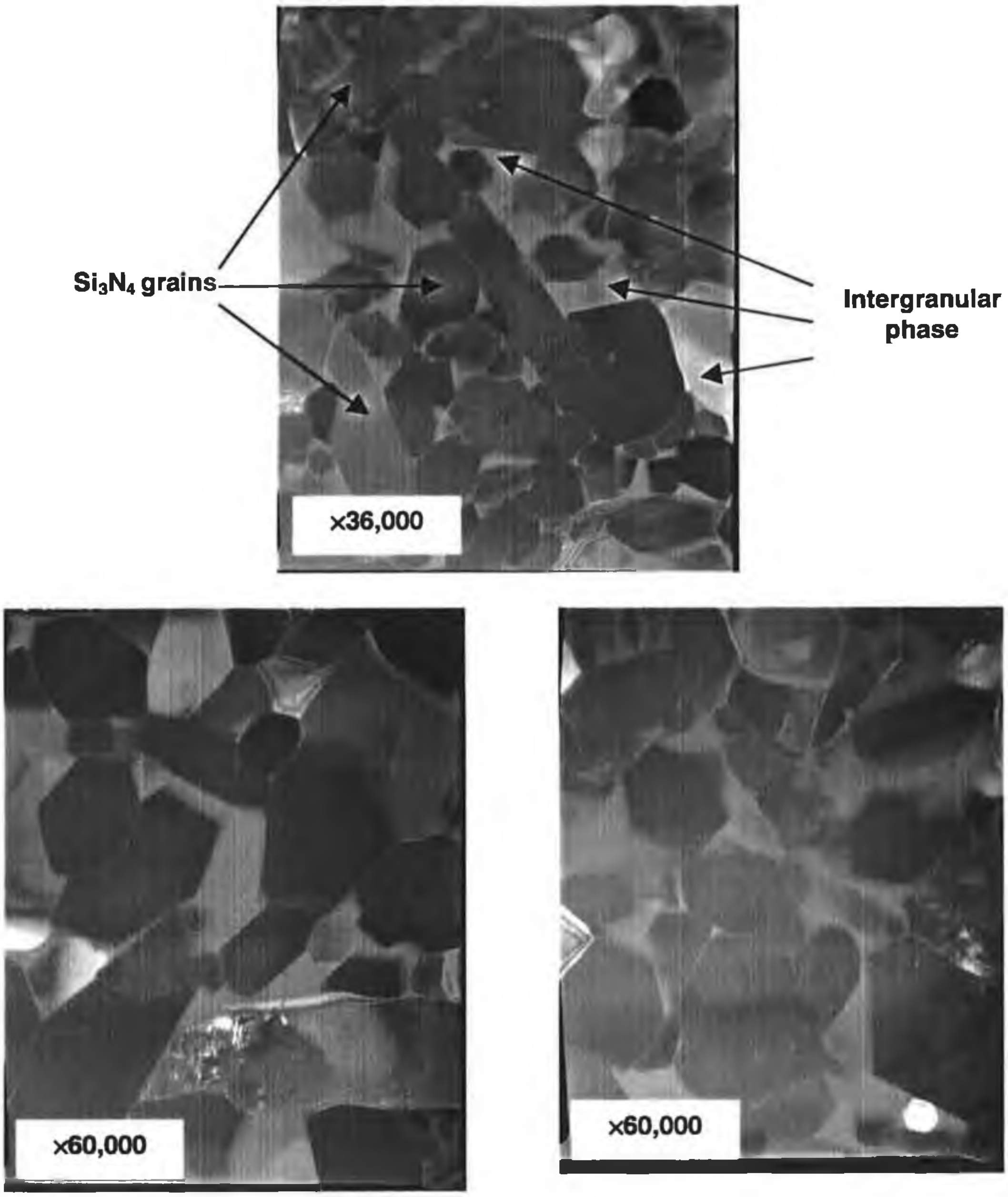

Figure 4.21 TEM dark field images of sample 1AlN after sintering at 1500°C

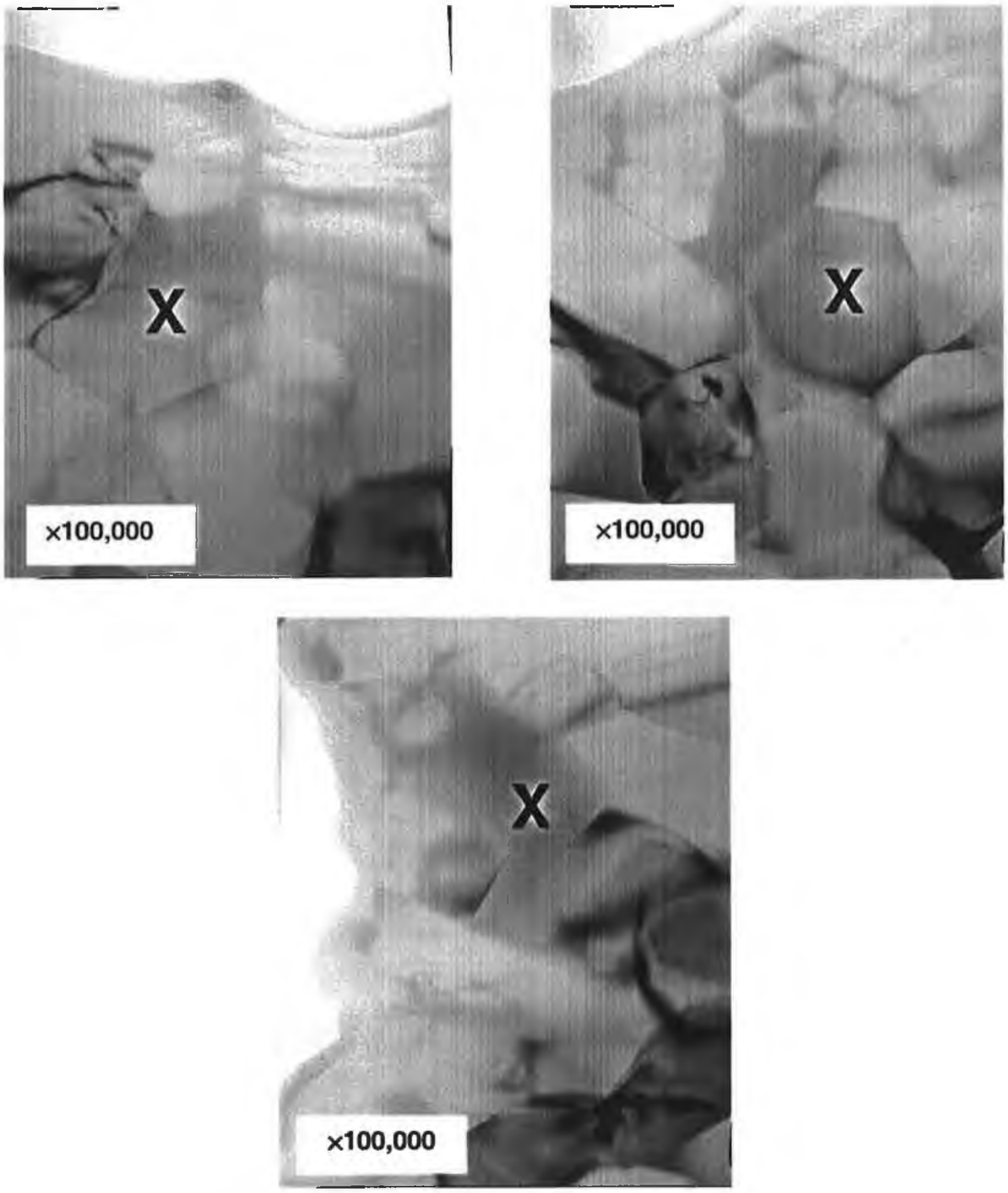

Figure 4.22 Glassy regions (X) selected for EDX analysis.

4.4.3. $Si_3N_4 + Y_2O_3 + Al_2O_3 + CaZrO_3$ Series

4.4.3.1. Densification Behaviour

The variation in density (expressed as percentage theoretical density, %TD) of the sintered samples with increasing sintering temperature is illustrated in Figure 4.23. Samples with constant sintering additive combinations increased in density with increased sintering temperature, for example, the density of sample 3.2CaZ (4.8wt% $CaZrO_3$, 2.6wt% Y_2O_3, 2.6wt% Al_2O_3) increases from 73.3%TD after sintering at 1400°C to 96.97%TD at 1700°C. Samples with the compositions 4.8wt% $CaZrO_3$ and 6.4wt% $CaZrO_3$ are seen to reach higher densities than the reference material after sintering at temperatures <1600°C. The addition of calcium zirconate to the Si-Y-Al-O-N system is seen to significantly enhance densification at lower sintering temperatures (<1600°C) and in particular the sample with composition 3.2CaZ, densifies better than the reference material at each sintering temperature, reaching close to full density (>95%TD) at 50°C lower than the reference material.

Figure 4.24 illustrates in more detail the densification results of the 3.2-6.4wt% $CaZrO_3$ compositions between 1550°C and 1700°C. At all temperatures above 1600°C, the 3.2CaZ composition densifies best, producing a >98%TD. The 4.8CaZ sample also performs well, reaching close to full density after sintering at 1600°C, obtaining maximum density of 97%TD after sintering at 1700°C. The densification of the sample with composition 6.4wt% CaZ (6.4wt% $CaZrO_3$, 1.8wt% Y_2O_3, 1.8wt% Al_2O_3) is comparatively good at 1550°C, but achieves lower density after sintering at higher temperatures.

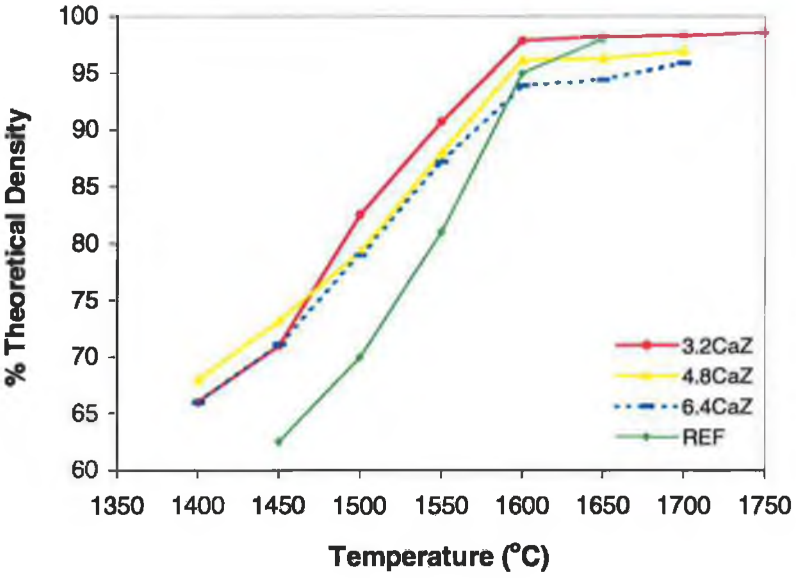

Figure 4.23 Variation of %TD with temperature for each composition in the CaZ series and the reference material.

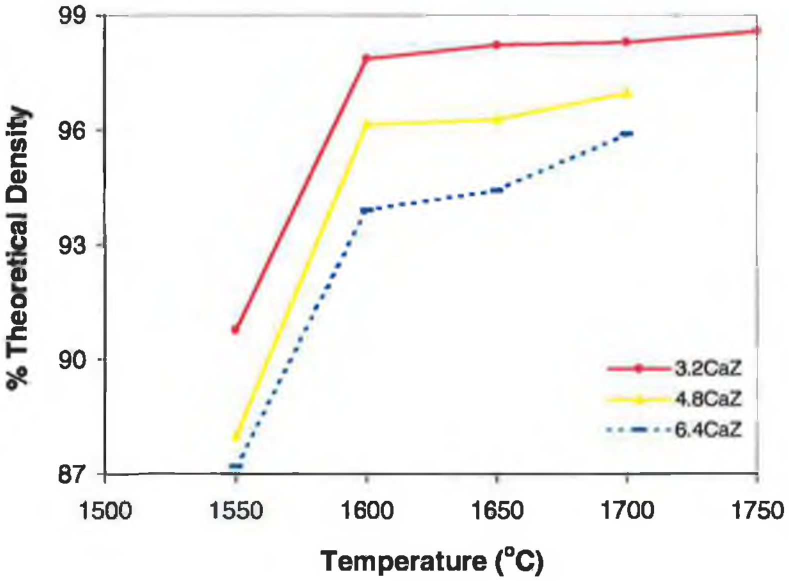

Figure 4.24 Variation of %TD with temperature (>1550°C) for each composition in the CaZ series.

As with the other compositions studied, the densification follows the three step mechanism of rearrangement, solution-diffusion-reprecipitation and coalescence [48], so that the liquid properties of the sintering additive phase will be the factor primarily controlling each mechanism step of the densification process, and ultimately the final densification achieved (discussed in Section 2.3). The present series of compositions is complex, with four sintering additives employed; Al_2O_3, Y_2O_3, and $CaZrO_3$ (CaO and ZrO_2). However, since the ratio of Al_2O_3 and Y_2O_3 added is kept constant at 1wt%:1wt%, the sintering mechanisms and percent theoretical density obtained can be considered to be dependent on the content of the novel sintering additive $CaZrO_3$ with respect to the content of Al_2O_3 and Y_2O_3. Figure 4.25 illustrates the variation of sintered %TD with the content of each sintering additive over the range of sintering temperatures studied and clearly shows the beneficial effect of adding $CaZrO_3$ on the densification behaviour of the Y-Si-Al-O-N system. For example, the reference material (standard YAG additive combination) densifies little after sintering at 1400°C, reaching just 57%TD, whereas the sample with composition 3.2CaZ (3.2wt% $CaZrO_3$ + 3.4wt% Al_2O_3 + 3.4wt% Y_2O_3) reached 66%TD, while at 1500°C an even more significant improvement was observed, with reference material reaching 70%TD and 3.2CaZ reaching 83%TD. Increasing the $CaZrO_3$ content to 4.8wt% results in a minor improvement in densification at 1400°C and 1450°C reaching 68%TD and 73%TD respectively, in comparison to 66%TD and 71%TD achieved by 3.2CaZ. However, above 1450°C, the sample 3.2CaZ exhibits better sintering behaviour. A further increase in the $CaZrO_3$ content is not seen to improve the densification behaviour as the sample with highest $CaZrO_3$ content (6.4wt%) densifies to the same extent as 3.2CaZ at 1400°C and 1450°C, but exhibits poorer densification at higher temperatures.

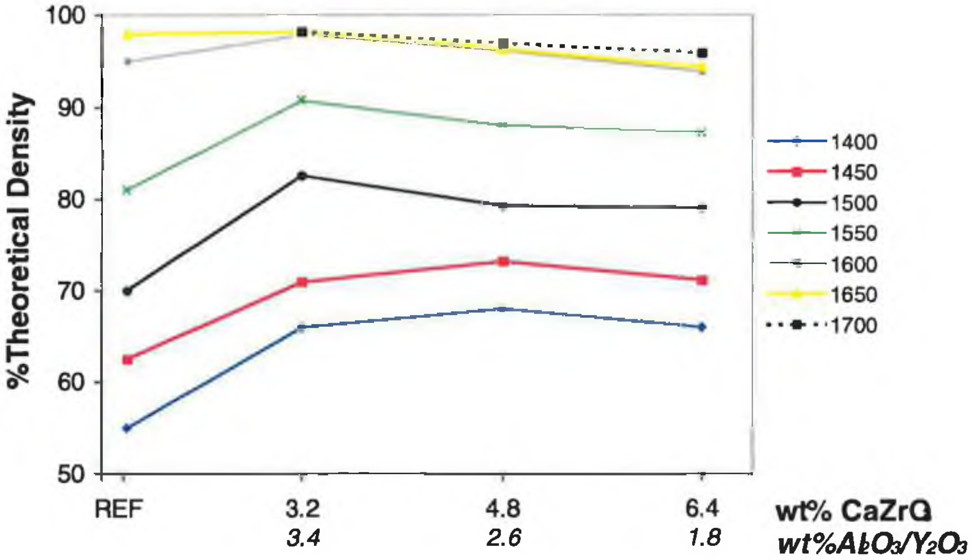

Figure 4.25 Influence of sintering additive content on the final density after sintering for 2hrs at the given temperatures.

4.4.3.2. Mass Loss Measurements

Table 4.8 shows the mass losses observed for each composition in the Si_3N_4-Y_2O_3-Al_2O_3-$CaZrO_3$ series and the reference material. These values observed are very low compared to those reported for similar Si_3N_4-based ceramics (typically 3-6%) [199][201]. Since the experimental procedure used in sintering this series of compositions is identical to that used for the Si_3N_4-Y_2O_3-Al_2O_3-AlN series, the observed low mass losses can be attributed similarly to:

- The low sintering temperatures used in this study
- The application of a relatively high pressure
- The use of graphite pieces to compact the sinter powder bed around the sample

As before, these factors help minimise the decomposition of Si_3N_4, and reduce the volatilisation of gaseous products from the sample surface [180] [203] and again, it may be that the densification kinetics for the present composition are advantageously rapid [202].

Sample Composition Label	**%Mass Loss**						
Sintering Temperature (°C)	**1400**	**1450**	**1500**	**1550**	**1600**	**1650**	**1700**
3.2CaZ	0.5	0.4	0.53	0.5	0.3	0.6	0.2
4.8CaZ	0.4	0.13	0.56	0.5	0.2	0.3	0.2
6.4CaZ	0.1	0.2	0.4	0.4	0.2	0.2	0.3
REF	0.4	0.32	0.43	0.5	0.55	0.5	-

Table 4.8 Measured %mass losses for compositions in the CaZ series and the reference material sintered at the given temperatures.

4.4.3.3. Shrinkage Results

A set of dilatometry experiments were carried out for each composition in the Si_3N_4-Y_2O_3-Al_2O_3-$CaZrO_3$ series to further investigate and help determine the effect of varying the individual additive content on the densification mechanisms and behaviour of these compositions. Rectangular green bars of samples of each composition were heated to 1600°C at a rate of 5°C/min and held at temperature for up to 8 hours (see Section 3.4.3 for details). Figure 4.26 illustrates the resultant dilatant curves, which confirm the sintering results obtained; that is, sample 3.2CaZ reaches the highest shrinkage of 15.89%, slightly less shrinkage occurred in sample 4.8CaZ and the sample with highest $CaZrO_3$ content, 6.4CaZ shows considerably lower shrinkage of 14.15%.

Table 4.9 outlines the influence of hold time at temperature on resultant percent shrinkage values. Significant increases in shrinkage (approximately 4.5%) are seen to occur during the first 2 hours at temperature. For each composition, prolonging the holding time at temperature resulted in very low increases in shrinkage of approximately 0.16%. These results confirm densification results in preliminary experiments, outlined in the introduction to this chapter, that a hold time of 2 hours is sufficient for good densification.

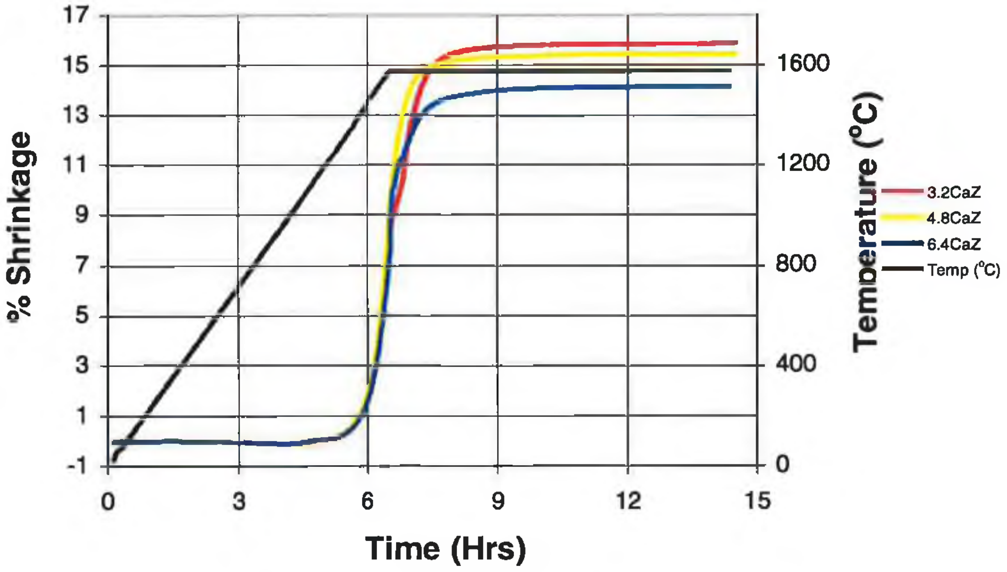

Figure 4.26 Dependence of dynamic shrinkage on temperature and time for compositions 3.2-6.4CaZ.

Sample Label Composition	% Shrinkage				
Hold Time at Temperature (Hrs)	0	2	4	6	8
3.2CaZ	9.99	15.71	15.85	15.88	15.89
4.8CaZ	11.72	15.32	15.44	15.46	15.47
6.4CaZ	8.44	14	14.12	14.15	14.15

Table 4.9 Percent shrinkage values after hold time at temperature for the CaZ series.

4.4.3.4. *α- to β-Si_3N_4 Transformation*

Table 4.10 outlines the %β-Si_3N_4 detected in each composition within the Si_3N_4 + Y_2O_3 + Al_2O_3 + $CaZrO_3$ series after sintering at the given temperature. Analysis of samples sintered at lower temperatures was focussed on the sample with composition 3.2CaZ (3.2wt% $CaZrO_3$ + 3.4wt% Y_2O_3 + 3.4wt% Al_2O_3) as this composition exhibited superior densification. As expected the degree of transformation increases as the sintering temperature increases, for example, the sample with composition 3.2CaZ consists of 0% β-Si_3N_4 after sintering at 1400°C and is completely transformed to β-Si_3N_4 after sintering at 1700°C, while in the sample with composition 4.8CaZ, 76.52%β-Si_3N_4 was measured in the sample sintered at 1600°C and complete transformation was observed in the sample sintered in 1700°C. This behaviour corresponds to the thermodynamic instability of the α-phase which at temperatures above 1400°C transforms to the more stable β-phase [106].

The influence of the sintering additive composition, that is the $CaZrO_3/Al_2O_3/Y_2O_3$ content, on the transformation behaviour is illustrated in Figure 4.27. The addition of increased amounts of $CaZrO_3$ to the Y-Si-Al-O-N system clearly encourages the α to β phase transformation during sintering at 1600°C and 1650°C. For example, after sintering at 1600°C 71.43% β-Si_3N_4 was measured in sample 3.2CaZ compared to 76.52% in the sample 4.8CaZ and 80.45% in the sample 6.4CaZ. Similar increases in the % β-Si_3N_4 detected were observed after sintering at 1650°C. Each composition had completely transformed after sintering at temperatures ≥1700°C.

Although the XRD results shown in Figure 4.27 are limited, comparing this figure and Figure 4.25 (Influence of $CaZrO_3$ and Al_2O_3/Y_2O_3 content on the final density) suggests that factors influencing densification at lower temperatures encourage the retention of the α-Si_3N_4 structure in the sample 3.2CaZ. At higher temperatures the α- to β-Si_3N_4 transformation is seen to be concurrent with densification.

Sample Composition Label	Temperature (°C)							
	1400	1450	1500	1550	1600	1650	1700	1750
3.2CaZ	0	30.77	52.3	70.54	71.43	75	100	100
4.8CaZ	-	-	-	-	76.52	80.33	100	-
6.4CaZ	-	-	-	-	80.45	85.4	100	-

Table 4.10 %β-Si_3N_4 detected using XRD in materials densified at the specified temperatures.

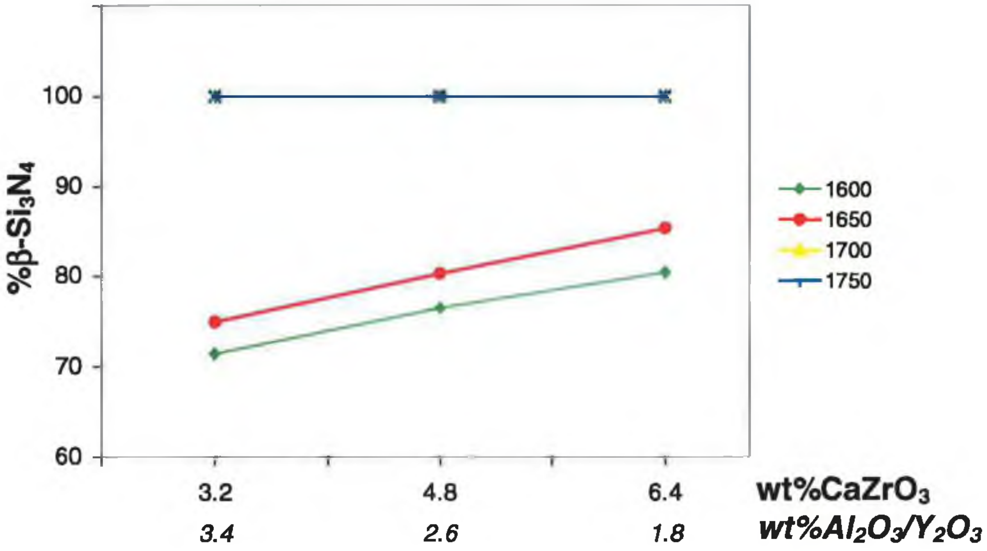

Figure 4.27 Influence of $CaZrO_3$ and Y_2O_3/Al_2O_3 content on the %β-Si_3N_4 detected sintering for 2hrs at the given temperatures.

4.4.3.5. Discussion on Reaction Sequences during Sintering

In the following discussion, CaO and ZrO_2 (added as the novel sintering additive $CaZrO_3$) are considered to behave as separate entities during the densification process since the compound $CaZrO_3$ was not detected by XRD analysis after sintering at any of the temperatures (Table 4.11).

The influence of the sintering additive combinations on the sintering behaviour can be seen in Figure 4.28, which illustrates the variation in the shrinkage rate observed for each composition. The start of measurable shrinkage occurs at approximately 1090°C for each composition, but the total shrinkage at this temperature is minimal. Significant shrinkage begins above 1200°C and continues up to maximum temperature. Samples 3.2CaZ and 4.8CaZ exhibit almost identical shrinkage behaviour, while sample 6.4CaZ has a lower shrinkage rate at temperatures greater than 1400°C.

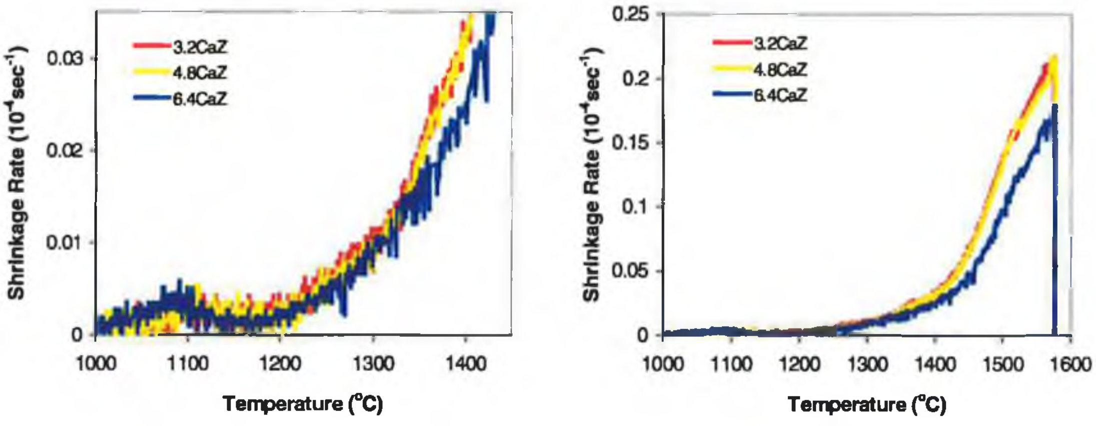

(a) (b)

Figure 4.28 Variation of shrinkage rate with temperature in the temperature range (a) 1000-1450°C and (b) 1000-1600°C.

The onset of shrinkage at 1050°C-1100°C may be attributed to the formation of a ternary eutectic oxide melt. The lowest eutectic in the present series, Si_3N_4-Y_2O_3-Al_2O_3-$CaZrO_3$, is formed when SiO_2, ever present on the surface of Si_3N_4 powders, reacts with Al_2O_3 and CaO. Since CaO and Al_2O_3 are present in much larger quantities than the very low concentration of SiO_2, the volume of liquid formed at this temperature is independent of starting composition. According to the CaO-SiO_2-

Al_2O_3 phase diagram the lowest eutectic temperature is 1170°C [210], slightly higher than that observed here. The principal densification mechanism at this stage is the redistribution of liquid phase, resulting in slightly closer packing (via rearrangement) of the powder particles. However this step contributes little to overall shrinkage/densification since as mentioned above, the amount of eutectic liquid oxide formed is limited by the amount of SiO_2 present in the starting compositions, estimated to be no more than 1wt%.

Significant shrinkage is seen to begin as the temperature increases above 1200°C. This is most probably due to the formation of larger amounts of the $CaO-SiO_2-Al_2O_3$ oxide melt, encouraging further particle rearrangement leading to enhanced close packing of the powder particles. The observed shrinkage at these temperatures corresponds well to the work carried out by Van Rutten et al [211] on Ca-α-SiAlONs, who reported the onset of shrinkage at 1225°C, rising to measurable shrinkage at 1350°C.

Also encouraging shrinkage, is the formation of the $Y_2O_3-SiO_2-Al_2O_3$ ternary eutectic oxide melt at approximately 1350°C [205]. The amount of liquid phase increases further at higher temperatures because the dissolution of nitrogen (from Si_3N_4) lowers the eutectic temperature of the system [212]. The shrinkage rate then continuously increases, reaching a maximum at the maximum temperature, 1600°C.

Working with bulk Ca-α-sialon phases, which may resemble the grain boundary phases in the present material, Van Rutten [211] analysed in detail, the sequential solution of crystalline phases into the eutectic melt, between 1300 and 1600°C. While the crystalline phases present in the current materials are too small to detect using XRD (Table 4.11), the shape of the shrinkage rate curves is compatible with his analysis. Accordingly, the significant increase observed in the present study between temperatures 1300-1350°C corresponds to the formation of significant quantities of liquid phase [211]. Van Rutten estimates that the solution of Si_3N_4 begins at 1450°C which is consistent with the distinct acceleration observed in Figure 4.28.

It is speculated that in the present systems zirconia plays a limited role in the densification behaviour, particularly during sintering at lower temperatures. Although the solubility of zirconia at low temperatures in the liquid phases formed in the present materials is not known, it is expected that the solubility in pure silicate liquids is low, because, as pointed out earlier, zirconia can be used as a nucleating agent in silicate glass systems [175] [176]. Also the lowest eutectic reported within the present system is most probably the ternary Al_2O_3-SiO_2-ZrO_2 eutectic at 1700-1710°C [213]. This is reflected in the XRD analysis results outlined in Table 4.11, where yttria-stabilised-zirconia and tetragonal zirconia were detected in sample 3.2CaZ after sintering at lower temperatures. At higher sintering temperatures zirconia may participate in liquid phase formation due to the formation of the eutectic above and a certain amount of zirconia may dissolve in the liquid phase. At 1700°C, Cheng and Thompson [176] observed that the solubility of ZrO_2 in Y_2O_3-Al_2O_3-SiO_2 liquids was around 10wt%, but that the dissolved ZrO_2 precipitated out of solution during cooling from sintering temperature. During the densification of a Si_3N_4/ZrO_2 composite ceramic, Falk and Holmstrom [214] also observed the solution and precipitation of ZrO_2. The XRD results in the present study are consistent with these observations, as ZrO_2 was observed in all sample compositions after sintering at higher temperatures.

As outlined in Table 4.11 the present materials contained only tetragonal zirconia. This may be due to the size and composition of the zirconia grains that allowed retention of the high temperature form by mechanical constraints enforced by the surrounding matrix [174]. Although not detected by XRD, it is also certainly possible in the present systems that the yttria and/or calcia present has been incorporated into the ZrO_2 grains during densification contributing to the stabilisation of the tetragonal phase [215].

Sample Composition Label	Temperature (°C)							
	1400	**1450**	**1500**	**1550**	**1600**	**1650**	**1700**	**1750**
3.2CaZ	ZrO_2	ZrO_2	ZrO_2	ZrO_2	ZrO_2	ZrO_2	ZrO_2/ZrN CaSiAlON	ZrO_2/ZrN CaSiAlON
4.8CaZ	-	-	-	-	ZrO_2	ZrO_2	ZrO_2/ZrN CaSiAlON	ZrO_2/ZrN CaSiAlON
6.4CaZ	-	-	-	-	ZrO_2	ZrO_2	ZrO_2/ZrN CaSiAlON	ZrO_2/ZrN CaSiAlON

Table 4.11 Crystalline phases detected in the selected materials after sintering at the given temperatures.

ZrO_2/ZrN – $ZrO_{2-3x/2}N_x$; CaSiAlON - $Ca_6Al_2Si_2O_{10}N_2$ phases.

As mentioned earlier, the XRD results are limited for samples 4.8CaZ and 6.4CaZ however, some correlation between the liquid forming abilities and wetting behaviour of Si_3N_4 and the α- to β-Si_3N_4 phase transformation behaviour are made. The good liquid forming properties of the sample with composition 3.2CaZ at temperatures >1550°C (resulting in good densification) corresponds to a lower degree of transformation, compared to samples 4.8CaZ and 6.4CaZ. This behaviour corresponds well with the hypothesis that the intergranular phases in the present materials are similar to the bulk Ca-α-sialon studied by Van Rutten et al. [211]. It is well documented that these materials have excellent liquid phase forming properties, and that CaO stabilises the α-Si_3N_4 structure [113][216][217]. It is thus not unreasonable to speculate that the sample with composition 3.2CaZ encourages the formation of an increased amount of these sialons compared to the samples with compositions 4.8CaZ and 6.4, which exhibit higher degrees of transformation. The complete transformation to β-Si_3N_4 observed in all sample compositions after sintering at temperatures >1650°C suggests that the possible Ca-α-sialons formed at lower temperatures redissolve into the liquid phase and reprecipitate as β-Si_3N_4.

To summarise, an improvement in densification behaviour compared to the standard Si_3N_4 + YAG system was observed in the range of compositions in the CaZ series selected. The samples with composition 3.2CaZ (3.2wt% $CaZrO_3$ + 3.4wt% Y_2O_3 + 3.4wt% Al_2O_3) exhibited superior densification over the compositions 4.8CaZ and 6.4CaZ. This is most likely due to the beneficial effect of the presence of CaO ($CaZrO_3$) in forming a low temperature melting eutectic and the presence of sufficient alumina forming large of amounts of liquid phase at each temperature. The intergranular phase formed in this composition probably resembles the bulk Ca-α- sialons studied by Van Rutten et al [211]. Also the densification behaviour of this composition is probably enhanced by the alumina and yttria content in sample 3.2CaZ, which is close to that reported by Itturiza [199] (5.5wt% Al_2O_3, 5.5wt% Y_2O_3) as the optimum for densification in the Si_3N_4-Y_2O_3-Al_2O_3 system. Composition 3.2CaZ thus seems to be the best candidate as a matrix phase material for the pressureless sintering of a ceramic matrix composite.

4.4.3.6. Microstructural Analysis

SEM ANALYSIS

Figure 4.29 (a)-(h) illustrates the variation in sintered microstructure of the sample with composition 3.2CaZ (3.2wt% $CaZrO_3$, 3.4wt% Al_2O_3, 3.4wt%Y_2O_3) with sintering temperature. After sintering at 1450°C a high degree of both micro and macro porosity is observed in the sample microstructure, which reflects the low percent theoretical density achieved after sintering at this temperature (73.2%TD), Figure 4.29 (a). Although at a lower magnification, the filling of micro porosity in the sample after sintering at 1600°C, can be seen in Figure 4.29 (b), corresponding to the larger amount of liquid phase formed at this temperature (as discussed in the sub-section 4.4.3.5). The microstructure includes a population of randomly distributed spherical macro pores. Further development of microstructure is seen in the sample sintered at 1700°C (Figure 4.29 (d)). Reduced quantities of macro pores remain which are well-separated and are slightly larger than those in the samples sintered at lower temperatures. Although these spherical macro pores have grown slightly, their average size remains relatively small ≤ 1μm. Complete removal of porosity is seen in the sample sintered at 1750°C (Figure 4.29 (e)). As with the AlN series, discussed in Section 4.4.2.6, the sequential removal of smaller pores in the microstructure of the present material occurs at lower temperatures also follows the analysis by Shaw [83] and corresponds to the observations by Kwon and Yoon [86]. Removal of larger pores requires an increased volume of liquid phase, which corresponds to the almost complete elimination of porosity after sintering at 1600°C and full densification after sintering at 1750°C.

The observed removal of porosity with temperature in the microstructure corresponds well with the calculated percent theoretical densities. The density increased from 71%TD to 97.9%TD to 98%TD to 99%TD after sintering at 1450°C, 1600°C, 1700°C, and 1750°C respectively.

No density variation through the samples was observed.

The development of the morphology of the Si_3N_4 grains with sintering temperature is also observed. The $\alpha \rightarrow \beta$-Si_3N_4 transformation with temperature (as detected by XRD) can be seen by comparing Figure 4.29 (a), (c) and (e) (although slightly out of focus, due to the high magnification used) which illustrate the microstructure of the samples sintered at 1450°C, 1600°C and 1750°C respectively. After sintering at 1450°C no prism shaped β-Si_3N_4 grains are visible, corresponding with the XRD results (0%β-Si_3N_4 detected). The development of rod-like, facetted prism shaped β-Si_3N_4 grains is apparent in the sample sintered at 1600°C (71% β-Si_3N_4 detected using XRD) and the microstructure of the sample sintered at 1750°C shows β-Si_3N_4 grains.

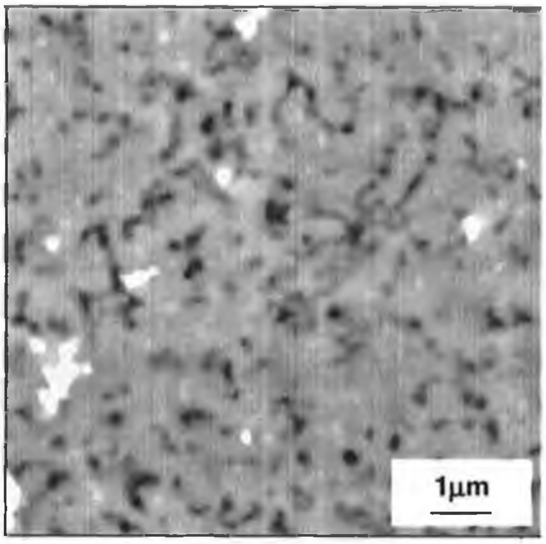

(a) – sintered at 1450°C

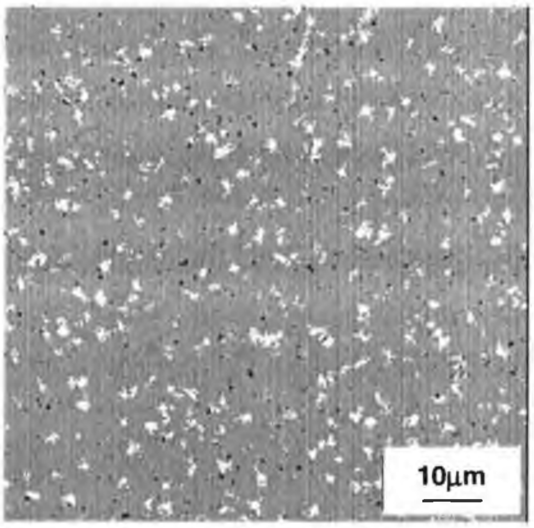

(b) – sintered at 1600°C

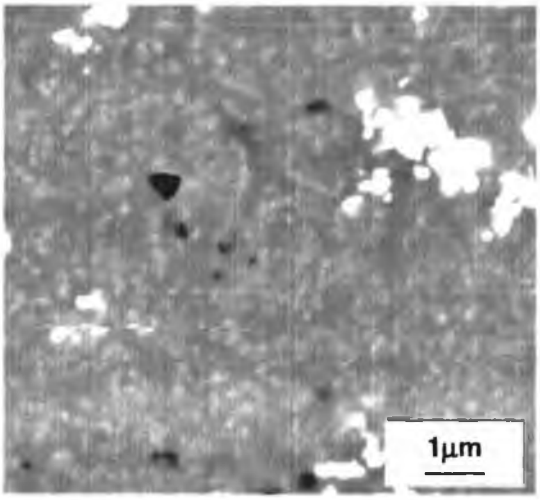

(c) - 1600°C-high magnification

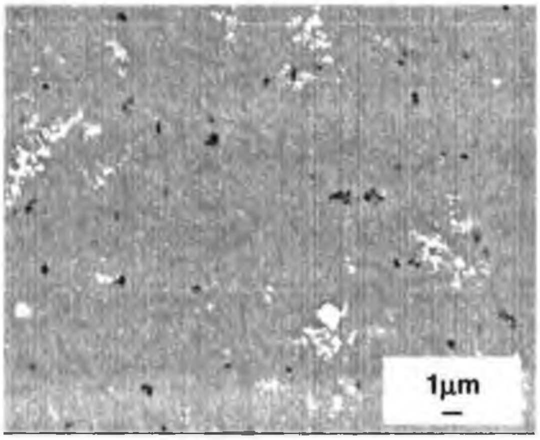

(d) - sintered at 1700°C

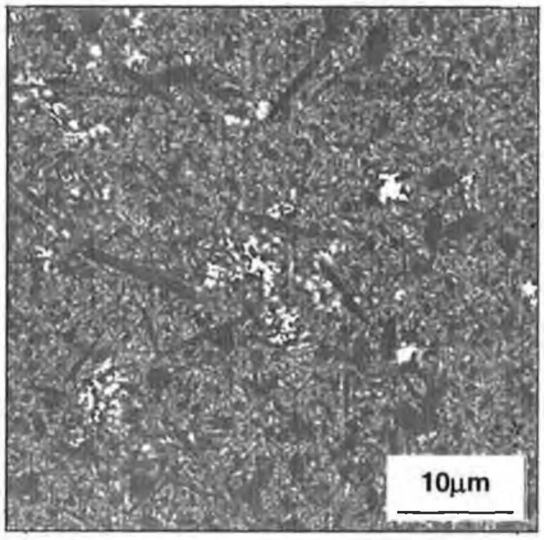

(e) - 1750°C - centre

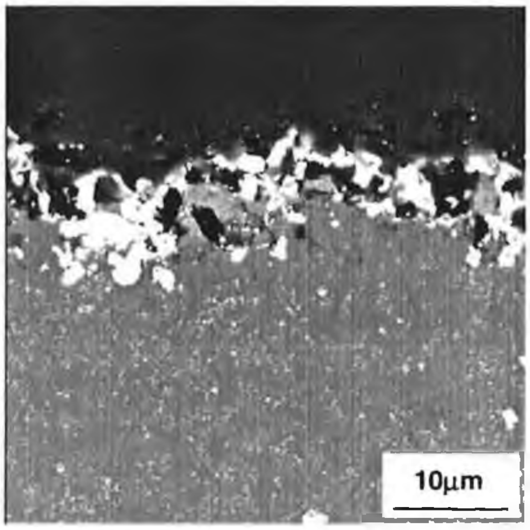

(f) - 1750°C – close to surface

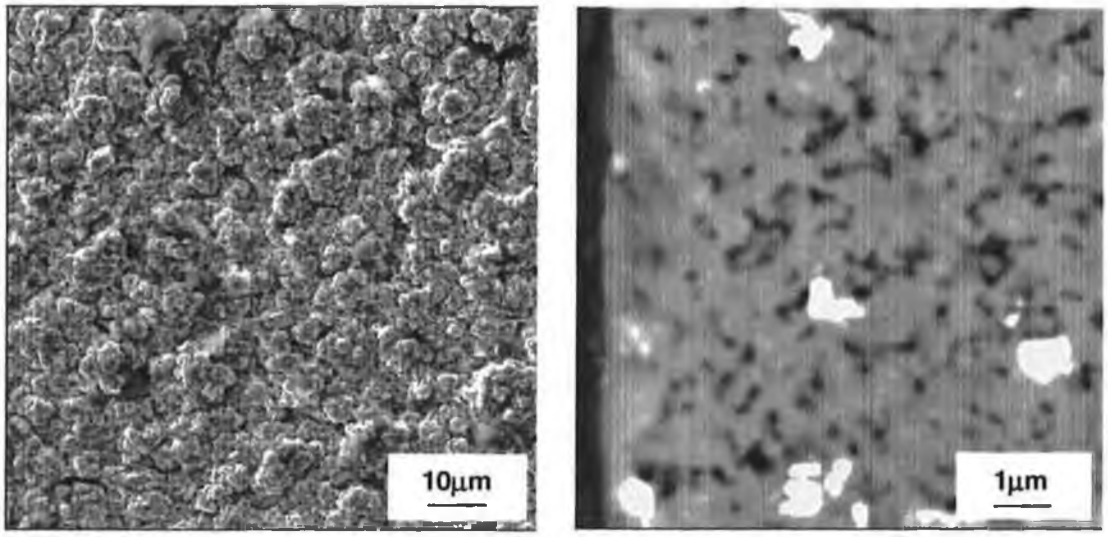

(g) 1750°C – surface scale **(h) 1450°C – close to surface**

Figure 4.29 (a-h) Variation of microstructure of sample 3.2CaZ sintered for 2hrs at the specified temperatures. (grey-Si_3N_4; white-Y/Zr-rich phase; black-pores)

As outlined in Section 3.5.3, back-scattered electron imaging (BSE) distinguishes between phases by elemental contrast where heavier elements appear brighter. In each sample composition examined using SEM, two possibly different secondary phases were formed. One has a light grey colour, and is present in fine quantities while the other is 'brighter' and is present in discrete particles (resembling precipitates). EDX analysis also suggested that the secondary phases observed in the present materials have different chemical compositions. Although the peaks for zirconium and yttrium lie very close together, the brighter phase is richer in zirconium (zirconium has a heavier atomic weight than yttrium), thus most likely corresponds to the ZrO_2 detected using XRD. No other crystalline phases were detected in the samples sintered at 1450°C and 1600°C suggesting that in these cases the "light grey" secondary phases observed in the SEM images are yttrium-rich glassy phases. Although traces of a calcium sialon were detected in the samples sintered at 1700°C and 1750°C, EDX analysis of the light grey phase detected significant quantities of yttrium, so it is most probable that the light grey phase observed is an yttrium-rich glass similar to that in the aforementioned samples. Both types of secondary phases are uniformly distributed throughout the samples sintered at 1450°C and 1600°C. In the samples sintered at 1700°C and 1750°C, a distinct increase in the concentration of the bright secondary phase at the surface was observed (Figure 4.31(f) and (g)), compared to for example, the sample 1450°C (Figure 4.31(h)). This phenomenon is discussed with respect to observations made using optical microscopy.

Although slightly poor in quality, the effect of sintering additive composition on the microstructure after sintering at 1700°C can be seen by comparing Figure 4.29 (d) and Figure 4.30 (a) and (b). The variation in the sintering additive content between samples 3.2CaZ, 4.8CaZ and 6.4CaZ does not have a significant effect on the microstructural development. The development of β-Si_3N_4 grains can be seen to some extent and the content and distribution of both secondary phases is very similar in each sample. The slightly superior densification behaviour of 3.2CaZ at this temperature is confirmed as an increasing degree of porosity is observed going from 3.2CaZ to 4.8CaZ to 6.4CaZ.

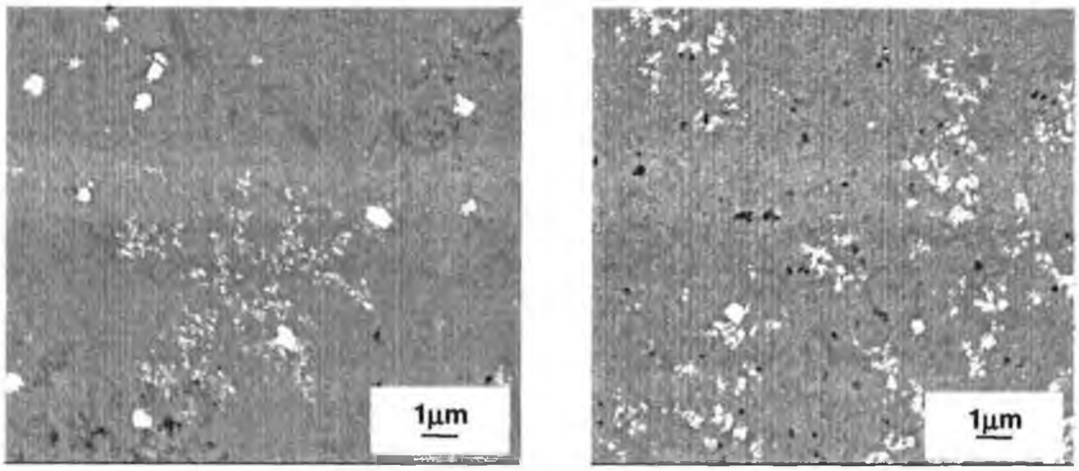

(a) 4.8CaZ **(b) 6.4CaZ**

Figure 4.30 Variation of microstructure with sample composition after sintering for 2 hours at 1700°C.

OPTICAL MICROSCOPY

Differentiating between the two types of secondary phases observed using SEM was easier using an oil immersion lens on an optical microscope, as the Zr-rich phase has a distinct orange/brown colour. illustrates a series of micrographs of the 3.2CaZ materials sintered at temperatures ≥1600°C.

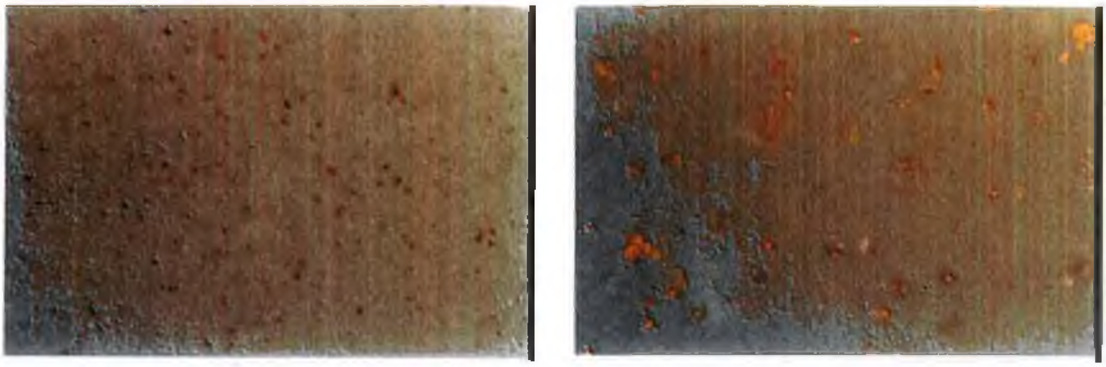

(a) Sintered at 1600°C - centre

(b) Sintered at 1700°C – centre

(c) Sintered at 1700°C - edge

(d) Sintered at 1750°C – centre

(e) Sintered at 1750°C - edge

Figure4.31 Variation of microstructure of sample 3.2CaZ sintered for 2hrs at the specified temperatures.

As mentioned earlier (Section 4.4.3.5), during the sintering process, CaO dissociates from $CaZrO_3$ at approximately 1170°C, as the CaO forms a ternary eutectic with Al_2O_3 and SiO_2. ZrO_2 is then released at the site of the original particle. Reference [176] suggests that the solubility of ZrO_2 in a Y_2O_3-SiO_2-Al_2O_3 liquid increases with temperature to approximately 10wt% at 1600°C, which is far above the nominal ZrO_2

concentration in the present material. Also referenced is the tendency of ZrO_2 to promote nucleation in similar glass systems, so that its solubility is assumed to approach zero at lower temperatures [175][177]. The current range of microstructures provides further indications of the behaviour of ZrO_2 during the sintering of the sample with composition 3.2CaZ, sintered at temperatures from 1600°C to 1750°C for two hours in a nitrogen atmosphere.

After sintering at 1600°C, the Zr-rich phase appears as small (approximately 1µm) discrete precipitates distributed at approximately 100µm distances from each other. The precipitates are all roughly of the same size and are uniformly distributed throughout the structure, and are clearly not coherent with the underlying matrix of the light grey Si_3N_4 matrix and white coloured yttrium-rich intergranular phase. There is no indication of further reaction with the surrounding constituents, either solid, liquid or gaseous, and no apparent coarsening or segregation to the edges of the samples. Although no nitride species was detected using XRD, it is possible that nitrogen has entered the ZrO_2 structure forming an oxynitride compound, as was possibly detected in the samples sintered at higher temperatures (Table 4.11). The volume fraction of these precipitates within the sample is very low (<1vol%) and does not account for the original concentration of Zr added to the starting materials in the form of $CaZrO_3$.

After sintering at 1650°C, the distribution of the Zr-rich phase is not significantly different. The particles seem to contain a higher proportion of the black granular species than observed in the sample sintered at 1600°C, but apart from this, the morphology of the samples is not noticeably different.

Sintering at 1700°C introduces significant changes to the sample morphology. All of the Zr-containing particles are considerably larger, approximately 3-5µm in diameter, and seem to contain two distinct compounds, nominally; orange coloured single crystals, normally associated with a nitride species, and a small black granular precipitate (possibly oxide). The general interparticle spacing, however, is similar to that observed in the 1600°C and 1650°C sintered material, so that the overall volume fraction of the discrete Zr-precipitates has increased three-fold. Concurrently, the

Si_3N_4 bulk material has darkened. At the surface a Zr-rich layer is seen to have formed, and a subscale area depleted in orange precipitates is observed. These observations correspond with the XRD data (Table 4.11), as ZrO_2 and a Zr-rich compound were detected in the surface of this sample. It was difficult, however, to determine the exact composition of this Zr-rich phase. The X-ray patterns were slightly shifted from those of ZrN, which may be caused by the presence of oxygen in the lattice. This Zr-rich compound may be ZrN or a Zr-oxynitride ($ZrO_{2-2x}N_{4x/3}$) formed by direct nitridation of ZrO_2 [164], at the surface and with amounts, below XRD detection level, formed by possible reaction with Si_3N_4 towards the centre.

After sintering at 1750°C, the sample's morphology exhibits the same development trends, but are even more pronounced. The Zr-precipitates are well-facetted and uniformly orange in colour. However, the most significant changes are seen in the surface areas. A distinct surface scale of orange crystals has formed over an extensive subscale zone of some 100μm of matrix, which is totally depleted in orange precipitates. This is indicative of the development of a composition gradient within the material, by the reaction of a Zr-species with gaseous N_2 from the external sinter gas, and subsequent diffusion of the mobile dissolved Zr-compound down the concentration gradient of the depleted surface layer. Also, within this zone the bulk Si_3N_4 phase retains its light grey colour.

Thus, for this particular sample composition and sintering conditions, the material stability changes at approximately 1650°C. At 1600°C, ZrO_2 released after decomposition of $CaZrO_3$, appears to dissolve in the local liquid phases, remain in solution and to reprecipitate partially on cooling as a mixed nitride and oxide. The low precipitate volume fraction observed in the sample sintered at 1600°C, suggests that the majority of Zr remains in the bulk phase. The high mobility of the Zr-phase seen in the large subscale depleted zone of the 1700°C sintered material indicates that the dissolved species are well distributed in the 1600°C and 1650°C sintered material. However, here the precipitates are invariably small and well distributed with no indication of segregation and coarsening so that they are most probably precipitated during the final cooling stage.

After sintering at temperatures ≥1700°C, a significant change in the bulk Si_3N_4 matrix remote from the surface zone coincides with a general formation of more coarse Zr-O-N precipitate. The requirement for increased free nitrogen suggests that the observed colour change in Si_3N_4 is associated with a change in its stoichometry (possibly the start of decomposition), releasing nitrogen for reaction with the Zr-phase. This speculation is supported by the retention of the normal Si_3N_4 light grey morphology in the high nitrogen content zone of the subscale region, which will inhibit decomposition. Concurrently, reaction between the dissolved Zr-phase and external N_2 is favoured, resulting in the formation of large amounts of a Zr-O-N scale and segregation of the mobile Zr-phase to the surface, as occurs in functionally gradient materials.

Thus there appears to be significant dissolution of ZrO_2 into the liquid phase at temperatures ≥1700°C, which will have some effect on the sintering behaviour and crystallinity of the grain boundaries of the present material. However, of greatest importance in the present study is the sintering behaviour at lower temperatures, which is clearly independent of ZrO_2.

TEM Analysis

To further examine the different characteristics observed using optical microscopy between the surface and the centre of the 3.2CaZ material sintered at 1750°C, Transmission Electron Microscopy (TEM) was carried out. Also in situ EDX analysis on five selected areas within each phase detected was carried out. Thin foil samples were prepared from a region as close to the sample surface as possible, and also from a region in the centre of the material.

The microstructure of the Si_3N_4 grains in the surface and the centre was similar, consisting of predominantly prismatic/hexagonal β-Si_3N_4 grains (Figure 4.32).

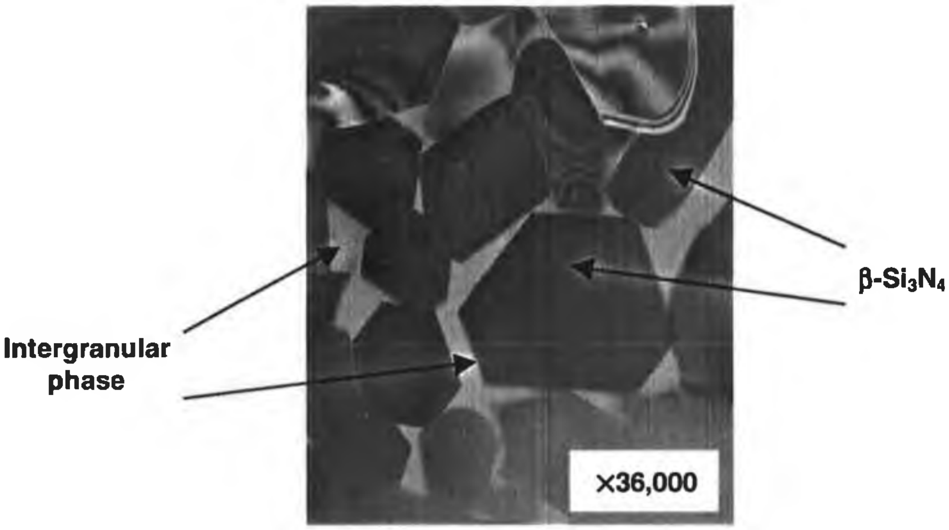

Figure 4.32 Overall microstructure observed in the CaZ sample.

However a difference in the nature of intergranular phases formed and their compositions was observed. In the foil taken from the material's surface, a glassy phase and two types of crystalline intergranular (secondary) phases were detected. Comparing Figure 4.33 (a) and (b), which illustrate dark field and bright field images respectively, the glassy phase is that phase which has fixed contrast in both fields. Using semi-quantitative EDX analysis (Figure 4.34 illustrates an example area), the glassy phase was determined to be homogenous to within ±1 atomic percent, containing N, O, Al, Si, Y, Ca, Zr (27.7, 40.2, 9.2, 14, 4.6, 3.3 and 1 atomic % respectively).

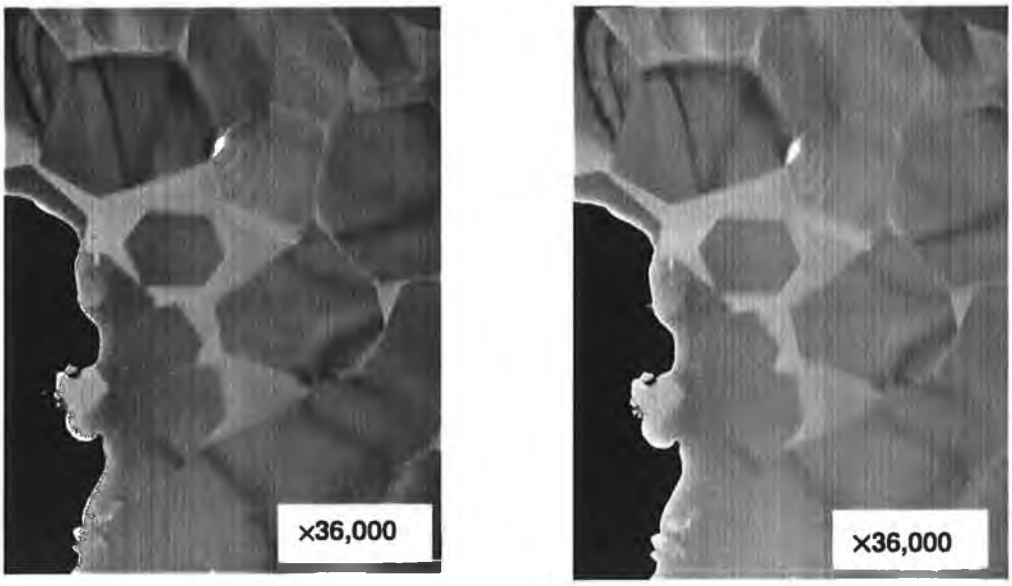

Figure 4.33 (a-b) Typical dark and bright field images observed in the region close to the surface of the CaZ sample analysed.

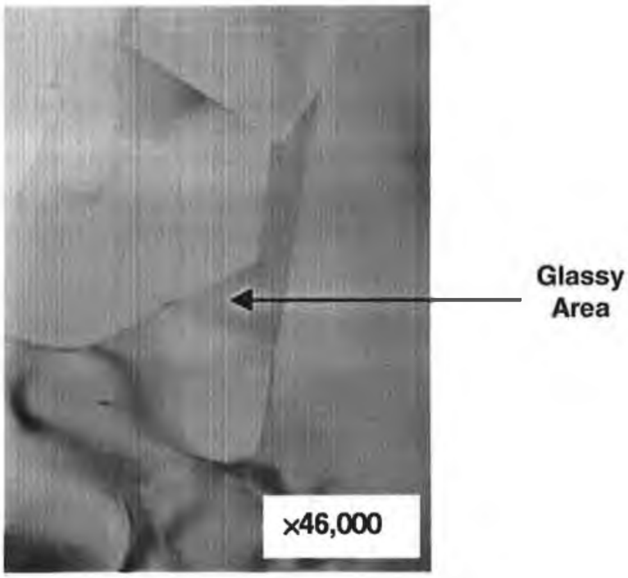

Figure 4.34 Example glassy area selected for EDX analysis.

One of the two types of crystalline phases was seen to be more dense and to have a irregular shape, and to be rich in zirconium (Figure 4.35 shows two examples of this phase). Its composition, in atomic percent (at%), was determined to contain within ±1 atomic percent, 17at%N, 15at%O, 2.5at%Al, 9.7at%Si, 1.1at%Y, 1at%Ca and 53.7at%Zr.

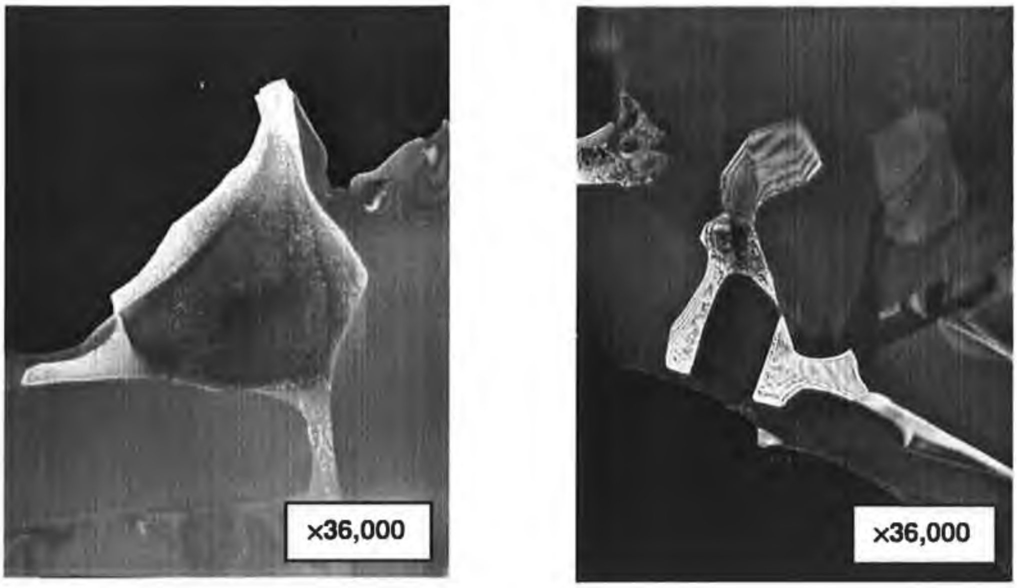

Figure 4.35 Examples of the Zr-rich crystalline phase detected in the region close to the surface of the CaZ material.

Figure 4.36 illustrates a typical area of the second, less dense, crystalline phase detected. This phase was determined to contain a significantly lower concentration of zirconium, just 0.2at% (compared to 53.7at% detected in the crystalline phase described above) and to consist also of N, O, Al, Si, Y, Ca (24, 44.3, 1.2, 14.5 12.8, and 3.1 atomic % respectively).

Figure 4.36 Typical area of the second type of crystalline phase detected in the region close to the surface of the CaZ material.

A glassy intergranular phase and only one crystalline phase were detected in the foil taken from the centre of the sample. The glassy phase was determined to contain N, O, Al, Si, Y, Ca, Zr (31.9, 37.8, 6.5, 15, 4.7, 3.4, and 0.6 atomic % respectively, homogeneous to within ±1 at%), Figure 4.37 sows an example of an area selected for EDX analysis.

Figure 4.37 Example of the glassy phase (X) detected in the centre of the CaZ sample.

The crystalline phase detected was similar to the Zr-rich crystalline phase found in the surface, in that it had a composition with a high Zr concentration, had a high density and an irregular shape, which indeed was even more pronounced (Figure 4.38). Its composition was determined to consist of 14.5at%N, 8.7at%O, 1at%Al, 7.3at%Si, 1.4at%Y, 1.4at%Ca and 65.9at%Zr.

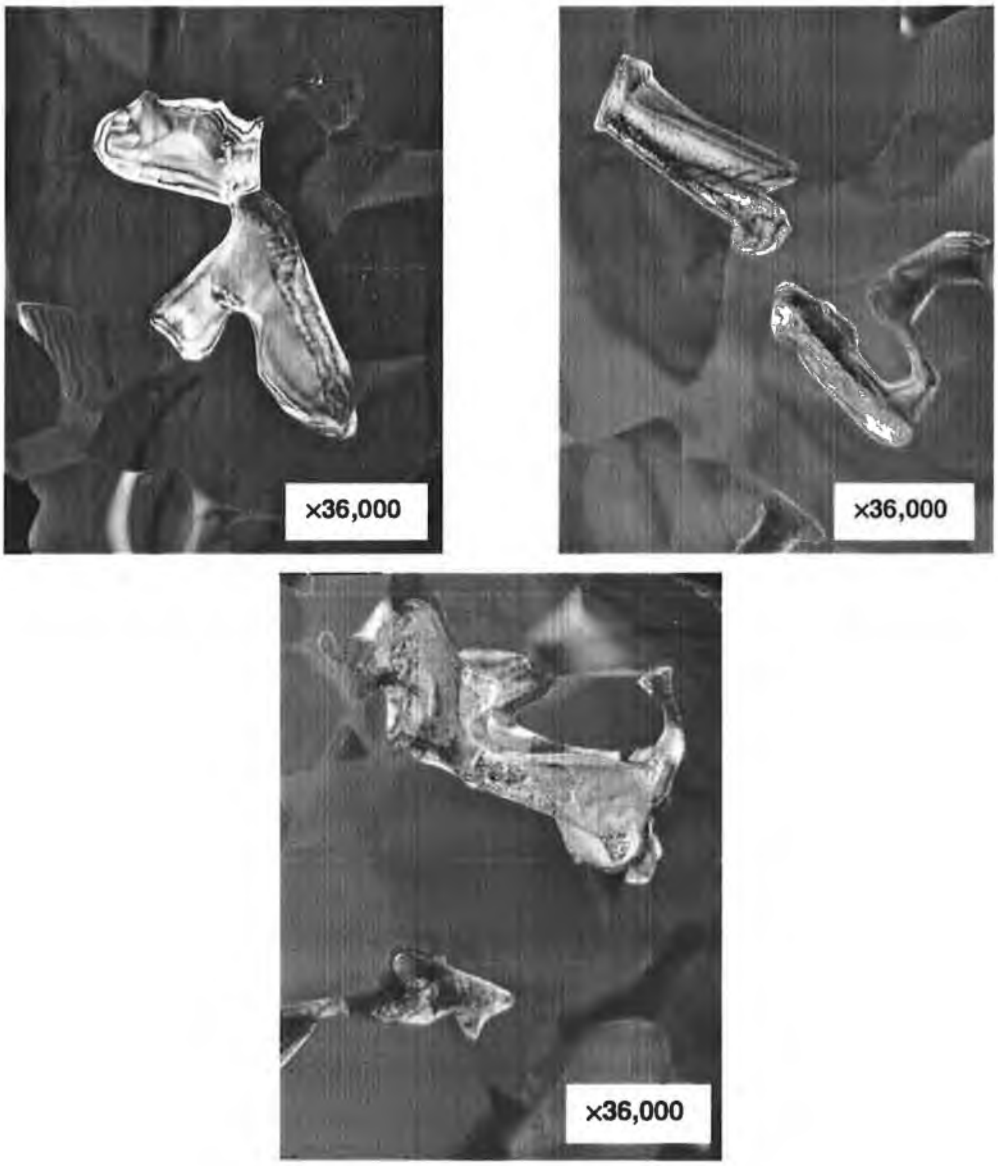

Figure 4.38 Examples of the irregular shaped, Zr-rich crystalline phases detected in the centre of the CaZ sample.

4.5. Hardness

4.5.1. Introduction

Vickers Hardness (HV5) was calculated using the standard equation,

$$HV = \frac{1.8544F}{d^2} \qquad 4.5$$

where,
F = the indentation load (kg)
d = the average indentation diagonal (mm)

Resulting hardness values are expressed in kgf/mm^2. 5-10 indentations were made for each specimen and the error of measurement was estimated in terms of standard deviation from the mean.

Section 2.5.1.1 outlines the factors that govern the hardness of these materials including grain size, porosity, amount of residual α-Si_3N_4 present, and the load used. The effect of the load was removed by using a standard 5kg load for all tests and the variation of grain size between the samples is assumed to be minimal as discussed and illustrated in Section 4.4.2.6 and Section 4.4.3.6. Therefore, apart from composition, the factors that may be responsible for variations in hardness in the present materials are the degree of densification and residual α-Si_3N_4 content.

4.5.2. $Si_3N_4 + Y_2O_3 + Al_2O_3 + AlN$ Series

Table 4.12 contains data on sample label, percentage theoretical density (%TD), phase content (% residual α-Si_3N_4, and crystalline phases) and Vickers hardness values under 5kg load (HV5) for samples tested from the $Si_3N_4 + Y_2O_3 + Al_2O_3 +$

AlN series and the reference material. These particular samples of (0-4) AlN., were chosen as they have similar densities, in an attempt to minimise the influence of porosity on hardness (as outlined in Section 2.5.1.1), so that the effect of composition and residual α-Si_3N_4 could be observed. It is recognised that the sample of the reference material tested has a lower density than desired, however this was the only sample of this material remaining and is taken into consideration in the discussion of the results.

Sample Composition Label	**%TD**	**HV5** ***(standard deviation)***	**%Residual α-Si_3N_4 ($\alpha/\alpha+\beta$).100**	**Crystalline Phases** *(Trace amounts)*
4AlN	98.3	1715.15 *(43.43)*	21	Y_2O_3
3AlN	98.1	1557 *(71.77)*	5	Y_2O_3
2AlN	98.2	1451.65 *(73.78)*	0	-
1AlN	98.7	1633.76 *(56.65)*	0	-
REF	94	1495.56 *(30.04)*	14	YAG

Table 4.12 Percentage theoretical density (%TD), Vickers hardness, and XRD data for the tested materials.

Figure 4.39 illustrates the variation of hardness with sample composition for the Si_3N_4-Y_2O_3-Al_2O_3-AlN series of samples and the reference material. Within error limits the difference in hardness in the samples is not great. The plot does seem to suggest that, with the exception of the sample with composition 2AlN, the addition of AlN to the Si_3N_4-Y_2O_3-Al_2O_3 system slightly improves the hardness of the Si_3N_4 material. For example, samples with compositions 1AlN and 4AlN have a HV5 value of 1634 and 1712 respectively, compared with a HV5 value of 1496 of the reference material. Also the hardness of the samples with compositions 0AlN and 2AlN lie in the lower range of the hardness values measured within the 0-4AlN composition series.

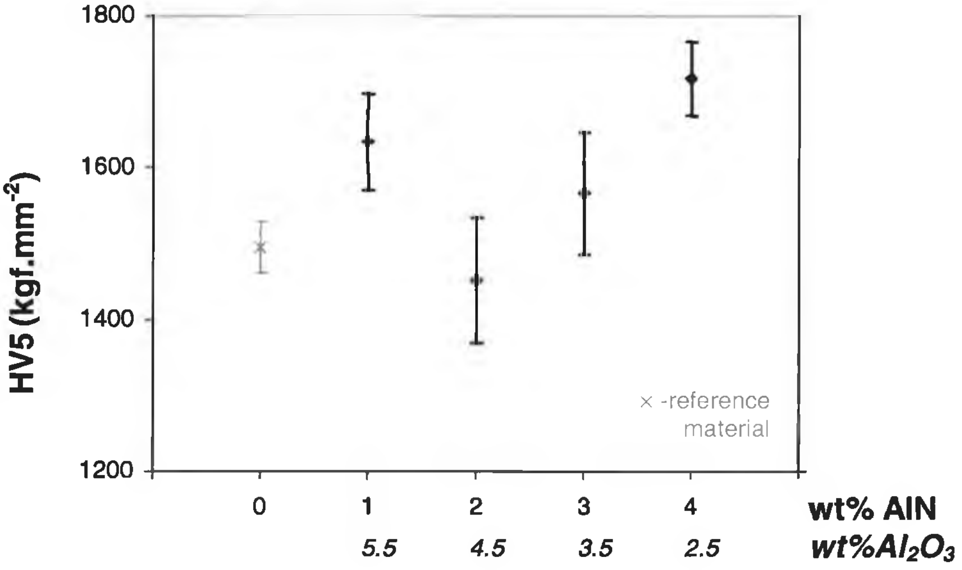

Figure 4.39 Variation of hardness with sample composition for samples in the Si_3N_4-Y_2O_3-Al_2O_3-AlN series and the reference material.

Figure 4.40 illustrates the variation of hardness with composition against the %TD of the samples. As expected, the slight variation in the %TDs of the 0-4AlN samples is not significant enough to directly influence their hardness values, Figure 4.2. As mentioned above, the reference sample tested had a lower density than desired for true comparison of hardness values and it can be seen in Figure 4.40, the high porosity of the reference material reduces it hardness value.

The influence of percentage residual α-Si_3N_4 on the hardness of the materials is illustrated in Figure 4.41. A general trend of increasing hardness with percent residual α-Si_3N_4 is observed going from 2AlN, with 0% residual α-Si_3N_4 (HV5 = 1451.65) to 4AlN, with the highest % residual α-Si_3N_4 content, having the highest hardness; HV5 = 1715.15. One exception to this trend is the 1AlN sample, which has a high hardness but with 0% residual α-Si_3N_4. Also the reference material has a high percentage of residual α-Si_3N_4 but low hardness.

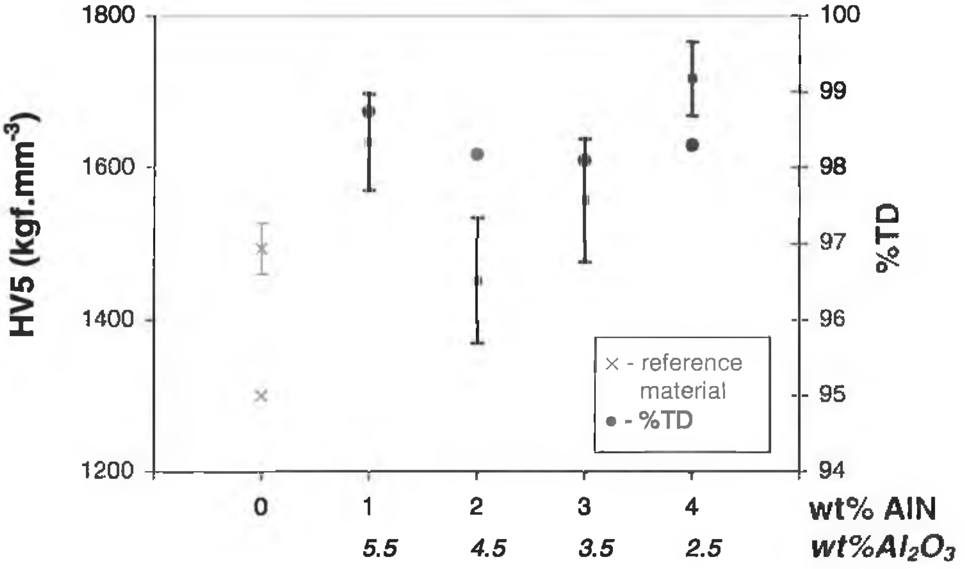

Figure 4.40 Influence of sample compositions on the resulting hardness and on the %TD for samples in the Si_3N_4-Y_2O_3-Al_2O_3-AlN series and the reference material.

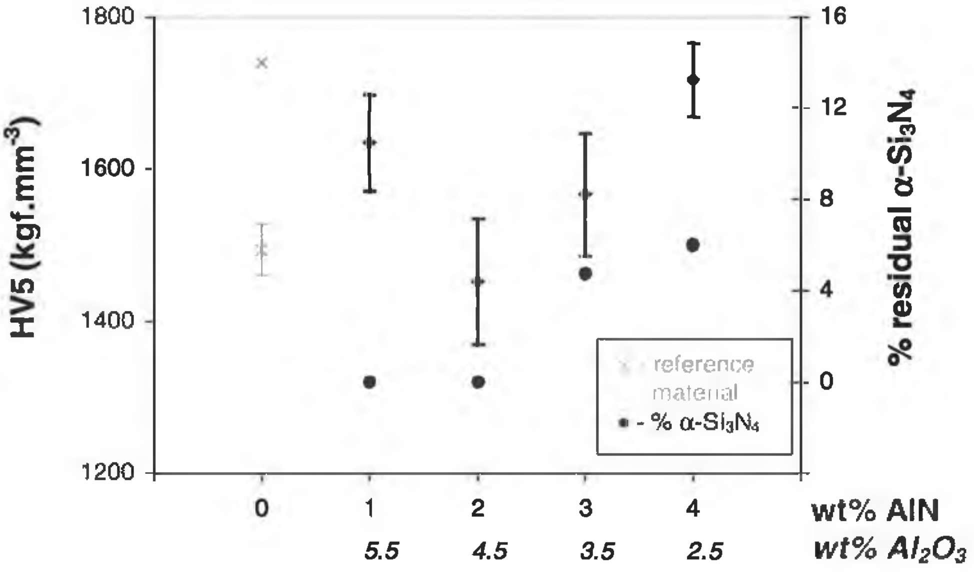

Figure 4.41 Influence of sample compositions on the resulting hardness and % residual α-Si_3N_4 for samples in the Si_3N_4-Y_2O_3-Al_2O_3-AlN series and the reference material.

An exact analysis of the Vickers hardness of complex materials, such as the Si_3N_4-based materials studied here is very difficult, as there is more than one contributing factor. The pronounced negative effect upon the hardness exerted by the presence of porosity, seen for the reference material, confirms the work carried out by many authors [140][218][219][220]. Since the sample has a high %residual α-Si_3N_4 content but low hardness it is most likely that the porosity effect overrides the other influences on its hardness. Therefore, it is most probable, that if a sample of the reference material with a sintered density close to the %TD of 1-4AlN samples was tested, it would have improved hardness over the sample in this testing series and might lie in the same range as the hardness values for the 1-4AlN samples measured here. When the influence of porosity was removed for the samples within the Si_3N_4-Y_2O_3-Al_2O_3-AlN series, the observed hardness values of samples with compositions 2-4wt%AlN, are seen to be directly dependent on the percent residual α-Si_3N_4 content. The high hardness of 1AlN cannot be explained on this basis however, as it has 0% residual α-Si_3N_4. It has just a slightly higher percentage theoretical density; ~0.4% higher than the other compositions which may increase its hardness slightly but since the difference is so small, this suggests that its chemical composition must be influencing its hardness. In Section 4.4.2.5 it was suggested that the excellent sinterability of the composition 1AlN was due to sintering additive phase combination resulting in the formation of α-, β-, or α/β-sialons as the intergranular phase. The high hardness of 1AlN, supports this speculation since sialons, in particular, α-sialons are known to have higher hardness than bulk Si_3N_4 materials [140].

4.5.3. $Si_3N_4 + Y_2O_3 + Al_2O_3 + CaZrO_3$ Series

Data on sample label, percentage theoretical density (%TD), phase content (%residual α-Si_3N_4 and crystalline phases) and Vickers hardness values under a 5kg load (HV5) with the percentage coefficient of variation, for samples tested from the $Si_3N_4 + Y_2O_3 + Al_2O_3$ +$CaZrO_3$ series, is listed in Table 4.13. As with the materials tested from the $Si_3N_4 + Y_2O_3 + Al_2O_3$ +AlN series, these specific samples from the CaZ series were tested as they were samples available (those remaining after microstructural analysis) with densities closest to each other. This should help to minimise the influence of porosity on the measured hardness, and thus the effect of composition and residual α-Si_3N_4 should be more easily observed. Again it is recognised that the reference material sample tested has a lower density than desired which is taken into account in the discussion of the results.

Sample Composition Label	**%TD**	**(HV5)** ***(standard deviation)***	**%Residual α-Si_3N_4 $(\alpha/\alpha+\beta)\times100$**	**Crystalline Phases** *(Trace Amounts)*
3.2CaZ	97.1	1468.17 *(47.41)*	29.47	ZrO_2(t)
4.8CaZ	96	1346.51 *(32.95)*	23.48	ZrO_2(t)
6.4CaZ	96	1338.41 *(35.41)*	14.6	ZrO_2(t)
REF	94	1495.56 *(30.04)*	14	YAG

Table 4.13 Percentage theoretical density (%TD), Vickers hardness, and XRD data for the tested materials.

The variation of hardness with sample composition for the Si_3N_4 + Y_2O_3 + Al_2O_3 +$CaZrO_3$ series of samples and the reference material tested is shown in Figure 4.42. Within error limits, the difference in hardness between the samples is not very great. It is clear from the plot, however, that the addition of increased amounts of $CaZrO_3$ to the Si_3N_4 + Y_2O_3 + Al_2O_3 system slightly decreases the hardness of the Si_3N_4-based material. For example, the hardness of the sample with composition 3.2CaZ (HV5 1468) compares well with the reference material (HV5 1496), while samples with compositions 4.8CaZ and 6.4CaZ have hardness values of 1347 and 1338 respectively.

Figure 4.43 shows the variation of hardness with composition against the %TD of the samples. The slight variation in %TD of the 3.2-6.4CaZ samples is reflected to some extent in their hardness values. The sample with the highest density, 3.2CaZ, has the highest hardness value while the increased level of porosity in samples 4.8CaZ and 6.4CaZ results in lower hardness values. This is not unexpected, since, as was explained in Section 2.5.1.1, the hardness is strongly dependent on the sample density. What is surprising however, is that the reference material, with a lower %TD, relative to the samples in the CaZ series, has a higher hardness value.

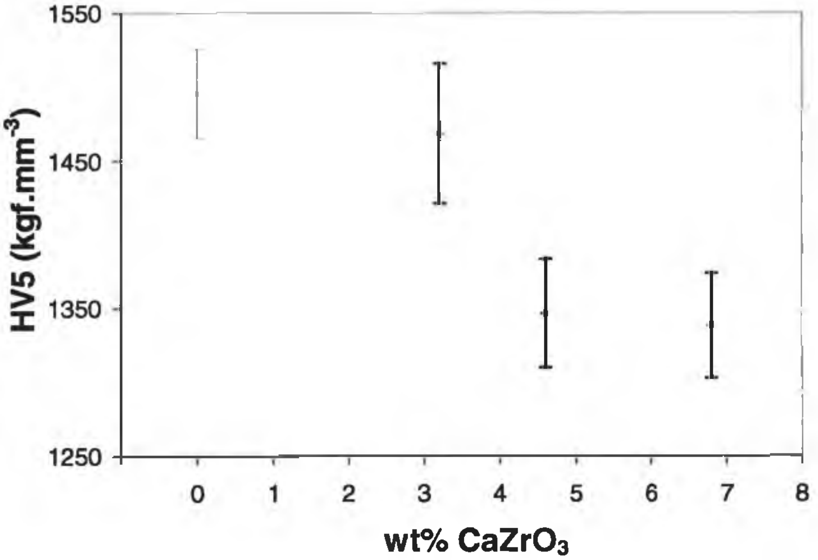

Figure 4.42 Variation of hardness with sample composition for samples in the Si_3N_4-Y_2O_3-Al_2O_3-$CaZrO_3$ series and the reference material.

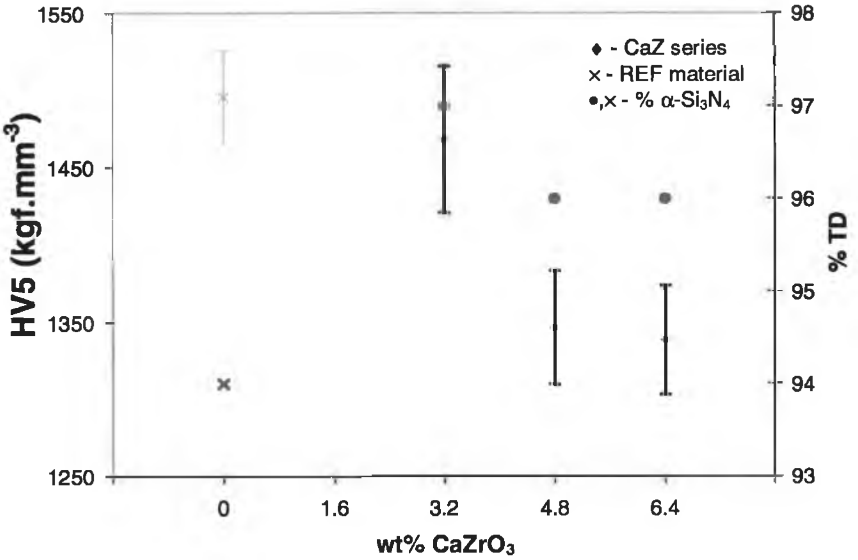

Figure 4.43 Influence of sample compositions on the resulting hardness and on the %TD for samples in the Si_3N_4-Y_2O_3-Al_2O_3-$CaZrO_3$ series and the reference material.

Figure 4.44 illustrates the influence of percent residual α-Si_3N_4 on the hardness of the tested materials. Within the CaZ series, a general increase in the percent residual α-Si_3N_4 results in an increase in the hardness values measured. Going from 6.4CaZ with 14.6% residual α-Si_3N_4 content (HV5 = 1338) to 3.2CaZ with the highest residual α-Si_3N_4 content, having the highest hardness value; HV5 = 1468. Again comparing these results for the CaZ series with the reference material leads to an unexpected result, as the residual α-Si_3N_4 content in the reference material is low, similar to that in the 6.4CaZ sample, but has a much higher hardness value.

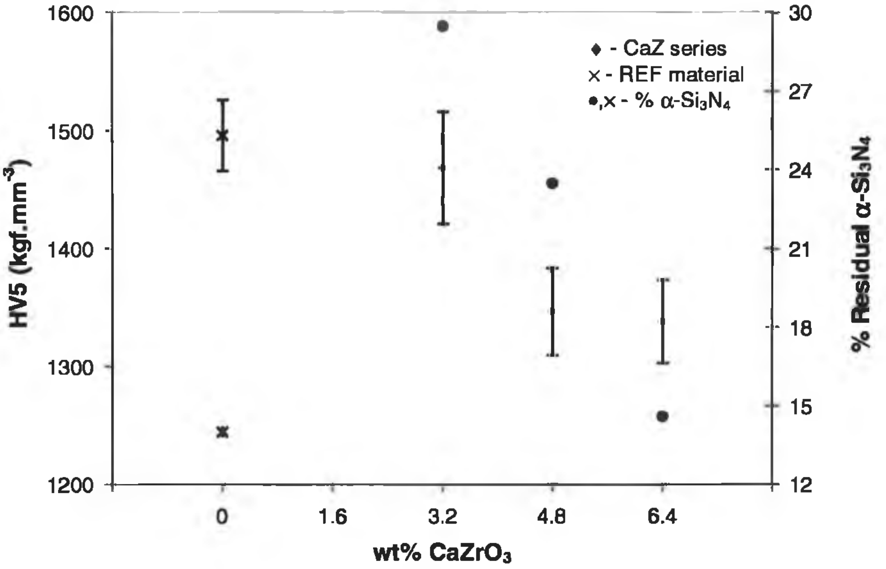

Figure 4.44 Influence of sample compositions on the resulting hardness and % residual α-Si_3N_4 for samples in the Si_3N_4-Y_2O_3-Al_2O_3-$CaZrO_3$ series and the reference material.

As with the AlN series of materials, there are a number of contributing factors in the complex Si_3N_4-Y_2O_3-Al_2O_3-$CaZrO_3$ based materials studied here, an exact analysis of Vickers hardness values is very difficult (as was outlined in Section.2.5.1.1 and Section 4.5.2) [140][218][219][220]. In the comparison of the samples within the CaZ series and the reference material the chemical composition seems to have the strongest influence on the resulting hardness values, as the reference sample tested had lower theoretical density and percent residual α-Si_3N_4. The addition of $CaZrO_3$ to the Y-Si-Al-O-N system is therefore considered to have a slightly negative effect on hardness. However, Ca α-sialons, formed by the substitution of CaO to the Si-Al-O-N (possibly occurred in the intergranular phases of the present series of materials, Section 4.4.3.6) are reported to have enhanced hardness over other Si_3N_4-based materials. The poorer hardness of the materials in the present series is thus thought to be due to the presence of zirconia, detected by XRD, in each of the samples tested, see Table 4.11, as it has a fairly low hardness, approximately 970-1070 (HV10) [140]. It is not surprising, therefore, that as the amount of ZrO_2 (added in the form of $CaZrO_3$) is increased slightly within the CaZ series, the resulting hardness decreases slightly, Figure 4.43. This observation corresponds well with the work carried by other researchers [165] [221], who observed that the measured hardness of bulk Si_3N_4-ZrO_2 composites decreased with increasing amounts of ZrO_2 added. It is most likely, however, that the increase in ZrO_2 content alone is not wholly responsible for the observed progressive decrease in hardness in going from sample 3.2CaZ to 4.8CaZ to 6.4CaZ. As was shown in Figure 4.43 and Figure 4.44, a decrease in both percent theoretical density and percent residual α-Si_3N_4 also occurs within the CaZ series, which most definitely contribute to the observed decrease in HV5 values.

4.5.3.1. *Effect of Percentage Density on Hardness*

The data presented in Table 4.14 shows that the hardness measured under a 5kg load, increases with increasing percentage theoretical density for a given composition. For example, sample 3.2CaZ sintered at 1400°C with 66%TD has a HV5 value of 463.8, whereas sample 3.2CaZ sintered at 1750°C with almost full density (98.2%TD), has a HV5 value of 1532.2. Mukhopadhyay et al [219], in defining a quantitative relationship between density and microhardness for Si_3N_4 and Sialon ceramics, found equation 4.2 best described their data.

$$H = [0.19\exp(4.49D)] \pm 0.55(GPa) \qquad \mathbf{4.6}$$

The applicability of Equation 4.6 to the present data is illustrated in Figure 4.45. It is seen that the equation fits quite well to the experimental data and therefore could be used to predict hardness close to actual experimental data on the basis of theoretical density only, for similar Si_3N_4-based materials.

Sample Composition Label *(Sintered Temperature)*	**%TD**	**Vickers Hardness (HV5)**
3.2CaZ*(1400)*	66	463.79 (20.85)
3.2CaZ*(1500)*	82.5	1076.83 (16.06)
3.2CaZ*(1600)*	97.1	1468.17 (47.41)
3.2CaZ*(1750)*	98.2	1532.15 (49.93)

Table 4.14 Percentage theoretical density (%TD), Vickers hardness data for the tested materials.

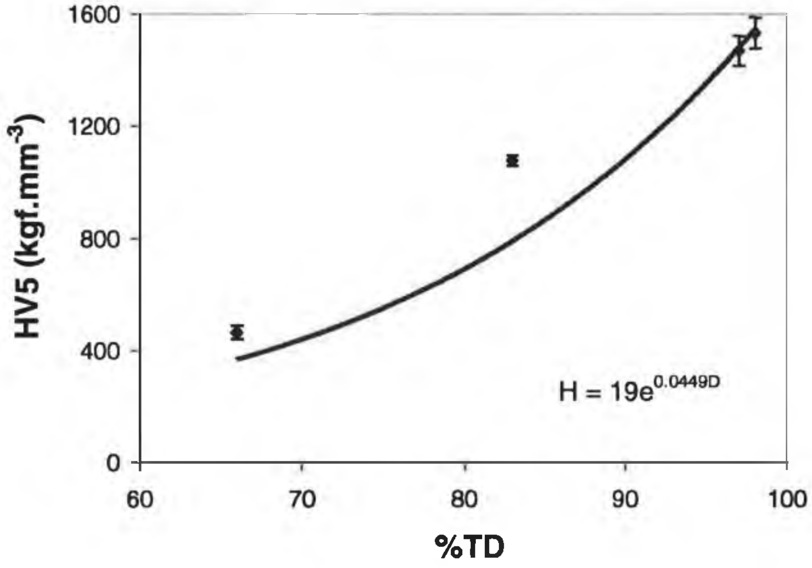

Figure 4.45 Relationship between percentage theoretical density and Vickers hardness of samples with composition Si_3N_4 + 3.4wt%Y_2O_3 + 3.4wt%Al_2O_3 + 3.2wt%$CaZrO_3$.

4.5.4. Comparison of the Materials Studied here with Published Data

Table 4.15 outlines a comparison between the Vickers hardness, HV2, of fully dense Si_3N_4-based materials observed by Chakraborty and co-workers. [135] and the HV5 values measured in the present study. Although the difference in loads used for testing does not allow for a direct comparison [221], the values indicate that the hardness of the materials tested in this study fit well to those tested by Chakraborty et al.

Sample Composition	Hardness HV2
Chakraborty	
β-Si_3N_4 + YAG	1630
α-Si_3N_4 + β-Si_3N_4 + YAG	1745
α-SiAlON	2261
β-SiAlON	1686
Present Study	**Hardness HV5**
1AlN	1634
2AlN	1452
3AlN	1557
4AlN	1712
3.2Caz	1468
4.8CaZ	1347
6.4CaZ	1338
REF	1496

Table 4.15 Comparative Vickers hardness values measured by Chakraborty and those measured in the present study.

4.6. Fracture Toughness

4.6.1. Calculations

Several expressions to calculate the fracture toughness, the critical stress intensity factor, K_{Ic}, from indentation tests exist, as outlined in Section 3.6.2. The choice of which one to employ depends primarily on the type of crack formed. Serial polishing of the surfaces of the materials tested in this study has shown that the cracks are Palmqvist type in all cases, as shown in Figure 4.46, where the crack end is not touching the indentation diagonal. Further polishing of the surfaces revealed however, that the cracks are much deeper than the classically presented Palmqvist shape as shown in Figure 4.47, where the indentation has been completely polished away but the cracks are still present. This suggests that the crack type may fall between Palmqvist and median, agreeing with observations made on similar Si_3N_4-based ceramics [223][224].

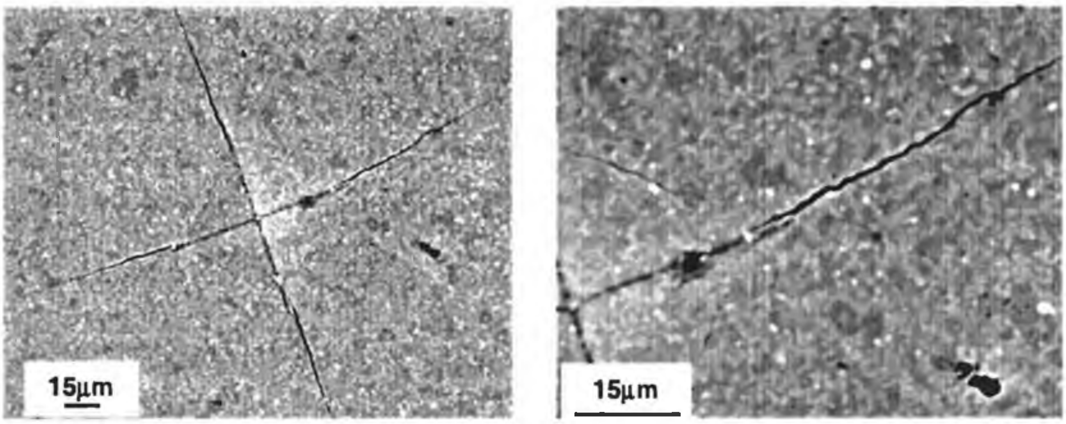

Figure 4.46 Typical indentation observed in the samples tested (a) and at higher magnification (b) showing the crack tip detached from the indentation diagonal.

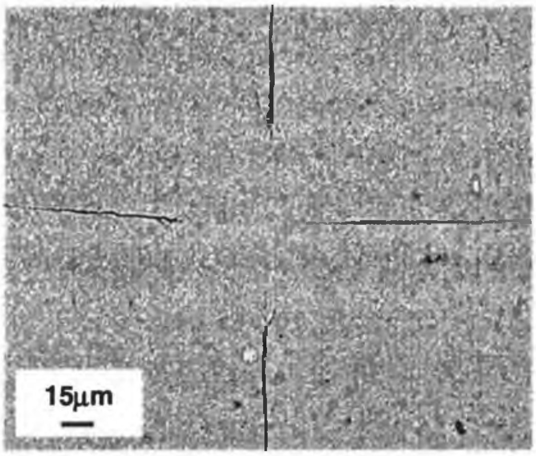

Figure 4.47 Typical observation where the diamond indentation has been completely removed by serial polishing, showing that the cracks are deeper than the indentation but do not link to form median cracks.

Table 4.16 lists a selection of equations proposed in the literature for the analysis of Vickers indentation fracture measurements. The equations are divided into two groups; those based on the median crack geometry, M and those based on the Palmqvist crack geometry, P. K_{Ic} values for each sample composition were then calculated from these equations, when applied to the data obtained from the Vickers hardness testing.

Reference	Designation	Equation
Anstis et al. [225]	AN/M	$K_{Ic} = 0.016(E/H_v)^{1/2}(P/c^{3/2})$
Niihara et al. [226]	NI/M	$K_{Ic} = 0.0309(E/H_v)^{2/5}(P/c^{3/2})$
Laugier [227]	LA/P	$K_{Ic} = 0.015(E/H_v)^{2/3}(P/c^{3/2})(a/l)^{1/2}$
Niihara [228]	NI2/P	$K_{Ic} = 0.0122(E/H_v)^{2/5}P/(al^{1/2})$
Shetty et al. [229]	SH/P	$K_{Ic} = 0.031P/(al^{1/2})$

Table 4.16 List of equations presented in literature for the analysis of Vickers indentation fracture tests.

E – Young's Modulus (GPa)
H_v – Vicker's Hardness (GPa)
P – Load (N)
c – crack length from the center of indent to the crack tip (m)
l – crack length from the corner of the indent of the indent to the crack tip (m)
a – indent radius (m).

Table 4.18 and Table 4.20 outlines the K_{1c} values for the AlN series and CaZ series of compositions respectively, calculated from the fracture measurements listed in Table 4.17 and Table 4.19.

Sample Composition Label	a (× 10^{-5}m)	c (× 10^{-5}m)	l (× 10^{-5}m)	H_v (GPa)
1AlN	3.68	8.58	4.9	16.85
2AlN	4	8.25	4.25	14.4
3AlN	3.85	8.35	4.5	15.36
4AlN	3.68	9.33	5.65	16.85
REF	3.94	8.14	4.2	14.67

Table 4.17 Indentation fracture measurement results for sample compositions in the Si_3N_4-Y_2O_3-Al_2O_3-AlN series and for the reference material.

Sample Composition Label	K_{1c} (MPa.$m^{1/2}$)				
Equation	**AN**	**NI1**	**LA**	**NI2**	**SH**
1AlN	4.17±0.08	6.03±0.09	5.47±0.14	7.35±0.11	6.08±0.21
2AlN	4.80±0.14	6.83±0.16	7.21±0.28	7.76±0.18	6.00±0.26
3AlN	4.54±0.11	6.51±0.13	7.59±0.15	7.60±0.15	6.05±0.15
4AlN	3.67±0.05	5.32±0.06	4.49±0.09	6.84±0.08	5.66±0.21
REF	4.83±0.05	6.90±0.06	7.25±0.11	7.83±0.07	6.13±0.21

Table 4.18 Fracture toughness, K_{1c}, values calculated for samples compositions in the Si_3N_4-Y_2O_3-Al_2O_3-AlN series and for the reference material.

Sample Composition Label	a ($\times 10^{-5}$m)	c ($\times 10^{-5}$m)	l ($\times 10^{-5}$m)	H_v (GPa)
3.2CaZ	3.98	8.48	4.5	14.4
4.8CaZ	4.15	8.73	4.576	13.21
6.4CaZ	4.16	8.81	4.65	13.13
REF	3.94	8.14	4.2	14.67

Table 4.19 Indentation fracture measurement results for sample compositions in the Si_3N_4-Y_2O_3-Al_2O_3-$CaZrO_3$ series and for the reference material.

Sample Composition Label	K_{1c} (MPa.m$^{1/2}$)				
Equation	**AN**	**NI1**	**LA**	**NI2**	**SH**
3.2CaZ	4.58±0.08	6.47±0.09	6.71±0.16	7.55±0.11	5.60±0.18
4.8CaZ	4.59±0.06	6.49±0.07	7.11±0.13	7.82±0.08	5.62±0.16
6.4CaZ	4.60±0.07	6.54±0.07	7.14±0.13	7.83±0.08	5.79±0.18
REF	4.83±0.05	6.90±0.06	7.25±0.11	7.83±0.07	6.13±0.21

Table 4.20 Fracture toughness, K_{1c}, values calculated for samples compositions in the Si_3N_4-Y_2O_3-Al_2O_3-$CaZrO_3$ series and for the reference material.

The K_{1c} values calculated using the selection of equations differ considerably. The Anstis equation is likely to result in an underestimation of the materials' fracture toughness, as it is a model for materials more brittle than those studied here, which form classic median indentation cracks, while relations for true Palmqvist cracks, Laugier and Niihara2, result in somewhat higher values than expected. Following the observations made above on the crack profiles, it is most probable that the actual K_{1c} values for the present materials lie between the values calculated using Niihara1 for median cracks and Shetty for Palmqvist cracks. This is supported by work carried out by Duszca [224] who compared K_{1c} values measured by the indentation method to those measured from bending tests of single edge notched beams (SENB) for a Si_3N_4 + Si_3N_4 - whisker system and found that the Niihara1 and Shetty equations resulted in K_{1c} values closest to those measured by SENB method. The fracture toughness values calculated using the Shetty equation were selected for discussion, as the equation does not include the Young's Modulus, E, of the material, which for the present series of material is an estimate value.

4.6.2. $Si_3N_4 + Y_2O_3 + Al_2O_3 + AlN$ Series

Figure 4.48 illustrates the variation of K_{1c} values with composition for samples in the Si_3N_4-Y_2O_3-Al_2O_3-AlN series and the reference material. Samples with compositions 1-3AlN are seen to have very similar fracture toughness values; 6.08, 6.05 and 6.05 respectively. Although the reference material has a lower theoretical density (as mentioned above), it has a good fracture toughness value of 6.13, slightly higher than samples 1-3AlN. A significant decrease in fracture toughness is observed for the sample with composition 4AlN.

As outlined in Section 2.5.1.2, the fracture toughness of monolithic Si_3N_4 ceramics is reported in the literature to be mainly governed by the morphology of the Si_3N_4-matrix grains, that is, the grain diameter and aspect ratio of the grains [149]. As was explained in Section 4.4.2.6. although different sintering additive combinations were employed, the samples used in the present study (sintered at 1600°C) exhibit similar fine-grained microstructures, which might be considered unfavourable for fracture toughness. However, the K_{1c} values calculated here compare well to those calculated for similar systems (4-7 $MPa.m^{1/2}$ [223]). The observed fracture toughness values may be attributed to the compositions of the grain boundary phases present in the sintered materials [150] [152], which are controlled by the starting compositions. Differences in the thermal expansion coefficients of the Si_3N_4 matrix phase and the surrounding grain boundary phase introduce residual stresses in the material, which as reported by Peterson et al. [151] influence crack deflection around the Si_3N_4 grains. The fracture toughness is improved if tensile stress in the grain boundary phase and compressive stress in the silicon nitride grains are present [151], this occurs when the thermal expansion coefficient of the grain boundary phase is greater than that of the silicon nitride grains.

The high fracture toughness observed for the reference material, is most probably due therefore to the presence of YAG in the grain boundary as the thermal expansion coefficient of silicon nitride and YAG are 3.6 and 8.0 respectively. Although measurement of the thermal expansion coefficients of the grain boundary phases of the materials in the Si_3N_4-Y_2O_3-Al_2O_3-AlN was beyond the scope of the present study, the variation in their fracture toughness can be explained qualitatively. It is reasonable to correlate the good fracture toughness observed to differences in the thermal expansion coefficients of the Si_3N_4 matrix grains and the grain boundary phases present in the sintered materials. The similarity in K_{1c} values calculated for samples 1-3AlN in the Si_3N_4-Y_2O_3-Al_2O_3-AlN series suggests varying the AlN: Al_2O_3 within this range, does not result in a significant alteration in the thermal expansion coefficient of the grain boundary phase in the sintered materials. On increasing the AlN: Al_2O_3 ratio to 4AlN: 2.5Al_2O_3 (sample 4AlN) a significant decrease in fracture toughness is observed (Figure 4.48). This result corresponds well to work carried by Peterson et al. [150] and Kleebe et al. [152] who reported that increasing the nitrogen content of the grain boundary phase in a Si_3N_4-based ceramic decreased the thermal expansion coefficient of the phase, resulting in poorer fracture toughness.

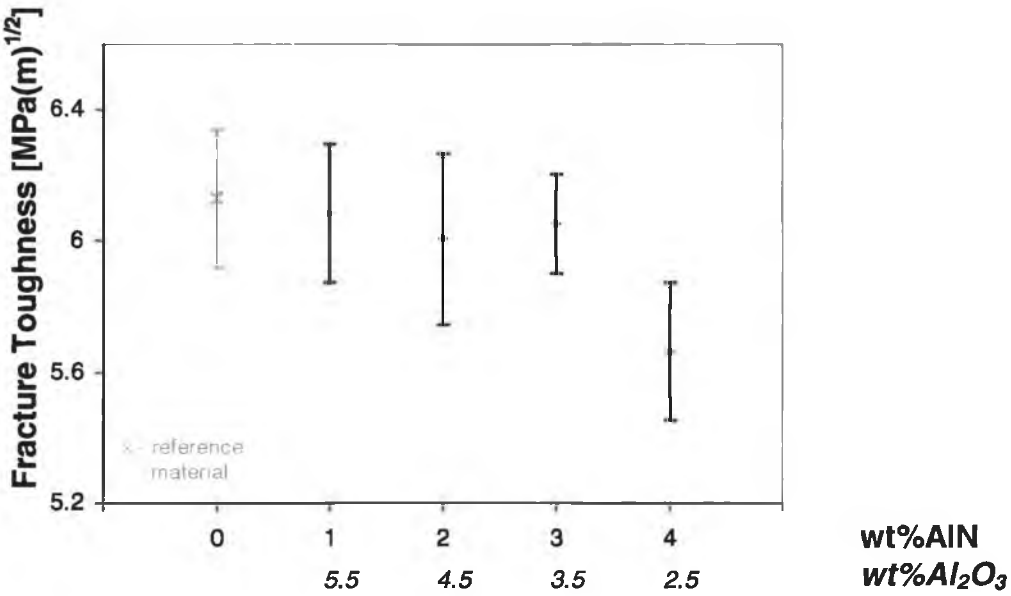

Figure 4.48 Relationship between fracture toughness (K_{1c}) and composition for samples in the Si_3N_4-Y_2O_3-Al_2O_3-AlN and the reference material.

4.6.3. Si_3N_4 + Y_2O_3 + Al_2O_3 +$CaZrO_3$ Series

The variation of K_{IC} values with composition for samples in the Si_3N_4-Y_2O_3-Al_2O_3-$CaZrO_3$ series and the reference material is shown in Figure 4.49. Within the CaZ series of materials, the sample with composition 6.4CaZ exhibits superior toughness; 5.79MPa.m$^{1/2}$. Very similar fracture toughness values were calculated for samples with compositions 3.2-4.8CaZ; 5.6 and 5.62 respectively. The reference material (although with higher porosity) has a slightly higher fracture toughness value, 6.13, than each composition within the CaZ series.

As was outlined for the AlN series, the morphology of Si_3N_4-matrix grains primarily governs the fracture toughness of monolithic Si_3N_4-based materials [149]. A study of the microstructure of the samples from the CaZ series tested here (Section 4.4.3.6), shows that although different combinations of sintering additives were employed, all samples had similar fine-grained microstructure, with the random distribution of small quantities of prismatic-shaped β-Si_3N_4 grains. The presence of such grains enhances the fracture toughness of a material by deflecting the crack path [147][148]. Indeed the fracture toughness of the present materials compares very well with those calculated for similar systems (4-7MPa$^{1/2}$) [223].

It is well documented that a suitable dispersion of tetragonal zirconia (t-ZrO_2) particles in composite materials improves fracture toughness by transformation toughening [7]. Thus the slight increase in K_{Ic} going from 3.2 to 4.8CaZ and the more significant increase observed in 6.4CaZ is not surprising and is probably due to the increased amount of ZrO_2.

The comparatively high fracture toughness value of the reference material was discussed in the previous section.

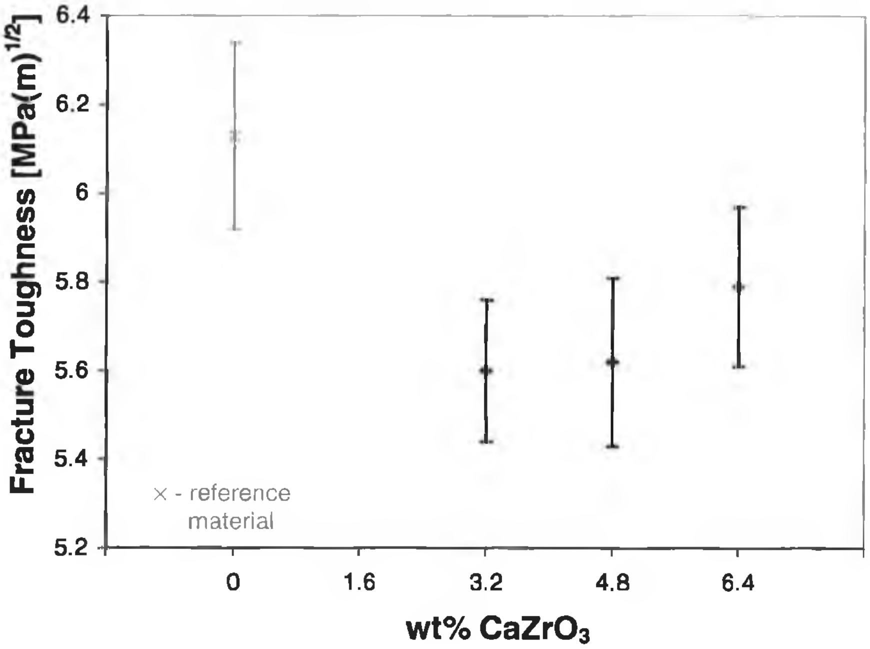

Figure 4.49 Relationship between fracture toughness (K_{Ic}) and compositions for samples in the Si_3N_4-Y_2O_3-Al_2O_3-$CaZrO_3$ and the reference material.

4.7. Oxidation Behaviour of the 3.2CaZ Material

4.7.1. Introduction

The addition of ZrO_2 (as $CaZrO_3$, in the current study) to the Y-Si-Al-O-N system introduces the potential formation of zirconium oxynitride (Zr-O-N) phases, which if present result in catastrophic degradation during oxidation at lowers temperatures; 600°C $\leq$ T $\leq$1000°C (discussed in Section 2.5.1.3) [163] [164]. Evidence in the literature suggests that the minimum wt% of ZrO_2 in the starting composition resulting in the formation of the easy-to-oxidise Zr-O-N phases is approximately 20wt% [163]. Although the weight percent (%wt) of ZrO_2 in the current CaZ series of materials (2.2wt%, 3.3wt%, 4.4wt%) is significantly lower than this value, and that no Zr-O-N phases were detectable by XRD in the sample tested (discussed in section 4.4.3.5) a preliminary set of oxidation tests was carried out, as even trace amounts of the phases have been reported to significantly lower the oxidation resistance of Si_3N_4-based materials. The material with composition 3.2CaZ (3.2wt%$CaZrO_3$ + 3.4wt%Y_2O_3 + 3.4wt%Al_2O_3) sintered at 1600°C, was selected for testing, as this material exhibited superior densification and so was chosen as a potential matrix for the fabrication of a pressureless sintered ceramic matrix composite.

4.7.2. Thermogravimetric Analysis

Figure 4.50 shows the mass gain detected with increasing temperature (at a constant heating rate of 2°C/min) for the sample with composition 3.2CaZ, sintered at 1600°C. No detectable oxidation occurs at temperatures <1000°C, suggesting that this sample does not contain any easy-to-oxidise zirconium oxynitride phases. Detectable mass gain is seen to start at >1100°C and slowly increases as the temperature is raised to approximately 1350°C. Above 1350°C, the mass gain detected increases rapidly.

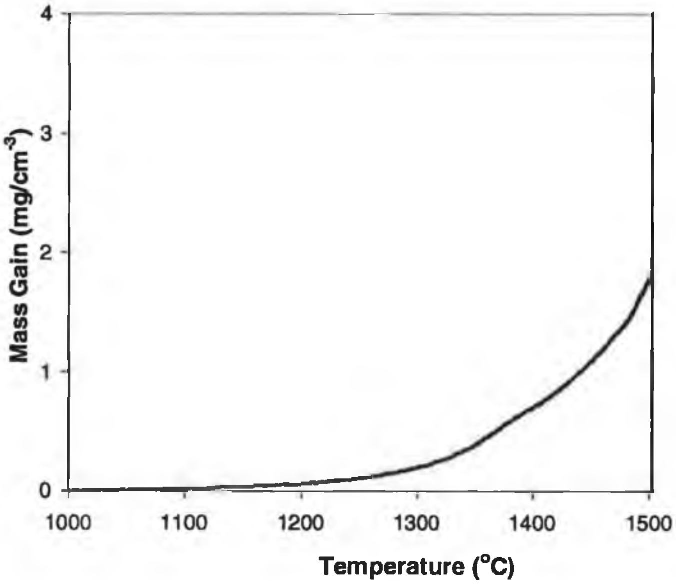

Figure 4.50 Thermogravimetric curve for sample 3.2CaZ, sintered at 1600°C, showing the mass gain detected with increasing temperatures.

4.7.3. Long and Short Term Tests

3.2CaZ samples (after sintering at 1600°C) were oxidised for 100 hours, at 600°C, 700°C, 800°C, 900°C and 1000°C. As mentioned above, this temperature range is that over which Zr-O-N phases, if present, result in catastrophic failure. No mass gains were detected at each temperature, and no oxidation products were detected using XRD. Both of these results support the hypothesis that no zirconium oxynitride phases are present in the 3.2CaZ material after sintering at 1600°C, and that the ceramic is stable to oxidation at lower temperatures.

Short-term oxidation tests (20 hours) at 1200°C, 1300°C and 1400°C were carried out to gain a basic understanding of the oxidation kinetics and mechanisms of the 3.2CaZ material. The mass gain versus time curves for the 3.2CaZ samples oxidised at the given temperatures are shown in Figure 4.51. Mass gain follows the classical parabolic relation:

$$\left(\frac{\Delta m}{S}\right)^2 = Kt + b \approx Kt \qquad \textbf{4.7}$$

where ($\Delta m/S$) = the mass gain ($g.m^{-2}$) at time, t, $K = K_0 \exp(\Delta H/RT)$ ($g^2.m-^4.s^{-1}$) is the parabolic rate constant and b is a constant which accounts for the effect of a non-parabolic initial stage, because initial oxidation occurs with the formation of an 'oxide' film by a 1st-order process, followed by diffusion-controlled parabolic growth. Figure 4.52 illustrates the parabolic behaviour at each oxidation temperature. Oxidation at 1200°C follows parabolic behaviour over the 20 hour hold time, while oxidation at 1300°C and 1400°C deviates from parabolic behaviour after limited time intervals; approximately 10 hours and 2.4 hours, respectively. Oxidation rate constants calculated using equation 4.1, for parabolic behaviour at each temperature are outlined in Table 4.21.

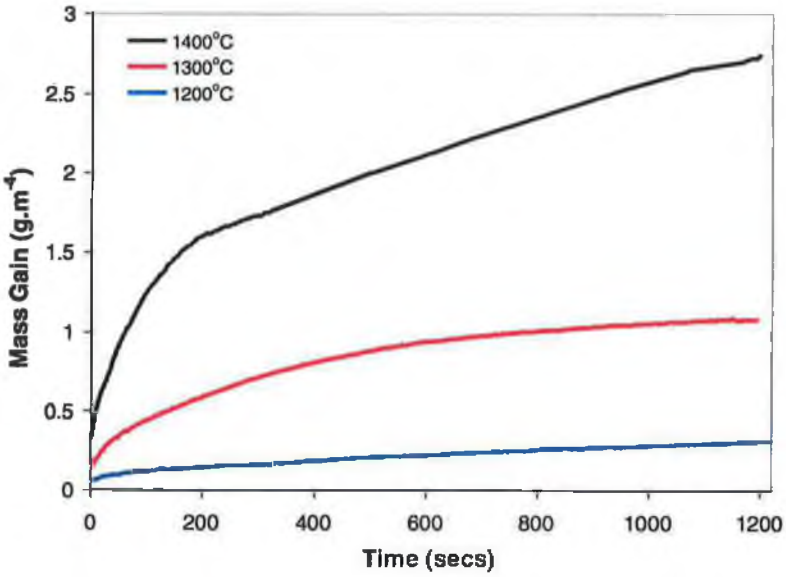

Figure 4.51 Mass gain for sample 3.2CaZ oxidised at various temperatures for a 20 hour hold time.

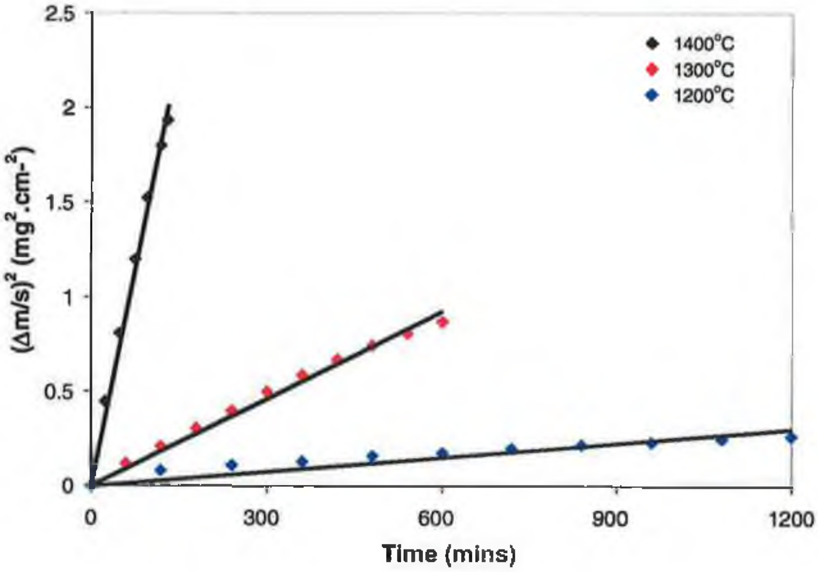

Figure 4.52 Parabolic mass gain for sample 3.2CaZ oxidised at various temperatures for a 20 hour hold time.

Oxidation Temperature (°C)	Oxidation rate constant (mg^2/cm^4.min)
1200	2.51×10^{-4}
1300	1.54×10^{-3}
1400	1.53×10^{-2}

Table 4.21 Values of the oxidation rate constant after oxidation for 20 hours at different temperatures.

4.7.4. Oxidation Products and Surface Morphology

Table 4.22 lists the crystalline phases, detected using XRD, in the samples after oxidation at each temperature. Figure 4.53 illustrates approximate semi-quantitative analysis of the XRD results. As expected, crystabolite, SiO_2, formed by the direct oxidation of Si_3N_4 was the principal oxidation product detected, with increasing amounts of calcium aluminium silicate, $Ca_3Si_2Al_6O_{16}$ detected with increasing oxidation temperature. Trace amounts ($I/I_0 \leq 5$) of zircon, $ZrSiO_2$ and calcium silicate, $CaSiO_4$ were detected after oxidising at 1300°C and 1400°C.

Oxidation Temperature (°C)	1200	1300	1400
Phases Detected	SiO_2 $Ca_3Si_2Al_6O_{16}$	SiO_2 $Ca_3Si_2Al_6O_{16}$ $CaSiO_4$ $ZrSiO_2$	SiO_2 $Ca_3Si_2Al_6O_{16}$ $CaSiO_4$ $ZrSiO_2$

Table 4.22 Crystalline phases detected in the samples after oxidation at the given temperatures.

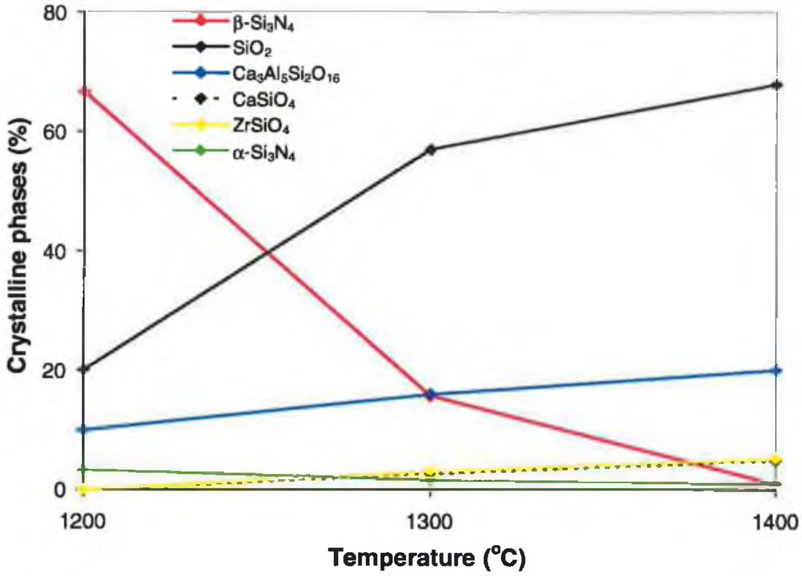

Figure 4.53 Development of crystalline phases in the samples after 20 hour hold at the outlined temperatures.

Although slightly out of focus, the formation of an oxide layer on the sample surface oxidised at 1400°C is shown in Figure 4.54 (a). Figure 4.54 (b) illustrates the development of an oxide layer in a crack formed from the surface towards the centre of the sample.

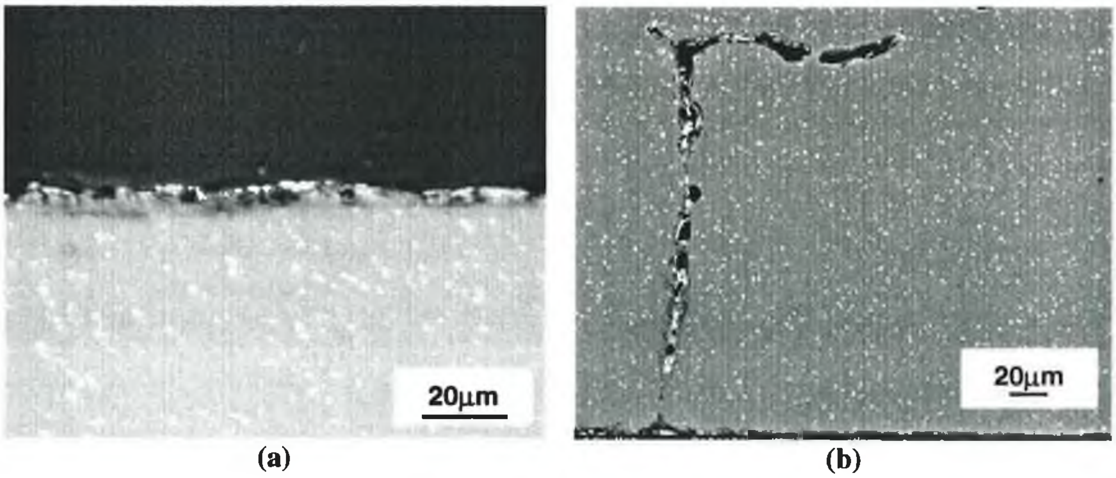

(a) (b)

Figure 4.54 (a-b) An oxide layer formed at the surface and in a crack of the sample oxidised at 1400°C, respectively.

4.7.5. Discussion on the Oxidation Mechanism

Although the oxidation tests carried out were limited, some conclusions can be made on the oxidation behaviour of the Si_3N_4-Y_2O_3-Al_2O_3-$CaZrO_3$ material studied. The good oxidation resistance at low temperatures of the 3.2CaZ material tested in the current study is most likely a result of the absence of any easy-to-oxidise Zr-O-N phases. ZrO_2 in the current material is thought not to directly influence oxidation, and at oxidising temperatures >1300°C reacts with the SiO_2 on the surface forming $ZrSiO_2$. Bellosi et al [161] studying the stability of Si_3N_4-Al_2O_3-ZrO_2 composites in oxygen environments made similar observations.

As was outlined in Section 2.5.1.3 although there is good evidence for cation diffusion through intergranular phases in some cases, the majority opinion seems to support oxygen diffusion as rate controlling in most examples [156] [157]. The present materials appear to behave similarly to other Si_3N_4 materials (containing Y_2O_3 and Al_2O_3), that is, an initial relatively rapid oxidation of the intergranular glassy silicate material accompanied by a volume expansion with accompanying growth of an 'oxide' film on the surface (non-parabolic kinetics) is followed by, oxygen diffusion-controlled growth of the oxide film by reaction at the film/Si_3N_4 interface. The product, silica dissolves in the silicate glass until the liquidus composition concentration of silica is reached (parabolic kinetics) as seen in the present data (Figure 4.51). At this point crystalline silica can form at the interface, which then dramatically reduces the oxidation rate as diffusion of oxygen through silica is some orders of magnitude slower than through silicates (crystalline or glassy).

4.8. Composite Densification and Microstructure

4.8.1. Densification Results

Densification Conditions	1600°C 10bar N_2	1600°C 60bar N_2	1600°C hot-pressed	1700°C hot-pressed
Matrix %TD	85	85.7	99.7	99.9
Composite %TD	88	88.7	99.8	99.9
Vf %	30.8	31.2	36.5	38.7
% Shrinkage	12.9	16.2	36.2	38.7
% Mass Loss	9.2	3.8	4.1	2.9

Table 4.23 Physical properties of the 1AlN/P25C composite after densification under specified conditions.

Densification Conditions	1600°C 10bar N_2	1600°C 60bar N_2	1600°C hot-pressed	1700°C hot-pressed
Matrix %TD	75	82.7	96.7	97.1
Composite %TD	75.5	86.3	97.6	97.9
Vf %	31.39	31.1	40.3	38.2
% Shrinkage	15.8	16.7	39.1	37.6
% Mass Loss	8.2	3.8	5.2	4.2

Table 4.24 Physical properties of the 3.2CaZ/P25C composite after densification under specified conditions.

The physical changes induced in the samples during densification by pressureless sintering (10 bar N_2), gas-pressure sintering (60 bar N_2) and hot-pressing (uniaxial 127 bar N_2) of the 1AlN/P25C and 3.2CaZ/P25 composites are summarised in Table 4.23 and Table 4.24 respectively. Both of the novel composite systems show a higher propensity to densify than the standard reference composition; the 1AlN and 3.2CaZ matrix phase compositions reaching 85 and 75 percent theoretical density respectively compared with 68 percent for a standard YAG matrix composite prepared as a reference material in the present study.

The application of a higher N_2 pressure (60 bar) in gas-pressure sintering is seen to have a minimal effect on the densification of the 1AlN/P25C composite, increasing the density of both the matrix phase and the whole composite by approximately 0.7 percent. However, under these conditions the density of the matrix phase in the 3.2CaZ/P25C composite increases by more than 10 percent and the density of the whole composite by 7 percent.

The results show that for both composites, the application of a high uniaxial mechanical pressure (127 bar N_2), that is hot-pressing, leads to good densification and closed porosity. After hot-pressing at the lower temperature, 1600°C, the 1AlN/P25C composite is fully dense (99.7%TD), with only a slightly higher density of 99.9%TD, achieved at the higher hot-pressing temperature, 1700°C. The 3.2CaZ/P25C composite reaches close to full density after hot-pressing at 1600°C (97.6%TD), again with only a minimal density increase to 97.9%TD after hot-pressing at 1700°C.

In the 1AlN/P25C composite the percent volume fraction of fibres, %Vf, is seen to increase as the density increases. For example, the %Vf increases from 30.8% to 38.7% as the density increases from 88%TD to 99.9%TD. The %Vf results for the 3.2CaZ/P25C composite are somewhat inconsistent with the density values. The %Vf calculated for the pressureless sintered material, which is 76% dense and in the gas-pressure-sintered material, which reaches 82.7%TD is essentially the same. The composite hot-pressed at 1600°C, with 96.7%TD does have an increased %Vf value, 40.3%, but a slightly reduced %Vf value of 38.2% is seen for the sample with 97.1%TD after hot-pressing at 1700°C. The %Vf results for both composite compositions indicate that hot-pressing is required to ensure that the %Vf in the final material corresponds to the optimum value of approximately 40 vol% for good mechanical properties [230].

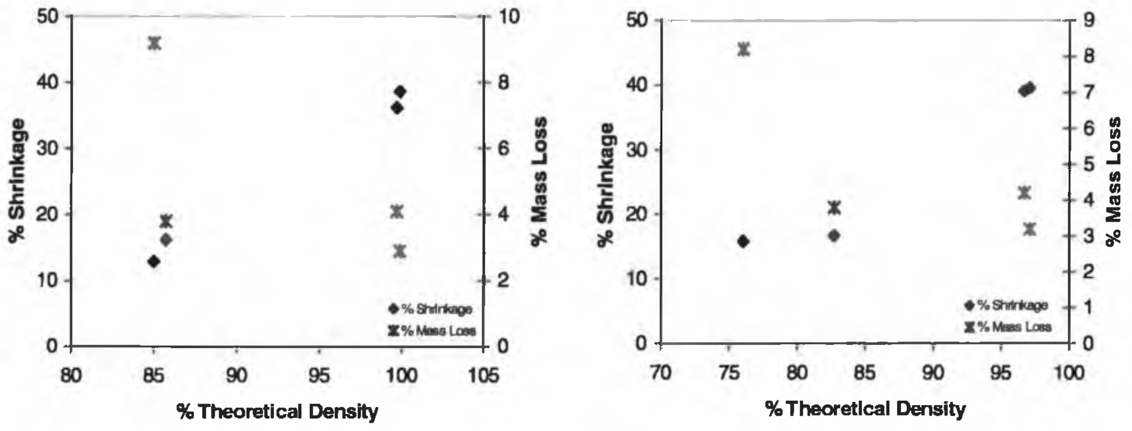

(a)

(b)

Figure 4.55 The variation of % Shrinkage and % Mass Loss with % Theoretical Density for (a) the 1AlN/P25C composite and (b) the 3.2CaZ/P25C composite.

Figure 4.55 illustrates the variation in %shrinkage and %mass loss with composite theoretical density for the 1AlN/P25C composite (a) and the 3.2CaZ/P25C composite (b). The shrinkage values outlined represent the change in linear thickness of the sample after the densification procedure. As expected, the shrinkage of both composite compositions corresponds with sample percent theoretical density achieved, that is, composite shrinkage increases with increasing percent theoretical density.

The observed mass losses for both the 1AlN/P25C and 3.2CaZ/P25C composites also correspond well with the composites' %TD, given that the mass loss values are seen to decrease as the percent theoretical density values increase. As expected, the mass losses are minimal after hot-pressing, as the densification kinetics are rapid and good densification is achieved. The significant decrease in %mass loss seen between the pressureless sintered materials and the gas-pressure sintered materials however, is not reflected in a significant rise in theoretical density. Mass losses during sintering of these types of materials are usually associated with volatilisation of gaseous products and are viewed as a competitive phenomenon to densification. It was expected that employment of the sintering procedures outlined below, which were successful in the pressureless sintering of the monolithic sample, (Sections 4.4.2.2

and 4.4.3.2) would also be successful in minimising volatilisation reactions in the composite materials. That is, the use of:

- Sinter powder bed
- Graphite pieces
- Overpressure of N_2
- Low sintering temperature

4.8.2. Microstructural Observations

4.8.2.1. Fibre Distribution

Image analysis was performed to determine the distribution of fibres within the gas-pressure sintered 1AlN/P25C and 3.2CaZ/P25C composites. Images suitable for analysis were selected based on the guidelines outlined in Section 3.5.4. These analysis results are approximations since high accuracy with such a disperse distribution of fibres would require the analysis of several hundreds of images. Figure 4.56 shows an example of a typical SEM original image of the composite samples, with the contour of the measured phase overlaid in red. The fibre distribution through the sample depth was determined by examining the area fraction of fibres calculated for a number of images taken of the sample, as listed in Table 4.25. Of the two samples, a more uniform distribution of fibres was observed within the 1AlN/P25C composite sample, with the average area fraction value of 27.59±3.89 corresponding well with the calculated volume fraction value, V_f of 31.2% (outlined above). In the 3.2CaZ/P25C composite sample variation in distribution of fibres was seen between the upper surface, which contained fewer fibres (Figure 4.57) and the bulk of the sample. This structure arises as a result of the 'squeezing out' of a monolithic ceramic layer due to over-pressing the fibres in the mould during the green forming process (Section 3.3). These monolithic surface layers were considered misrepresentative of the bulk 'composite' structure and were omitted from the area fraction calculations. The resultant calculated value of 30.39 ± 3.63 based on the SEM images, relates well to the calculated V_f of 31.39%.

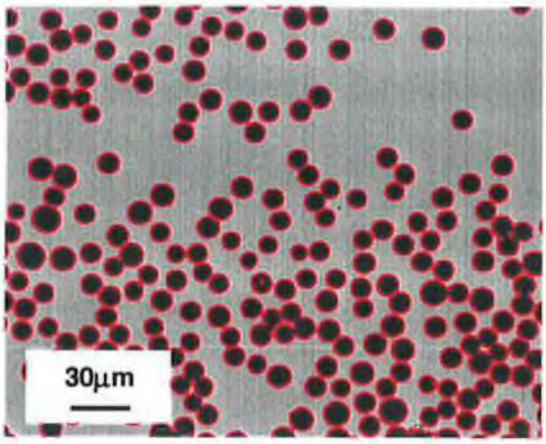

Figure 4.56 An example of an SEM image used area fraction calculations. The measured phase is overlaid in red.

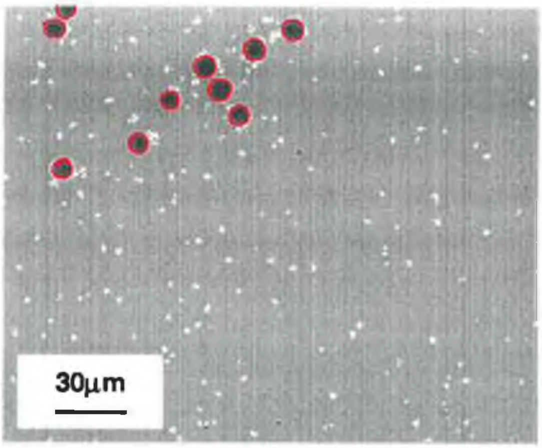

Figure 4.57 An area containing few fibres close to the surface of the CaZ/CP25 composite material.

1AlN/P25C GPS		3.2CaZ/P25C GPS	
	Area Fraction (%)		**Area Fraction (%)**
Image 1	27.1	Image 1	29.3
Image 2	30.6	Image 2	24.3
Image 3	23.7	Image 3	30.2
Image 4	28.8	Image 4	29.4
Image 5	21.8	Image 5	31.4
Image 6	28.8	Image 6	33.7
Image 7	25.8	Image 7	32.0
Image 8	34.1	Image 8	31.2
Average	**27.59**	Image 9	36.8
Standard Deviation	**3.89**	Image 10	25.6
		Average	**30.39**
		Standard Deviation	**3.63**

Table 4.25 Area fraction measurement results on SEM images using image analysis.

4.8.2.2. Cracks and Porosity

Figure 4.58 and Figure 4.59 illustrate the microstructure of a transverse section typically observed in both composite compositions after pressureless sintering and gas-pressure sintering respectively. Matrix macro-cracking is seen in all samples, particularly in areas of closely-packed fibres, although the extent of cracking is significantly less in the gas pressure sintered composite samples. These cracks are clearly related to the facility for the matrix components to migrate and densify in the different morphology zones of the composite. As discussed in sub-sections 4.4.2 and 4.4.3 the matrix phases in both composites densify by liquid phase sintering, where ‘particle-rearrangement’ is the dominant stage in the shrinkage and densification. The larger areas of free matrix material (Figure 4.58) densify well with no visible macro flaws. Areas containing few fibres, also sinter without visible flaws. However, the ready densification and shrinkage of these areas will set up uniform hydrostatic tensile stresses in surrounding areas. Where these surrounding areas of matrix are not free to move, that is, are constrained by closely packed or interwoven fibres, void formation and macro-cracking is seen to develop, particularly at the surface of the fibres. This occurrence has been reported extensively for particulate- and whisker-reinforced ceramic matrix composites [125][129] and [231].

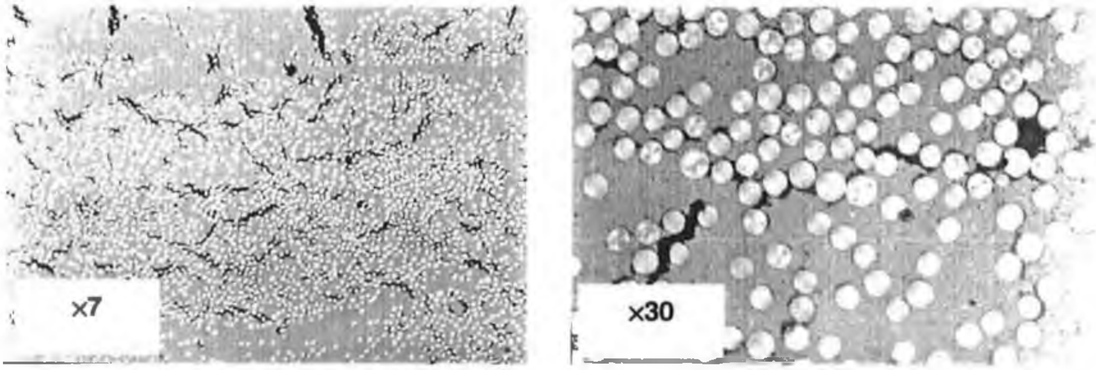

(a) (b)

Figure 4.58 Typical microstructure, illustrating sintering cracks observed in composite materials pressureless sintered at 1600°C.

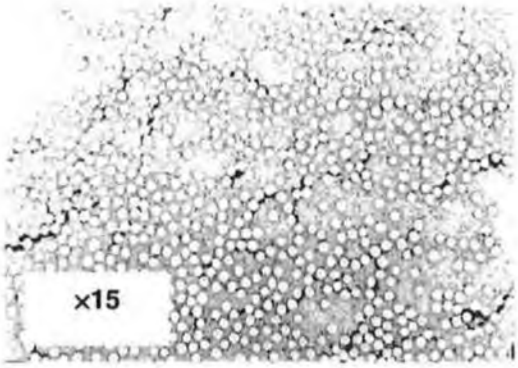

Figure 4.59 Typical microstructure, with some sintering cracks, observed in composite materials gas pressure sintered at 1600°C.

The composite green form contains approximately 35% porosity and has little or no interparticle bond strength. Such porosity may be considered as a population of intrinsic flaws, which provide a route to relieve the tensile stress in the matrix, that is, the cracks or flaws will open further during constrained sintering. The matrix region adjacent to the crack continues to densify by kinetically transferring pores to the open crack [129]. The morphology of the composition studied here suggests that the macro-cracks or flaws tend to initiate at the fibre-matrix interface (weakest link) leading to the matrix shrinking away from and detaching from the fibres, resulting in the microstructure observed in Figure 4.58. Figure 4.58 (b) highlights this phenomenon more clearly; a 'large' void/pore is seen to have formed in an area completely surrounded by fibres, while the adjacent matrix has densified reasonably well.

Even in composites that are 'crack-free' after fabrication, retarded densification is expected to occur along the surfaces of the reinforcing phase, as predicted by Lange [127]. In low fibre density areas in the composites, the concentration of cracks is less, and the inhibition of the fibres on the sintering of the matrix is less as the matrix is seen to have densified well. The resultant effect of the inhibiting role of the non-sintering fibres on matrix sintering, is a composite with inhomogeneous densification throughout the matrix and a less than theoretical final matrix and composite density.

It is possible that the formation of these localised 'differential-sintering' cracks in the composites during pressureless sintering contributes to the higher mass losses observed in these samples as the surface area of both matrix and fibre susceptible to decomposition is greatly increased.

As reported above and illustrated in Figure 4.59, cracking along the fibre-matrix interface is less in the composites densified by gas-pressure sintering. The increased N_2 pressure tends to inhibit decomposition of the matrix and gaseous attack of the fibres at the crack surface. Lower mass losses are observed in the gas-pressure sintered composites, and slightly improved densification compared with the pressureless composites.

The effect of applied pressure is confirmed in Figure 4.60 (a) and (b) which illustrate the microstructures typically observed for both composite compositions after hot-pressing at 1600°C and 1700°C respectively (under an applied mechanical load of 127bar). These microstructures verify the almost 100% theoretical density values calculated for these materials. The matrices are seen to have minimal porosity and no cracking is seen. In this case the applied pressure acts not only to inhibit pressure acts not only to inhibit decomposition but more significantly to improve the matrix mobility and to remove intrinsic porosity.

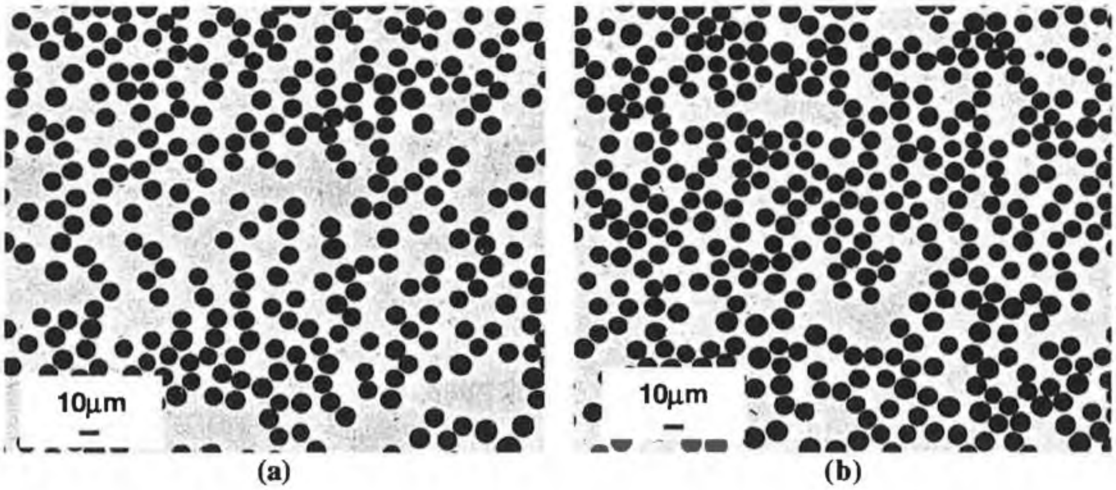

(a) (b)

Figure 4.60 Typical 'crack-free' microstructure observed in composite materials hot-pressed at 1600°C (a) and 1700°C (b).

4.8.2.3. Fibre-Matrix Interface

As discussed in Section 2.4.1, one of the major factors negating the feasibility of manufacturing ceramic matrix composites without the use of uniaxial mechanical pressure (hot-pressing) is the potential of fibre-matrix interaction during processing which leads to poorer mechanical behaviour in the final composite [50]. The guidelines outlined in Section 2.4.1. for preventing such reactions were carefully followed in the present work and the observations of the pressureless and gas-pressure sintered composites are very encouraging. Figure 4.61 shows the typical microstructure observed in longitudinal cross-sections of the pressureless sintered composites. Minimal fibre-matrix interaction is seen to have occurred with the fibres essentially intact. The black tips to the fibres observed are polishing artefacts. Negligible interaction was also seen in the gas-pressure-sintered materials, as seen in Figure 4.62. Figure 4.63 illustrates that no reaction between the fibre and matrix phases is visible in SEM after hot pressing at both 1600°C and 1700°C.

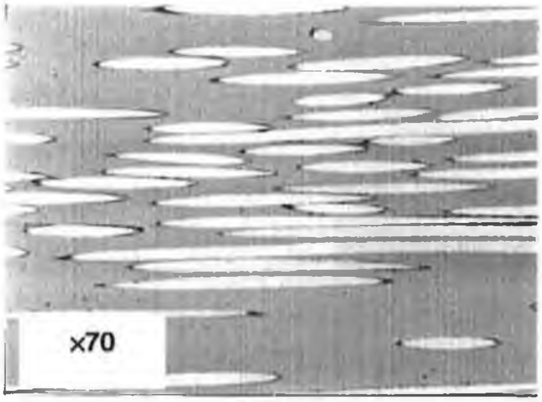

Figure 4.61 Typical microstructure, showing intact fibres, observed in a longitudinal cross-section of composite materials pressureless sintered at 1600°C.

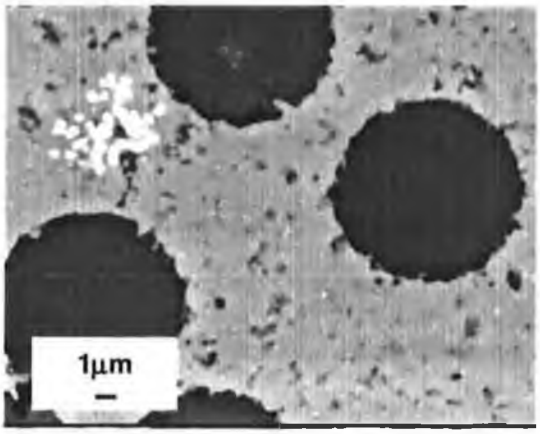

Figure 4.62 Typical microstructure, showing little fibre-matrix interaction, observed composite materials gas pressure sintered at 1600°C.

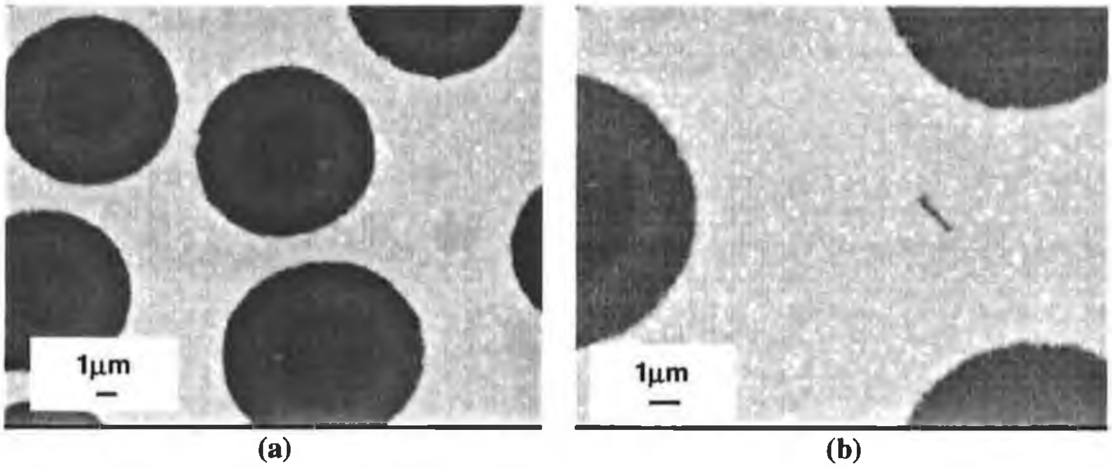

(a) (b)

Figure 4.63 Typical microstructure, showing completely intact fibres, observed composite materials hot-pressed at 1600°C (a) and 1700°C (at a higher magnification).

Image Analysis was carried out on a series of SEM images of the gas-pressure sintered 1AlN/P25C and 3.2CaZ/P25C composites. The SEM images selected for analysis were corrected according to the guidelines outlined in Section 3.5.4. Figure 4.64 shows an example of an adjusted result image. Table 4.26 outlines the results for the fibre diameters in these composites. Figure 4.65 and Figure 4.66 illustrate the results graphically. These figures should be compared with equivalent data for the starting material, measured in the same condition using the same technique. The manufacturer's specification for fibre diameter is a single figure, 11μm, with no indication of variation within the sample or of method of measurement. Preparation of comparative samples of as-received fibres raises problems of consistency, fibres mounted in epoxy resin are difficult to polish without rounded edges and the edge definition is by no means the same as in the ceramic matrix. This is important as an error of say, 1μm in a diameter of 10μm introduces a 20% error. Green form composites were very difficult to polish. Finally, a good comparison could be made with fibres in the hot pressed composite, where SEM showed very clean, smooth and wholly unattacked edges for fibres in the AlN composite and only very marginally roughened edges in the CaZ matrix material. The AlN sample was taken to indicate the original fibre diameter. Diameters were measured in an optical microscope at magnification of 1000, taking 20 measurements per sample.

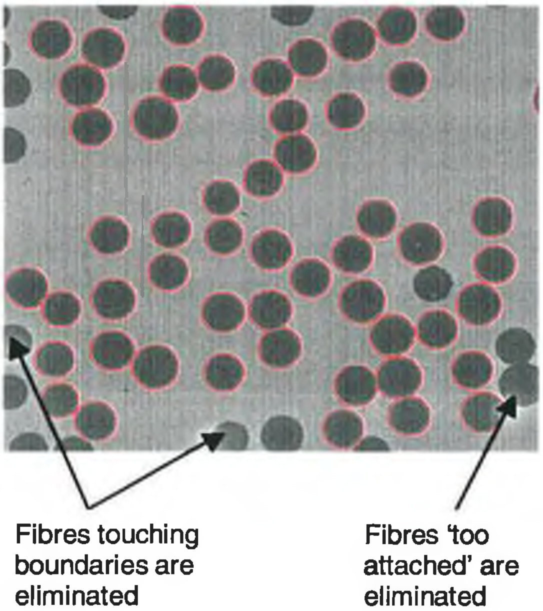

Figure 4.64 An example of an SEM image adjusted for image analysis. The measured diameter is outlined in red.

Sample Composition Label	Preparation technique	Total number of fibres	Mean (μm)	Standard deviation
1AlN/CP25	Hot pressed	20	10.58	0.8
	Gas pressure sintered	132	10.4	0.5
3.2CaZ/CP25	Hot pressed	20	10.44	0.88
	Gas pressure sintered	102	10.0	0.7

Table 4.26 Fibre diameter measurement using optical microscopy for the hot-pressed material and SEM / image analysis for the gas pressure sintered material.

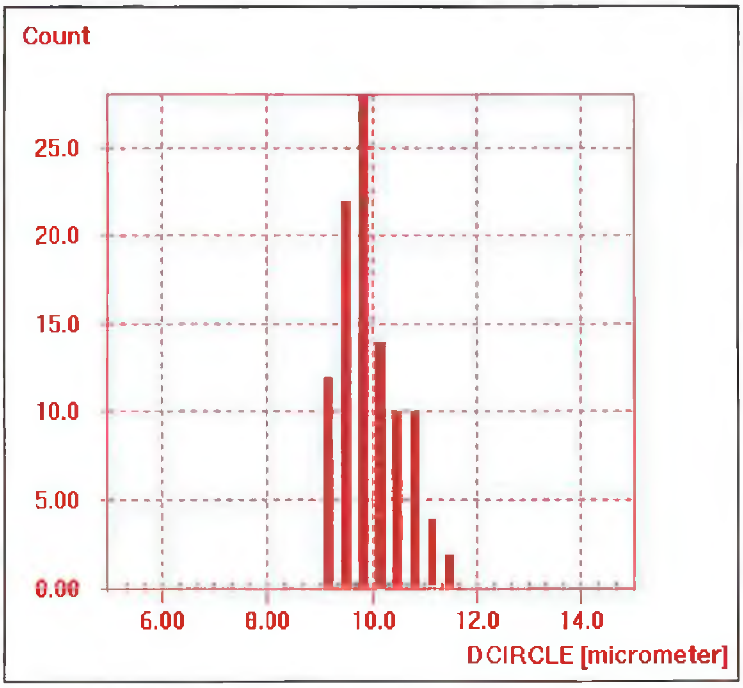

Figure 4.65 Graphical representation of image analysis results of fibre diameter for the 1AlN/P25C composite gas pressure sintered at 1600°C.

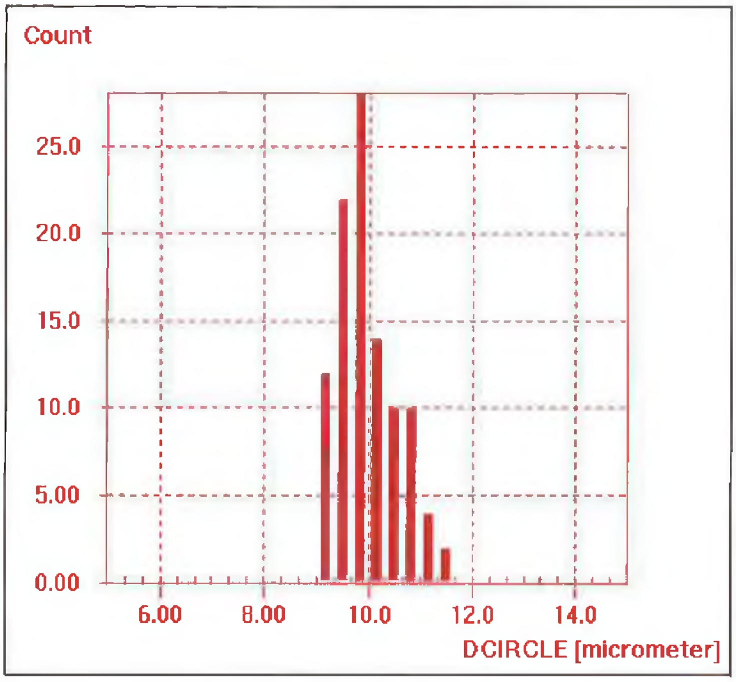

Figure 4.66 Graphical representation of image analysis results of fibre diameter for sample 3.2CaZ/P25C gas pressure sintered at 1600°C.

These results are valuable in confirming the thermal stability of the two systems studied but not conclusive in predicting composite behaviour. The diameter of the totally undamaged fibres in the AlN hot pressed material varied from 12.08 to 9.43μm, which even allowing for some operator inconsistency (certainly not more than 0.2μm, in 10μm) represents a huge variation across the batch, (not recognised by the manufacturer). The increasingly roughened surface of the other fibres introduces a degree of uncertainty of the determination of the fibre edge. Nevertheless, the reductions in diameter are completely insignificant for both AlN materials and for the CaZ hot pressed composite, and only marginally significant for the gas pressure sintered CaZ composite. No new phases corresponding to possible reaction products were ever detected using XRD analysis.

In practice, the degree of degradation of the fibre-matrix interface which is required to influence composite fracture properties needs be of the order of only nanometers [50][232] which is not at all visible using the above techniques. But what is shown here confirms that the materials selected for this study, in a fully unprotected and non-optimised condition are nevertheless chemically stable for the intended purpose and will form viable composites, where the phases retain their intrinsic properties.

4.8.2.4. Phase Analysis and Distribution

Table 4.27 lists the phases detected using XRD in both composite compositions after densification under the specified conditions. The composites were found to include silicon nitride, carbon and an intergranular phase (in the 3.2CaZ/CP25 composites). As reported above no fibre/matrix reaction products were detected.

Complete conversion from α- to β-Si_3N_4 occurred in the matrix phase of the 1AlN/CP25 composite during each densification process and temperature. Hot-pressing at 1700°C of the 3.2CaZ/CP25 composite was required for full transformation. However, increased N_2 pressure applied during sintering at 1600°C is seen to promote transformation of α-Si_3N_4; the % β-Si_3N_4 detected increased from 63% to 78% as the N_2 pressure applied increased from 10 bar to 60 bar. Hot-pressing (uniaxial 127 bar N_2) at the same temperature resulted in a further increase to 93% β-Si_3N_4 transformed. These results for both composite compositions are consistent with results for the monolithic ceramic matrices, outlined in Table 4.6, Section 4.4.2.4 and Table 4.10, Section 4.4.3.4.

No intergranular crystalline phase was detected in the composite 1AlN/CP25. This indicates clearly that the white, yttrium-rich phase, observed in significant quantities using SEM is non-crystalline; probably an yttrium-rich glass with the same chemical composition as the glassy phase observed in the pressureless sintered monolithic samples (Section 4.4.2.5). These intergranular phases are randomly distributed throughout the bulk composite with no obvious segregation to the fibre/matrix interface or surface of the samples (Figure 4.63).

Detection of yttrium-stabilised zirconia and tetragonal zirconia in the 3.2CaZ/CP25 is consistent with XRD results of the pressureless sintered samples (Section 4.4.3.5) and corresponds to the large white precipitates observed using SEM (Figure 4.62). The second intergranular white phase seen in the SEM micrographs is most probably glassy, as it was not detected by XRD. These phases are randomly distributed throughout the bulk material however, with the exception of the pressureless sintered sample, significant local migration to the surface of the secondary phases was observed (Figure 4.62).

The reader is referred to Sections 4.4.2.6 and 4.4.3.6 for more comprehensive discussion on these intergranular phases.

Sample Label	**Densification Conditions**			
	PS 1600°C	**GPS 1600°C**	**HP 1600°C**	**HP 1700°C**
AlN/CP25	100%β-Si_3N_4 C	100%β-Si_3N_4 C	100%β-Si_3N_4 C	100%β-Si_3N_4 C
CaZ/CP25	63%β-Si_3N_4 C Y-ZrO_2	78%β-Si_3N_4 C ZrO_2(t)	93%β-Si_3N_4 C ZrO_2(t)	100%β-Si_3N_4 C ZrO_2(t)

Table 4.27 Phases detected in the composite materials after densification under the specified conditions.

Y-ZrO_2 – ytrria stabilised zirconia; ZrO_2(t) – tetragonal zirconia

PS – Pressureless sintered, GPS – Gas Pressure sintered, HP – Hot Pressed.

4.8.2.5. Cooling Cracks

Figure 4.67 illustrates two other types of macro-cracking (not explained by localised differential sintering) observed in samples of both composite compositions after pressureless and gas-pressure sintering. The very large cracks illustrated in Figure 4.67 (a) are located in the middle of the samples and are most likely a result of differential cooling due to the position of the samples in the furnace. The walls of the furnace begin cooling slightly earlier than the inside of the furnace, and in turn the sides of the composite samples close to the walls start cooling before the middle of the sample. Shrinkage from the outside of the material will then exert a tensile stress on the centre of the material. This effect was seen earlier during cooling of plates of sintered monolithic Si_3N_4, which were packed in a powder bed with no constraining graphite piece above. Without the graphite piece acting as thermal insulation, cooling occurred from above and the Si_3N_4 plates warped considerably during cooling due to advanced shrinkage of the upper surface of the plate compared with the lower. The positioning of a restraining graphite piece provided weight and improved thermal insulation and flat sintered plates were attained.

The second type is an array of macro-cracks transverse to the longitudinal fibre axis, observed in the pressureless and gas-pressure sintered composite materials are shown in Figure 4.67 (b). This type of cracking is widely reported as arising from differences in the physical properties of the component phases in fibre reinforced composites, leading to the development of internal stresses. Thus, on cooling from high temperatures, a mismatch in coefficient of thermal expansion (CTE) between fibres and matrix will generate stress levels capable of cracking the matrix phase. In this study a mismatch in coefficients of thermal expansion (CTE) exists between the Si_3N_4-based matrix and the CP25 fibres (Si_3N_4, $\alpha = 2.25\text{-}2.87\times10^{-6\,\circ}C^{-1}$, CP25 fibres, $\alpha = 22 \times 10^{-6}\ K^{-1}$). Similarly where the phases have significantly different E_{mod} values, the application of mechanical stress leads to the development of internal (interfacial) stresses. The distance between these cracks is related to of the composites' interfacial shear stress, τ and is discussed more extensively in the section dealing with the mechanical bending tests of the hot-pressed materials (Section 4.9.3)

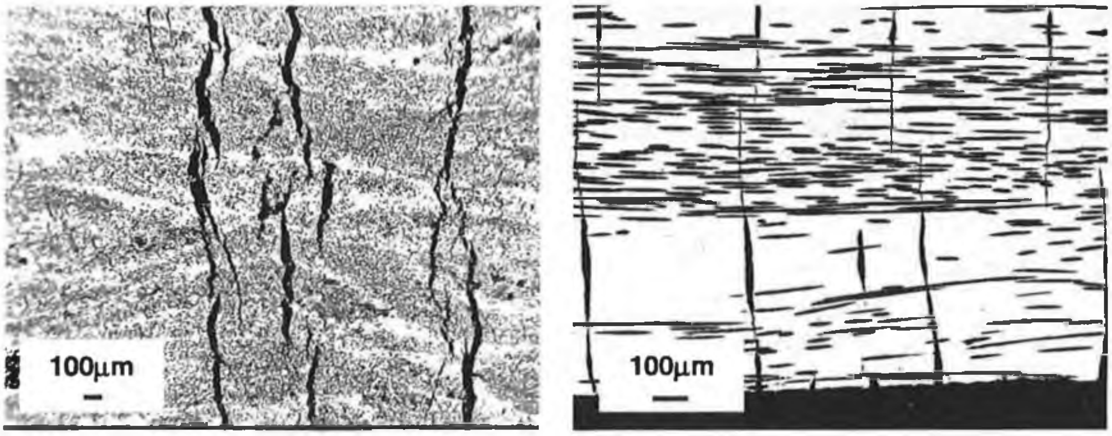

(a) (b)

Figure 4.67 Cracks observed during cooling, due to differential cooling (a) and CTE mismatch (b).

4.9. Composite Mechanical Properties

Composite samples hot-pressed to high densities were selected for mechanical property testing, to establish that the phases selected will indeed form a viable composite, however poorly optimised; to confirm that these materials exhibit "composite" failure behaviour of the systems under mechanical stress and to examine the thermal stability of the phases in the composites during typical processing conditions of temperature and environment during sintering under mechanical pressure. Materials selected for testing corresponded with the matrix phase compositions; 1AlN and 3.2CaZ hot-pressed at 1600°C and at 1700°C. 3-point bending tests were carried out as described in Section 3.7.

4.9.1. Deformation Behaviour

Figure 4.68 illustrates typical examples the stress/displacement plots obtained for each sample tested. The behaviour observed is typical of composite failure behaviour, and can be described as the following three distinctive steps [127] (as outlined in detail in Section 2.5.2.1):

- an initial elastic region where no damage to the composite occurs
- a period of progressive matrix micro-cracking where increasing displacement is non-linear with increasing load, and small load drops occur. This continues until the capacity for the matrix to micro-crack is saturated. At this stage load transfer to the fibres approaches 100%
- a close-to-elastic region where the fibres sustain the full load until maximum stress where catastrophic failure occurs.

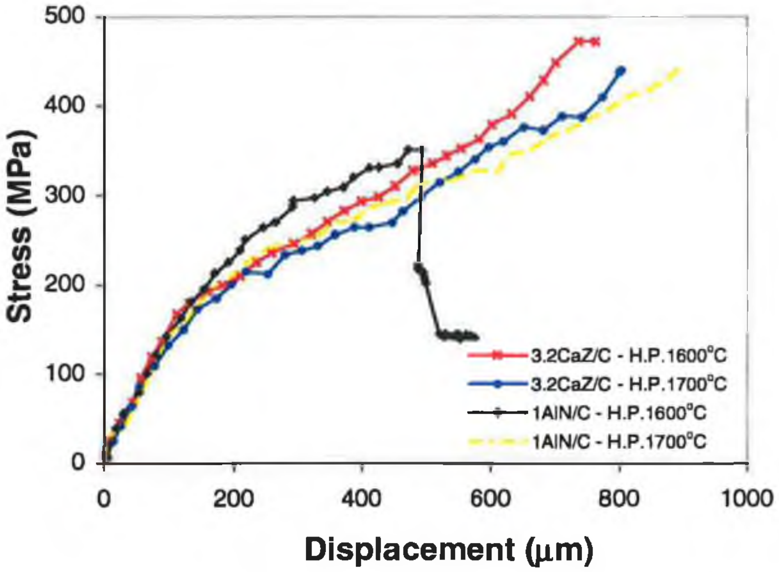

Figure 4.68 Representative bending Stress-Displacement curves for the composites tested.

4.9.2. Mechanical Properties Values

Table 4.28 outlines the Young's Modulus, E, the matrix cracking stress, σ_c, and the maximum failure stress, σ_f, for each composite sample tested. The mechanical property values of these composites are determined by several factors:

- chemical integrity of the phases – degradation at high temperatures

- density of the composite
- morphology of the composite; defect population size, shape, distribution, uniformity of the fibre distribution
- interphase/interfacial relationships

In discussing the values measured for the composites tested the following limitations must be recognised:

- All specimens from each batch were cut from the same plate, so that any variations in the processing conditions of the plate will affect all 6 test pieces. While both the green forming and hot pressing stages were performed using well-developed long-established techniques, the occasional discrepancy in plate quality is unavoidable, especially as the hot pressing work was contracted out. Neither time nor financial constraints allowed for the preparation of a series of replication plates.

- Degradation of the chemical integrity arises from spontaneous decomposition of the phases or by reaction between the component phases themselves or with the external gas environment. These reactions almost inevitably involve gaseous attack or evolution so that the physical transport of gas to and from the reaction site will influence reactivity. Hot pressing was conducted in 27bar N_2 pressure to minimise gas reactions, but nevertheless the possibility for reaction will clearly increase from the centre of the plate to the edge. Inevitably, this introduces a variation in homogeneity across the plate. Specimens cut from the centre of the plate are then expected to have superior quality and better mechanical properties, than those cut from the edge.

1AlN/P25 Composite					
Hot-pressed at 1600°C			Hot-pressed at 1700°C		
E (GPa)	σ_c (MPa)	σ_f (MPa)	E (GPa)	σ_c (MPa)	σ_f (MPa)
127	271	301.6	132.5	149.5	444
154	232.5	465.2	128.2	151.3	316.8
158.7	256.1	271.1	145.9	154.2	507.6
131.9	217.3	221.5	142.4	127.8	269.9
161	346.9	347.1	143.7	145.5	369.7
116.7	226.8	353.6	130.2	149.9	415
					617.8
Mean ± Standard Deviation			Mean ± Standard Deviation		
141.6±18.7	258.4±47.7	326.7±83.8	137.2±7.7	146.4±9.5	420.1±117.7

3.2CaZ/P25 Composite					
Hot-pressed at 1600°C			Hot-pressed at 1700°C		
E (GPa)	σ_c (MPa)	σ_f (MPa)	E (GPa)	σ_c (MPa)	σ_f (MPa)
144.4	250	382.9	84.9	120	301.8
154.2	281.7	464.9	100.6	153.1	360.5
144.7	243.2	625.8	116	152	439.5
146.4	272.4	448	133.3	153.1	630.7
142.5	271.6	475.6	99	145.2	438.5
138.7	253.6	347.4	96.1	153.9	1067.1
152.9	250	484.2			
Mean ± Standard Deviation			Mean ± Standard Deviation		
146.3±5.5	260.4±14.6	461.3±88	105±17.1	146.3±13.2	539.7±281.2

Table 4.28 Elastic modulus (E), matrix cracking stress (σ_c), and failure stress (σ_f) measurements for bend samples.

4.9.2.1. Young's Modulus

The initial stress-strain behaviour at room temperature is clearly dominated by the matrix phase. If no major differences in chemical degradation occur during processing and the specimen densities are equivalent, the variation in E_{mod} should not be great. The results reflect not only the similarity in this property, but also a high precision (low standard deviation) between specimens. The close similarity in the E_{mod} values of AlN composite processed at 1600°C and 1700°C points to good chemical integrity even after exposure to the higher hot pressing temperature. The almost identical E_{mod} values of the 3.2CaZ system at 1600°C suggests that this system is also not degraded, but the consistently lower values for 1700°C material raises some concern as to the higher temperature stability of the material. However, as reported in Section 4.4.3.2, the mass loss observed in the 3.2CaZ composite after hot pressing at 1700°C was not significantly greater than in the other systems, implying that the phases within the composite remain stable after hot pressing. The reason behind the reduction in Young's Modulus with increasing hot pressing temperature remains unclear and requires analysis beyond the scope of this study.

4.9.2.2. Matrix Microcracking

The onset of matrix microcracking depends upon the ability of the matrix to withstand elastic strain, which is controlled not only by the matrix phase itself, but is also influenced by the defect population morphology and distribution, especially the presence of macro defects, and particularly upon the fibre-matrix bonding properties. Both systems show a consistent reduction in σ_c in raising the processing temperatures from 1600°C to 1700°C, significantly outside the standard deviations of the results. It is assumed that this reduction is not a result of the macro defect structure as this is introduced at the green forming stage and is unlikely to change during hot pressing. Preliminary SEM analysis of the fibre-matrix interfaces of the composites studied showed the interfaces to be very similar after hot pressing at 1600°C and 1700°C, (Section 4.8.2.3), however, it is possible that differences do exist but confirmation of this would require TEM or HRTEM analysis, which were not possible in the present study. The observed loss of matrix strength might therefore be influenced by localised fibre-matrix interaction at the interface. This supposition is supported by the work carried by Sabouret et al. [233], on comparable composite systems densified under identical processing conditions. Using TEM and HREM analysis reference [233] observed that the properties of the fibre-matrix interface significantly influenced the matrix cracking.

4.9.2.3. Ultimate Composite Fracture

The ultimate fracture strength of the composite is strongly fibre dominated. In principle, under simple uniaxial tensile loading where all fibres can be gripped equally, the tensile strength of a bundle of parallel fibres will be the sum of the individual filaments. In bending, the maximum stress is borne by the extreme outer layer of the convex surface. In a continuous fibre composite the strength of the outer layer is very dependent upon the fibre distribution. Ideal composite design with approximately 10 micrometer diameter fibres, is targeted to a uniform distribution where the interfibre spacing is much less than the critical flaw size of the matrix phase, that is, less than ~30 micrometers for a well densified sintered silicon nitride.

From these considerations the large scatter in ultimate fracture strength is attributed to poor uniformity of fibre distribution in the composite. As discussed in Section 4.8.2.1. macrography studies of the hot pressed composites showed that the fibre array is often distorted under these conditions, losing the regular architecture of straight, parallel filaments. The result is a loss of fibre distribution uniformity introducing a large variation in interfibre spacing. Figure 4.69 (a) and (b) illustrate typical layered structure of composites studied. The significant feature of this is the formation of layers of pure matrix phase of appreciable thickness, which provide easy fracture paths, negating the toughening effect of a 10 micrometer interspaced reinforcing phase.

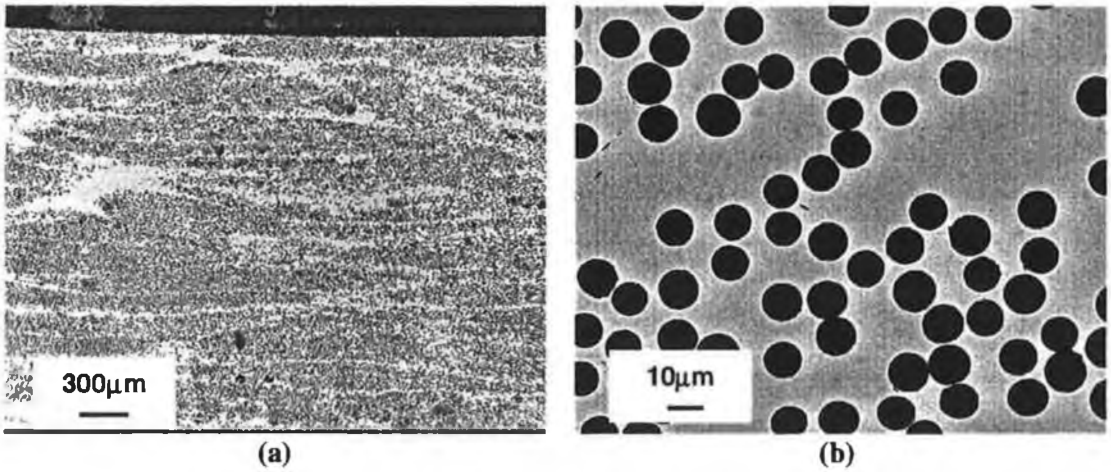

(a) (b)

Figure 4.69 The layered structure observed (a), although a poor quality image, the non-uniform distribution of fibres is apparent at higher magnification (b).

The present results do not allow a convincing conclusion to be made about the effects of sintering temperature or composition. The differences in fracture strength of the particular combinations are proportionately large compared with the total averages, but all are within the standard deviation values. It is then not useful to make absolute comparison between them. Since all combinations involve the same fibres in the same volume fraction, the results only demonstrate the need for an improved uniformity of structure. To achieve such optimum architecture requires rigorous optimisation of all processing steps, as carried out by Sabouret et al [20]. Although such developments in processing are beyond the scope of the present study, the present results do show that the quality of the composite, and the resulting mechanical properties, are very sensitive to composite morphology, and that this is eminently engineerable.

4.9.3. Interfacial Shear Stress

The development of transverse matrix cracking with increasing strain allowed an an estimation of the interfacial stress, τ, to be made, which determines the length over which the stress is transferred from the fibres back to the matrix (see Section 2.5.2.1). Control of τ is critical, since by varying τ, the prevalent failure mechanism and the resultant non-linearity in the stress/displacement plots can be modified.

Marshall and Evans [234] demonstrated Equation 4.8 to be accurate for application to bend tests:

$$\tau = \frac{\sigma_c R}{4dV_f} \bullet \frac{1}{\left(1+\frac{E_f V_f}{E_m V_m}\right)} \qquad \textbf{4.8}$$

where, σ_c is the matrix cracking stress (the stress at which the stress/displacement curve deviates from linearity), R is the fibre radius, d is half the average crack spacing, E is the Young's Modulus and V is the volume fraction of the component (matrix or reinforcement). Figure 4.70 illustrates the typical micro-crack spacing observed, with average $d = 1.75\text{x}10^{-4}$ m. Following equation 4.7, a value of 1.32MPa for τ, was obtained for a composite typical of those in the present study, which is low compared to those measured for similar composites [235][236].

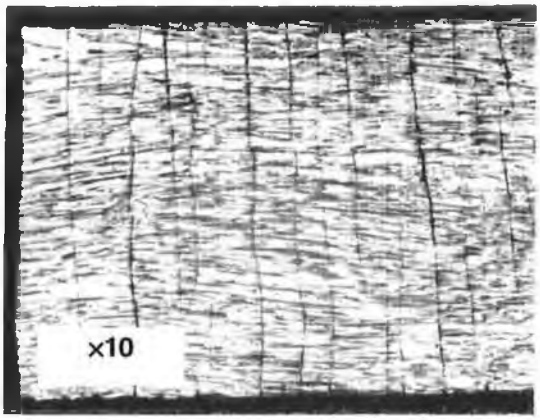

Figure 4.70 Matrix micro-crack spacing behind the fracture surface.

4.9.4. Crack Growth and Failure Behaviour

In unreinforced ceramics the growth of a single flaw and its propagation as a crack can result in total failure. The improvement in the composite failure behaviour over the monolithic ceramic was investigated through comparative tests on three samples of a commercial silicon nitride ceramic, which were machined and tested following the same procedure as the composite samples. The presence of fibres clearly influences the growth and propagation of cracks. Figure 4.71 illustrates the brittle nature of these monolithic ceramic samples, compared to the composite samples.

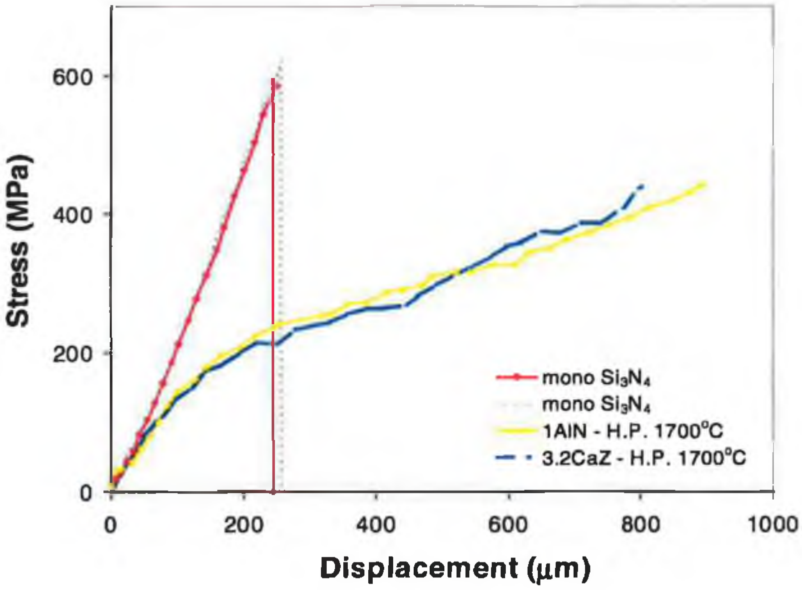

Figure 4.71 The brittle fracture of a commercial Si_3N_4 monolith ceramic compared to typical composite behaviour of samples tested.

Microscopic evaluation of the fractured specimens provides insight into the fracture mechanisms. At distances remote from the fracture surface, Figure 4.72(a) clearly illustrates the crack-bridging by the fibres in the composite during the matrix micro-cracking stage. During the fracture process itself, Figure 4.72 (b) shows that the initial fracture is transverse, and brittle with no fibre-matrix debonding or fibre pull-out. In a small number of cases the curves show this first crack as a partial fracture at lower stresses before complete failure of the specimen (3.2CaZ-hot-pressed at 1600°C in Figure 4.68).

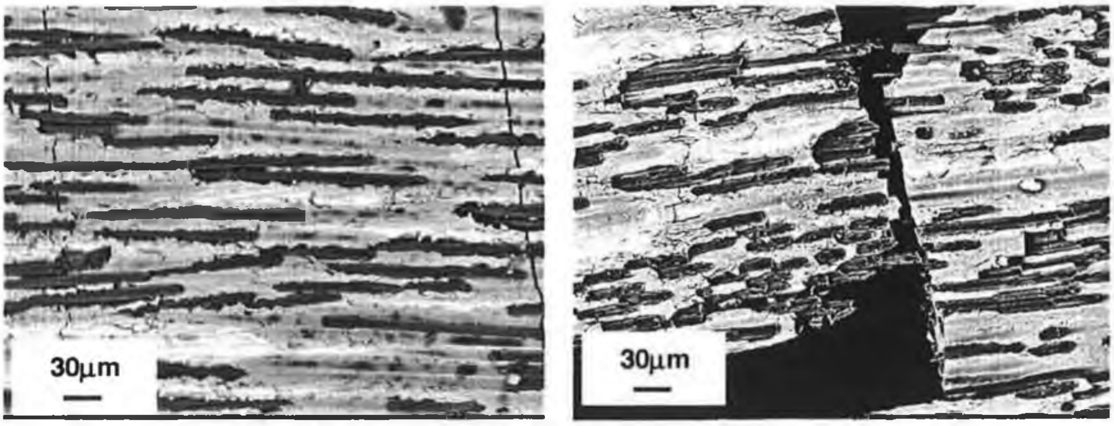

(a) (b)

Figure 4.72 Typical periodic matrix micro-cracking (a) followed by clean fracture (b).

Optical microscopy of failed test pieces also illustrates ‘step-like’ growth after the initial crack, suggesting delamination between fibre and matrix and dispersion of the crack path along the fibre surface Figure 4.74 (a) and (b). All specimen fracture surfaces showed extensive cracking along the fibre orientation away from the fracture surface. In most cases the delaminated surfaces are irregular through the fracture surface but in some cases show a distinct fracture step from the convex bending surface before becoming more typically irregular. This evidence coincides with the early, partial failure and sudden stress-drop observed in the load-displacement curves (Figure 4.68) and almost certainly results from poor fibre distribution in the composite leading to a plane of weakness (only ceramic matrix phase present) as explained earlier, and thus premature crack propagation in the micro-cracking stage.

Again the comparison between composite and monolith crack growth and failure behaviour can be seen in the respective optical microscope images. Figure 4.73(a) shows the crack deflection by the fibres in a composite sample and Figure 4.73 (c) showing the growth of a crack resulting in total failure in a monolithic ceramic sample.

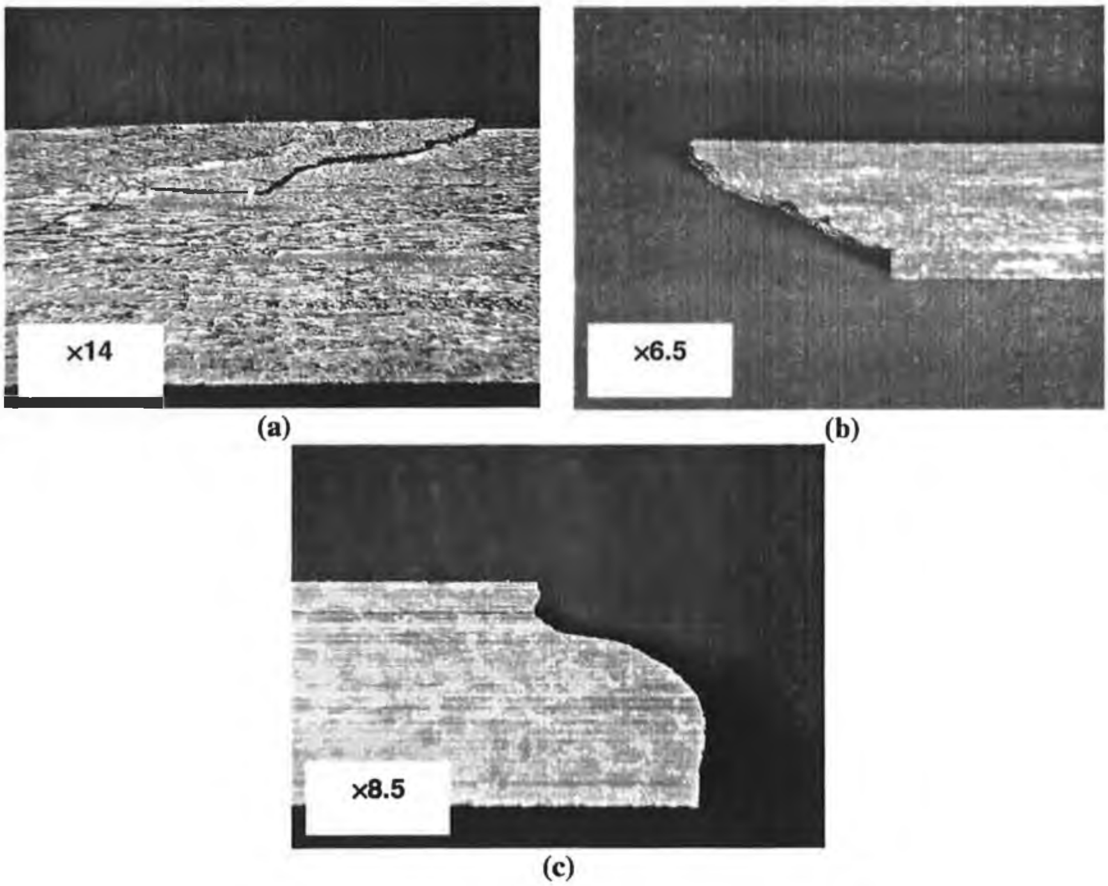

Figure 4.73 Typical crack growth in the composites samples (a) and final fracture surface (b) in comparison to the brittle behaviour of the monolithic samples (c).

4.9.5. Matrix-Fibre Interface

Matrix-fibre interfacial mechanical behaviour can be seen from the extent of fibre pull-out in the fracture surfaces and the regular transverse cracking behind the fracture surface. Figure 4.74 (a) and (b) show the typical fibre pull-out observed in the samples tested, which is not extensive, suggesting strong matrix-fibre bonding. This confirms results from many authors [237][238][239] who then applied fibre coatings to weaken the matrix-fibre interface. Distinguishing between the relatively small fibre-matrix debonding (Figure 4.74 (b)) and the fairly massive longitudinal cracking observed in Figure 4.74 (a) implies that while the matrix and fibre are strongly bonded prior to the application of the load and during the matrix micro-cracking, the propagation of the major crack until complete failure is still preferred along the direction of the fibres.

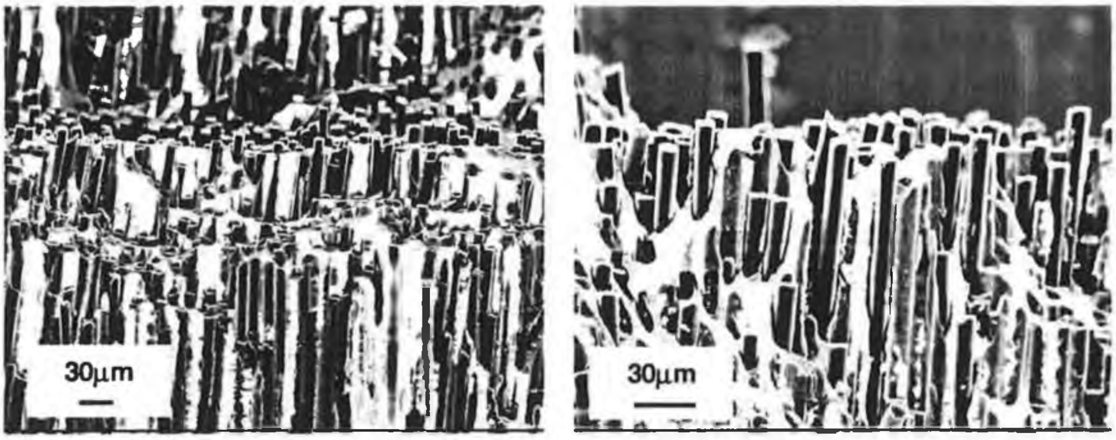

Figure 4.74 Typical fracture surfaces with little fibre pullout.

4.9.6. Summary of Results

The densities and average mechanical properties of the composites studied are summarised in Table 4.29. The composite failure stress, for each composition, increases with increasing final density, corresponding well with previous studies carried out on similar systems studied [197][240]. Within error limits, the Young's modulus changes little with increasing density for each composite composition.

The important engineering property for the composite is however, the avoidance of brittle failure in the initial elastic region. The design stress limits for components in service will ensure that the material remains within the elastic stress range for normal operation. What is important then, is that failure by brittle fracture in the elastic range is eliminated so that deviations from normal stress conditions do not lead to catastrophic failure. All of the composites tested in the present series show an extensive range of matrix microcracking above the elastic region, confirming the ability of the materials to confer a degree of toughness and defect tolerance to the matrix ceramic. Thus, the observed failure mechanisms and microstructural analysis along with the comparative values, demonstrate that the present composites have typical composite failure behaviour whose phases are not degraded during high temperature processing.

Composite Hot-Pressing Temp. & Composition	Composite Density (%TD)	Matrix Density %TD	Volume % Fibre	E (GPa)	σ_f (MPa)	σ_c (MPa)
1600°C 1AlN/P25	99.81	99.75	36.51	141.6±9.5	326.7±84.2	258.4±47.7
1700°C 1AlN/P25	99.98	99.97	38.65	137.2±7.7	420.1±117.7	146.4±18.7
1600°C 3.2CaZ, P25	97.64	96.72	40.33	146.3±5.5	461.3±88	260.4±14.6
1700°C 3.2CaZ/P25	97.85	97.85	38.22	116±16.8	539.7±281.2	146.2±5.5
1700°C Si_3N_4/P25*	-	-	-	211±4	664±88	174±44
1600°C Si_3N_4/P25*	-	-	-	207±7	558±37	129±7
1700°C Si_3N_4/P25♦				200±15	430±20	140±20

Table 4.29 Summary of composite sample densities and average mechanical properties (± standard deviation).

*- optimised silicon nitride composite fabricated and tested by Sabouret [10].

♦- optimised silicon nitride composite fabricated and tested by Olivier [11].

5. CONCLUSIONS, CONTRIBUTIONS AND PROPOSED FURTHER RESEARCH

5.1. Conclusions

The identification of sinter aid compositions which allow densification of the candidate matrix phases at lower temperatures by liquid phase sintering to greater than 95% Theoretical Density (TD) was achieved. Selected matrix compositions proved to be suitable for use matrix phases in the fabrication of carbon fibre reinforced silicon nitride compositions.

5.1.1. Materials development

- Compositional engineering of the liquid phase formed during sintering of monolithic Si_3N_4 led to a reduction of up to 150°C in the sintering temperature required for near-full densification (>95%TD) compared to the reference YAG sinter additive composition.

- Densification of green body Si_3N_4 forms with varying additive concentration within $Y_2O_3 + Al_2O_3 + AlN$ series showed that the addition of 1wt% AlN was optimum for good densification at lower temperatures, reaching near-full densification at 1450°C. Within the CaZ series, the addition of just 1wt%CaO (corresponding to $3.2CaZrO_3$) was beneficial for densification achieving near-full densification at 50°C lower than the reference material. In both series of compositions the Al_2O_3 content was a crucial factor in final densification achieved.

- Chemical stability of these novel materials was maintained during sintering.

- The reaction sequences occurring during sintering of the AlN series and the CaZ series materials followed work carried out in parallel by Bandyopadhyay et al. [204] and Van Rutten [211], respectively.

- Densification of both series of compositions was seen to occur by sequential filling of smaller pores first, observed using SEM. Homogeneous densification was also observed, accompanied by the development of a fine-grained microstructure.

- α- to β-Si_3N_4 transformation was seen to accompany densification at each sintering temperature for each composition within the 1AlN series. At lower temperatures (<1600°C) enhanced densification of the sample 3.2CaZ occurred with retention of the α-Si_3N_4 structure.

- Sample porosity and percent residual α-Si_3N_4 were the dominant factor affecting the hardness of the sintered materials in both series. Hardness values in the range HV5 1452-1715 were measured for the AlN series of materials. The presence of ZrO_2 reduced the hardness of the samples in the 3.2CaZ resulting in hardness values in the range HV5 1338-1468.

- The crack type formed around the indent during hardness testing was intermediate between Palmqvist and median type. The Shetty equation for fracture toughness calculation was selected to best suit the present materials. The K_{1c} values calculated here compare well to those calculated for similar systems (4-7MPa.m$^{1/2}$).

- Preliminary oxidation tests on the selected 3.2CaZ material showed that the formation of easy-to-oxidise Zr-O-N phases has been avoided. The material showed good oxidation resistance (oxidation rate constant of 1.53×10^{-2} mg^2/cm^4.min at 1400°C).

- Using the selected novel matrix phases, 1AlN and 3.2CaZ, successful fabrication of Si_3N_4/C composite green bodies by pressure casting was achieved.

- A reduction of 100°C hot-pressing temperature required for full density was achieved for both composite compositions. The matrix and fibres in these composites had excellent thermal and chemical stability during the processing conditions. Under preliminary 3-point bend tests these composites exhibited `composite failure behaviour`.

- Fibre-matrix interactions were successfully limited in the composites densified by gas-pressure and pressureless sintering. However, constrained sintering caused by the presence of the fibres occurs, resulting in less than full theoretical density.

5.1.2. Processing Developments

- Incorporation of water-sensitive powders, AlN and CaO was successfully achieved by using an AlN water-resistant powder and adding CaO as its zirconate $CaZrO_3$.

- Matec^{TM} studies proved a dependable method for analysing suspension behaviour.

- Green body cracking was prevented by using a casting pressure of 7 bar for 10 minutes followed by very slow pressure release, and the application of a mould release agent. Application of a vacuum for 10-15 minute completely dried the surface of samples in the casting mould. Controlled drying helped prevent warping.

- Homogeneous distribution of fibres in the composite material was seen to be essential for good densification.

- Surrounding the samples with a sinter powder bed prevent volatilisation of gaseous products and placing a graphite piece above a layer of powder bed resulted in flat sintered monolithic samples.

- The use of graphite pieces in pressureless and gas-pressure sintering of the composite materials prevented warping, however, due to differences in the CTE between the matrix and fibre, cooling cracks were observed.

- Good sintering temperature control was maintained by using pyrometric contol with a window cleaning device, along with constant, regular calibrations and temperature checks using Philips Temperature Control Rings.

5.2. Contributions

- The present study has provided an insight into the densification behaviour of novel Si_3N_4-based ceramics.

- These novel Si_3N_4-based ceramics exhibit excellent potential as matrices for the fabrication of long fibre reinforced ceramic matrix composites without the need for expensive hot-pressing.

5.3. Proposed Further Research

The following research and development steps are proposed to contribute to the present field of study.

5.3.1. Monolithic Si_3N_4

- An extensive analysis, using Transmission Electron Microscopy, of the grain boundary phases formed during sintering of the material studied.

- An investigation into the development and composition of Zr-rich phases observed.

5.3.2. Si_3N_4/C Fibre Composite

- A systematic processing investigation using various combinations of fibre wetting agents, fibre volume, types of fibre (SiC fibres and coated fibres are suggested).

- Investigation into varying the sintering parameters, temperature, pressure, heating rate to enhance composite densification.

REFERENCES

1. European Commission, The World Growth Forecast for CMC Materials, 1993.
2. US Department of Energy Report: DE-AC01-91CE40956.
3. Prewo K.M., Brennan J.J., and Layden, G.K., Fiber Reinforced Glass Ceramic Matrix Composites Exhibiting High Strength and Toughness, Journal of Materials Science 17, pp. 2371-2383, 1986.
4. Warren R., Ceramic Matrix Composites, Chapman and Hall, NY, pp 55, 1992.
5. Designated WG 300, Greenleaf Corporation, Saegertown, PA, USA.
6. Noma T.and Sawaoka A., Effect of Heat Treatment on Fracture Toughness of Alumina-Diamond Composites Sintered at High Pressures, Journal of the American Ceramic Society Vol. 68, No. 2, pp. C-36-37, 1985.
7. Lange F.F., Transformation Toughening, Part IV: Fabrication, Fracture Toughness and Strength of Al_2O_3-ZrO_2 Composites, Journal of Materials Science Vol. 16, pp. 247-253, 1982.
8. Tsukuma K. Ueda K. and Shimada M., Strength and Fracture Toughness of Isostatically Hot-Pressed Composites of Al_2O_3 and Y_2O_3 Partially Stabilized ZrO_2, Journal of the American Ceramic Society Vol. 68, No. 1, pp. C4-5, 1985.
9. Tsukuma K. Ueda K. and Shimada M., High-Temperature Strength and Fracture Toughness of Y_2O_3-Partially Stabilized ZrO_2/Al_2O_3 Composites, Journal of the American Ceramic Society Vol. 68, No. 2, pp. C56-58, 1985.
10. Prewo K.M., Brennan J.J. and Layden G. K., Fiber Reinforced Glasses and Glass Ceramics for High Performance Applications, American Ceramic Society Bulletin, Vol. 65, No. 2, pp. 305-313, 1986.
11. Fitzer E. and Gadow R., Fiber-Reinforced Silicon Carbide, American Ceramic Society Bulletin, Vol. 65, No. 2, pp. 326-335, 1986.
12. Stinton D.P. Caputo A.J. and Lowden R. A., Synthesis of Fiber-Reinforced SiC Composites by Chemical Vapor Infiltration, American Ceramic Society Bulletin, Vol. 65, No. 2, pp. 347-350, 1986.
13. Hirai T. and Goto T., Preparation of Amorphous Si_3N_4-C Plate by Chemical Vapor Deposition, Journal of Materials Science, Vol. 16, pp. 17-23, 1981.
14. Hirai T. and Hayashi S., Synthesis of Si_3N_4-TiN Composite by Chemical Vapor Deposition, Proceedings 8th International Conference on CVD, Eds., J. Blocher,

G. Vuillard and G. Wahl, Electrochemical Society, Pennington, NJ, pp. 790-797, 1981.

15. Hirah, T, Goto, T. and Sakai T., Preparation of Amorphous Si_3N_4-BN Composites by Chemical Vapor Deposition, Materials Science Research, Vol. 17, pp. 347-358, 1984.
16. Mazdiyasni K.S. and Ruh R., High/Low Modulus Si_3N_4-BN Composite for Improved Electrical and Thermal Shock Behavior, Journal of the American Ceramic Society, Vol. 64, No. 7, pp. 415-419, 1981.
17. Dutta S. and Buzek B., Microstructure, Strength, and Oxidation of 10wt% Zyttrite-Si_3N_4 Ceramic, Journal of the American Ceramic Society, Vol. 67, No. 2, pp. 89-92, 1984.
18. Sahlek P.D., Petrovic J.J., Hurley G.F. and Gac, F.D., SiC Whisker-Hot Pressed Si_3N_4 Matrix Composites, American Ceramic Society Bulletin, Vol. 65, No. 2, pp. 351-356, 1986.
19. Olivier C.. Veyret J- B and Vidal-Setif M.H., Mechanical Properties of Hi-Nicalon Fibre-Reinforced Silicon Nitride Matrix Composites, Ceramic and Metal Matrix Composites I, Key Engineering Materials, Edited by. M. Fuentes, J.M. Martinez-Esnaola, and A.M. Daniel, San Sebastian, Vol 127-31, pp. 753-760, 1997.
20. Sabouret E., Veyret J. –B., Bullock E., Verwerft M. and Bronsveld P.M., Tailoring Interfaces in Long Carbon Fibre Reinforced Silicon Nitride Matrix Composites, Proceedings of the 4th International Symposium on Composite Materials, edited by S.A. Paipetis and A.G. Youtsos, September, 1995.
21. ONERA, Process for Fabricating a Ceramic Matrix Composite Incorporating Woven Fibers and Materials with Different Compositions and Properties in the Same Composite, Materials Technology, Vol. 10, pp. 89-103, 1995.
22. Burkland C.V., Bustamante W.E., Klacka R. and Yang J.-M., Whisker- and Fiber Toughnened Ceramics, ASM International, Materials Park, Ohio, pp. 225, 1988.
23. Montanaro L. and Guilhot B., Preparation of Microspheres from an Alumina-Zirconia Sol, American Ceramic Society Bulletin, 68, pp. 1017-1020, 1989.
24. Hatakeyama F. and Kanzaki S., Synthesis of Monodispersed Spherical β-Silicon Carbide Powder by Sol-Gel Process, Journal of the American Ceramic Society, Vol. 73, p. 2107-2110, 1990.

25. Rice R.W. and Lewis III D., Reference Book for Composites Technology, Eds. Lee, S. M., Technomic, Lancaster, PA, Vol. 1,Chapter 6, 1989.
26. Warren R., Ceramic Matrix Composites, Chapman and Hall, NY, pp. 7, 1992.
27. Richerson D.W., Design, Processing Development and Manufacturing Requirements of Ceramics and Ceramic Matrix Composites, Contractor Report, OTA, 1985.
28. Prewo K. M. and Brennan J. J., SiC Yarn Reinforced Glass Matrix Composites, Journal of Material Science, Vol. 17, pp.1201-1206, 1982.
29. Warren R., Ceramic Matrix Composites, Chapman and Hall, NY, pp. 5, 1992.
30. Warren R., Ceramic Matrix Composites, Chapman and Hall, NY, pp. 68, 1992.
31. Prewo K.M. and Brennan J.J., High-Strength Silicon Carbide Fibre-Reinforced Glass-Matrix Composites, Journal of Materials Science, Vol. 15, pp. 463-468, 1980.
32. Fitzer E., Hegen D.and Strohmeirer H., Chemical Vapour Deposition of Silicon Notride and Its Application for Preparation of Improved Silicon Ceramics, Proceedings of the Seventh International Conference on Chemical Vapour Deposition, Eds. T.O. Sedwich and H. Lydin, Electrochemical Society, Princeton, pp. 525-535, 1979.
33. Pfeifer W.H., Consolidation of Composite Structures by CVD, Second International Conference on Chemical Vapour Deposition, Eds. J.M. Blocher Jr. and J.C. Withers, Electrochemical Society, pp. 463-483, 1970.
34. Thesis Jr. J.C, The Process Development and Mechanical Testing of a Carbon/Carbon Composite Fabricated by Chemical Vapour Infiltration of a Filament-Wound Substrate, Third International Conference on Chemical Vapour Deposition, Eds. F.A. Glask, American Nuclear Society, pp. 561-573, 1972.
35. Christin F., Naslain R. and Bernard C., A Thermodynamic and Experimental Approach of Silicon Carbide CVD. Application to the CVD-Infiltration of Porous Carbon Composites, Proceedings of the 7th International Conference on CVD, Eds. T.O. Sedwich and H. Lydin, Electrochemical Society, Princeton, pp. 499, 1974.
36. Heraud L., Properties and Applications of Oxidation-Resistant Composite Materials Obtained by SiC-infiltration, Proceedings of the 8th International Conference on CVD, Edited by J.M. Blocher et al., The Electrochemical Society, Pennington, pp. 782 1981.

37. Fitzer E. and Gadow R., Fibre-Reinforced Silicon Carbide, American Ceramic Society Bulletin, Vol. 65, pp. 326-335, 1986.
38. Caputo A.J. and Lackey W.J., Fabrication of Fibre-reinforced Ceramic Composites by Chemical Vapour Infiltration, Ceramic Engineering Proceedings, Vol. 5,No. 7-8, pp. 654-667, 1984.
39. Caputo A.J. and Lackey W.J., Fabrication of Fibre-reinforced Ceramic Composites by Chemical Vapour Infiltration, ORNL/TM-9235, Oak Ridge National Laboratory, Oak Ridge, TN, October 1984.
40. .Caputo A.J., Lackey W.J. and Stinton D.P., Development of a New, Faster Process for the Fabrication of Fibre-reinforced Ceramic Composites by Chemical Vapour Infiltration, Ceramic Engineering Proceedings, Vol. 6, No. 7-8, pp. 694-706, 1985.
41. Colomban J.P., Gel Technology in Ceramics, Glass-Ceramics and Ceramic-Ceramic Composites, Ceramic International, Vol. 15, pp. 23-50, 1989.
42. Zelinski A.J. and Uhlman D.R., Gel Technology in Ceramics, Journal of Physics and Chemistry of Solids, Vol. 45, pp. 1069-1090, 1984.
43. Seyferth A. and. Wiseman G.H., A Novel Polymeric Organosilazane Precursor to Si_3N_4/SiC Ceramics, Science of Ceramic Chemical Processing, Edited by L.L. Hench and E.R. Ulrich, Published by John Wiley, New York, pp. 354-362, 1986.
44. Chi F. and. Stark G., US patent 4,460,639.
45. Chi F. and Stark G., US Patent 4,460,640.
46. Philips D.C., Fibre Reinforced Ceramics, Handbook of Composites, Fabrication of Composites, Edited by A. Kelly and S.T. Mileiko, North Holland, Amsterdam, Vol. 4: pp. 373-423, 1983.
47. Philips D. C. Fibre-Reinforced Ceramics, Survey of the Technological Requirements for High Temperature Materials Research and Development, Section 2: Ceramic Composites for High Temperature Engineering Applications, European Commission EUR 9565, pp. 48-73, 1985.
48. Kingery W.D., Densification during Sintering in the Presence of a Liquid Phase. I. Theory, Journal of Applied Physics, Vol. 30, No. 3, pp.301, 1959.
49. Kooner S., Campaniello J.J., Pickering S. and Bullock E., Fibre Reinforced Ceramic Matrix Composite Fabrication by Electrophoretic Infiltration, Proceedings of the 2nd Conference on High Temperature Ceramic Matrix Composites, Santa Barbara, August 1995.

50. Lange F.F., Constrained Network Model for Predicting Densification Behaviour of Composite Powders, Journal of Material Research, Vol. 2, No. 2, pp. 59-65, 1987.
51. Guo J.K., Carbon Fibre-reinforced Silicon Nitride Composites, Journal of Materials Science, Vol. 17, pp. 3611-3616, 1982.
52. Lange F.F., Powder Processing of Ceramic Matrix Composites, Materials Science and Engineering, A144, pp. 143-152, 1991.
53. Derjaguin A. and Landau L. Acta, Physiochim, No.14, pp.633 1941.
54. Verwey A.and Overbeek J.Th.G., Theory of the Stability of Lyophobic Colloids, Published by Elsevier, Amsterdam, 1948.
55. Bleir A., Acid-Base Properties of Ceramic Powder, Advances in Materials Characterisation., Edited by Rossington et al., Plenum Press, pp. 499-514, 1983.
56. Hackley V.A. and Malghan S.G., The Surface Chemistry of Silicon Nitride Powder in the Presence of Dissolved Ions, Journal of Materials Science, Vol. 29, pp. 4420-4430, 1994.
57. Parfitt G.D., Fundamental Aspects of Dispersion, Dispersion of Powders in Liquids, Applied Science, London, Chapter 1, pp. 1-49, 1981.
58. Liden A., Carlsson R., Persson M. and Bergstrom L., Surface Modification of Ceramic Powders, Euro Ceramics II-Basic Science and Processing of Ceramics, Edited by G. Ziegler and H. Hausner, Vol. 1, pp. 283-298, 1991.
59. Hackley V.A. and Malghan S.G., Polyelectrolytes as Dispersants in Colloidal Processing of Silicon Nitride Ceramics. Polymer Pre-prints, No. 34, pp. 1024, 1993.
60. Busca A., Lorenzelli V., Porcile G., Baraton, M.I., Quintard P., and Marchand R., FT-IR Study of the Surface Properties of Silicon Nitride, Materials Chemistry and Physics, Vol.14, pp.123 1986.
61. Bergstrom L. and Bostedt E., Surface Chemistry of Silicon Nitride Powders: Electrokinetic Behaviour and ESCA Studies, Colloids and Surfaces, Vol. 49, pp.183, 1990.
62. Bergstrom L. and Pugh R., Interfacial Characterisation of Silicon Nitride Powders, Journal of American Ceramic Society, Vol. 72, pp. 103-109, 1989.
63. Goodwin J.W., Colloidal Dispersions, Edited by J.W. Goodwin, The Royal Society of Chemistry, London, Chapter 8, 1982.

64. Dekker P., Principals of Colloid and Surface Chemistry, Edited by Langonski, Chapter 2, 1977.
65. Tiller F.M. and Tsai C. –D., Theory of Filtration of Ceramics: I Slip Casting, Journal of American Ceramic Society, Vol.69, No. 12, pp.882, 1986.
66. Rahaman M.N., Ceramic Processing and Sintering, Dekker, Incorporated, NY, Chapter 5, pp. 227, 1995.
67. Lange F.F. and Miller K.T., Pressure Filtration: Consolidation Kinetics and Mechanics, American Ceramic Society Bulletin, Vol. 66, No. 10, 1987.
68. Grenet C., Plunkett L., Veyret J. -B., and Bullock E., Carbon Fibre Reinforced Silicon Nitride Composite Fabricated by Slurry Infiltration, Proceeding of 2nd on High Temperature Ceramic Matrix Composites, Santa Barbara, August 1995.
69. Scherer W., Theory of Drying, Journal of the American Ceramic Society, Vol. 73 No. 1, pp. 3-14, 1990.
70. Macey A., Clay-Water Relationships and Internal Mechanism of Drying, Trans. British Ceramic Society Vol. 41, No. 4, pp. 73-121, 1942.
71. Moore F., The Mechanism of Moisture Movement in Clays with Particular Reference to Drying: A Concise Review", Trans. British Ceramic Society, Vol. 60, pp. 517-539, 1961.
72. Greskovich C. and Rosolowski H.H., Journal of the American Ceramic Society, Vol. 59, pp.337, 1976.
73. Shimada M., Tanaka, A., Yamada T. and Koizumi M., Ceramic Powder, Edited by P. Vincenzini, Elsevier Scientific, Amsterdam, pp. 871-879, 1983.
74. Rahaman M.N., Ceramic Processing and Sintering, Dekker, Incorporated, New York, Chapter 5, pp. 527, 1995.
75. Rahaman M.N., Ceramic Processing and Sintering, Dekker, Incorporated, New York, Chapter 5, pp. 528, 1995.
76. Rahaman M.N., Ceramic Processing and Sintering, Dekker, Incorporated, New York, Chapter 5, pp. 529, 1995.
77. Rahaman M.N., Ceramic Processing and Sintering, Dekker, Incorporated, New York, Chapter 5, pp. 532, 1995.
78. Rahaman M.N., Ceramic Processing and Sintering, Dekker, Incorporated, New York, Chapter 5, pp. 533, 1995.
79. Rahaman M.N., Ceramic Processing and Sintering, Dekker, Incorporated, New York, Chapter 5, pp. 537, 1995.

80. Rahaman M.N., Ceramic Processing and Sintering, Dekker, Incorporated, New York, Chapter 5, pp. 523, 1995.
81. German, R.M., Liquid Phase Sintering, Plenum, New York, 1985.
82. Kwon O. –J. and Yoon D.N., International Journal of Powder Metallurgy and Powder Technology, Vol. 17, pp. 127, 1981.
83. Shaw, T.M., Preparation and Sintering of Homogeneous Silicon Nitride Green Compacts, Journal of the American Ceramic Society, Vol. 69, pp. 88-93, 1986.
84. Huppmann W.J. and Riegger H., Acta Metallurgy, Vol. 23, pp. 965, 1975.
85. Rahaman M.N., Ceramic Processing and Sintering, Dekker, Incorporated, NY, Chapter 5, pp. 548, 1995.
86. Yoon D.N and Huppmann W.J., Grain Growth and Densification During Liquid Phase Sintering of W-Ni, Acta Metallography, Vol. 27, pp. 693-698, 1979.
87. Greenwood G.W., Acta Metall., Vol. 4, pp.243, 1956.
88. Lifshitz I.M. and Slyozov V.V., Physics and Chemistry of Solids, Vol. 19, pp. 35, 1961.
89. Wagner C., Z. Electrochem., Vol. 65, pp. 581, 1961
90. Kang S. –J.L., Kim K. –H. and Yoon D.N., Densification and Shrinkage During Liquid-Phase Sintering, Journal of the American Ceramic Society, Vol. 74, pp. 425-427, 1991.
91. Park H.H., Cho S.J. and Yoon D.N., Pore-Filling Process in Liquid-Phase Sintering, Metall. Trans. A, 15A, pp. 1075-1080, 1984.
92. Kingery W.D., Woulbroun J.M. and Charvat F.R., Effects of Applied Pressure on Densification During Sintering in the Presence of a Liquid Phase, Journal of the American Ceramic Society, Vol. 46, No. 8, 1963.
93. Ziegler G., Heinrich J. and Wotting G., Relationship between Properties of Dense and Reaction-Bonded Silicon Nitride, Journal of Materials Science, Vol. 22, pp. 3041-3086, 1987.
94. Lange F.F., Nitrogen Cermaics, Edited by F.L. Riley, Noordhoff/NATO, pp. 491, 1977.
95. Drew, P. and Lewis, M.H., Journal of Materials Science, Vol. 9, pp. 261-269, 1974.
96. Deeley G.G., Herbert J.M. and Moore N.C., Powder Metallurgy, Vol. 8, pp. 145-141, 1961.

97. Lange F.F., Journal of the American Ceramic Society, Vol. 60, No. 5-6, pp.249, 1977.

98. Lange F.F., Development of Surface Stress During the Oxidation of Several Si_3N_4/CeO_2 Materials, Journal of the American Ceramic Society, Vol. 62, pp.629-631, 1979.

99. Gazza G.E., Hot-Pressed Si_3N_4, Journal of the American Ceramic Society, Vol. 56, pp. 662-664, 1973.

100. Gazza G.E., American Ceramic Society Bulletin, Vol. 54, pp. 778-781, 1975.

101. Lange F.F., Phase Relations in the System Si_3N_4-SiO_2-MgO and Their Interrelation with Strength and Oxidation, Journal of the American Ceramic Society, Vol. 61, pp.53-56, 1978.

102. Greskovich C. and Prochazka C., Journal of the American Ceramic Society, Vol. 60, pp. 471, 1977.

103. Abe O., Sintering Process of Y_2O_3 - and Al_2O_3-Doped Si_3N_4, Journal of Materials Science, Vol. 25, pp. 4018-4026, 1990.

104. Loehman R.E. and Rowcliffe D.J., Sintering of Si_3N_4-Y_2O_3-Al_2O_3, Journal of the American Ceramic Society, Vol. 63, No. 3-4, pp. 144-148, 1980.

105. Lewis M.H., Sialons and Silicon Nitride Ceramics: Microstructural Design and Performance, Materials Research Society Symposium Proceedings, Vol. 287, pp. 172-175.

106. Turkdogan E.T., Bills P.M. and Tippet V.A., Silicon Nitrides: Some Physico-Chemical Properties, Journal of Applied Chemistry, Vol. 8, No. 5, pp. 296, 1958.

107. Hardie D. and Jack K.H., Nature, Vol. 180, pp.332, 1957.

108. Messier D.R. and Wong P., Kinetics of Nitridation of Si Powder Compacts, Journal of the American Ceramic Society, Vol. 56, pp. 480-485, 1973.

109. Longland P. and Mouslon A.J., The Growth of α- and β-Si_3N_4 Accompanying the Nitriding of Silicon Powder Compacts, Journal of Materials Science, Vol. 13, pp. 2279-2280, 1978.

110. Boyer S.M. and Mouslon A.J., A Mechanism for the Nitriding of Fe-Contaminated Silicon, Journal of Materials Science, Vol. 13, pp. 1637-1646, 1978.

111. Oyama Y. and Kamigaito O., Japanese Journal of Applied Physics, Vol. 10, pp. 1637, 1971.

112. Jack, K.H. and Wilson W.I., Ceramics Based on the Si-Al-O-N and Related Systems, Nature (London) Physical Science, Vol. 238, pp. 28, 1977.

113. Cao G.Z. and Metselaar R., α-Silaon Ceramics: A Review, Chemistry of Materials, Vol. 3, pp. 242-252, 1991.

114. Hampshire S., Park H.K., Thompson D.P. and Jack K.H., α`-Sialon Ceramics, Nature, Vol. 274, pp. 880-882, 1978.

115. Hampshire S., Nitride Ceramics, Structure and Properties of Ceramics, Materials Science and Technology, Vol. 11, pp. 155, 1994.

116. Ekstrom T. and Nygren M., SiAlON Ceramics, Journal of the American Ceramic Society, Vol. 75, No. 2, pp. 259-276, 1992.

117. Nickel K.G., Hoffmann, M.J. Greil P. and Petzow G., Thermodynamic Calculations for the Formation of SiC-Whisker-Reinforced Si_3N_4 Ceramics, Advanced Ceramic Materials, Vol. 3, No. 6, pp. 557-562, 1988.

118. Luthra K.L. and Park H.D., Chemical Considerations in Carbon-Fiber/Oxide-Matrix Composites, Journal of the American Ceramic Society, Vol. 75, No. 7, pp. 1889-1898, 1992.

119. Huang Z.K., Greil P. and Petzow G., Formation of α-Si_3N_4 Solid Solutions in the System Si_3N_4-AlN-Y_2O_3, Advanced Ceramic Materials, No. 66, Vol. 6, pp. C-96-97, 1983.

120. Lange F.F., Davies B.I., and Graham H.C., Compressive Creep and Oxidation Resistance of and Si_3N_4 Material Fabricated in the System Si_3N_4-Si_2N_2O-$Y_2Si_2O_7$, Advanced Ceramic Materials, No. 66, Vol. 6, pp. C-98-99, 1983.

121. Hseuh C –H., Evans A.G. and McMeeking R.M., Influence of Multiple Heterogeneities on Sintering Rates, Journal of the American Ceramic Society, Vol. 69, No. 4, C64-C66, 1986.

122. Raj R. and Bordia R.K., Sintering Behaviour of Bi-Modal Powder Compacts, Acta Metallurgy, Vol. 32, No. 7, pp. 1003-1019.

123. Scherer G.W., Sintering with Rigid inclusions, Journal of the American Ceramic Society, Vol. 70, No. 11, pp. 719-725, 1987.

124. Rahaman M.N., Ceramic Processing and Sintering, Dekker, Incorporated, NY, Chapter 5, pp. 609, 1995.

125. De Jonghe L.C. and Rahaman M.N., Densification of Particulate Ceramic Composites: The Role of Hetrogeneities, Materials Research Society Symposium Proceedings, Vol. 155, pp. 353-360, 1989.

126. Lange F.F., Densification of Powder Rings Constrained by Dense Cylindrical Cores, Acta Metallurgy, Vol. 37, No. 2, pp. 697-704, 1989.

127. Lange F.F., Lam D.C.C., Sudre O., Flinn B.D., Folsom C., Velamakanni B.V., Zok F.W. and Evans A.G., Powder Processing of Ceramic Matrix Composites, Materials Science and Engineering, A144, pp. 143-152, 1991.

128. Dalgleish B.J., Slamovich E. and Evans A.G., Journal of Material Energy Systems, Vol 8, pp. 211-225, 1986.

129. Lange F.F., Powder Processing of Continuous Fiber Ceramic Matrix Composites: Incorporating Reinforcements and Matrix Strengthening, Proceedings of High Temperature Ceramic Matrix Composites I., Edited by R. Naslain, J. Lamon and D. Doumeingts, pp. 119-142, 1993.

130. Amin, K.E., Toughness, Hardness, and Wear, Engineering Materials Handbook, Vol.4, pp. 599-609, 1991

131. Parr, N.L., Mastin G.F. and May E.R.W., Special Ceramics. London, Haywood and Co. Ltd, pp. 102, 1960.

132. Pratt, P.L., Mechanical Properties of Engineering Ceramics, New York, Interscience, pp. 507,1961.

133. Dunegan, H.C., Mechanical Properties of Engineering Ceramics, New York, Interscience, pp. 521, 1961.

134. Noakes, P.B. and Pratt P.L., Special Ceramics 5, Stoke-on-Trent, British Ceramic Research Association, pp. 299, 1972.

135. Chakraborty, D. and Mukerji J., Characterization of Silicon Nitride Single Crystals and Polycrystalline Reaction Sintered Silicon Nitride by Microhardness Measurements, Journal of Materials Science, Vol.. 15, pp. 3051-3056, 1980.

136. Chakraborty, D. and Mukerji J., Effect of Crystal Orientation, Structure and Dimension on Vickers Microhardness Anistropy of β-, α-Si_3N_4, α-SiO_2 and α-SiC Single Crystals, Materials Research Bulletin, Vol. 17, pp. 843-849, 1982.

137. Jack, K.H., The Characterisation of α`-Sialons and the α-β Relationships in Sialons and Silicon Nitride, Progress in Nitrogen Ceramics, Netherlands, Nijhoff Publishers, pp. 45-60, 1983.

138. Greskovich, C. and Gazza G.E., Hardness of Dense α- and β-Si_3N_4 Ceramics, Journal of Materials Science Letters, Vol. 4, pp. 195-196.

139. Jasper, C.A. and Lewis M.H., Novel α/β Sialon Ceramics, Ceramic Materials and Components for Engines, London, Elsevier, pp. 424-431, 1991.

140. Ekstrom, T., Hardness of Dense Si_3N_4 Based Ceramics, Journal of Hard Materials, Issue 4, pp. 77-95, 1993.

141. Broek, D., Elementary Engineering Fracture Mechanics of Engineering Materials, Dordrecht, Nijhoff, Chapters 2-5, 1987.

142. Kanninen M.F. and Popelar C.H., Advanced Fracture Mechanics, New York, Oxford University Press, Chapter 3, 1985.

143. Hertzberg R.W., Deformation and Fracture Mechanics of Engineering Materials, 2nd Edition, New York, Wiley, Chapters 7-8, 1983.

144. Sakai M. and Bradt R.C., Fracture Toughness Testing of Brittle Materials, International Materials Reviews, Vol. 38, No. 2, pp. 53-78, 1993.

145. Davidge R.W., Mechanical Behaviour of Ceramics, Cambridge, Cambridge University Press, Chapters 2-3, 1979.

146. Sakai M. and Bradt R.C., Fracture Mechanics of Ceramics, New York, Plenum Press, Vol. 7, pp. 127-142, 1986.

147. Hirosaki N., Akimune Y. and Mitomo M., Effect of Grain Growth of β-Silicon Nitride on Strength, Weibull Modulus, and Fracture Toughness, Journal of the American Ceramic Society, Vol. 76, No. 7, pp. 1892-1894, 1993.

148. Hirosaki N., Akimune Y. and Mitomo M., Microstructure Characterisation of Gas-Pressure-Sintered β-Silicon Nitride Containing Large β-Silicon Nitride Seeds, Journal of the American Ceramic Society, Vol. 78, No. 1, pp. 211-214, 1995.

149. Kawashima T., Okamoto H., Yamamoto H. and Kitamura A., Grain Size Dependence of the Fracture Toughness of Silicon Nitride Ceramics, Journal of the Ceramic Society Japan, Vol. 99, No. 4, pp. 320-323, 1991.

150. Peterson M. and Tien T –Y., Effect of the Grain Boundary Thermal Expansion Coefficient on the Fracture Toughness in Silicon Nitride, Journal of the Ceramic Society, Vol. 78, No. 9, pp. 2345-2352, 1995.

151. Becher F., Hwang S.L., Lin T. and Tiegs T.N., Microstructural Contributions to the Fracture Resistance of Silicon Nitride, Tailoring of Mechanical Properties

of Si_3N_4 Ceramics, Edited by M.J. Hoffmann and G. Petzow, Kluwer, UK, pp. 85-100, 1994.

152. Kleebe H –J., Pezzotti G. and Ziegler G., Microstructure and Fracture Toughness of Si_3N_4 Ceramics: Combined Roles of Grain Morphology and Secondary Phase Chemistry, Journal of the Ceramic Society, Vol. 82, No. 7, pp. 1857-1867, 1999.

153. Hendry A. Proceeding of NATO Conference, Nitrogen Ceramics, Edited by F.L. Riley, Leiden, Elsevier, pp. 183, 1977.

154. Phelke R.D. and Elliot J.F., Transactions A.I.M.E., Vol. 215, pp. 718, 1959.

155. Kofstad P., High Temperature Oxidation of Metals, Wiley and Sons Incorporated, New York, 1966.

156. Lewis M. and Barnard P., Oxidation Mechanisms in Si-Al-O-N Ceramics, Journal of Materials Science, Vol. 15, pp. 443-448, 1980.

157. Gototsi, Y.G., Grathwohl G., Thummler, Yaroshenko, V.P., Herrmann M. and Taut C., Oxidation of Yttria- and Alumina-containing Dense Silicon Nitride Ceramics, Journal of the European Ceramic Society, Vol. 11, pp. 375-386, 1993.

158. Komeya K., Haruna Y., Meguro T., Kameda T. and Asayama M., Oxidation Behaviour of the Sintered Si_3N_4-Y_2O_3-Al_2O_3 System, Journal of Materials Science, Vol. 27, pp. 5727-5734, 1992.

159. Desmaison-Brut M. and Billy M., High Temperature Corrosion of Technical Ceramics, Edited by R.D. Fordham, London, Elsevier, pp. 131-140, 1990.

160. Lamkin M.A., Riley F.L. and Fordham R.J., Journal of the European Ceramic Society, Vol. 10, pp. 347, 1992.

161. Bellosi, A., Vincenzini P. and Babini G.N., Stability of Si_3N_4-Al_2O_3-ZrO_2 Composites in Oxygen Environments, Journal of Materials Science, Vol. 23, pp. 2348-2354, 1998.

162. Kodash V.Y., Kaidash O.N., Korablev S.F. and Danilenko N.V., Oxidation Resistance of Silicon Nitride Ceramics with ZrO_2 Additives, Electrochemical Society Proceedings, Vol. 97-139, pp. 820, 1995.

163. Lange F.F., Falk L.K.L. and Davies B.I., Structural Ceramics Based on Si_3N_4-ZrO_2 (+Y_2O_3) Compositions, Journal of Materials Research, Vol. 2, No. 1, pp. 66-76, 1987.

164. Lange F.F., Compressive Surface Stresses Developed in Ceramics by an Oxidation-Induced Phase Change, Journal of the American Ceramic Society, Vol. 63, No. 1-2, pp. 38-40, 1980.

165. Ekstrom T., Falk L.K.L. and Knutson-Wedel E.M., Si_3N_4-ZrO_2 Composites with small Al_2O_3 and Y_2O_3 Additions Prepared by HIP, Journal of Materials Science, Vol. 26, pp. 4331-4340, 1991.

166. Hirano S. Hayashi T. and Nakashima T., Sintering of β-Sialon with 5mol%Y_2O_3-ZrO_2 Additives, Journal of Materials Science, Vol. 24, pp. 3712-3716, 1989.

167. Tjernlund, A.K., Pompe R., Holmstrom M. and Carlsson R., On the Influence of Atmosphere on the Phase Reactions Involving the System Si_3N_4-ZrO_2, Special Ceramics 8, Edited by Howlett and Taylor, pp. 29-34, 1986.

168. Kerans R.J., Hay R.S., Pagano N.J. and Parthasarathy T.A., The Role of Fiber-Matrix Interface in Ceramic Composites, Ceramic Bulletin, Vol. 68, No. 2, pp. 429-442, 1989.

169. Aveston J., Cooper G.A. and Kelly A., Single and Multiple Fracture, The Properties of Fibre Composites, NPL, IPC Science and Technology Press Ltd., pp. 15-24, 1971.

170. Philips D.C., Fibre Reinforced Ceramics, Handbook of Composites, Edited by A. Kelly and S.T. Mileiko, London, Elsevier, Vol. 4, pp. 409-410, 1983.

171. Komeya, K., Komatsu M., Kameda T., Goto Y. and Tsuge A., High-strength Silicon Nitride Ceramics Obtained by Grain-Boundary Crystallization, Journal of Materials Science, Vol. 26, pp. 5513-5516, 1991.

172. Hwang S-L. and Chen I-W., Reaction Hot-Pressing of α'- and β'-SiAlON Ceramics, Journal of the American Ceramic Society, Vol. 77, No. 1, pp. 165-171.

173. Levis E.M., Robbins C.R., McMurdie H.F. and Reser M.K., Phase Diagrams for Ceramists, American Ceramic Society, Columbus, Ohio, Figure 630.

174. Ryshewitch E., Oxide Ceramics, Academic Press, Chapter 5, pp.360, 1960.

175. Vomacka P. and Babushkin O., Yttria-Alumina-Silica Glasses with the Addition of Zirconia, Journal of the European Ceramic Society, Vol. 15, pp. 921-928, 1995.

176. Cheng Y. and Thompson D.P., The Behaviour of ZrO_2 in Y_2O_3-Al_2O_3-SiO_2 Glasses, British Ceramic Transaction Journal, Vol. 87, pp. 107-110, 1988.

177. Vomacka P. Ramesh R. and Hampshire S., Influence of Zirconia Addition on the Crystallisation Kinetics of a Y-Si-Al-O-N Glass, Journal of the European Ceramic Society, Vol. 16, pp. 1253-1262, 1997.

178. O'Brien R.W., Electroacoustic Equations for Colloidal Suspensions, Journal of Fluid Mechanics, Vol. 2212, pp. 81-93, 1990.

179. Szegvari A. and Yang M., Attritor Grinding and Dispersing Equipment, Seminar on Dispersion of Pigments and Resins in Fluid Media, Kent State University, Kent, Ohio, May 1984.

180. Pompe R. and Carlsson R., Sintering of Si_3N_4-Based Materials Using the Powder Bed Technique, Progress in Nitrogen Ceramics, Edited by F. L. Riley, The Hague: Martinus Nijhoff, pp. 219-224.

181. Ashworth D.R., A Method of Determining the Bulk Density of Ceramics, Journal of the British Ceramic Society, Vol. 7, pp. 70-72, 1969.

182. Cullity D., Elements of X-Ray Diffraction, 2nd Publication, Addison-Wesley, 1978.

183. Klug A.P. and Alexander L.E., X-ray Diffraction Procedures for Polycrystalline and Amorphous Materials", Edited by J. Wiley and Sons, 2nd Edition, 1974.

184. "Invitation to the SEM World". JEOL publication.

185. ASM Handbook, Metallography and Microstructures, Vol. 9, 1992.

186. P. Moretto, CEN/VAMAS Round Robin on Phase Volume Fraction, 2, private communication, 1999.

187. Van der Voort G.F. and Lucas G.M., "Microindentation Hardness Testing". Advanced Materials and Processes, Vol. 9, pp.21-25, 1998.

188. D.M. Butterfield, D.J. Clinton and R. Morrell, The VAMAS Hardness Test Round-Robin on Ceramic Materials, Report No. 3. National Physics Laboratory, Teddington, England, pp. 1, Apr. 1989

189. Evans A.G., Fracture Toughness, the Role of Indentation Techniques, STP 678, American Society for Testing and Materials, pp. 113, 1979.

190. Marshall D.B., Lawn B.R. and Evans A.G., Elastic/Plastic Indentation Damage in Ceramics – The Lateral Crack System, Journal of the American Ceramic Society, Vol. 65, No. 11, pp. 561, 1982.

191. Kwon O.H. and Trogolo J.A., Postindentation Slow Crack Growth in Zirconia Ceramics, Conference Proceedings, Annual ACS Meeting, Indianapolis, US, April, 1989.

192. Ponton C.B. and Rawlings R.D. Vickers Indentation Fracture Toughness Test Part 1 Review of Literature and Formulation of Standardised Indentation Toughness Equations, Materials Science and Technology, Vol. 5, pp. 865-872, 1989.

193. Ponton C.B. and Rawlings R.D. Vickers Indentation Fracture Toughness Test Part 2 Application and Critical Evaluation of Standardised Indentation Toughness Equations, Materials Science and Technology, Vol. 5, pp. 961-976, 1989.

194. Hills D.A., The Use of Indentation Tests to Determine the Fracture Toughness of Brittle Materials, Journal of Mechanical Engineering Science, Vol. 203, pp. 333-341, 1989.

195. Bowen P., Highfield J.G., Mocellin A. and Ring T.A., Degradation of Aluminium Nitride Powder in an Aqueous Environment, Journal of the American Ceramic Society, Vol. 73, No. 3, pp. 724-728, 1990.

196. Morz T.J., Aluminium Nitride, American Ceramic Bulletin, Vol. 73, No. 6, pp. 77-80, 1994.

197. Sabouret E., PhD Thesis, IAM, JRC, Petten, NL., 1996.

198. Plunkett L., Grenet C., Veyret J. –B. and Bullock E., Internal Publication, European Commission, Joint Research Centre, Institute of Materials, Petten, The Netherlands, 1993.

199. Itturiza I., Castro F. and Fuentes M., Sinter and sinter-HIP of Silicon Nitride Ceramics with Yttria and Alumina Additions, Journal of Materials Science, Vol. 24, pp. 2947-2056, 1989.

200. Terwillinger G.R. and Lange F.F., Presureless Sintering of Si_3N_4, Journal of Materials Science, Vol. 10, No. 7, pp.1169-1174, 1976.

201. Greskovich C. and Prochazka, Stability of Si_3N_4 and Liquid Phase(s) During Sintering, Communications of the American Ceramic Society, Vol. 64,No. 7, C-96-C-97, 1981.

202. Lange F.F., Volatilization Associated with the Sintering of Polyphase Si_3N_4 Materials, Communications of the American Ceramic Society, Vol. 65, C-120-C-121, 1982.

203. Lange F.F., Silicon Nitride Polyphase Systems: Fabrication, Microstructure and Properties, International Metals Review, Review 247, No. 1, pp. 1-20, 1980.

204. Bandyopadhyay S., Hoffmann M.J. and Petzow G., Densification Behaviour and Properties of Y_2O_3-Containing α-SiAlON-Based Composites, Journal of the American Ceramic Society, Vol. 79, No. 6, pp. 1537, 1545, 1996.

205. Levin E.M., Robbins C.R., McMurdie H.F. and Reser M.K., Phase Diagrams for Ceramists, American Ceramic Society, Columbus, Ohio, Figure 2586, pp.165, 1969.

206. Takata H., Martin C. and Ishizaki, Effect of Particle Size and Additives in Silicon Nitride Sintering, Journal of the Ceramic Society of Japan, International Edition, Vol. 96, pp. 847-881, 1988.

207. Jack K.H., Sialons: A Study in Materials Development, Non-Oxide Technical and Engineering Ceramics, Edited by S. Hampshire, London, Elsevier, pp. 1-30, 1986.

208. Hampshire S., Nitride Ceramics, Structure and Properties of Ceramics, Materials Science and Technology, Vol. 11, pp. 133, 1994.

209. Gob O., Herrmann M., Siegel S. and Obernaus P., Origins and Avoidance of Colour Inhomogeneities in Silicon Nitride Ceramics, Proceedings of Euro Ceramics V, Key Engineering Materials, Vol 132-136, pp. 751-754, 1998.

210. Levin E.M., Robbins C.R., McMurdie H.F. and Reser M.K., Phase Diagrams for Ceramists, American Ceramic Society, Columbus, Ohio, Figure 630, 1969.

211. Van Rutten J.W.T., Hintzen H.T. and Metselaar R., Phase Formation of Ca-α-sialon by Reaction Sintering, Journal of the European Ceramic Society, Vol. 16, pp. 995-999, 1996.

212. Hampshire S., Nitride Ceramics, Structure and Properties of Ceramics, Materials Science and Technology, Vol. 11, pp. 136, 1994.

213. Phase Diagrams for Zirconia and Zirconium Systems, Edited by M.K. Reser, American Ceramic Society, Columbus, OH, USA.

214. Falk L.K.L. and Holmstrom M.M., Microstructural Development During Processing of a Si_3N_4/ZrO_2 Material, Euro-Ceramics I, Edited by G. De Width, R.A. Terpstra and R. Metselaar, London Elsevier, 1989.

215. Lange F.F., Transformation Toughening, Part III: Experimental Observations in the ZrO_2-Y_2O_3 System, Journal of Materials Science Vol. 17, pp. 240-246, 1982.

216. Hewett C.L., Cheng Y.-B-, Muddle B.C. and Trigg M.B., Calcium Sialon Ceramics, Materials Research 96, Conference Proceedings Vol. 1, The Institute of Metals and Materials Australasia Ltd., Brisbane, pp. 101-104, 1996.

217. Mandal H., Thompson D.P. and Ekstrom T:, Reversible α-β Sialon Transformation in Heat-Treated Sialon Ceramics, Journal of the European Ceramic Society, Vol. 12, pp. 421, 1993.

218. Mukhopadyay A.K., Datta S.K. and Chakraborty D., Hardness of Silicon Nitride and Sialon Ceramics, Ceramics International, No. 17, pp. 121-127, 1990.

219. Mukhopadyay A.K., Datta S.K. and Chakraborty D., On the Microhardness of Silicon Nitride and Sialon Ceramics, Journal of the European Ceramic Society, Vol. 6, pp. 303-311, 1990.

220. Babini G.N., Bellosi A. and Galassi C., Characterisation of Hot-Pressed Silicon Nitride Based Materials by Microhardness Measurements, Journal of Materials Science, Vol. 22, pp. 1678-1693, 1987.

221. Knutson-Wedel E.M., Falk L.K.L., Bjorklund H. and Ekstrom T., Si_3N_4 Ceramics Formed by HIP Using Different Oxide Additions – Relation between Microstructure and Properties, Journal of Materials Science, Vol. 26, pp. 5575-5584, 1991.

222. Li H. and Bradt R.C., The Microhardness Indentation Load/Size Effect in Rutil and Cassiterite Single Crystals, Journal of Materials Science, Vol. 28, pp. 917-926, 1993..

223. Guillou M. –O., Henshall J.L., Hooper R.M. and Carter G.M., Indentation Fracture Testing and Analysis, and Its Application to Yirconia, Silicon Carbide and Silicon Nitride Ceramics, Journal of Hard Materials, Vol. 3, No. 3-4, pp. 421-434, 1992.

224. Dusza J., Comparison of Fracture Toughness Testing Methods Applied to Si_3N_4 + Si_3N_4-whisker System, Scripta Metallurgia et Materiala, Vol. 26, pp. 337-342, 1992.

225. Anstis G.R., Chantikul O., Lawn B.R. and Marshall D.B., A Critical Evaluation of Indentation Techniques for Measuring Fracture Toughness: I,

Direct Crack Measurements, Journal of the American Ceramic Society, Vol. 64, No. 9, pp. 533-538, 1981.

226. Niihara K., Morena R. and Hasselman D.P.H., Evaluation of K_{1c} of Brittle Solids by the Indentation Method with Low Crack-to Indent Ratios, Journal of Materials Science Letter, Vol. 1, pp. 13-16, 1982.

227. Laugier M.T., New Formulae for Indentation Fracture Toughness in Ceramics, Journal of Materials Science Latters, Vol. 6, pp. 335-356, 1987.

228. Niihara K., A Fracture Mechanics Analysis of Indentation-Induced Palmqvist Crack in Ceramics, Journal of Materials Science Letters, Vol. 2, pp. 221-223, 1983.

229. Shetty D.K., Wright I.G., Mincer P.N. and Clauer A.H., Indentation Fracture of Wc-Co Cerments, Journal of Materials Science, Vol. 20, pp. 1872-1882, 1985.

230. Philips D.C., Fibre Reinforced Ceramics, Handbook of Composites, Edited by A. Kelly and S.T. Mileiko, London, Elsevier, Vol. 4, pp. 405, 1983.

231. Clegg W.J., Mc Alford N. and Birchaöö J.D., Back Stresses and the Sintering of Composites, British Ceramic Proceedings, Vol. 39, pp. 247-254, 1987.

232. Evans A.G. and Zok F.W., The Physices and Mechanics of Fibre-Reinforced Brittle Matrix Composites, Journal of Materials Science, Vol. 29, pp. 3857-3896, 1994.

233. Sabouret E. and Veyret J. –B., Internal Communication, European Commission, Joint Research Centre, Institute for Advanced Materials, Petten, The Netherlands, 1995.

234. Marshall D.B. and Evans A.G., Failure Mechanisms in Ceramic-Fiber/Ceramic Matrix Composites, Journal of the American Ceramic Society, Vol. 68, No. 5, pp. 225-231, 1985.

235. Lamon, J., Interfaces and Interfacial Mechanics: Influence on the Mechanical Behaviour of Ceramic Matrix Composites (CMC), Journal De Physique IV, C7, Vol. 3, pp. 1607-1616, 1993.

236. Naslain R., Fibre-matrix Interphases and Interfaces in Ceramic Matrix Composites Processed by CVI, Composite Interfaces, Vol. 1, No. 3, pp. 253-286, 1993.

237. Lowden R.A., Advanced Composite Materials, Ceramic Transactions, American Ceramic Society, Vol. 19, pp. 619, 1991.

238. Kamiya K., Kikuo N., Sigeharu M., Toru I. and Hiroshi I., Mechanical Properties of Unidirectional Hi-Nicalon Fiber-Reinforced Si_3N_4 Matrix Composites, Journal of the Japanese Ceramic Society, Vol. 102, No. 10, pp. 957-960.

239. Veyret J. –B., Tambuyser P., Olivier C., Bullock E. and Vidal-Set M. –H., Hi-Nicalon Reinforced Silicon Nitride Matrix Composites, Journal of Materials Science, Vol. 32, pp. 3457-3462, 1997.